ABSTRACT

Title of dissertation: MULTISCALE MODELING
AND SIMULATION OF
STEPPED CRYSTAL SURFACES

Joshua P. Schneider, Doctor of Philosophy, 2016

Dissertation directed by: Professor Dionisios Margetis
Department of Mathematics

A primary goal of this dissertation is to understand the links between mathematical models that describe crystal surfaces at three fundamental length scales: The scale of individual atoms, the scale of collections of atoms forming crystal defects, and macroscopic scale. Characterizing connections between different classes of models is a critical task for gaining insight into the physics they describe, a long-standing objective in applied analysis, and also highly relevant in engineering applications. The key concept I use in each problem addressed in this thesis is *coarse graining*, which is a strategy for connecting fine representations or models with coarser representations. Often this idea is invoked to reduce a large *discrete* system to an appropriate *continuum* description, e.g. individual particles are represented by a continuous density. While there is no general theory of coarse graining, one closely related mathematical approach is asymptotic analysis, i.e. the description of limiting behavior as some parameter becomes very large or very small. In the case of crystalline solids, it is natural to consider cases where the number of

particles is large or where the lattice spacing is small. Limits such as these often make explicit the nature of links between models capturing different scales, and, once established, provide a means of improving our understanding, or the models themselves. Finding appropriate variables whose limits illustrate the important connections between models is no easy task, however. This is one area where computer simulation is extremely helpful, as it allows us to see the results of complex dynamics and gather clues regarding the roles of different physical quantities. On the other hand, connections between models enable the development of novel multiscale computational schemes, so understanding can assist computation and vice versa. Some of these ideas are demonstrated in this thesis. The important outcomes of this thesis include: (1) a systematic derivation of the step-flow model of Burton, Cabrera, and Frank, with corrections, from an atomistic solid-on-solid-type models in 1+1 dimensions; (2) the inclusion of an atomistically motivated transport mechanism in an island dynamics model allowing for a more detailed account of mound evolution; and (3) the development of a hybrid discrete-continuum scheme for simulating the relaxation of a faceted crystal mound. Central to all of these modeling and simulation efforts is the presence of *steps* composed of individual layers of atoms on vicinal crystal surfaces. Consequently, a recurring theme in this research is the observation that mesoscale defects play a crucial role in crystal morphological evolution.

MULTISCALE MODELING AND SIMULATION OF STEPPED CRYSTAL SURFACES

by

Joshua P. Schneider

Dissertation submitted to the Faculty of the Graduate School of the
University of Maryland, College Park in partial fulfillment
of the requirements for the degree of
Doctor of Philosophy
2016

Advisory Committee:
Professor Dionisios Margetis (Chair)
Professor Theodore L. Einstein
Professor Maria Cameron
Professor Konstantina Trivisa
Professor John D. Weeks

Acknowledgments

I would like to express my gratitude to Dio Margetis, my adviser, whose steady encouragement, constructive criticism, and invariable patience enabled me to become the applied mathematician I am today. I also thank Ted Einstein, who taught me an incredible amount about statistical mechanics and the physics of crystal growth in my time at the University of Maryland. And I give my sincere thanks to my committee members for all of their support throughout the last several years, and useful feedback on my thesis.

There are a myriad of other professors and graduate students who helped cultivate me as a young researcher. In particular, I would like to thank Patrick Fitzpatrick, Howard Elman, Stuart Antman, Ricardo Nochetto, Kanna Nakamura, and Paul Patrone for all of their assistance and advice during my graduate years.

My deepest thanks go out to my wife, Erin Lynn, and my children Samantha Jane and Mary Clare Ann. Without their unfailing love and support, I would not be where I am today. In the same vein, I am eternally grateful for the encouragement of my wonderful family, loyal friends, and so many caring community members from the Catholic Student Center, St. Jerome's Parish, and the University of Maryland.

I acknowledge partial support of the National Science Foundation, Division of Mathematical Sciences, through grants DMS-0847587 and DMS-1412769 at the University of Maryland. Additionally, many of the results in this dissertation were made possible by Jeff McKinney, who provided extraordinary technical assistance and computational resources on behalf of the University of Maryland.

Table of Contents

List of Figures

Chapter 1: Introduction

The study of crystal growth has inspired a plethora of mathematical models that aim to capture the essential aspects of the growth process. These models come in a variety of forms, depending on the range of length and time scales they describe. At the macroscale, crystal surface morphologies are often represented by continuous height profiles, which presumably evolve according to partial differential equations (PDEs). At atomistic scales, the motion of atoms may be specified by ordinary differential equations (ODEs), such as those resulting from Newton's second law, or by stochastic processes, e.g. by Markov chains.

At a rich middle-ground between continuum and atomistic are *mesoscale* models, which often describe the motion of collections of atoms forming *defects* on a crystal surface. One such treatment of crystal growth was introduced in the seminal work by Burton, Cabrera, and Frank (BCF) [12], which identified *steps* formed by monatomic layers of atoms on a crystal surface as critical components of the growth process. Mathematically, the BCF model is a Stefan problem [81] where steps act as free boundaries separating large, flat terraces. On terraces, adsorbed atoms (adatoms) are represented by a mean-field density, assumed to satisfy a diffusion equation [12]. Typically, the PDE governing adatom density is supplied with

Robin boundary conditions, equating the normal derivative of adatom density at the step edge to a linear function of density [36, 59, 74]. Additionally, by mass conservation, a step retreats or advances as atoms leave the step or are incorporated into the step from ajoining terraces; this is expressed by a "Stefan condition" known as the step velocity law [36, 59, 74].

Each type of model discussed above has its own set of weaknesses. Continuum models, for example, may not properly account for discrete dynamics at interfaces. On the other hand, atomistic models often involve restrictions on system size due to computational limitations. It is interesting, then, to ask what insight might be gained from *multiscale* approaches describing crystal morphological evolution. This thesis attempts to provide some answers to this question. Accordingly, we study atomistic and continuum models in connection with the BCF description of crystal surface dynamics. To do so, we employ a variety of analytical and computational tools. The analytical aspects of this work touch upon classical theories of stochastic processes, ODEs and PDEs, and asymptotic analysis. Computational tools include kinetic Monte Carlo (KMC) [9,87,106], the level set method [65,66,90], and standard solvers for ODEs and PDEs [99]. The results obtained in this thesis often require the integration of analysis and computations, a common feature of multiscale approaches (see, e.g., [10, 109]). Likewise, the notion of coarse graining is a frequently invoked heuristic.

Of the two parts in this thesis, Part I is more analytical, but makes judicious use of KMC simulations in an effort to understand the atomistic processes leading to the BCF model in one dimension (1D). Part II, on the other hand, focuses on the

simulation of crystal growth at atomistic, mesoscopic, and macroscopic scales in 2D. The common thread among these is the BCF description of stepped crystal surfaces. As such, we start by investigating the atomistic origins of the BCF model using a kinetic, restricted solid-on-solid (KRSOS) model of a single step in 1D, whereby atoms with multiple nearest neighbor bonds are immobile [70, 71]. To this end, we exploit properties of the Markov process underlying the KRSOS model, such as detailed balance, to derive a discrete analog of the BCF model. The discrete BCF-like model that emerges from our analysis involves correction terms, which we characterize using a blend of analytical and numerical methods.

Although the KRSOS model assumes that adatoms do not interact with one another energetically, we identify "kinetic interactions" between adatoms as the source of certain corrections to the discrete analog of the BCF model. These kinetic interactions result from atomistic transitions included in the KRSOS model. In an effort to better understand the nature of corrections to the BCF model, at the end of Part I we explore the properties an "alternate" KRSOS model that does *not* include the kinetic interactions between adatoms in the original KRSOS model. Subsequent analysis of the alternate KRSOS model, together with KMC simulation results, leads us to conclude that discrete corrections to the BCF diffusion equation for adatom density sensitively depend on the choice of transition rates in Markov process describing our atomistic model.

After a thorough investigation of the connection between KRSOS and BCF models in 1D, we venture into the 2D setting (Part II). The first problem we address in 2D is the incorporation into a mesoscale island dynamics model [68] of certain

atomistic mass transport mechanisms associated with external material deposition, i.e. transient mobility [32, 60] and downward funneling [16, 26, 46]. This is accomplished by effectively introducing each mechanism in the island dynamics model by modification of deposition near steps as well as step velocities. We are able to show qualitative agreement between the mesoscale model and the results of KMC simulations including transient mobility [94].

The last problem addressed in this thesis concerns relaxation dynamics of a faceted crystalline mound. In this work, we connect the mesoscale BCF model of step flow to a thermodynamics-based PDE for the surface height of a crystalline mound. Here, the height profile includes a macroscopically flat region called a *facet*, which is treated as a free boundary in our PDE formulation of the problem. We find that discrete dynamics near the facet play a critical role in macroscale surface evolution, and devise a discrete-continuum hybrid scheme coupling the motion of discrete steps to the continuous slope profile of the mound. This scheme enables the efficient simulation of faceted mound decay and highlights the distinct nature of the chemical potential on the facet [86].

The remainder of this dissertation is organized as follows. Part I, which explores the atomistic origins of the BCF model of a single step, is divided into three chapters. In Chapter 2, we introduce a KRSOS model which enriches the one in [70, 71] with external deposition and adatom desorption. This KRSOS model is formulated as a Markov process, which we describe using a variety of master equations. The long-time behavior of the KRSOS model is also characterized in that chapter. Next, Chapter 3, is devoted to the derivation of a discrete version of

the BCF model, given in terms of averages over KRSOS microstates. The analysis here makes direct use of master equations from Chapter 2. The discrete BCF-like equations have corrections, for which we compute estimates in terms of model parameters. In the last stage of our derivation of the BCF model, we assume appropriate scaling of model parameters with lattice spacing before taking the continuum limit. Finally, the discrete corrections are computed using KMC simulations with several parameter sets.

The final component of Part I, Chapter 4, introduces an alternate KRSOS model by a small modification of the original KRSOS model in Chapter 2. We go on to study several key differences between the two KRSOS models, as well as the corrections that emerge from their respective derivations of the BCF model. In the end, we find that the corrections resulting from the alternate KRSOS model are universally smaller than those from the original KRSOS model, computed via KMC simulations. Moreover, our comparative study reveals that two types of corrections are possible; one set of corrections results from the choice of the atomistic model, while the other is more fundamental, i.e., certain corrections result from a wide class of atomistic models.

In Part II, we investigate mound evolution in 2D. First, Chapter 5 addresses the incorporation of transient mobility and downward funneling in an island dynamics model well suited for simulation by the level set method. The main results include level set simulations that qualitatively agree with KMC simulations of mound growth. In each case, slope stabilization is observed. Second, we study the decay of a semi-infinite, faceted crystalline mound. Here, we formulate a hybrid scheme that

couples a PDE for continuum height with the motion of a few steps, whose trajectories are given by the BCF model. It is shown that our hybrid scheme produces height profiles in excellent agreement with many-step simulations. Note that this work was published in reference [86].

PART I

Atomistic origins of BCF model in 1+1-dimensions

Chapter 2: Atomistic model of a single step

In this chapter, we introduce a kinetic, restricted solid-on-solid (KRSOS) model of a single step, based on the foundational work of [70]. This KRSOS model serves as the starting point for our investigation of the atomistic origins of the BCF model of crystal growth. It describes transitions between atomistic configurations through the processes of adatom hopping, attachment to and detachment from the step, external material deposition, and desorption. Mathematically, the KRSOS model is a Markov process with a discrete, countable state space of atomistic configurations. Accordingly, the evolution of a time-dependent probability density function (PDF) over atomistic configurations is governed by a master equation. For Part I of this thesis, we make use of *several*, related master equations with appropriately defined transition rates. The analysis carried out in Chapter 3, for example, makes heavy use of two of the master equations introduced in this chapter.

Once we have fully specified the KRSOS model, we characterize its long-time behavior in three parameter regimes: The first is a parameter regime that results in conservative dynamics, for which no mass is gained or lost by the system via external deposition or desorption of atoms. The second regime involves parameters that dictate mass is constant *on average* for long times, which we describe as

"quasi-conservative" dynamics, where the external deposition and desorption rates are roughly the same order of magnitude. And the third parameter regime leads to non-conservative dynamics, where mass continuously increases in the long-time limit because the deposition rate greatly exceeds the desorption rate. Of the three parameter regimes we consider, the case of conservative dynamics is treated in [70,71]. Specifically, in [71], the authors give an expression for the equilibrium distribution of KRSOS configurations on the basis of the canonical ensemble from statistical mechanics. In this chapter, we improve upon this result by deriving a simple, closed form formula for the equilibrium distribution of the Markov process governing the KRSOS model. Going beyond conservative dynamics, we also determine the equilibrium distribution in the quasi-conservative parameter regime by invoking detailed balance. Furthermore, in the non-conservative case, we formally derive a steady-state distribution for the Markov process describing the KRSOS model.

The final result presented in this chapter is a proposition that allows us to estimate time-dependent PDFs with corresponding stationary distributions. This proposition is a generalization of the so-called "maximum principles" found in [70, 71]. This "maximum principle" is a cornerstone of Part I of this thesis; together with the equilibrium and steady-state distributions we determine, it enables rigorous estimates of corrections that emerge from the discrete version of the BCF model derived in Chapter 3. *Note that this "maximum principle" bears no connection to the maximum principle in potential theory of Markov chains [11], or maximum principles invoked in the theory of second-order, elliptic PDEs [29]. For continuity with past works, however, we will use this loose terminology, but include it in quotations*

in an attempt to reduce confusion.

2.1 The kinetic, restricted solid-on-solid model

At the microscale, we consider a simple-cubic crystal surface with a single step [70, 71]. The surface consists of distinct height columns on an 1D lattice of lateral spacing a, with total length $L = Na$; see Fig. 2.1. We consider $L = \mathcal{O}(1)$ as $a \to 0$, e.g., by setting $L = 1$. Screw-periodic boundary conditions are applied in the x-direction.

Atoms of the top layer that have two in-plane nearest neighbors are *step atoms* [70, 71]; these atoms are immobile in our model. In contrast, the atom of the step edge, which lies at one end of the top layer, has a single in-plane nearest neighbor and is referred to as an *edge atom*; it may detach from the step and move to one of the adjacent terraces. By this picture, the adatoms are movable atoms that are neither edge atoms nor step atoms [70, 71].

To establish a meaningful SOS model in 1D, we do not allow islands to nucleate [71]; thus, if any two adatoms become nearest neighbors on a terrace, they do not form a bond with each other. Adatoms are free to diffuse across the surface until they reach the step, which acts as a sink or source of them. Externally deposited atoms are assumed to become adatoms on the terrace instantly, and may not attach to the step directly [49]. Similarly, neither step atoms nor edge atoms may desorb from the surface.

2.1.1 Atomistic processes and system representation

Our model is characterized by transitions between discrete configurations of adatoms. The total mass of these configurations is not conserved when deposition or desorption events are included. The transitions are controlled by F, the rate that particles are deposited into the system, as well as by Arrhenius rates proportional to $\exp[-E/(k_BT)]$, where T is the absolute temperature, k_B is Boltzmann's constant, and E is an appropriate activation energy; see [71]. These kinetic rates correspond to atomistic processes of surface diffusion, attachment/detachment at the step, and desorption from terraces.

The basic processes allowed by our 1D atomistic model are shown in Fig. 2.1. The requisite atomistic rates can be described as follows [71]. First, the rate $D = \nu \exp[-E_S/(k_BT)]$ accounts for unbiased adatom hopping on terraces sufficiently away from a step edge; the prefactor ν is an attempt frequency. The extra factor $\phi_\pm = \exp[-E_\pm/(k_BT)]$ expresses additional energy barriers, $E_\pm$, corresponding to adatom attachment to the step edge from the lower (+) or upper (−) terrace. The factor $k = \exp[-E_N/(k_BT)]$ accounts for the extra energy, E_N, that is necessary for the breaking of the nearest-neighbor bond between an edge atom and step atom, so that an atom detaches from the step edge. Lastly, $\tau^{-1} = \nu_e \exp[-E_e/(k_BT)]$ is the desorption rate, which indicates the rate at which adatoms evaporate from the surface. It is important to note that atoms may not be deposited directly to, or desorb directly from the step edge in this formulation of the model.

Following [71], we are compelled to represent atomistic configurations by *mul-*

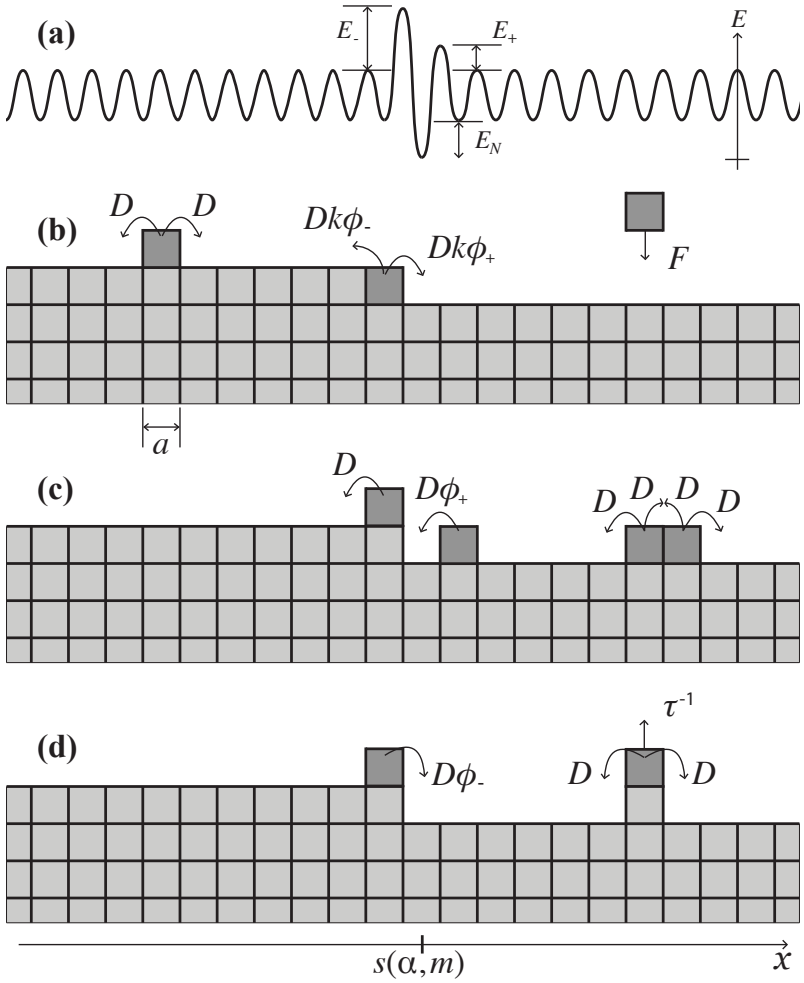

Figure 2.1: Microscopic picture: Schematic of atomistic processes allowed by the 1D atomistic model on a lattice with lateral spacing a. The configuration-dependent step position is labeled $s(\boldsymbol{\alpha}, m)$; see Definition 2. Movable atoms (adatoms) are shown in dark grey. (a) First panel: Illustration of the potential energy surface describing Arrhenius transition rates in the KRSOS model. E_N accounts for bonding energy and $E_\pm$ are Ehrlich-Schwoebel barriers to the right $(+)$ and left $(-)$ of the step. (b) Second panel: Hopping of adatoms on each terrace with rate D, detachment of edge atom from step to upper $(-)$ or lower $(+)$ terrace with rate $Dk\phi_\pm$, and deposition of atoms from above with rate F. (c) Third panel: Hopping of an adatom at the step to same terrace with rate D, attachment of an adatom from lower terrace to step edge with rate $D\phi_+$, and hopping of (unbonded) adatoms forming a pair with rate D. Adatoms cannot form islands. (d) Fourth panel: Attachment of adatom from upper terrace to step edge, hopping of an adatom to same terrace, and desorption of an adatom from a terrace. Only the top adatom in a stack is mobile.

tisets. A multiset, $\boldsymbol{\alpha}$, is an unordered list whose entries correspond to the positions of adatoms on the 1D lattice; in particular, $\boldsymbol{\alpha} = \{\}$ expresses a configuration that is void of adatoms. Accordingly, repeated entries in $\boldsymbol{\alpha}$ indicate multiple adatoms occupying the same lattice site; for example, the system configuration represented by $\boldsymbol{\alpha} = \{\hat{\imath}, \hat{\jmath}, \hat{\jmath}\}$ has one adatom at site $\hat{\imath}$ and two adatoms at site $\hat{\jmath}$. The number of adatoms corresponding to $\boldsymbol{\alpha}$ is simply $|\boldsymbol{\alpha}|$, the cardinality of the multiset. Without any restriction on its cardinality, there is a countably infinite number of adatom configurations $\boldsymbol{\alpha}$. We make one notable departure from previous uses of this notation [70, 71]; in this thesis the multisets $\boldsymbol{\alpha}$ contain adatom positions *in Lagrangian coordinates*, that is, in a frame of reference relative to the step edge. An example illustrating the connection between Eulerian and Lagrangian indices is provided in Figure 2.2. For notational convenience, indices i and j are used to reference lattice sites in Eulerian coordinates, while $\hat{\imath}$ and $\hat{\jmath}$ are used to reference lattice sites in Lagrangian coordinates throughout this thesis.

In connecting the atomistic model to one-step flow with $F = 0$, $\tau^{-1} = 0$ in 1D, our approach relies on explicitly determining the position of the step edge at time $t > 0$ from the number of adatoms, $|\boldsymbol{\alpha}|$, and the initial adatom configuration [70, 71]. This is a consequence of mass conservation. If deposition or desorption are included, however, more information is needed in order to track the step edge: At every atomistic transition, one must account for the atoms entering or leaving the system through processes not conserving total mass.

For our purposes, a system representation that allows this bookkeeping results from using an integer, m, in addition to using $\boldsymbol{\alpha}$. This m is the total *mass*, or

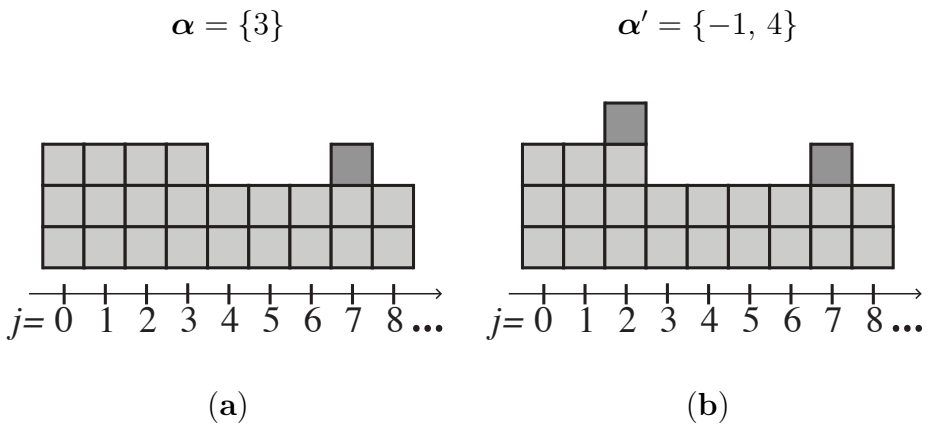

Figure 2.2: Illustration of multiset $\boldsymbol{\alpha}$ before and after a detachment event. For each Eulerian lattice site, indexed by j, the corresponding Lagrangian index is $\hat{\jmath} = j - s(\boldsymbol{\alpha}, m)$; see Definition 2. (a) Before a detachment event, the step position is $s(\boldsymbol{\alpha}, m) = 4$, an adatom (dark grey) is located at $j = 7$ in the Eulerian coordinate frame, and the corresponding Lagrangian multiset is $\boldsymbol{\alpha} = \{3\}$. (b) After the edge atom detaches to the upper terrace, the step position is $s(\boldsymbol{\alpha}', m) = 3$, adatoms (dark grey) are located at $j = 2, 7$ in the Eulerian coordinate frame, and the corresponding Lagrangian multiset is $\boldsymbol{\alpha}' = \{-1, 4\}$.

number of atoms, of the system. Thus, if m_0 is the initial mass then $m - m_0$ measures the overall mass increase because of external deposition. Finally, given the initial position of the the site to the right of the step edge, s_0, in a fixed (Eulerian) coordinate system, we can explicitly track the step for all time $t > 0$.

Definition 1. (Representation of atomistic system.) *The pair* $(\boldsymbol{\alpha}, m)$ *defines the* state *of the atomistic system: the multiset* $\boldsymbol{\alpha}$ *expresses the adatom configuration and the index* m *is an integer that counts the overall mass of the system. Thus, if* m_0 *is the initial mass then* $m - m_0$ *accounts for net mass gain or loss due to deposition and desorption events.*

Definition 2. (Discrete step position.) *For each state* $(\boldsymbol{\alpha}, m)$*, the discrete* step position *in Eulerian coordinates is* $s(\boldsymbol{\alpha}, m) = s_0 - |\boldsymbol{\alpha}| + m - m_0$*. For fixed mass* m*, the step position is uniquely determined from the number of adatoms* $|\boldsymbol{\alpha}|$ *and the initial position of the site to the right of the step edge,* s_0*. Accordingly,* $s(\boldsymbol{\alpha}, m)$ *also references the site to the right of the step edge; see Figure 2.1.*

2.2 Master equations

In this section, we define equations governing the time-evolution of the KRSOS model in two scenarios: When mass variable m is explicitly required, and when it is not. In each case, the time-dependent probability distribution over atomistic configurations evolves according to a *master equation*, of which we give three: The first, our "full" master equation, describes the time rate-of-change of a mass-dependent PDF; the second "marginalized" master equation is defined for marginal PDFs;

and the final "symbolic" master equation is a restatement of the full master equation. The symbolic master equation is introduced as a pragmatic tool to be used in Chapter 3, where certain calculations are simplified or made more transparent by symbolic manipulation. All three master equations will be utilized at various points in Part I of this thesis.

2.2.1 Full master equation

At this stage we introduce the full master equation describing evolution of the atomistic system. Let $p_{\boldsymbol{\alpha},m}(t)$, defined over the domain of discrete states $(\boldsymbol{\alpha}, m)$, denote time-dependent PDF characterizing the KRSOS model. Accordingly, the time evolution of the system is described by master equation

$$\dot{p}_{\boldsymbol{\alpha},m}(t) = \sum_{\boldsymbol{\alpha}',m'} T_{(\boldsymbol{\alpha},m),(\boldsymbol{\alpha}',m')} p_{\boldsymbol{\alpha}',m'}(t) \ , \tag{2.1}$$

under given initial data, $p_{\boldsymbol{\alpha},m}(0)$. In the above, $T_{(\boldsymbol{\alpha},m),(\boldsymbol{\alpha}',m')}$ expresses the overall transition of the system from state $(\boldsymbol{\alpha}', m')$ to state $(\boldsymbol{\alpha}, m)$. Master equation (2.1) governs a Markov process with a countably infinite state space.

Next, we describe the rates $T_{(\boldsymbol{\alpha},m),(\boldsymbol{\alpha}',m')}$. The nonzero transition rates obey

the following rules:

$$T_{(\boldsymbol{\alpha},m),(\boldsymbol{\alpha}',m')} = D\ , \qquad \text{if } m = m' \text{ and } |\boldsymbol{\alpha}| = |\boldsymbol{\alpha}'| \text{ and } |\boldsymbol{\alpha} \setminus \boldsymbol{\alpha}'| = 1 \text{ and } \Big|\,||\boldsymbol{\alpha} \setminus \boldsymbol{\alpha}'|| - ||\boldsymbol{\alpha}' \setminus \boldsymbol{\alpha}||\,\Big| = 1; \tag{2.2a}$$

$$T_{(\boldsymbol{\alpha},m),(\boldsymbol{\alpha}',m')} = D\phi_{\pm}\ , \qquad \text{if } m = m' \text{ and } |\boldsymbol{\alpha}| = |\boldsymbol{\alpha}'| - 1 \text{ and } \boldsymbol{\alpha}' \setminus \tilde{\boldsymbol{\alpha}} = \{\pm 1\}; \tag{2.2b}$$

$$T_{(\boldsymbol{\alpha},m),(\boldsymbol{\alpha}',m')} = Dk\phi_{\pm}\ , \qquad \text{if } m = m' \text{ and } |\boldsymbol{\alpha}| = |\boldsymbol{\alpha}'| + 1 \text{ and } \boldsymbol{\alpha} \setminus \tilde{\boldsymbol{\alpha}}' = \{\pm 1\}; \tag{2.2c}$$

$$T_{(\boldsymbol{\alpha},m),(\boldsymbol{\alpha}',m')} = \frac{1}{\tau}\ , \qquad \text{if } m = m' - 1 \text{ and } |\boldsymbol{\alpha}| = |\boldsymbol{\alpha}'| - 1 \text{ and } |\boldsymbol{\alpha}' \setminus \boldsymbol{\alpha}| = 1; \tag{2.2d}$$

$$T_{(\boldsymbol{\alpha},m),(\boldsymbol{\alpha}',m')} = \frac{F}{N-1}\ , \qquad \text{if } m = m' + 1 \text{ and } |\boldsymbol{\alpha}| = |\boldsymbol{\alpha}'| + 1 \text{ and } |\boldsymbol{\alpha} \setminus \boldsymbol{\alpha}'| = 1; \tag{2.2e}$$

and, so that probability is conserved,

$$T_{(\boldsymbol{\alpha}',m'),(\boldsymbol{\alpha}',m')} = \quad - \sum_{\substack{(\boldsymbol{\alpha},m) \\ (\boldsymbol{\alpha},m)\neq(\boldsymbol{\alpha}',m')}} T_{(\boldsymbol{\alpha},m),(\boldsymbol{\alpha}',m')}\ , \qquad \text{for all } (\boldsymbol{\alpha}',m'). \tag{2.2f}$$

All transition rates not listed in (2.2) are zero. Here, we introduce the multiset difference $\boldsymbol{\alpha} \setminus \boldsymbol{\alpha}'$, which itself is a multiset containing the elements in $\boldsymbol{\alpha}$ that are not in $\boldsymbol{\alpha}'$, counting multiplicity. For example, $\{\hat{\imath},\hat{\jmath},\hat{\jmath}\} \setminus \{\hat{\jmath}\} = \{\hat{\imath},\hat{\jmath}\}$. Additionally, the symbol $||\cdot||$ indicates the ℓ^p-norm with $p \geq 1$, and the "multiset-increment operation", $\tilde{\boldsymbol{\alpha}}$, is the multiset $\boldsymbol{\alpha}$ after each element has been incremented by one. Setting $F = 0$, $\tau^{-1} = 0$, and assuming $p_{\boldsymbol{\alpha},m}(0) = \delta_{m,m_0} p_{\boldsymbol{\alpha}}(0)$, (2.1) reduces to the master equation governing surface relaxation [71].

Among the transition rates that are zero, notable examples include

$$T_{(\boldsymbol{\alpha},m),(\boldsymbol{\alpha}',m')} = 0 \ , \qquad \text{if } m = m' \text{ and } |\boldsymbol{\alpha}| < |\boldsymbol{\alpha}'| - 1 \text{ or } |\boldsymbol{\alpha}| > |\boldsymbol{\alpha}'| + 1; \tag{2.3a}$$

$$T_{(\boldsymbol{\alpha},m),(\boldsymbol{\alpha}',m')} = 0 \ , \qquad \text{if } m = m' \text{ and } |\boldsymbol{\alpha}| = |\boldsymbol{\alpha}'| + 1 \text{ and } -1 \in \boldsymbol{\alpha}'; \tag{2.3b}$$

$$T_{(\boldsymbol{\alpha},m),(\boldsymbol{\alpha}',m')} = 0 \ , \qquad \text{if } m = m' - 1 \text{ and } |\boldsymbol{\alpha}| \geq |\boldsymbol{\alpha}'|; \tag{2.3c}$$

$$T_{(\boldsymbol{\alpha},m),(\boldsymbol{\alpha}',m')} = 0 \ , \qquad \text{if } m = m' + 1 \text{ and } |\boldsymbol{\alpha}| \leq |\boldsymbol{\alpha}'|. \tag{2.3d}$$

Equation (2.3a) indicates that no more than one atom may attach to or detach from the step in a single transition. Equation (2.3b) asserts that no atoms may detach if the site directly above the edge atom is occupied, Equation (2.3c) ensures that only adatoms may desorb, and (2.3d) prevents atoms from being deposited at $s(\boldsymbol{\alpha}, m)$. Note that the transitions described in (2.2a)-(2.2c), along with (2.3a) and (2.3b) are subject to detailed balance [49, 71].

Master equation (2.1) along with transition rates (2.2) and (2.3) completely govern the full mass-dependent microscale model.

2.2.2 Marginalized master equation

There is one parameter regime, i.e. $F \gg \tau^{-1}$ (including the case where $\tau^{-1} = 0$), where we make use of a master equation that describes the evolution of a *marginalized* probability density function, $p_{\boldsymbol{\alpha}}(t)$, such that the mass variable has been summed. For nonzero deposition flux, $p_{\boldsymbol{\alpha}}(t)$ amounts to a PDF over states in a frame of reference co-moving with the step.

Definition 3. (Marginal probability density function.) *The marginal probability density is*

$$p_{\boldsymbol{\alpha}}(t) = \sum_{m} p_{\boldsymbol{\alpha},m}(t) \ , \tag{2.4}$$

where $p_{\boldsymbol{\alpha},m}(t)$ satisfies equation (2.1) with transition rates (2.2) and (2.3).

The marginal PDF in Definition 3 satisfies what what will be referred to as the marginalized master equation, found by summing over the mass variable on both sides of equation (2.1). It is important to note that a sum over m on the right hand side of (2.1) requires care since both the transition rates, $T_{(\boldsymbol{\alpha},m),(\boldsymbol{\alpha}',m')}$, and the PDF, $p_{\boldsymbol{\alpha},m}(t)$, each depend on m. This can be done by first decomposing $T_{(\boldsymbol{\alpha},m),(\boldsymbol{\alpha}',m')}$ into contributions from various mass states, i.e. $m' = m-1$, m, and $m+1$, or using the symbolic master equation outlined in Section 2.2.3.

Next, we give the marginalized master equation and rules for the associated transition rates. The master equation for the marginalized PDF of Definition 3 is

$$\begin{aligned} \dot{p}_{\boldsymbol{\alpha}}(t) &= \sum_{\boldsymbol{\alpha}'} T_{\boldsymbol{\alpha},\boldsymbol{\alpha}'} p_{\boldsymbol{\alpha}'}(t) \\ &= D \sum_{\boldsymbol{\alpha}'} \left[A_{\boldsymbol{\alpha},\boldsymbol{\alpha}'} + \epsilon B_{\boldsymbol{\alpha},\boldsymbol{\alpha}'} \right] p_{\boldsymbol{\alpha}'}(t) \ . \end{aligned} \tag{2.5}$$

Here, $A_{\boldsymbol{\alpha},\boldsymbol{\alpha}'}$ accounts for the atomistic processes of attachment and detachment at the step edge, and adatom hopping on each terrace, as described in [71]; and $B_{\boldsymbol{\alpha},\boldsymbol{\alpha}'}$, together with the non-dimensional parameter $\epsilon := F/D$, accounts for material deposition onto and desorption from the surface. In equation (2.5), ϵ plays the role of a Péclet number, measuring the deposition rate relative to terrace diffusion. Note that the symbol R has previously been used for the inverse ratio, $R = D/F$, in part

of the physics literature [3].

The scaled, nonzero transition rates $A_{\boldsymbol{\alpha},\boldsymbol{\alpha}'}$ and $B_{\boldsymbol{\alpha},\boldsymbol{\alpha}'}$ can be described by rules similar to those in (2.2). They are

$$A_{\boldsymbol{\alpha},\boldsymbol{\alpha}'} = 1 \ , \ \text{if } |\boldsymbol{\alpha}| = |\boldsymbol{\alpha}'| \text{ and } \ |\boldsymbol{\alpha} \setminus \boldsymbol{\alpha}'| = 1 \text{ and } \Big| ||\boldsymbol{\alpha} \setminus \boldsymbol{\alpha}'|| - ||\boldsymbol{\alpha}' \setminus \boldsymbol{\alpha}|| \Big| = 1; \quad (2.6a)$$

$$A_{\boldsymbol{\alpha},\boldsymbol{\alpha}'} = \phi_{\pm} \ , \qquad \text{if } \ |\boldsymbol{\alpha}| = |\boldsymbol{\alpha}'| - 1 \text{ and } \boldsymbol{\alpha}' \setminus \tilde{\boldsymbol{\alpha}} = \{\pm 1\}; \quad (2.6b)$$

$$A_{\boldsymbol{\alpha},\boldsymbol{\alpha}'} = k\phi_{\pm} \ , \qquad \text{if } \ |\boldsymbol{\alpha}| = |\boldsymbol{\alpha}'| + 1 \text{ and } \boldsymbol{\alpha} \setminus \tilde{\boldsymbol{\alpha}}' = \{\pm 1\}; \quad (2.6c)$$

$$B_{\boldsymbol{\alpha},\boldsymbol{\alpha}'} = \sum_{\hat{\imath} \in \boldsymbol{\alpha}} \frac{1}{F\tau} \ , \qquad \text{if } |\boldsymbol{\alpha}| = |\boldsymbol{\alpha}'| - 1 \text{ and } \ |\boldsymbol{\alpha}' \setminus \boldsymbol{\alpha}| = 1; \quad (2.6d)$$

$$B_{\boldsymbol{\alpha},\boldsymbol{\alpha}'} = \frac{1}{N-1} \ , \qquad \text{if } |\boldsymbol{\alpha}| = |\boldsymbol{\alpha}'| + 1 \text{ and } \ |\boldsymbol{\alpha} \setminus \boldsymbol{\alpha}'| = 1; \quad (2.6e)$$

$$A_{\boldsymbol{\alpha}',\boldsymbol{\alpha}'} = -\sum_{\substack{\boldsymbol{\alpha} \\ \boldsymbol{\alpha} \neq \boldsymbol{\alpha}'}} A_{\boldsymbol{\alpha},\boldsymbol{\alpha}'} \ , B_{\boldsymbol{\alpha}',\boldsymbol{\alpha}'} = -\sum_{\substack{\boldsymbol{\alpha} \\ \boldsymbol{\alpha} \neq \boldsymbol{\alpha}'}} B_{\boldsymbol{\alpha},\boldsymbol{\alpha}'} \ , \qquad \text{for all } \boldsymbol{\alpha}'. \quad (2.6f)$$

In the spirit of [71], one may view master equation (2.5) as a kinetic hierarchy of coupled particle equations for adatoms. Using a combinatorial argument, for fixed number of adatoms, $|\boldsymbol{\alpha}| = n$, there are

$$\omega(n) = \begin{pmatrix} n+N-2 \\ n \end{pmatrix} \quad (2.7)$$

distinct atomistic configurations on the 1D lattice of size N ($N \geq 2$), where the step site, $s(\boldsymbol{\alpha}, m)$, is left vacant. From equation (2.7) we find

$$\Omega(M) = \sum_{n=0}^{M} \omega(n) = \begin{pmatrix} M+N-1 \\ M \end{pmatrix} \ , \quad (2.8)$$

which is the total number of configurations with M or fewer adatoms, $|\boldsymbol{\alpha}| \leq M$. By Stirling's formula, it can be shown that $\ln \Omega(M)$ grows as $\mathcal{O}(M)$ for $M \gg 1$ with $M = \mathcal{O}(N)$. Thus, the state space of the PDF satisfying master equation (2.5),

or (2.1) for fixed m, grows quite rapidly with the number of particle states considered. In [70, 71] this complication is avoided by restricting attention to a "dilute" regime, in which the dynamics of (2.5) are dominated primarily by 0- and 1-particle states.

In this thesis, we seek to address parameter regimes for which high particle states play an important role. Master equations (2.1) and (2.5) reflect this insofar as $|\boldsymbol{\alpha}|$ is unrestricted. Yet, for one case considered, when $F \gg \tau^{-1}$, we will need to assume that the number of adatoms cannot exceed a certain bound, M: $|\boldsymbol{\alpha}| \leq M$, where M is a fixed yet arbitrary positive integer. For this purpose, we introduce the *truncated* master equation

$$\begin{aligned} \dot{\mathbf{p}}^{\epsilon}(t) &= \mathfrak{T}\mathbf{p}^{\epsilon}(t) \\ &= D(\mathfrak{A} + \epsilon\mathfrak{B})\mathbf{p}^{\epsilon}(t) \ , \end{aligned} \tag{2.9}$$

where $\mathbf{p}^{\epsilon}$ is the ϵ-dependent vector of dimension $\Omega(M)$ formed by $p_{\boldsymbol{\alpha}}$, and the $\mathfrak{T}$ matrix is split into the (finite-dimensional) attachment/detachment matrix, $\mathfrak{A}$, and the deposition/desorption matrix, $\epsilon\,\mathfrak{B}$, in correspondence to the $A_{\boldsymbol{\alpha},\boldsymbol{\alpha}'}$ and $\epsilon B_{\boldsymbol{\alpha},\boldsymbol{\alpha}'}$ of (2.6). When referring to truncated master equation (2.9), we will assume ϵ-independent initial data, $\mathbf{p}(0) =: \mathbf{p}_0$.

2.2.3 Symbolic master equation

In this section, we represent master equation (2.1) in a form that is more amenable to the type of analysis performed in this thesis. By doing so, it is easy to identify how (2.5) results from marginalizing (2.1) over the mass variable m, as well

as symbolically perform calculations involving the master equation. The symbolic version of the master equation presented in this section is the primary tool used in the derivation of discrete, BCF-like equations of motion presented in Chapter 3.

Before giving the alternate representation of the master equation (2.1), let us first introduce some notation.

Definition 4. (Multiset operations)

(i) The multiset-increment operation is

$$\tilde{\boldsymbol{\alpha}} = \{\hat{\imath} + 1 | \textit{ for all } \hat{\imath} \in \boldsymbol{\alpha}\} \ , \tag{2.10a}$$

i.e., an over-tilde expresses the multiset after each element is increased by one.

(ii) Analogously, the multiset-decrement operation is

$$\underset{\sim}{\boldsymbol{\alpha}} = \{\hat{\imath} - 1 | \textit{ for all } \hat{\imath} \in \boldsymbol{\alpha}\} \ . \tag{2.10b}$$

(iii) The multiset $\boldsymbol{\alpha}$ after a rightward (+) or leftward (−) detachment is

$$\boldsymbol{\alpha}_{\pm} = \tilde{\boldsymbol{\alpha}} \cup \{\pm 1\} \ . \tag{2.10c}$$

In the above, $\{\pm 1\}$ is added to the Lagrangian multiset $\boldsymbol{\alpha}$ after *each element is increased by one since the positions of adatoms on the terrace change relative to the step after a detachment event.*

(iv) The multiset $\boldsymbol{\alpha}$ after an attachment event from the right (+) or from the left (−) is

$$\boldsymbol{\alpha}^{\pm} = \begin{cases} \underset{\sim}{\boldsymbol{\alpha}} \setminus \{\pm 1 - 1\} \ , & \textit{if } \pm 1 \in \boldsymbol{\alpha} \\ \{\emptyset\} \ , & \textit{otherwise,} \end{cases} \tag{2.10d}$$

where the multiset-decrement operation is used since the positions of adatoms on the terrace change relative to the step after an attachment event.

(v) The multiset $\boldsymbol{\alpha}$ *after an additional adatom has been placed on the surface at (Lagrangian) site* $\hat{\imath}$*, e.g. after a deposition event, is*

$$\boldsymbol{\alpha}_{\hat{\imath}} = \boldsymbol{\alpha} \cup \{\hat{\imath}\} \ . \tag{2.10e}$$

(vi) The multiset $\boldsymbol{\alpha}$ *after an adatom has been removed from the surface at site* $\hat{\imath}$*, e.g. after a desorption event, is*

$$\boldsymbol{\alpha}^{\hat{\imath}} = \begin{cases} \boldsymbol{\alpha} \setminus \{\hat{\imath}\} \ , & \text{if } \hat{\imath} \in \boldsymbol{\alpha} \\ \{\emptyset\} \ , & \text{otherwise.} \end{cases} \tag{2.10f}$$

Note that $|\tilde{\boldsymbol{\alpha}}| = |\underset{\sim}{\boldsymbol{\alpha}}| = |\boldsymbol{\alpha}|$*. Also, it is the case that* $|\boldsymbol{\alpha}_{\pm}| = |\boldsymbol{\alpha}_{\hat{\imath}}| = |\boldsymbol{\alpha}| + 1$*, and* $|\boldsymbol{\alpha}^{\pm}| = |\boldsymbol{\alpha}^{\hat{\imath}}| = |\boldsymbol{\alpha}| - 1$*. With regard to (2.10d) and (2.10f), we include the case involving* $\{\emptyset\}$ *to prevent situations where we would remove an adatom from a site that is vacant;* $p_{\{\emptyset\}} := 0$ *in this scenario.*

In addition to the multiset operations given in Definition 4, there are a few functions and operators that can be defined for multisets $\boldsymbol{\alpha}$ and PDFs $p_{\boldsymbol{\alpha},m}(t)$ and $p_{\boldsymbol{\alpha}}(t)$ which will simplify the symbolic master equation, and any analysis thereof.

Definition 5. (Discrete functions and operators)

(i) We define the function $\nu_{\hat{\imath}}(\boldsymbol{\alpha})$ *of a multiset as the number of instances of* $\hat{\imath}$ *in* $\boldsymbol{\alpha}$*. For example, if* $\boldsymbol{\alpha} = \{\hat{\imath}, \hat{\imath}, \hat{\jmath}\}$*, then* $\nu_{\hat{\imath}}(\boldsymbol{\alpha}) = 2$*.*

(ii) The indicator function, $\mathbb{1}(\cdot)$*, is 1 when its argument is true, and 0 otherwise. Example:* $\mathbb{1}(\nu_{\hat{\imath}}(\{\hat{\imath}, \hat{\imath}, \hat{\jmath}\}) > 0) = 1$ *and* $\mathbb{1}(\nu_{\hat{\imath}}(\{\hat{\imath}, \hat{\imath}, \hat{\jmath}\}) = 0) = 0$*.*

(iii) The multiset difference operator, $\Delta_{\boldsymbol{\alpha}}$, is defined by

$$\begin{aligned}\Delta_{\boldsymbol{\alpha}} p_{\boldsymbol{\alpha},m}(t) = &\sum_{\substack{\hat{\imath}\in\boldsymbol{\alpha}\\ \hat{\imath}\neq 0,\pm 1}} \left[p_{\boldsymbol{\alpha}^{\hat{\imath}}_{\hat{\imath}-1},m}(t) - 2p_{\boldsymbol{\alpha},m}(t) + p_{\boldsymbol{\alpha}^{\hat{\imath}}_{\hat{\imath}+1},m}(t)\right] \\ &+ \mathbb{1}(\nu_1(\boldsymbol{\alpha}) > 0)\left[p_{\boldsymbol{\alpha}^1_2,m}(t) - p_{\boldsymbol{\alpha},m}(t)\right] \\ &+ \mathbb{1}(\nu_{-1}(\boldsymbol{\alpha}) > 0)\left[p_{\boldsymbol{\alpha}^{-1}_{-2},m}(t) - p_{\boldsymbol{\alpha},m}(t)\right]. \end{aligned} \tag{2.11a}$$

This last definition allows all hopping events on the terrace, excluding attachment and detachment events, to be represented in a compact way.

Using Definitions 4 and 5, master equation (2.1) can now be expressed *symbolically* as follows:

$$\begin{aligned}\dot{p}_{\boldsymbol{\alpha},m}(t) = &D\Delta_{\boldsymbol{\alpha}} p_{\boldsymbol{\alpha},m}(t) + \frac{F}{N-1}\sum_{\hat{\imath}\in\boldsymbol{\alpha}} p_{\boldsymbol{\alpha}^{\hat{\imath}},m-1}(t) - F p_{\boldsymbol{\alpha},m}(t) \\ &+ \frac{1}{\tau}\sum_{\hat{\imath}>0} p_{\boldsymbol{\alpha}_{\hat{\imath}},m+1}(t) - \frac{1}{\tau}\sum_{\hat{\imath}\in\boldsymbol{\alpha}} p_{\boldsymbol{\alpha},m}(t) \\ &+ D\phi_-\left[\mathbb{1}(\nu_{-1}(\boldsymbol{\alpha})=0)p_{\boldsymbol{\alpha}_-,m}(t) - \mathbb{1}(\nu_1(\boldsymbol{\alpha})=0)\mathbb{1}(\nu_{-1}(\boldsymbol{\alpha})>0)p_{\boldsymbol{\alpha},m}(t)\right] \\ &+ Dk\phi_-\left[\mathbb{1}(\nu_1(\boldsymbol{\alpha})=0)\mathbb{1}(\nu_{-1}(\boldsymbol{\alpha})>0)p_{\boldsymbol{\alpha}^-,m}(t) - \mathbb{1}(\nu_{-1}(\boldsymbol{\alpha})=0)p_{\boldsymbol{\alpha},m}(t)\right] \\ &+ D\phi_+\left[\mathbb{1}(\nu_{-1}(\boldsymbol{\alpha})=0)p_{\boldsymbol{\alpha}_+,m}(t) - \mathbb{1}(\nu_1(\boldsymbol{\alpha})=1)p_{\boldsymbol{\alpha},m}(t)\right] \\ &+ Dk\phi_+\left[\mathbb{1}(\nu_1(\boldsymbol{\alpha})=1)p_{\boldsymbol{\alpha}^+,m}(t) - \mathbb{1}(\nu_{-1}(\boldsymbol{\alpha})=0)p_{\boldsymbol{\alpha},m}(t)\right]. \end{aligned} \tag{2.12}$$

In the symbolic master equation (2.12), each term corresponds to certain atomistic processes included in the KRSOS model. Specifically, (2.12) includes: (i) Terms involving the multiset-difference operator correspond to hopping events on the terrace, not involving the step; (ii) terms involving the prefactor F correspond to deposition from states of lower mass index or deposition into states of higher mass

index; (iii) the second line in (2.12) corresponds to desorption events from states of higher mass index or into states of lower mass index; (iv) the third line describes attachment events from the left of the step; (v) the fourth line corresponds to leftward detachment; (vi) the fifth line describes attachment events from the right of the step; and (vii) the last line corresponds to rightward detachment.

Remark 1. *Since the multisets* $\boldsymbol{\alpha}$ *use Lagrangian coordinates, both* $\Delta_{\boldsymbol{\alpha}}$ *and* $\nu_i(\boldsymbol{\alpha})$ *are independent of the mass index,* m*. Hence, marginalizing (2.12) over* m *is straightforward. By doing so, transition rates (2.6) of marginalized master equation (2.5) are easily deduced from the resulting marginalized, symbolic master equation.*

2.3 Analysis of the kinetic, restricted solid-on-solid model

In this section, we expose certain properties of the KRSOS model by recourse to master equations (2.1) and (2.5). Chief among our interests is the long-time behavior of the KRSOS model, which will be a critical component of the analysis carried out in Chapter 3. Accordingly, we determine explicit formulas for equilibrium and steady-state distributions satisfying (2.1) and (2.5). For the same reason, the "maximum principle", proved at the end of this section, is another important result.

2.3.1 Long-time behavior

At this stage, it is useful for us to characterize the long-time behavior of systems described by master equations (2.1) and (2.5). In particular, we seek station-

ary distributions and statistical descriptions of important quantities in the KRSOS model. As an irreducible Markov process with countable state space, the KRSOS model is amenable to analysis using tools from the theory of stochastic processes; Appendix A provides an overview of results relevant to this thesis. Among the most significant of concepts therein is *detailed balance*, which is well known in statistical physics communities as well as in mathematics communities. In Chapters 2 and 4, detailed balance is the critical property invoked to determine equilibrium distributions of master equations under a variety of circumstances.

There are two parameter regimes in which equilibrium can be established in the long-time limit of the KRSOS model, to be discussed in this chapter. The first is the case of *conservative dynamics*, where no mass is added to our single-step system through deposition ($F = 0$), or lost via desorption ($\tau^{-1} = 0$). In that case, the number of adatoms on the terrace, $|\boldsymbol{\alpha}|$ and the step position (Definition 2) are quantities of particular interest. The second parameter regime will be referred to as the case of *quasi-conservative dynamics*, for which the total mass is not strictly conserved, but for long enough times a balance between deposition and desorption processes leads to constant $\langle m \rangle$. The equilibrium distribution in this case, found by utilizing the detailed balance property, generalizes the equilibrium distribution from the conservative case.

The final parameter regime we consider is the case of *non-conservative dynamics*, i.e. $F \gg \tau^{-1}$, where mass continually increases for long times. A distinguishing feature of this case is the non-existence of an equilibrium distribution. In fact, for extreme values of deposition rate, we are able to show no stationary distribution

of (2.5) exists. However, for moderate values of F, we believe a steady-state distribution describes the asymptotic behavior of the KRSOS model. Indeed, we are able to provide empirical evidence for such a steady-state using KMC simulations of the non-conservative KRSOS model. To complement our numerics, we heuristically derive a formula for the steady-state of truncated master equation (2.9). This formula is essential to our analysis in Chapter (3).

2.3.1.1 Conservative dynamics

Now we consider the case without external deposition or desorption, $F = 0$ and $\tau^{-1} = 0$, so that the total mass of the system is conserved. For this purpose we will assume the system is initially in a state whose mass index is m_0 with probability one. Then, for ease of notation, we will suppress the m-dependence of PDF $p_{\boldsymbol{\alpha},m}(t)$ since $m = m_0$ for all times $t > 0$. Accordingly, we will refer to master equation (2.5) when dynamics are conservative, though full master equation (2.1) and marginalized master equation (2.5) are equivalent in this case.

When dynamics are conservative, master equation (2.5) has an equilibrium solution, $p^{eq}_{\boldsymbol{\alpha}}$. The existence and uniqueness of this distribution may be deduced from Kolmogorov's criterion (Theorem 3 in Appendix A) [71], or from the detailed balance property of the master equation, by Theorem 2 in Appendix A. An expression for $p^{eq}_{\boldsymbol{\alpha}}$ was given in [71] by recourse to the canonical ensemble of statistical mechanics. We will follow the same approach and complement the result of [71] in two ways: We (i) represent $p^{eq}_{\boldsymbol{\alpha}}$ in closed form, and (ii) provide an alternate derivation of $p^{eq}_{\boldsymbol{\alpha}}$

by inspection of transition rates (2.6).

Recall that $Dk\phi_{\pm}$ is the detachment rate, where $k = \exp[-E_N/(k_BT)]$ and E_N measures the energy of the adatom resulting from detachment of an edge atom. We apply the formalism of the canonical ensemble to particle states of our system [33].

In the KRSOS model, the energy of each adatom configuration, $\boldsymbol{\alpha}$, is simply $|\boldsymbol{\alpha}|E_N$. By applying the Boltzmann-Gibbs distribution at equilibrium, we can assert that the probability of having n adatoms follows $\mathrm{P}(|\boldsymbol{\alpha}| = n) \propto \exp[-nE_N/(k_BT)]$. Consequently, the partition function, Z, for adatoms is computed by

$$\begin{aligned} Z &= \sum_{\boldsymbol{\alpha}} e^{-|\boldsymbol{\alpha}|E_N/(k_BT)} \\ &= \sum_{n=0}^{\infty} \omega(n)\, e^{-nE_N/(k_BT)} = \frac{1}{(1-k)^{N-1}} \ , \end{aligned} \tag{2.13}$$

by using (2.7) and the binomial theorem. Thus, the equilibrium solution is

$$p_{\boldsymbol{\alpha}}^{eq} = \frac{1}{Z} e^{-|\boldsymbol{\alpha}|E_N/T} = (1-k)^{N-1} k^{|\boldsymbol{\alpha}|} \ . \tag{2.14}$$

Alternatively, equilibrium distribution (2.14) can be deduced directly from the detailed balance property of master equation (2.5); see Theorem 2 in Appendix A. Specifically, the transition rates (2.2) for $F = 0$ and $\tau^{-1} = 0$ satisfy

$$T_{\boldsymbol{\alpha},\boldsymbol{\alpha}'} k^{|\boldsymbol{\alpha}'|} = T_{\boldsymbol{\alpha}',\boldsymbol{\alpha}} k^{|\boldsymbol{\alpha}|} \ . \tag{2.15}$$

Normalizing $\{k^{|\boldsymbol{\alpha}|}\}$ reproduces (2.14).

With partition function (2.13) and equilibrium distribution (2.14) at hand, we can compute important statistics for the KRSOS model in equilibrium, e.g. the mean and variance for the number of adatoms. First, the expected number of adatoms is

$$\langle n \rangle = \frac{k}{Z} \frac{dZ}{dk} = \frac{(N-1)k}{1-k} \ . \tag{2.16}$$

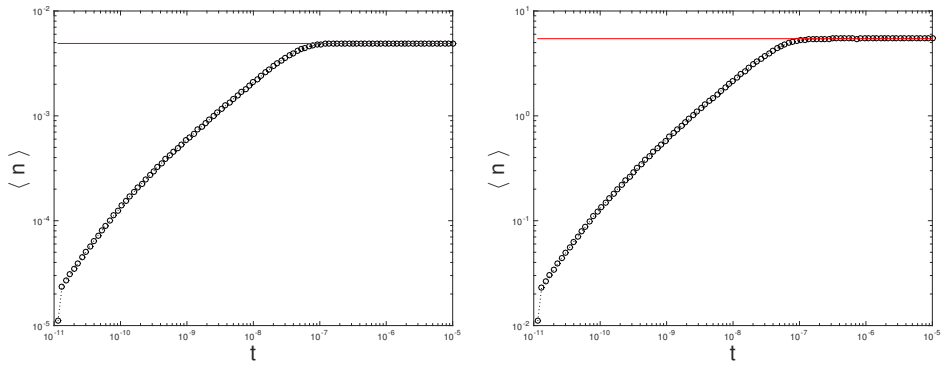

(**a**) (**b**)

Figure 2.3: The average particle number, $\langle n \rangle$, versus time t computed from KMC simulations of the KRSOS model with conservative dynamics, where $F = 0$ and $\tau^{-1} = 0$. Simulation data (black circles) agrees with the predicted value (red line) found from equation (2.16) when (a) $k = 0.0001$ and (b) $k = 0.1$. In both cases $N = 50$, $D = 10^{10}$ and $\phi_{\pm} = 1$. Averages were obtained using (a) 10^8 and (b) 10^6 simulations.

The second moment is computed similarly, resulting in the variance in n:

$$\langle n^2 \rangle - \langle n \rangle^2 = \frac{(N-1)k}{(1-k)^2} \ . \tag{2.17}$$

KMC simulations verifying the expected number of adatoms, $\langle n \rangle$, equation (2.16), are shown in Figure 2.3.

Interestingly, when $k \ll 1$, (2.16) and (2.17) indicate the mean and variance in particle number n are both given by $(N-1)k$, which is reminiscent of the Poisson distribution. Indeed, we can show that the distribution of particle states is Poisson in the limit of large N. The probability of n-particle states is given by

$$\mathrm{P}\left(|\boldsymbol{\alpha}| = n\right) = \frac{1}{Z} \begin{pmatrix} n+N-2 \\ n \end{pmatrix} k^n \ . \tag{2.18}$$

Let us assume $\chi = Nk = \mathcal{O}(1)$ as $N \to \infty$, i.e. χ is finite in the limit of large

lattice size, then equation (2.18) implies

$$\begin{aligned} \mathrm{P}\left(|\boldsymbol{\alpha}| = n\right) &= (1-k)^{N-1}\frac{(n+N-2)!}{(N-2)!n!}k^n \\ &\sim N^n\frac{k^n}{n!}(1-k)^N \\ &= \frac{\chi^n}{n!}(1-\frac{\chi}{N})^N \\ &\sim \frac{\chi^n}{n!}e^{-\chi} \quad \text{as } N\to\infty\,. \end{aligned} \tag{2.19}$$

In the above, we made use of Stirling's formula for the factor $\frac{(n+N-2)!}{(N-2)!}$ to reach the second line, and the limit definition of the exponential to find the final result.

Equations (2.16)-(2.19) give us a great deal of insight about the long-time behavior of particle number in the conservative KRSOS model. Even more interesting conclusions, perhaps, can be drawn regarding the *step position*. By recourse to Definition 2, in the conservative case, the step position is $s_0 - |\boldsymbol{\alpha}|$, s_0 a constant. Thus, the average step position is $s_0 - \frac{(N-1)k}{(1-k)}$, and its variance is the same as the one in (2.17). Consequently, for fixed $k \ll 1$, the relative importance of *fluctuations* compared to overall change in step position is $[(N-1)k]^{-1/2}$, which vanishes as $N\to\infty$. Hence, the equilibrium position of a 1D step is deterministic [49].

2.3.1.2 Quasi-conservative dynamics

In this section we consider a "quasi-conservative" parameter regime, where the external deposition rate and adatom desorption rate are compatible in magnitude. We will show that it is possible to choose F and τ^{-1} such that adatoms on the terrace establish equilibrium with the above vapor. In particular, when F and τ^{-1} are nonzero, the full, mass-dependent, master equation (2.1) obeys detailed balance

since deposition and desorption are reverse processes. In this scenario, the long time dynamics of the KRSOS model conserve mass on average. The quasi-conservative case, therefore, provides a meaningful extension of the results in Section 2.3.1.1.

The quasi-conservative case occupies an interesting position in the spectrum of dynamical behavior of the KRSOS model. On one hand, dynamics are not conservative, so it is not clear that equilibrium can be established. On the other, the detailed balance property, as demonstrated in Section 2.3.1.1, is an extremely useful tool for identifying potential equilibrium distributions satisfying the KRSOS master equation. The deciding factor whether or not an equilibrium exists is suggested by Theorem 2 in Appendix A: An equilibrium distribution exists only if a candidate distribution satisfying the detailed balance conditions is *normalizable*. If the normalization constant is infinite, no equilibrium exists[1]. With this in mind, consider the following distribution that satisfies the detailed balance conditions for master equation (2.1) with transition rates (2.2):

$$T_{(\boldsymbol{\alpha},m),(\boldsymbol{\alpha}',m')}k^{|\boldsymbol{\alpha}'|}\left(\frac{F\tau}{(N-1)k}\right)^{m'} = T_{(\boldsymbol{\alpha}',m'),(\boldsymbol{\alpha},m)}k^{|\boldsymbol{\alpha}|}\left(\frac{F\tau}{(N-1)k}\right)^{m}. \tag{2.20}$$

The normalization constant is

$$\begin{aligned}\mathcal{Z} =& \sum_{\boldsymbol{\alpha}} k^{|\boldsymbol{\alpha}|}\sum_{m=m_0}^{\infty}\left(\frac{F\tau}{(N-1)k}\right)^{m}\\ =& \frac{1}{(1-k)^{N-1}}\frac{\mathcal{R}^{m_0}}{1-\mathcal{R}}\,,\end{aligned} \tag{2.21}$$

where $\mathcal{R} := \frac{F\tau}{(N-1)k}$ is a dimensionless factor measuring the ratio of deposition rate and mean desorption rate. In the above calculation, we assume $\mathcal{R} < 1$ and that the

[1]This does not preclude existence of a steady-state distribution satisfying the master equation.

infinite sum over the mass index is one-sided, i.e. starting from $m = m_0$ instead of $m = -\infty$, resulting in a convergent geometric series. Thus, an equilibrium distribution exists for appropriately chosen parameters. It is

$$p^{eq}_{\boldsymbol{\alpha},m} = (1-k)^{N-1}k^{|\boldsymbol{\alpha}|}(1-\mathcal{R})\mathcal{R}^{m-m_0} \ . \tag{2.22}$$

Reconciling (2.22) with the grand canonical ensemble of statistical mechanics, which postulates that the equilibrium probability of configuration $(\boldsymbol{\alpha}, m)$ is proportional to $\exp([m\mu - |\boldsymbol{\alpha}|E_N]/k_BT)$, we identify the chemical potential of the system as $\mu = k_BT \ \ln \mathcal{R}$.

We now fully define the quasi-conservative parameter regime.

Definition 6. (Quasi-conservative dynamics) *The KRSOS model described by master equation (2.1) and transition rates (2.2) is considered* quasi-conservative *if mass is bounded below, $m \geq m_0$, and*

$$\frac{1}{\tau} \leq F < \frac{(N-1)k}{\tau} \tag{2.23}$$

with $0 < k < 1$, $F > 0$, and $\tau^{-1} > 0$. In this case, an equilibrium distribution exists and is given by equation (2.22).

Definition 6 includes a lower bound on the deposition rate, $F \geq \tau^{-1}$, which we impose for physical reasons. Specifically, it does not make sense to require $m \geq m_0$ in a parameter regime where the desorption rate is larger than the deposition rate. In this vein, we should mention that the KRSOS model with an upper bound on mass and $\mathcal{R} > 1$ could be an interesting starting point to study evaporation

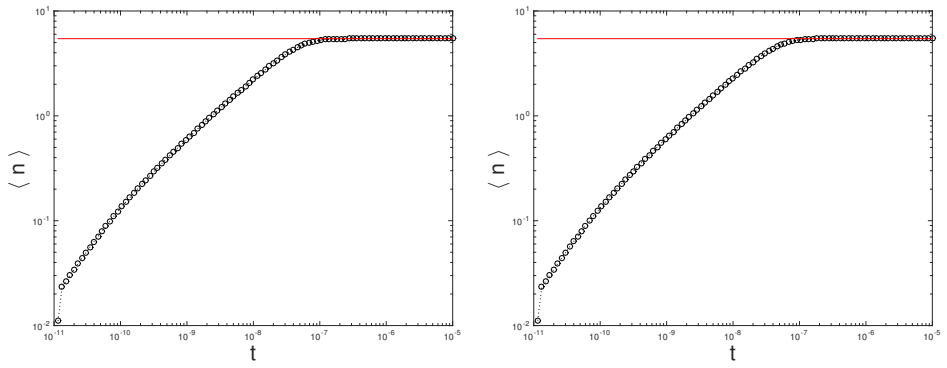

(**a**) (**b**)

Figure 2.4: The average particle number, $\langle n \rangle$, versus time t computed from KMC simulations of the KRSOS model with quasi-conservative dynamics, where F, τ^{-1}, and m_0 satisfy Definition 6. Simulation data (black circles) agrees with the predicted value (red line) found from equation (2.16) when (a) $F = 10^7$ and (b) $F = 2 \times 10^7$. In particular, note that $\langle n \rangle$ tends to the *same value* in both plots as t increases, even though the deposition rate is doubled. In both cases $\tau^{-1} = 10^7$, $N = 50$, $k = 0.1$, $D = 10^{10}$ and $\phi_{\pm} = 1$. Averages were obtained using 10^6 simulations.

dynamics. Since we are mainly interested in the effects of external deposition, cf. Section 2.3.1.3, we do not entertain this idea further.

Next, we seek to understand the consequences of partition function (2.21) on the average particle number and step position, as well as their fluctuations in equilibrium. Notice that the leading factor on the right hand side of (2.21) is Z, partition function (2.13) of the conservative case. This factorization of $\mathcal{Z}$ implies that $\langle n \rangle$ and $\langle n^2 \rangle - \langle n \rangle^2$ result in formulas identical to ones in equations (2.16) and (2.17). See Figure 2.4 for numerical evidence of this fact.

Before obtaining formulas for step position, let us calculate the first and second moment of the mass. Using appropriate derivatives of partition function (2.21), we

find that

$$\langle m \rangle = m_0 + \frac{\mathcal{R}}{1-\mathcal{R}} \ , \tag{2.24}$$

and

$$\langle m^2 \rangle - \langle m \rangle^2 = \frac{\mathcal{R}}{(1-\mathcal{R})^2} \ , \tag{2.25}$$

where $\mathcal{R} = \frac{F\tau}{(N-1)k}$. Finally, by Definition 2 and equations (2.16), (2.17), (2.24) and (2.25), it is straightforward to obtain the mean and variance of step position, i.e.

$$\langle s \rangle = s_0 - \frac{(N-1)k}{1-k} + \frac{\mathcal{R}}{1-\mathcal{R}} \ , \tag{2.26}$$

and

$$\langle s^2 \rangle - \langle s \rangle^2 = \frac{(N-1)k}{(1-k)^2} + \frac{\mathcal{R}}{(1-\mathcal{R})^2} \ . \tag{2.27}$$

Average step position (2.26) is the initial step position, less the expected number of adatoms on the terrace, plus a term accounting for any additional mass resulting from the competition between deposition and desorption processes. The variance (2.27) is just the sum of (2.17) and (2.25), as expected. Figure 2.5 demonstrates the prediction (2.26) for the equilibrium step position in the quasi-conservative case.

2.3.1.3 Non-conservative dynamics

In this subsection, we discuss a plausible steady-state solution of the KRSOS model in a parameter regime there $\frac{(N-1)k}{\tau} < F \ll D$. That is, the external deposition rate is large enough that it cannot be balanced by desorption, cf. Definition 6, but is small enough that dynamics are primarily dictated by diffusion (the Péclet

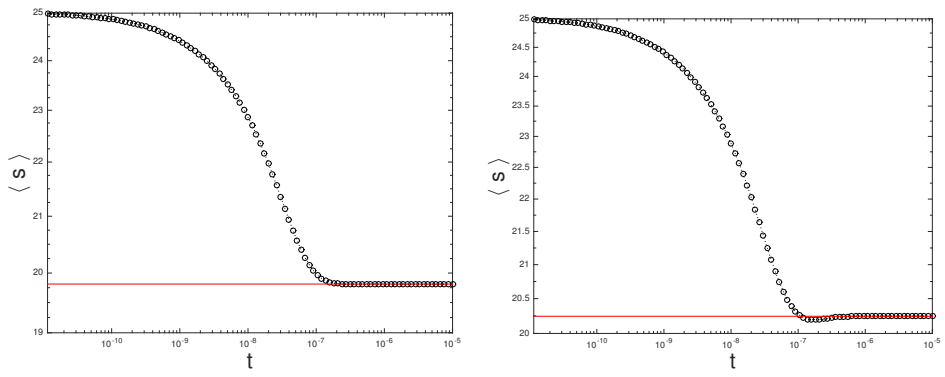

Figure 2.5: The average step position, $\langle s \rangle$, versus time t computed from KMC simulations of the KRSOS model with quasi-conservative dynamics, where F, τ^{-1}, and m_0 satisfy Definition 6. Simulation data (black circles) agrees with the predicted value (red line) found from equation (2.26) when (a) $F = 10^7$ and (b) $F = 2 \times 10^7$. In both cases $\tau^{-1} = 10^7$, $N = 50$, $k = 0.1$, $D = 10^{10}$ and $\phi_\pm = 1$. Averages were obtained using 10^6 simulations.

number $\epsilon = F/D$ is small). To this end, we employ a formal argument based on the assumption that only a finite number of particle (adatom) states contribute to the system evolution; $|\boldsymbol{\alpha}| \leq M$ for arbitrary yet fixed M.

In contrast to the quasi-conservative case, for which the detailed balance conditions (2.20) imply existence of equilibrium distribution (2.22), the non-conservative case is defined by the *nonexistence* of equilibrium. The lack of an equilibrium distribution can be brought about in one of two ways: Either (i) $F > 0$ and $\tau^{-1} > 0$, but partition function (2.21) is infinite, or (ii) $F > 0$ and $\tau^{-1} = 0$, so that microscopic reversibility is lost. A further complication of the non-conservative case is that no steady-state solutions to the master equation (2.5) may exist for large enough deposition rate. In Appendix B, it is proven that no steady-state of the KRSOS model can be established in the kinetic regime with $F > D(\phi_+ + \phi_-) + \frac{N-1}{\tau}$. This condi-

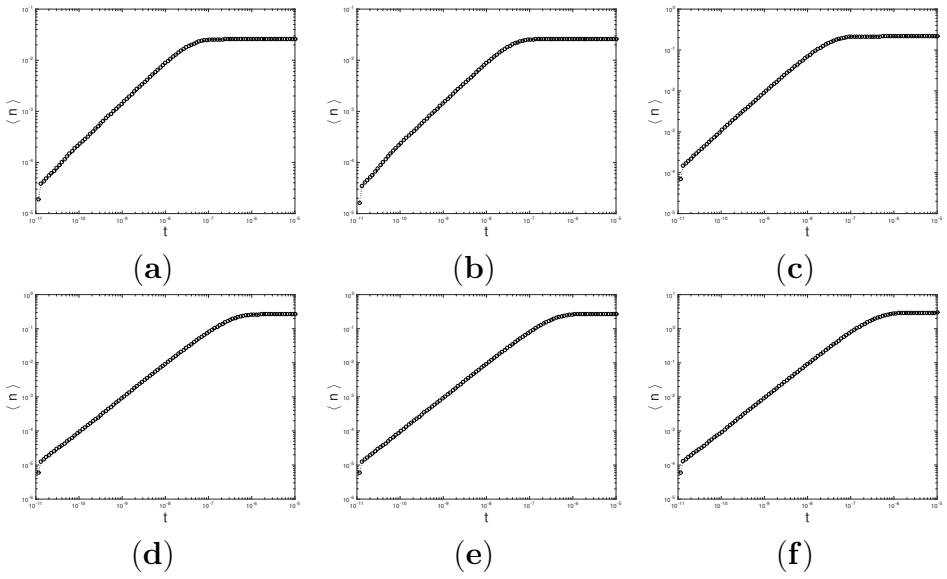

Figure 2.6: The average particle number, $\langle n \rangle$, versus time t computed from KMC simulations of the KRSOS model with Non-conservative dynamics, where $F > (N-1)k/\tau$. These plots indicate that the mean number of adatoms on the terrace tend to a finite value for long times. Parameters in each case include: (a) $F = 10^6$, $\tau^{-1} = 10^5$, $\phi_\pm = 1$; (b) $F = 10^6$, $\tau^{-1} = 0$, $\phi_\pm = 1$; (c) $F = 10^7$, $\tau^{-1} = 0$, $\phi_\pm = 1$; (d) $F = 10^6$, $\tau^{-1} = 10^5$, $\phi_\pm = 0.01$; (e) $F = 10^6$, $\tau^{-1} = 0$, $\phi_\pm = 0.01$; and (f) $F = 10^7$, $\tau^{-1} = 0$, $\phi_\pm = 0.01$. In all cases $N = 50$, $D = 10^{10}$, and $k = 0.0001$. The computed values of $\langle n \rangle$ at time $t = 10^{-5}$ are (a) 0.0262, (b) 0.0263, (c) 0.219, (d) 0.264, (e) 0.271, and (f) 2.92, obtained using 10^7 simulations in all cases.

tion implies that adatoms enter the system via deposition at a faster rate than they leave through attachment and desorption; consequently, from a physical viewpoint, a steady accumulation of adatoms on the terrace occurs for long times.

In the remainder of this section, we make the conjecture (but do not prove) that a finite number of particle states contribute to the system evolution. Accordingly, we restrict attention to the kinetic regime with sufficiently small ϵ ($\epsilon \ll 1$). This conjecture is favored by KMC simulations, a sample of which are shown in Figure 2.6.

By enforcement of restriction $|\boldsymbol{\alpha}| \leq M$, master equation (2.5) reduces to the truncated master equation, (2.9). The approximation of the full microscopic model by the truncated master equation offers a few obvious advantages. First, the solution of (2.9) always exists since the system is finite dimensional [39, 104]. Second, the time-dependent solution can be expressed conveniently in terms of a matrix exponential. And third, the steady-state distribution of this formulation is the normalized eigenvector of the $\mathfrak{T}$ matrix with zero eigenvalue.

We proceed to formally express the steady-state solution, $\mathbf{p}^{ss,\epsilon}$, of (2.9) as an appropriate series expansion in ϵ. This task can be carried out in several ways; for example, through the conversion of (2.9) to a Volterra integral equation, an approach that we choose to apply here. By treating $\epsilon D\mathfrak{B}\mathbf{p}^{\epsilon}(t)$ as a forcing term in (2.9), variation of parameters yields

$$\mathbf{p}^{\epsilon}(t) = \Phi(t)\left[\mathbf{p}_0 + \epsilon D\int_0^t \Phi^{-1}(t')\mathfrak{B}\mathbf{p}^{\epsilon}(t')dt'\right] , \tag{2.28}$$

where $\Phi(t) := \exp(D\mathfrak{A}\,t)$. We mention in passing that, by the usual theory of Volterra equations, (2.28) has a unique solution locally in time [103].

The matrix $\mathfrak{A}$ is diagonalizable because it corresponds to the transition matrix of a Markov process satisfying detailed balance [104]. Thus, we apply the decomposition $\mathfrak{A} = V\Lambda V^{-1}$ where $\Lambda = \mathrm{diag}\{\lambda_j\}_{j=1}^{\Omega(M)}$, $\{\lambda_j\}$ are the (non-dimensional) eigenvalues of $\mathfrak{A}$, and V is a matrix whose column vectors are the respective eigenvectors. Let $\{\lambda_j\}_{j=1}^{\Omega(M)}$ be ordered, $0 = \lambda_1 > \lambda_2 \geq \cdots \geq \lambda_{\Omega(M)}$ [104]. By $\Phi(t) = Ve^{Dt\Lambda}V^{-1}$, we have $\Phi^{-1}(t) = Ve^{-Dt\Lambda}V^{-1}$. Hence, (2.28) is recast as

$$\mathbf{p}^{\epsilon}(t) = Ve^{Dt\Lambda}V^{-1}\mathbf{p}_0 + \epsilon D\int_0^t Ve^{D(t-t')\Lambda}V^{-1}\mathfrak{B}\mathbf{p}^{\epsilon}(t')dt' . \tag{2.29}$$

At this stage, a formula for $\mathbf{p}^\epsilon(t)$ ensues by standard methods. We resort to the Laplace transform, $\widehat{\mathbf{p}}^\epsilon(s) = \int_0^\infty e^{-st}\,\mathbf{p}^\epsilon(t)\,dt$, of $\mathbf{p}^\epsilon(t)$ with Re $s > c > 0$ for some positive number c; by (2.29), we directly obtain

$$\widehat{\mathbf{p}}^\epsilon(s) = \left[I - \epsilon D\, V\mathfrak{D}(s)V^{-1}\mathfrak{B}\right]^{-1} V\mathfrak{D}(s)V^{-1}\mathbf{p}_0\ , \tag{2.30}$$

where $\mathfrak{D}(s) := \mathrm{diag}\{(s - D\lambda_j)^{-1}\}_{j=1}^{\Omega(M)}$ and I is the unit matrix. In (2.30), we assume that ϵ is small enough so that the requisite inverse matrix makes sense.

The next step in this approach is to compute the inverse transform of (2.30). However, in principle, this choice requires carrying out in the right half of the s-plane the inversion of the matrix $I - \epsilon D\, V\mathfrak{D}(s)V^{-1}\mathfrak{B}$ for arbitrary M. This task is considerably simplified for the steady-state solution, $\mathbf{p}^{ss,\epsilon}$, in the limit $t \to \infty$, as shown in Appendix C. The resulting formula reads

$$\mathbf{p}^{ss,\epsilon} = \mathbf{p}^0 + \sum_{l=1}^{\infty} \left(-\epsilon\mathfrak{A}^\dagger\mathfrak{B}\right)^l \mathbf{p}^0\ . \tag{2.31}$$

In the above, $\mathbf{p}^0$ corresponds to the equilibrium solution in the absence of external deposition ($\epsilon = 0$), and $\mathfrak{A}^\dagger$ denotes the Moore-Penrose pseudoinverse of $\mathfrak{A}$ [15]. Equation (2.31) indicates the relative contributions of external deposition/desorption processes and diffusion/attachment/detachment processes to the steady-state of the hypothetical M-particle KRSOS model underlying this calculation.

Our heuristics leaves several open questions regarding the meaning of (2.31) for large particle number M. For instance, the behavior with M of the bound for ϵ needed for convergence has not been addressed. A related issue is to estimate the error by the truncation of series (2.31), after a finite number of terms are summed. We expect that (2.31) ceases to be meaningful as $M \to \infty$

2.3.2 "Maximum principle"

In this section, we state and prove a "maximum principle" that applies to a wide class of Markov processes described by master equations. In particular, it applies to master equations (2.1) and (2.5), and allows us to estimate time-dependent PDFs, describing KRSOS evolution, with corresponding stationary distributions. This forms an extension of the "maximum principle" in [71]. The proof only relies on the existence of a steady-state solution and the conservation of probability property of transition rates of master equations, i.e. (2.2f), making it quite general.

On account of the generality of the ensuing proposition, we will use slightly more general notation: Instead of indexing PDFs and transition rates with $(\boldsymbol{\alpha}, m)$, or $\boldsymbol{\alpha}$ in the case of marginal master equation (2.5), we will make use of the indices $i, j \in \mathfrak{S}$ as is done in Appendix A. Here $\mathfrak{S}$ denotes the discrete, countable state space of the process.

Proposition 1. ("Maximum principle") *If a non-trivial steady-state solution, p_i^{ss}, of master equation (A.2) exists, then any solution $p_i(t)$ satisfies*

$$\max_{i\in\mathfrak{S}} \frac{p_i(t)}{p_i^{ss}} \leq \max_{i\in\mathfrak{S}} \frac{p_i(0)}{p_i^{ss}} \ , \quad t > 0 \ . \tag{2.32}$$

Proof. We proceed to prove Proposition 1 by invoking the identity

$$\sum_{j\in\mathfrak{S}} T_{ij} p_j^{ss} = 0 \ . \tag{2.33}$$

Equation (A.2) can be written as

$$\begin{aligned}\dot{p}_i(t) &= \sum_{j\in\mathfrak{S}} T_{ij}p_j(t) \\ &= T_{ii}p_i(t) + \sum_{j\neq i} T_{ij}p_j(t) \\ &= T_{ii}p_i^{ss}\frac{p_i(t)}{p_i^{ss}} + \sum_{j\neq i} T_{ij}p_j^{ss}\frac{p_j(t)}{p_j^{ss}} \\ &= \sum_{j\neq i} T_{ij}p_j^{ss}\left\{\frac{p_j(t)}{p_j^{ss}} - \frac{p_i(t)}{p_i^{ss}}\right\} . \end{aligned} \tag{2.34}$$

Note that $T_{ij}p_j^{ss} \geq 0$ for all $j \neq i$. Thus, the sign of $\dot{p}_i(t)$ is determined by the quantity in brackets. In particular, if i maximizes (minimizes) $p_j(t)/p_j^{ss}$ over all j, then $\dot{p}_i(t) \leq 0$ ($\dot{p}_i(t) \geq 0$). This assertion implies the desired "maximum principle" (and corresponding "minimum principle"), thus concluding the proof. □

A few remarks are in order regarding Proposition 1 and its application.

Remark 2. *If the initial data $p_i(0)$ satisfies*

$$\max_{i\in\mathfrak{S}} \frac{p_i(0)}{p_i^{ss}} \leq C , \tag{2.35}$$

for a parameter-independent constant C, then Proposition 1 implies that $p_i(t) \lesssim p_i^{ss}$ for all $t > 0$. Here we introduce the symbol $\lesssim$ to indicate boundedness up to a positive constant factor. This property will enable us to estimate certain averages in Section 3.3.

Remark 3. *Proposition 1 and Remark 2 apply to master equation (2.1) in both the conservative and quasi-conservative cases since they each possess equilibrium distributions.*

Remark 4. *In the non-conservative case, Proposition 1 and Remark 2 only apply to the marginalized master equation, (2.5). The "maximum principle" cannot be applied to full, mass-dependent master equation (2.1) in the non-conservative case since the assumption of existence of a steady-state, and therefore equation (2.33), is violated when $\epsilon > 0$; as $t \to \infty$, the mass of the system increases without bound.*

Remark 5. *Proposition 1 and Remark 2 apply to the truncated master equation (2.9)* unconditionally *since a steady-state is guaranteed to exist. Note that $\mathfrak{S}$ is finite dimensional in this case.*

2.4 Summary

In this chapter, we define an atomistic SOS-type model of a single step as a Markov process described by three master equations: (i) Full master equation (2.1), which governs the evolution of mass-dependent PDF, $p_{\boldsymbol{\alpha},m}(t)$; (ii) marginalized master equation (2.5), for which mass dependence has been summed out; and (iii) symbolic master equation (2.12), which is a convenient restatement of the full master equation.

We also define three parameter regimes for the KRSOS model that correspond to conservative, quasi-conservative, and non-conservative dynamics. For conservative dynamics, we obtain equilibrium distribution (2.14) and determine that particle states in equilibrium follow a Poisson distribution with parameter $Nk = \mathcal{O}(1)$ in the limit of large N. In the case of quasi-conservative dynamics, we invoke the detailed balance property of the full master equation to determine equilibrium dis-

tribution (2.22), which generalizes the equilibrium distribution for the conservative case. To make progress in the case of non-conservative dynamics, we convert a truncated version of marginalized master equation (2.9) into an integral equation, for which asymptotic analysis of the Laplace transform results in a formal power-series expansion in $\epsilon = F/D$ for the steady-state distribution.

Finally, we state and prove the "maximum principle", Proposition 1, which applies to: (i) The full master equation for conservative and quasi-conservative dynamics; (ii) the marginalized master equation for non-conservative dynamics; and (iii) the truncated master equation in all cases. This result, in conjunction with the equilibrium and steady state solutions found in this chapter, is a key element in the estimation of discrete corrections to the BCF-like model derived in the next chapter.

Chapter 3: Discrete BCF equations and their continuum limit

In this chapter, we systematically derive the BCF model of a single step in 1D. To do so, we first define discrete versions of BCF variables, including: (i) adatom flux at the step edge, (ii) adatom density, and (iii) step position. From (i), we are able to obtain exact expressions for discrete adatom fluxes at the step edge that make explicit a discrete, BCF-like kinetic relation for adatom fluxes at the step. For (ii) and (iii), we derive discrete equations of motion using symbolic master equation (2.12). In all three cases we find corrections to discrete BCF-like equations. Using results from Chapter 2, in particular Proposition 1, we are able to estimate the relative size of these corrections. Then, assuming appropriate scaling of KRSOS parameters, the discrete correction terms can be neglected in the continuum limit of our atomistic model. The result is a mesoscale BCF model.

Aside from deriving BCF, another important result of this chapter is our characterization of corrections. In addition to capturing corrections numerically using KMC, we are also able to relate the specific forms of the corrections to aspects of the KRSOS model. We find two types of corrections emerging from our analysis: The first type are corrections to the discrete analog of the linear kinetic relation for adatom flux. These corrective fluxes result from the KRSOS rules for attachment

and detachment of atoms at the step edge. The second type of corrections stem from atomistic configurations with multiple adatoms at a single lattice site. These high-occupancy corrections are brought about by the KRSOS rule for adatom hopping on the terrace that only allows the top adatom in a stack to move; cf. (2.2a) and Figure 2.1(d). We view this feature of the KRSOS model as inducing *kinetic interactions* between adatoms that are responsible for corrections to adatom diffusion.

The goal of this chapter is not unlike the objectives of [49,70,71,117]. However, in those works, the authors' focus is on near-equilibrium processes, whereas our interests include kinetic regimes that may be far from equilibrium. A similar task is undertaken in [72], albeit via a (coarse-grained) phenomenological "terrace-step-kink" model [14]. In this chapter, we avoid *a priori* approximations associated with the diluteness of the adatom system, which is a key, explicit assumption in [49,70,71]. Furthermore, our study has a perspective distinct from that of [1,83,116] in which extensive computations are carried out in 2+1 dimensions. In particular, in [1,116] the authors derive a set of refined boundary conditions at the step edge that depend on the local environment on the basis of a discrete diffusion equation with a *fixed* step position. In [83], only numerical comparisons of KMC simulations to aspects of the BCF model are shown. A different view is adopted in [115], where a high-dimensional master equation is reduced to a Langevin-type equation for height columns on the crystal lattice. We should also mention the probabilistic approach in [53], which addresses the passage from an atomistic description within a solid-on-solid model to a *fully* continuum picture.

One result we have yet to mention is an empirically deduced *nonlinear* relation for adatom flux at steps, cf. Section 3.5. Examples of works discussing situations where the mass flux toward the step edge may exhibit nonlinear behavior include [5, 18]. Specifically, in [5], the authors carry out numerical simulations of a terrace-step-kink model that reveal nonlinear behavior of adatom flux, and relate this behavior to the step-continuum thermodynamic approach of [18]. In the present treatment, we point out such a nonlinearity at the mesoscale from a kinetic atomistic perspective, in an effort to avoid continuum thermodynamic principles. By recourse to atomistic mechanisms, we argue that nonlinear terms in the boundary conditions for the mass flux naturally emerge as the system is driven farther from equilibrium.

This chapter can be outlined as follows: To begin, in Section 3.1, we review the BCF model of a single step in $1+1$ dimensions. Next, in Section 3.2, we derive a discrete BCF-like model for the evolution of averages of atomistic configurations. Correction terms that emerge alongside the discrete version of the BCF model are then estimated in Section 3.3 in terms of KRSOS model parameters. Section 3.4 demonstrates that a mesoscale BCF-like picture emerges from coarse graining our discrete equations, provided atomistic parameters are chosen such that the discrete corrections are negligible in the continuum limit. Finally, we characterize corrections using KMC simulations in Section 3.5, and offer some discussion in Section 3.6.

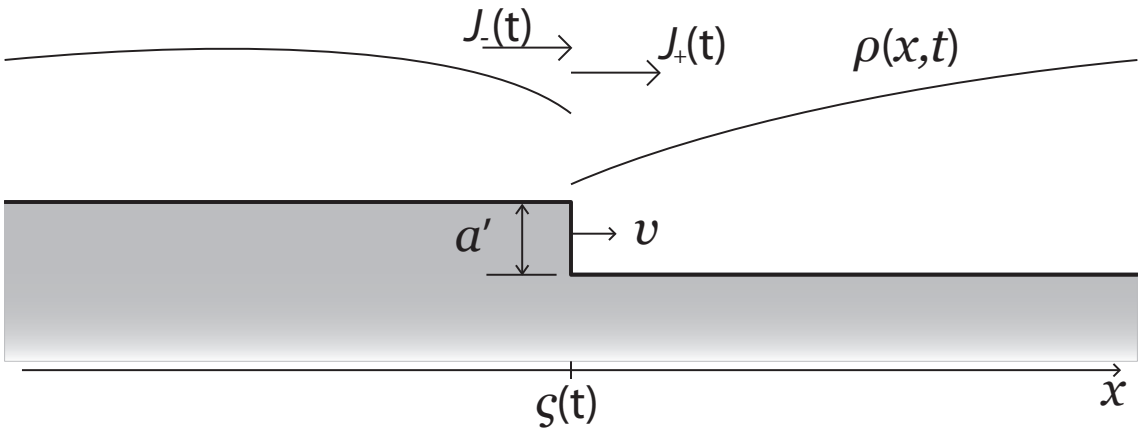

Figure 3.1: Mesoscale picture: Schematic of a step with atomic height a' ajoining two terraces. The dependent variable $\rho(x,t)$ is the adatom concentration field on each terrace in the laboratory frame. The step velocity, $v = \dot{\varsigma}(t)$, is determined by the adatom fluxes $J_{\pm}$ at the step edge on the lower $(+)$ or upper $(-)$ terrace via mass conservation; cf. (3.1).

3.1 Review of BCF model

The BCF model is a mesoscale description of crystal surfaces insofar as it retains discreteness in the vertical direction to resolve steps, yet represents adatoms as a mean-field density [12, 36]. Naturally, in 1D settings like the one addressed in this chapter, a step is represented by a single point. In either 1 or 2 dimensions, the BCF theory is comprised of the following major elements: (a) A step velocity law, which expresses mass conservation for adatoms; (b) a diffusion equation for the density of adatoms; and (c) a linear kinetic relation for the adatom flux normal to the step edge. It is important to point out that the latter two elements may be poor approximations of reality in systems where adatom-adatom interactions are significant.

The geometry of a step adjoining two terraces is depicted in Fig. 3.1. The upper $(-)$ terrace, on the left of the step edge, and lower $(+)$ terrace, on the right of the step edge, differ in height by a', an atomic length. Let $\varsigma(t)$ be the position of the step edge. We apply screw-periodic boundary conditions in the spatial coordinate, x. In this view, the adatoms are represented by the density field $\rho(x,t)$.

Now consider the motion of the step. The step velocity, $v(t) = \dot{\varsigma}(t)$, is determined by mass conservation:

$$v = \frac{\Omega}{a'}\left(J_- - J_+\right) \ , \tag{3.1}$$

where $J_\pm$ denotes the x-directed mass flux at the step edge on the upper $(-)$ or lower $(+)$ terrace, $\Omega = aa'$ is the atomic area, and a is the lattice spacing in the lateral (x-) direction.

For later algebraic convenience, we define $\hat{x} := x - \varsigma(t)$ which is the coordinate relative to the step edge. On each terrace, the variable $\mathcal{C}(\hat{x},t) = \rho(x,t)$ satisfies the diffusion equation [12]

$$\frac{\partial \mathcal{C}}{\partial t} = \mathcal{D}\frac{\partial^2 \mathcal{C}}{\partial \hat{x}^2} + v\frac{\partial \mathcal{C}}{\partial \hat{x}} + \mathcal{F} - \frac{1}{\tau}\mathcal{C} \ , \tag{3.2}$$

where $\mathcal{D}$ is the macroscopic adatom diffusivity, τ is the mean desorption time, and $\mathcal{F}$ is the mesoscopic external deposition flux [36,74]. Note the presence of the advection term, $v(\partial\mathcal{C}/\partial\hat{x})$, on the right-hand side of (3.2); this term originates from $\partial\rho/\partial t$ in the corresponding diffusion equation for $\rho(x,t)$, viz.,$\partial\rho/\partial t = \mathcal{D}(\partial^2\rho/\partial x^2)+\mathcal{F}$. Thus, the flux at the step edge consistent with Fick's law is

$$J_\pm = -\mathcal{D}(\partial\mathcal{C}/\partial\hat{x})_\pm - v\mathcal{C}_\pm = -\mathcal{D}(\partial\rho/\partial x)_\pm - v\rho_\pm \ . \tag{3.3}$$

The remaining ingredient of the BCF model is a set of boundary conditions for $\mathcal{C}$, or ρ, at the step edge through the mass flux, $J(x,t)$. BCF originally introduced Dirichlet boundary conditions, by which the restriction $\mathcal{C}_\pm$ of $\mathcal{C}$ at the step edge is set equal to an equilibrium value, c^{eq} [12]. Later on, a Robin boundary condition was imposed [20]. Note that the Robin boundary condition is typically a linear relation between the solution of a partial differential equation and its normal derivative at a domain boundary. This condition was later improved by incorporation of the Ehrlich-Schwoebel barrier [24, 88]; see [74]. The linear kinetic relation for the mass flux at the step is

$$J_\pm = \mp\kappa_\pm \left(\mathcal{C}_\pm - c^{eq}\right) \ , \tag{3.4}$$

where $\kappa_\pm$ describes the rate of attachment/detachment of atoms at the step in the presence of an Ehrlich-Schwoebel barrier.

The BCF model described here assumes that adatom density is low, and that evolution takes place near equilibrium [12,74]. Situations may arise, however, where adatom density is high, or the surface is driven far from equilibrium. For these cases, the model might need to include corrections. In particular, corrections to the diffusion equation on terraces or in the linear kinetic relation are expected when adatom densities are high. For example, with regard to the linear kinetic relation, numerical simulations in [5] based on a "terrace-step-kink" model suggest a nonlinear dependence of $J_\pm$ on $\mathcal{C}_\pm - c^{eq}$. The authors argue that this can be explained by the thermodynamic approach of [18]. The observation of such a nonlinear effect

motivates one to conjecture a generalized relation of form

$$J_{\pm} = \mp \sum_{n} \kappa_{\pm}^{(n)} \left(\mathcal{C}_{\pm} - c^{eq} \right)^{n} \ , \tag{3.5}$$

where the terms corresponding to $n \geq 2$ account for far-from-equilibrium or high-density corrections to the traditional linear kinetic law (3.4). In Section 3.5, we provide evidence for (3.5) as well as corrections to the diffusion equation (3.2) that emerge from kinetic aspects of our simplified 1D atomistic model.

3.2 Discrete equations of motion

In this section, we heuristically show how discrete variables that form averages of microscale quantities on the lattice are plausibly related to mesoscale BCF-type observables of physical interest. In particular, we derive the discrete counterparts of (i) linear kinetic relation (3.4), (ii) diffusion equation (3.2), (iii) Fick's law (3.3), and (iv) step velocity law (3.1). A noteworthy finding of our approach is that the discrete versions of (i)-(iii) involve *corrections* that are related to certain aspects of the KRSOS model. Later in this section, we determine *a priori* upper bounds for these corrections, as well as numerical calculations of their values via KMC simulations. Our analytical estimates for the size of corrections motivate a sufficient scaling of model parameters that yield BCF-like equations in the continuum limit.

One consequence of our approach, which involves the derivation of a discrete diffusion equation in Eulerian coordinates, is that a discrete counterpart of the advection term appearing in (3.2) is not made explicit. We address this deficiency by providing a plausibility argument for discrete advection terms consistent with

the one appearing in (Lagrangian) BCF diffusion equation (3.2).

3.2.1 Microscale averages

Before proceeding to the derivation of discrete BCF equations, we must define certain discrete averages over microscale states $(\boldsymbol{\alpha}, m)$ via PDFs $p_{\boldsymbol{\alpha},m}(t)$.

Definition 7. (Average step position) *The average step position is*

$$\varsigma(t) = a \sum_{\boldsymbol{\alpha},m} s(\boldsymbol{\alpha}, m) p_{\boldsymbol{\alpha},m}(t) \ , \tag{3.6}$$

where $s(\boldsymbol{\alpha}, m)$, given in Definition 2 (Chapter 2), is the integer that denotes the site to the right of the step edge in the fixed reference frame of the 1D lattice.

Note that, in Definition 7, $\big||\boldsymbol{\alpha}| - (m - m_0)\big|$ is the number of adatoms that are exchanged with the step edge and, thus, solely contribute to step motion.

Next, we define the adatom number per lattice site, which plays the role of the adatom density in the mesoscale picture. We use the following two interrelated variables: (i) The density, $c_{\hat{\jmath}}(t)$, of adatoms *relative* to the step, where $\hat{\jmath}$ counts the lattice sites to the *right* of the step (a Lagrangian variable); and (ii) the Eulerian density, $\rho_j(t)$, at site j in the fixed coordinate frame.

Definition 8. (Adatom density)

(i) The Lagrangian-type adatom density is defined by

$$\begin{aligned} c_{\hat{\jmath}}(t) &= \sum_{\boldsymbol{\alpha},m} \nu_{\hat{\jmath}}(\boldsymbol{\alpha}) p_{\boldsymbol{\alpha},m}(t)/a \\ &= \sum_{\boldsymbol{\alpha}} \nu_{\hat{\jmath}}(\boldsymbol{\alpha}) p_{\boldsymbol{\alpha}}(t)/a, \end{aligned} \tag{3.7a}$$

where $\nu_{\hat{\jmath}}(\boldsymbol{\alpha})$ is the number of adatoms at site $\hat{\jmath}$ for a system with adatom configuration $\boldsymbol{\alpha}$.

(ii) The Eulerian adatom density is

$$\rho_j(t) = \sum_{\boldsymbol{\alpha},m} \nu_{j-s(\boldsymbol{\alpha},m)}(\boldsymbol{\alpha}) p_{\boldsymbol{\alpha},m}(t)/a \ , \tag{3.7b}$$

where $j - s(\boldsymbol{\alpha}, m)$ is the Lagrangian coordinate corresponding to Eulerian j.

Regarding the above definition, it is important to note that $\nu_{\hat{\jmath}}(\boldsymbol{\alpha})$ is a function counting the number of instances of $\hat{\jmath}$ in multiset $\boldsymbol{\alpha}$. Since both $\hat{\jmath}$ and $\boldsymbol{\alpha}$ use the same coordinate system, $\nu_{\hat{\jmath}}(\boldsymbol{\alpha})$ is independent of m, allowing for $c_{\hat{\jmath}}(t)$ to be expressed in terms of the marginal PDF $p_{\boldsymbol{\alpha}}(t)$. In contrast, the definition of $\rho_j(t)$ cannot be written in terms of $p_{\boldsymbol{\alpha}}(t)$ based on the mass dependence in the index of $\nu_{j-s(\boldsymbol{\alpha},m)}(\boldsymbol{\alpha})$ required to change coordinates.

It should be noted that the prefactors $\nu_{\hat{\jmath}}(\boldsymbol{\alpha})$ weighting the distribution $p_{\boldsymbol{\alpha},m}(t)$ in Definition 8 were not included in [71]. Instead, the authors define an adatom density that measures only the presence of adatoms at a lattice site, not the number of adatoms. Since [70, 71] focus on a parameter regime dominated by 0- and 1-particle states, the so-called "dilute limit" of the adatom gas, the difference in definitions is insignificant. Interestingly, *dilute versions* of densities (3.7) will play a significant role in equations for $\dot{c}_j(t)$ and $\dot{\rho}_j(t)$. Accordingly, we define the dilute densities $\mathfrak{c}_{\hat{\jmath}}(t)$ and $\varrho_j(t)$ as follows:

Definition 9. (Dilute-adatom density)

(i) The dilute-adatom density in Lagrangian coordinates is defined by

$$\mathfrak{c}_{\hat{\jmath}}(t) = \sum_{\boldsymbol{\alpha}} \mathbb{1}(\nu_{\hat{\jmath}}(\boldsymbol{\alpha}) > 0) p_{\boldsymbol{\alpha}}(t)/a \ . \tag{3.8a}$$

(ii) The dilute-adatom density in Eulerian coordinates is

$$\varrho_j(t) = \sum_{\boldsymbol{\alpha},m} \mathbb{1}(\nu_{j-s(\boldsymbol{\alpha},m)}(\boldsymbol{\alpha}) > 0) p_{\boldsymbol{\alpha},m}(t)/a \ . \tag{3.8b}$$

The variables $c_{\hat{\jmath}}(t)$ and $\mathfrak{c}_{\hat{\jmath}}(t)$ are most useful in discrete equations for fluxes and boundary conditions at the step. On the other hand, $\rho_j(t)$ and $\varrho_j(t)$ are more convenient to use in the derivation of the discrete diffusion equation, at lattice sites sufficiently away from the step edge.

Remark 6. *The equilibrium adatom density, c^{eq}, at any lattice site can be computed using the definition of density (3.7a) and either (2.14) or (2.22); or, alternatively, directly from either partition function (2.13) or (2.21). The equilibrium density is*

$$c^{eq} = \frac{\langle n \rangle}{(N-1)a} = \frac{k/a}{1-k} \ , \tag{3.9}$$

where $\langle n \rangle$ is given by (2.16).

We now proceed to define the adatom fluxes at the step edge by virtue of our rules for atomistic transitions.

Definition 10. (Adatom flux at the step edge) *The flux $J_\pm$ on the right (+, lower terrace) or left (−, upper terrace) of the step edge is*

$$J_\pm(t) = \pm \sum_{\boldsymbol{\alpha},m} \mathbb{1}(\nu_{-1}(\boldsymbol{\alpha}) = 0) \left[T_{(\boldsymbol{\alpha}_\pm,m),(\boldsymbol{\alpha},m)} p_{\boldsymbol{\alpha},m}(t) - T_{(\boldsymbol{\alpha},m),(\boldsymbol{\alpha}_\pm,m)} p_{\boldsymbol{\alpha}_\pm,m}(t) \right] . \tag{3.10}$$

Here, $\boldsymbol{\alpha}_{\pm}$, defined in (2.10c) denotes the adatom configuration resulting from a rightward (+) or leftward (−) detachment. The factor $\mathbb{1}(\nu_{-1}(\boldsymbol{\alpha}) = 0)$ excludes configurations that involve adatoms on top of the edge atom, i.e. those for which detachment is forbidden and are inaccessible via attachment events. Additionally, the external deposition of adatoms does not contribute to the mass flux $J_{\pm}$, and therefore only a single value of m enters (3.10); see (2.2) and (2.3).

3.2.2 Flux at the step edge

In this section, we derive exact expressions for the discrete flux at the left and right of the step edge. These expressions form the basis for characterizing *corrections* to linear kinetic law (3.4) in the discrete setting, which we pursue later, in Sections 3.3 and 3.5.

Proposition 2. (Discrete fluxes at the step edge) *The discrete fluxes, $J_{\pm}(t)$, defined in (3.10), can be written as*

$$J_{\pm}(t) = \mp D\phi_{\pm} a \left[c_{\pm 1}(t) - c^{eq}\right] \mp D\phi_{\pm} a f_{\pm}(t) \ . \tag{3.11}$$

The terms $f_{\pm}(t)$ are defined by

$$\begin{aligned} f_{+}(t) = k\Bigg[c^{eq} + \sum_{\boldsymbol{\alpha}} \mathbb{1}(\nu_{-1}(\boldsymbol{\alpha}) > 0) p_{\boldsymbol{\alpha}}(t)/a\Bigg] \\ - \sum_{\boldsymbol{\alpha}} \mathbb{1}(\nu_1(\boldsymbol{\alpha}) > 1)\nu_1(\boldsymbol{\alpha}) p_{\boldsymbol{\alpha}}(t)/a \end{aligned} \tag{3.12a}$$

and

$$
\begin{aligned}
f_-(t) = k \Bigg[c^{eq} + \sum_{\boldsymbol{\alpha}} \mathbb{1}(\nu_{-1}(\boldsymbol{\alpha}) > 0) p_{\boldsymbol{\alpha}}(t)/a \Bigg] \\
- \sum_{\boldsymbol{\alpha}} \mathbb{1}(\nu_1(\boldsymbol{\alpha}) > 0) \nu_{-1}(\boldsymbol{\alpha}) p_{\boldsymbol{\alpha}}(t)/a \\
- \sum_{\boldsymbol{\alpha}} \mathbb{1}(\nu_1(\boldsymbol{\alpha}) = 0) \mathbb{1}(\nu_{-1}(\boldsymbol{\alpha}) > 1) \\
\times \left[\nu_{-1}(\boldsymbol{\alpha}) - 1 \right] p_{\boldsymbol{\alpha}}(t)/a \ . \qquad (3.12b)
\end{aligned}
$$

The formulas (3.11) include the discrete analog of the linear kinetic relation of the BCF model, cf. (3.4), as well as corrective fluxes (3.12).

Proof. To derive (3.11), we must manipulate the formulas (3.10) to make manifest the differences $c_{\pm 1}(t) - c^{eq}$. We begin with $J_+(t)$, i.e.,

$$
\begin{aligned}
J_+(t) =& \sum_{\boldsymbol{\alpha},m} \mathbb{1}(\nu_{-1}(\boldsymbol{\alpha}) = 0) \left[T_{(\boldsymbol{\alpha}_+,m),(\boldsymbol{\alpha},m)} p_{\boldsymbol{\alpha},m}(t) - T_{(\boldsymbol{\alpha},m),(\boldsymbol{\alpha}_+,m)} p_{\boldsymbol{\alpha}_+,m}(t) \right] \\
=& Dk\phi_+ \sum_{\boldsymbol{\alpha},m} \mathbb{1}(\nu_{-1}(\boldsymbol{\alpha}) = 0) p_{\boldsymbol{\alpha},m}(t) - D\phi_+ \sum_{\boldsymbol{\alpha},m} \mathbb{1}(\nu_1(\boldsymbol{\alpha}) = 1) p_{\boldsymbol{\alpha},m}(t) \\
=& Dk\phi_+ \sum_{\boldsymbol{\alpha}} \mathbb{1}(\nu_{-1}(\boldsymbol{\alpha}) = 0) p_{\boldsymbol{\alpha}}(t) - D\phi_+ \sum_{\boldsymbol{\alpha}} \mathbb{1}(\nu_1(\boldsymbol{\alpha}) = 1) p_{\boldsymbol{\alpha}}(t) \\
=& Dk\phi_+ \left[1 - \sum_{\boldsymbol{\alpha}} \mathbb{1}(\nu_{-1}(\boldsymbol{\alpha}) > 0) p_{\boldsymbol{\alpha}}(t) \right] \\
& - D\phi_+ \sum_{\boldsymbol{\alpha}} \mathbb{1}(\nu_1(\boldsymbol{\alpha}) = 1) \nu_1(\boldsymbol{\alpha}) p_{\boldsymbol{\alpha}}(t) \\
=& D\phi_+ a \left[\frac{k/a}{1-k}(1-k) - k \sum_{\boldsymbol{\alpha}} \mathbb{1}(\nu_{-1}(\boldsymbol{\alpha}) > 0) p_{\boldsymbol{\alpha}}(t)/a \right] \\
& - D\phi_+ a \left[c_1(t) - \sum_{\boldsymbol{\alpha}} \mathbb{1}(\nu_1(\boldsymbol{\alpha}) > 1) \nu_1(\boldsymbol{\alpha}) p_{\boldsymbol{\alpha}}(t)/a \right] \\
=& - D\phi_+ a \left[c_1(t) - c^{eq} \right] - D\phi_+ a f_+(t) \ . \qquad (3.13a)
\end{aligned}
$$

In the above, the second equality results from substitution of transition rates (2.2); the third equality results from summing the mass variable; the fourth equality makes use of the complement rule, $\mathbb{1}(\nu_{-1}(\boldsymbol{\alpha}) = 0) = 1 - \mathbb{1}(\nu_{-1}(\boldsymbol{\alpha}) > 0)$; and the fifth equality involves adding and subtracting the last sum to make $c_1(t)$ appear. Similar steps are used to derive the corresponding formula for $J_-(t)$, viz.,

$$\begin{aligned}
J_-(t) =& \sum_{\boldsymbol{\alpha},m} \mathbb{1}(\nu_{-1}(\boldsymbol{\alpha}) = 0) \left[T_{(\boldsymbol{\alpha},m),(\boldsymbol{\alpha}_-,m)} p_{\boldsymbol{\alpha}_-,m}(t) - T_{(\boldsymbol{\alpha}_-,m),(\boldsymbol{\alpha},m)} p_{\boldsymbol{\alpha},m}(t)\right] \\
=& D\phi_- \sum_{\boldsymbol{\alpha},m} \mathbb{1}(\nu_1(\boldsymbol{\alpha}) = 0)\mathbb{1}(\nu_{-1}(\boldsymbol{\alpha}) > 0) p_{\boldsymbol{\alpha},m}(t) - Dk\phi_- \sum_{\boldsymbol{\alpha},m} \mathbb{1}(\nu_{-1}(\boldsymbol{\alpha}) = 0) p_{\boldsymbol{\alpha},m}(t) \\
=& D\phi_- \sum_{\boldsymbol{\alpha}} \mathbb{1}(\nu_1(\boldsymbol{\alpha}) = 0)\mathbb{1}(\nu_{-1}(\boldsymbol{\alpha}) > 0) p_{\boldsymbol{\alpha}}(t) - Dk\phi_- \sum_{\boldsymbol{\alpha}} \mathbb{1}(\nu_{-1}(\boldsymbol{\alpha}) = 0) p_{\boldsymbol{\alpha}}(t) \\
=& D\phi_- a \left[c_{-1}(t) - \sum_{\boldsymbol{\alpha}} \mathbb{1}(\nu_1(\boldsymbol{\alpha}) > 0)\nu_{-1}(\boldsymbol{\alpha}) p_{\boldsymbol{\alpha}}(t)/a\right] \\
& - D\phi_- a \sum_{\boldsymbol{\alpha}} \mathbb{1}(\nu_1(\boldsymbol{\alpha}) = 0)\mathbb{1}(\nu_{-1}(\boldsymbol{\alpha}) > 1) \left[\nu_{-1}(\boldsymbol{\alpha}) - 1\right] p_{\boldsymbol{\alpha}}(t)/a \\
& - D\phi_- a \left[\frac{k/a}{1-k}(1-k) - k \sum_{\boldsymbol{\alpha}} \mathbb{1}(\nu_{-1}(\boldsymbol{\alpha}) > 0) p_{\boldsymbol{\alpha}}(t)/a\right] \\
=& D\phi_- a \left[c_{-1}(t) - c^{eq}\right] + D\phi_- a f_-(t) \ . \qquad \text{(3.13b)}
\end{aligned}$$

Equations (3.13) demonstrate the intended result. □

Remark 7. *These averages $f_\pm$, defined in (3.12), measure the frequency by which the atomistic system visits configurations that forbid detachment of the edge atom or attachment of an adatom from the right (+) or left (−) of the step edge. We expect that the magnitudes of correction terms $f_\pm$ are negligibly small in the appropriate low-density regime for adatoms [70, 71].*

3.2.3 Evolution equation for $\rho_j(t)$

We now derive an evolution equation for adatom density in Eulerian coordinates. Our approach involves taking the time derivative of $\rho_j(t)$, defined in (3.7b), and formally applying symbolic master equation (2.12). In the resulting equation, there is a clear separation between (i) a discrete diffusion equation valid away from the step, and (ii) boundary conditions at the left and right of the step. Corrections to the discrete diffusion equation and the discrete version of Fick's law also become readily apparent in the equation for $\dot{\rho}_j(t)$. Each of the aforementioned aspects of the evolution equation for discrete density are discussed later, in Sections 3.2.3.1 and 3.2.3.2. First, we state and derive the equation for $\dot{\rho}_j(t)$, which is the focus of the next proposition.

Proposition 3. (Evolution of discrete density) *The time evolution of the discrete adatom density, $\rho_j(t)$, defined in (3.7b), is described by*

$$\begin{aligned}
\dot{\rho}_j(t) = {} & D\left[\varrho_{j-1}(t) - 2\varrho_j(t) + \varrho_{j+1}(t)\right] + \frac{F}{(N-1)a} - \frac{1}{\tau}\varrho_j(t) \\
& - \sum_{\boldsymbol{\alpha},m} \Bigg\{ \delta_{j,s(\boldsymbol{\alpha},m)} \Big[D\mathbb{1}(\nu_{-1}(\boldsymbol{\alpha}) > 0) + D\mathbb{1}(\nu_1(\boldsymbol{\alpha}) > 0) + \frac{F}{N-1} \Big] \\
& \quad - \delta_{j,s(\boldsymbol{\alpha},m)-1} \Big[D\mathbb{1}(\nu_{-1}(\boldsymbol{\alpha}) > 0) + Dk\phi_-\mathbb{1}(\nu_{-1}(\boldsymbol{\alpha}) = 0) \\
& \qquad\qquad - D\phi_-\mathbb{1}(\nu_1(\boldsymbol{\alpha}) = 0)\mathbb{1}(\nu_{-1}(\boldsymbol{\alpha}) > 0) \Big] \\
& \quad - \delta_{j,s(\boldsymbol{\alpha},m)+1} \Big[D\mathbb{1}(\nu_1(\boldsymbol{\alpha}) > 0) + Dk\phi_+\mathbb{1}(\nu_{-1}(\boldsymbol{\alpha}) = 0) \\
& \qquad\qquad - D\phi_+\mathbb{1}(\nu_1(\boldsymbol{\alpha}) = 1) \Big] \Bigg\} p_{\boldsymbol{\alpha},m}(t)/a \ . \qquad (3.14)
\end{aligned}$$

Equation (3.14) is a direct consequence of Definition 8 and the time evolution of the microscale KRSOS model.

Proof. We derive equation (3.14) directly via symbolic master equation (2.12). The time derivative of the discrete density $\rho_j(t)$ is

$$\begin{aligned}\dot{\rho}_j(t) = \sum_{\boldsymbol{\alpha},m} \nu_{j-s(\boldsymbol{\alpha},m)} \Big\{ & D\Delta_{\boldsymbol{\alpha}} p_{\boldsymbol{\alpha},m}(t) + \frac{F}{N-1} \sum_{\hat{\imath}\in\boldsymbol{\alpha}} p_{\boldsymbol{\alpha}^{\hat{\imath}},m-1}(t) - F p_{\boldsymbol{\alpha},m}(t) \\ & + \frac{1}{\tau} \sum_{\hat{\imath}>0} p_{\boldsymbol{\alpha}_{\hat{\imath}},m+1}(t) - \frac{1}{\tau} \sum_{\hat{\imath}\in\boldsymbol{\alpha}} p_{\boldsymbol{\alpha},m}(t) \\ & + D\phi_- \left[\mathbb{1}(\nu_{-1}(\boldsymbol{\alpha}) = 0) p_{\boldsymbol{\alpha}_-,m}(t) - \mathbb{1}(\nu_1(\boldsymbol{\alpha}) = 0)\mathbb{1}(\nu_{-1}(\boldsymbol{\alpha}) > 0) p_{\boldsymbol{\alpha},m}(t) \right] \\ & + Dk\phi_- \left[\mathbb{1}(\nu_1(\boldsymbol{\alpha}) = 0)\mathbb{1}(\nu_{-1}(\boldsymbol{\alpha}) > 0) p_{\boldsymbol{\alpha}^-,m}(t) - \mathbb{1}(\nu_{-1}(\boldsymbol{\alpha}) = 0) p_{\boldsymbol{\alpha},m}(t) \right] \\ & + D\phi_+ \left[\mathbb{1}(\nu_{-1}(\boldsymbol{\alpha}) = 0) p_{\boldsymbol{\alpha}_+,m}(t) - \mathbb{1}(\nu_1(\boldsymbol{\alpha}) = 1) p_{\boldsymbol{\alpha},m}(t) \right] \\ & + Dk\phi_+ \left[\mathbb{1}(\nu_1(\boldsymbol{\alpha}) = 1) p_{\boldsymbol{\alpha}^+,m}(t) - \mathbb{1}(\nu_{-1}(\boldsymbol{\alpha}) = 0) p_{\boldsymbol{\alpha},m}(t) \right] \Big\} / a \ . \end{aligned} \tag{3.15}$$

In (3.15), we simply re-write $\dot{p}_{\boldsymbol{\alpha},m}(t)$ using symbolic master equation (2.12). The remainder of this proof is devoted to simplifying the above formula for $\dot{\rho}_j(t)$ by expressing the right hand side of (3.15) in terms of averages over $p_{\boldsymbol{\alpha},m}(t)$ instead of "modified", yet related, states (i.e. $\boldsymbol{\alpha}^{\hat{\imath}}$, $\boldsymbol{\alpha}_{\hat{\imath}}$, etc.). This is done for five types of microscale dynamics: (I) diffusion, (II) deposition, (III) desorption, (IV) attachment/detachment on the left of the step and (V) attachment/detachment on the right of the step. The ensuing calculations, for each case, involve (a) application of appropriate change-of-variable formulas to the functions $\nu_{\hat{\imath}}(\boldsymbol{\alpha})$ and indicators thereof, and (b) re-indexing certain sums over states $(\boldsymbol{\alpha}, m)$.

Case I: Diffusion terms. First, let us expand the terms in (3.15) corresponding

to diffusive processes. By (2.11a), we may write

$$
\begin{aligned}
&\sum_{\boldsymbol{\alpha},m} \nu_{j-s(\boldsymbol{\alpha},m)}(\boldsymbol{\alpha}) \Delta_{\boldsymbol{\alpha}} p_{\boldsymbol{\alpha},m}(t) \\
&\quad = \sum_{\boldsymbol{\alpha},m} \nu_{j-s(\boldsymbol{\alpha},m)}(\boldsymbol{\alpha}) \Big\{ \sum_{\substack{\hat{\imath}\in\boldsymbol{\alpha} \\ \hat{\imath}\neq 0,\pm 1}} \Big[p_{\boldsymbol{\alpha}^{\hat{\imath}}_{\hat{\imath}-1},m}(t) - 2p_{\boldsymbol{\alpha},m}(t) + p_{\boldsymbol{\alpha}^{\hat{\imath}}_{\hat{\imath}+1},m}(t) \Big] \Big\} \\
&\qquad + \mathbb{1}(\nu_1(\boldsymbol{\alpha}) > 0) \Big[p_{\boldsymbol{\alpha}^1_2,m}(t) - p_{\boldsymbol{\alpha},m}(t) \Big] \\
&\qquad + \mathbb{1}(\nu_{-1}(\boldsymbol{\alpha}) > 0) \Big[p_{\boldsymbol{\alpha}^{-1}_{-2},m}(t) - p_{\boldsymbol{\alpha},m}(t) \Big] \\
&\quad = \sum_{\hat{\imath}\neq 0,\pm 1} \sum_{\boldsymbol{\alpha},m} \mathbb{1}(\nu_{\hat{\imath}}(\boldsymbol{\alpha}) > 0) \nu_{j-s(\boldsymbol{\alpha},m)}(\boldsymbol{\alpha}) \Big\{ \Big[p_{\boldsymbol{\alpha}^{\hat{\imath}}_{\hat{\imath}-1},m}(t) - 2p_{\boldsymbol{\alpha},m}(t) + p_{\boldsymbol{\alpha}^{\hat{\imath}}_{\hat{\imath}+1},m}(t) \Big] \\
&\qquad + \mathbb{1}(\nu_1(\boldsymbol{\alpha}) > 0) \Big[p_{\boldsymbol{\alpha}^1_2,m}(t) - p_{\boldsymbol{\alpha},m}(t) \Big] \\
&\qquad + \mathbb{1}(\nu_{-1}(\boldsymbol{\alpha}) > 0) \Big[p_{\boldsymbol{\alpha}^{-1}_{-2},m}(t) - p_{\boldsymbol{\alpha},m}(t) \Big] \Big\} \, . \qquad (3.16)
\end{aligned}
$$

When $\hat{\imath} \neq 0, \pm 1$, the averages involving $p_{\boldsymbol{\alpha}^{\hat{\imath}}_{\hat{\imath}\pm 1},m}(t)$ in (3.16) can be expressed as follows:

$$
\begin{aligned}
&\sum_{\boldsymbol{\alpha},m} \mathbb{1}(\nu_{\hat{\imath}}(\boldsymbol{\alpha}) > 0) \nu_{j-s}(\boldsymbol{\alpha}) p_{\boldsymbol{\alpha}^{\hat{\imath}}_{\hat{\imath}\pm 1},m}(t) \\
&\quad = \sum_{\boldsymbol{\alpha},m} \mathbb{1}(\nu_{\hat{\imath}\pm 1}(\boldsymbol{\alpha}^{\hat{\imath}}_{\hat{\imath}\pm 1}) > 0) \left[\nu_{j-s}(\boldsymbol{\alpha}^{\hat{\imath}}_{\hat{\imath}\pm 1}) + \delta_{\hat{\imath},j-s} - \delta_{\hat{\imath}\pm 1,j-s} \right] p_{\boldsymbol{\alpha}^{\hat{\imath}}_{\hat{\imath}\pm 1},m}(t) \\
&\quad = \sum_{\boldsymbol{\alpha}^{\hat{\imath}}_{\hat{\imath}\pm 1},m} \mathbb{1}(\nu_{\hat{\imath}\pm 1}(\boldsymbol{\alpha}^{\hat{\imath}}_{\hat{\imath}\pm 1}) > 0) \left[\nu_{j-s}(\boldsymbol{\alpha}^{\hat{\imath}}_{\hat{\imath}\pm 1}) + \delta_{\hat{\imath},j-s} - \delta_{\hat{\imath}\pm 1,j-s} \right] p_{\boldsymbol{\alpha}^{\hat{\imath}}_{\hat{\imath}\pm 1},m}(t) \\
&\quad = \sum_{\boldsymbol{\alpha},m} \mathbb{1}(\nu_{\hat{\imath}\pm 1}(\boldsymbol{\alpha}) > 0) \left[\nu_{j-s}(\boldsymbol{\alpha}) + \delta_{\hat{\imath},j-s} - \delta_{\hat{\imath}\pm 1,j-s} \right] p_{\boldsymbol{\alpha},m}(t) \, , \qquad (3.17)
\end{aligned}
$$

where $s = s(\boldsymbol{\alpha}, m) = s(\boldsymbol{\alpha}^{\hat{\imath}}_{\hat{\imath}\pm 1}, m)$. The above calculation relies on two key steps: (a) A change-of-variable formula (first equality), and (b) a re-indexing of the sum over states (second equality). The latter is valid because there is a one-to-one correspondence between states $\boldsymbol{\alpha}$ and $\boldsymbol{\alpha}^{\hat{\imath}}_{\hat{\imath}\pm 1}$. After re-indexing, the last equality in (3.17) reiterates the previous line with simplified notation.

Now we can re-write (3.16) using (3.17), and, at the same time, complete the sum over $\hat{\imath} \neq 0, \pm 1$ by adding and subtracting the appropriate terms, i.e.,

$$
\begin{aligned}
&\sum_{\boldsymbol{\alpha},m} \nu_{j-s}(\boldsymbol{\alpha}) \Delta_{\boldsymbol{\alpha}} p_{\boldsymbol{\alpha},m}(t) \\
&\quad = \sum_{\hat{\imath}} \sum_{\boldsymbol{\alpha},m} \Big\{ \nu_{j-s}(\boldsymbol{\alpha}) \left[\mathbb{1}(\nu_{\hat{\imath}-1}(\boldsymbol{\alpha}) > 0) - 2\mathbb{1}(\nu_{\hat{\imath}}(\boldsymbol{\alpha}) > 0) + \mathbb{1}(\nu_{\hat{\imath}+1}(\boldsymbol{\alpha}) > 0) \right] \\
&\qquad + \mathbb{1}(\nu_{\hat{\imath}-1}(\boldsymbol{\alpha}) > 0) \left[\delta_{\hat{\imath},j-s} - \delta_{\hat{\imath}-1,j-s} \right] \\
&\qquad + \mathbb{1}(\nu_{\hat{\imath}+1}(\boldsymbol{\alpha}) > 0) \left[\delta_{\hat{\imath},j-s} - \delta_{\hat{\imath}+1,j-s} \right] \Big\} p_{\boldsymbol{\alpha},m}(t) \\
&\quad + \sum_{\boldsymbol{\alpha},m} \Big\{ \nu_{j-s}(\boldsymbol{\alpha}) \left[\mathbb{1}(\nu_2(\boldsymbol{\alpha}) > 0) - \mathbb{1}(\nu_1(\boldsymbol{\alpha}) > 0) + \mathbb{1}(\nu_{-2}(\boldsymbol{\alpha}) > 0) - \mathbb{1}(\nu_{-1}(\boldsymbol{\alpha}) > 0) \right] \\
&\qquad + \mathbb{1}(\nu_2(\boldsymbol{\alpha}) > 0) \left[\delta_{j,s+1} - \delta_{j,s+2} \right] + \mathbb{1}(\nu_{-2}(\boldsymbol{\alpha}) > 0) \left[\delta_{j,s-1} - \delta_{j,s-2} \right] \Big\} p_{\boldsymbol{\alpha},m}(t) \\
&\quad - \sum_{\boldsymbol{\alpha},m} \Big\{ \nu_{j-s}(\boldsymbol{\alpha}) \Big[\mathbb{1}(\nu_{-2}(\boldsymbol{\alpha}) > 0) - 2\mathbb{1}(\nu_{-1}(\boldsymbol{\alpha}) > 0) + \mathbb{1}(\nu_0(\boldsymbol{\alpha}) > 0) \\
&\qquad\quad + \mathbb{1}(\nu_{-1}(\boldsymbol{\alpha}) > 0) - 2\mathbb{1}(\nu_0(\boldsymbol{\alpha}) > 0) + \mathbb{1}(\nu_1(\boldsymbol{\alpha}) > 0) \\
&\qquad\quad + \mathbb{1}(\nu_0(\boldsymbol{\alpha}) > 0) - 2\mathbb{1}(\nu_1(\boldsymbol{\alpha}) > 0) + \mathbb{1}(\nu_2(\boldsymbol{\alpha}) > 0) \Big] \\
&\qquad + \mathbb{1}(\nu_{-2}(\boldsymbol{\alpha}) > 0) \left[\delta_{j,s-1} - \delta_{j,s-2} \right] + \mathbb{1}(\nu_0(\boldsymbol{\alpha}) > 0) \left[\delta_{j,s-1} - \delta_{j,s} \right] \\
&\qquad + \mathbb{1}(\nu_{-1}(\boldsymbol{\alpha}) > 0) \left[\delta_{j,s} - \delta_{j,s-1} \right] + \mathbb{1}(\nu_1(\boldsymbol{\alpha}) > 0) \left[\delta_{j,s} - \delta_{j,s+1} \right] \\
&\qquad + \mathbb{1}(\nu_0(\boldsymbol{\alpha}) > 0) \left[\delta_{j,s+1} - \delta_{j,s} \right] + \mathbb{1}(\nu_2(\boldsymbol{\alpha}) > 0) \left[\delta_{j,s+1} - \delta_{j,s+2} \right] \Big\} p_{\boldsymbol{\alpha},m}(t) \ .
\end{aligned}
\tag{3.18}
$$

Considerable simplification in the above formula leads to our final equation for the

diffusion terms in (3.15), viz.,

$$\begin{aligned}
&\sum_{\boldsymbol{\alpha},m} \nu_{j-s}(\boldsymbol{\alpha}) \Delta_{\boldsymbol{\alpha}} p_{\boldsymbol{\alpha},m}(t) \\
&\quad = \sum_{\boldsymbol{\alpha},m} \Big\{ \mathbb{1}(\nu_{j-s-1}(\boldsymbol{\alpha}) > 0) - 2\mathbb{1}(\nu_{j-s}(\boldsymbol{\alpha}) > 0) + \mathbb{1}(\nu_{j-s+1}(\boldsymbol{\alpha}) > 0) \\
&\qquad + \mathbb{1}(\nu_{-1}(\boldsymbol{\alpha}) > 0) \left[\delta_{j,s-1} - \delta_{j,s}\right] + \mathbb{1}(\nu_{1}(\boldsymbol{\alpha}) > 0) \left[\delta_{j,s+1} - \delta_{j,s}\right] \Big\} p_{\boldsymbol{\alpha},m}(t) \\
&\quad = a \left[\varrho_{j-1}(t) - 2\varrho_j(t) + \varrho_{j+1}(t)\right] \\
&\qquad + \sum_{\boldsymbol{\alpha},m} \Big\{ \mathbb{1}(\nu_{-1}(\boldsymbol{\alpha}) > 0) \left[\delta_{j,s-1} - \delta_{j,s}\right] + \mathbb{1}(\nu_{1}(\boldsymbol{\alpha}) > 0) \left[\delta_{j,s+1} - \delta_{j,s}\right] \Big\} p_{\boldsymbol{\alpha},m}(t) \ ,
\end{aligned} \tag{3.19}$$

where again we simplify the notation by using $s = s(\boldsymbol{\alpha}, m)$. Here, (3.19) is written concisely with the use of dilute density (3.8b). The final expression involves a discrete diffusion-type difference scheme for $\varrho_j(t)$ when j is sufficiently away from the step, plus terms which account for the presence of the step via Kronecker delta functions.

Case II: Deposition terms. Next, we address contributions from deposition in our derivation of an evolution equation for $\rho_j(t)$. As in the previous case, we must re-write any averages in (3.15) that do not explicitly involve $p_{\boldsymbol{\alpha},m}(t)$. For the case

of deposition, we have

$$\begin{aligned}
\sum_{\boldsymbol{\alpha},m}\nu_{j-s}(\boldsymbol{\alpha})\sum_{\hat{\imath}\in\boldsymbol{\alpha}}p_{\boldsymbol{\alpha}^{\hat{\imath}},m-1}(t) &= \sum_{\hat{\imath}>0}\sum_{\boldsymbol{\alpha},m}\mathbb{1}(\nu_{\hat{\imath}}(\boldsymbol{\alpha})>0)\nu_{j-s}(\boldsymbol{\alpha})p_{\boldsymbol{\alpha}^{\hat{\imath}},m-1}(t) \\
&= \sum_{\hat{\imath}>0}\sum_{\boldsymbol{\alpha},m}\left[1-\mathbb{1}(\nu_{\hat{\imath}}(\boldsymbol{\alpha})=0)\right]\nu_{j-s}(\boldsymbol{\alpha})p_{\boldsymbol{\alpha}^{\hat{\imath}},m-1}(t) \\
&= \sum_{\hat{\imath}>0}\sum_{\boldsymbol{\alpha},m}\left[\nu_{j-s}(\boldsymbol{\alpha}^{\hat{\imath}})+\delta_{\hat{\imath},j-s}\right]p_{\boldsymbol{\alpha}^{\hat{\imath}},m-1}(t) \\
&\quad -\sum_{\hat{\imath}>0}\sum_{\boldsymbol{\alpha},m}\nu_{j-s}(\boldsymbol{\alpha})\mathbb{1}(\nu_{\hat{\imath}}(\boldsymbol{\alpha})=0)p_{\boldsymbol{\alpha}^{\hat{\imath}},m-1}(t) \\
&= \sum_{\hat{\imath}>0}\sum_{\boldsymbol{\alpha},m}\left[\nu_{j-s}(\boldsymbol{\alpha})+\delta_{\hat{\imath},j-s}\right]p_{\boldsymbol{\alpha},m}(t) \\
&= (N-1)\sum_{\boldsymbol{\alpha},m}\nu_{j-s}(\boldsymbol{\alpha})p_{\boldsymbol{\alpha},m}(t)+1-\sum_{\boldsymbol{\alpha},m}\delta_{j,s}p_{\boldsymbol{\alpha},m}(t)\ . \qquad (3.20)
\end{aligned}$$

The above calculation makes use of the complement rule for probability and (2.10f). By (3.20), the contribution to $\dot{\rho}_j(t)$ from deposition in (3.15) may be written as

$$\begin{aligned}
&\sum_{\boldsymbol{\alpha},m}\nu_{j-s}(\boldsymbol{\alpha})\Big\{\frac{1}{N-1}\sum_{\hat{\imath}\in\boldsymbol{\alpha}}p_{\boldsymbol{\alpha}^{\hat{\imath}},m-1}(t)-p_{\boldsymbol{\alpha},m}(t)\Big\} \\
&\qquad =\frac{1}{N-1}-\frac{1}{N-1}\sum_{\boldsymbol{\alpha},m}\delta_{j,s}p_{\boldsymbol{\alpha},m}(t)\ . \qquad (3.21)
\end{aligned}$$

The term involving the Kronecker delta in (3.21) implies that there is no contribution from deposition at the step edge, as expected. On the other hand, away from the step, the contribution to the evolution equation for $\rho_j(t)$ from deposition is a constant: $\frac{F}{(N-1)a}$, or the deposition rate per terrace length.

Case III: Desorption terms. The derivation of terms pertaining to desorption follow the same pattern as the deposition terms in Case II. We write the first

desorption term in (3.15) as

$$\begin{aligned}
&\sum_{\boldsymbol{\alpha},m} \nu_{j-s}(\boldsymbol{\alpha}) \sum_{\hat{\imath}>0} p_{\boldsymbol{\alpha}_{\hat{\imath}},m+1}(t) \\
&\quad = \sum_{\hat{\imath}>0} \sum_{\boldsymbol{\alpha},m} \nu_{j-s}(\boldsymbol{\alpha}) \mathbb{1}(\nu_{\hat{\imath}}(\boldsymbol{\alpha}_{\hat{\imath}}) > 0) p_{\boldsymbol{\alpha}_{\hat{\imath}},m+1}(t) \\
&\quad = \sum_{\hat{\imath}>0} \sum_{\boldsymbol{\alpha},m} \left[\nu_{j-s}(\boldsymbol{\alpha}_{\hat{\imath}}) - \delta_{\hat{\imath},j-s}\right] \mathbb{1}(\nu_{\hat{\imath}}(\boldsymbol{\alpha}_{\hat{\imath}}) > 0) p_{\boldsymbol{\alpha}_{\hat{\imath}},m+1}(t) \\
&\quad = \sum_{\hat{\imath}>0} \sum_{\boldsymbol{\alpha},m} \left[\nu_{j-s}(\boldsymbol{\alpha}) - \delta_{\hat{\imath},j-s}\right] \mathbb{1}(\nu_{\hat{\imath}}(\boldsymbol{\alpha}) > 0) p_{\boldsymbol{\alpha},m}(t) \ . \qquad (3.22)
\end{aligned}$$

Since desorption events do not change the step position, $s = s(\boldsymbol{\alpha}, m+1) = s(\boldsymbol{\alpha}_{\hat{\imath}}, m)$ in the above. Notice that (3.22) and the second desorption term in (3.15) simplify to

$$\begin{aligned}
&-\sum_{\hat{\imath}>0} \sum_{\boldsymbol{\alpha},m} \delta_{\hat{\imath},j-s} \mathbb{1}(\nu_{\hat{\imath}}(\boldsymbol{\alpha}) > 0) p_{\boldsymbol{\alpha},m}(t) \\
&\qquad = -\sum_{\hat{\imath}} \sum_{\boldsymbol{\alpha},m} \delta_{\hat{\imath},j-s} \mathbb{1}(\nu_{\hat{\imath}}(\boldsymbol{\alpha}) > 0) p_{\boldsymbol{\alpha},m}(t) \\
&\qquad = -a\varrho_j(t) \ . \qquad (3.23)
\end{aligned}$$

Here we have used the fact that $\mathbb{1}(\nu_0(\boldsymbol{\alpha}) > 0) = 0$. The final contribution of desorption, therefore, is proportional to the dilute density.

Case IV: Attachment/detachment terms (left of step). Next, using similar techniques as the previous three cases, we derive explicit averages corresponding to attachment and detachment terms on the left of the step, most easily identified by

the prefactor ϕ_- in (3.15). For attachment, consider

$$\begin{aligned}
&\sum_{\boldsymbol{\alpha},m} \nu_{j-s(\boldsymbol{\alpha},m)}(\boldsymbol{\alpha}) \mathbb{1}(\nu_{-1}(\boldsymbol{\alpha}) = 0) p_{\boldsymbol{\alpha}_-,m}(t) \\
&\quad = \sum_{\boldsymbol{\alpha},m} \left[\nu_{j-s(\boldsymbol{\alpha}_-,m)}(\boldsymbol{\alpha}_-) - \delta_{j,s(\boldsymbol{\alpha}_-,m)-1}\right] \mathbb{1}(\nu_1(\boldsymbol{\alpha}_-) = 0) \mathbb{1}(\nu_{-1}(\boldsymbol{\alpha}_-) > 0) p_{\boldsymbol{\alpha}_-,m}(t) \\
&\quad = \sum_{\boldsymbol{\alpha},m} \nu_{j-s(\boldsymbol{\alpha},m)}(\boldsymbol{\alpha}) \mathbb{1}(\nu_1(\boldsymbol{\alpha}) = 0) \mathbb{1}(\nu_{-1}(\boldsymbol{\alpha}) > 0) p_{\boldsymbol{\alpha},m}(t) \\
&\qquad - \sum_{\boldsymbol{\alpha},m} \delta_{j,s(\boldsymbol{\alpha},m)-1} \mathbb{1}(\nu_1(\boldsymbol{\alpha}) = 0) \mathbb{1}(\nu_{-1}(\boldsymbol{\alpha}) > 0) p_{\boldsymbol{\alpha},m}(t) \ . \qquad (3.24)
\end{aligned}$$

Similarly, for detachment we have

$$\begin{aligned}
&\sum_{\boldsymbol{\alpha},m} \nu_{j-s(\boldsymbol{\alpha},m)}(\boldsymbol{\alpha}) \mathbb{1}(\nu_1(\boldsymbol{\alpha}) = 0) \mathbb{1}(\nu_{-1}(\boldsymbol{\alpha}) > 0) p_{\boldsymbol{\alpha}^-,m}(t) \\
&\quad = \sum_{\boldsymbol{\alpha},m} \left[\nu_{j-s(\boldsymbol{\alpha}^-,m)}(\boldsymbol{\alpha}^-) + \delta_{j,s(\boldsymbol{\alpha}^-,m)-1}\right] \mathbb{1}(\nu_{-1}(\boldsymbol{\alpha}^-) = 0) p_{\boldsymbol{\alpha}^-,m}(t) \\
&\quad = \sum_{\boldsymbol{\alpha},m} \nu_{j-s(\boldsymbol{\alpha},m)}(\boldsymbol{\alpha}) \mathbb{1}(\nu_{-1}(\boldsymbol{\alpha}) = 0) p_{\boldsymbol{\alpha},m}(t) \\
&\qquad + \sum_{\boldsymbol{\alpha},m} \delta_{j,s(\boldsymbol{\alpha},m)-1} \mathbb{1}(\nu_{-1}(\boldsymbol{\alpha}) = 0) p_{\boldsymbol{\alpha},m}(t) \ . \qquad (3.25)
\end{aligned}$$

Equations (3.24) and (3.25), along with the remaining attachment and detachment terms in (3.15), on the left of the step only, yield

$$\begin{aligned}
&\sum_{\boldsymbol{\alpha},m} \delta_{j,s(\boldsymbol{\alpha},m)-1} \big[Dk\phi_- \mathbb{1}(\nu_{-1}(\boldsymbol{\alpha}) = 0) \\
&\qquad\qquad - D\phi_- \mathbb{1}(\nu_1(\boldsymbol{\alpha}) = 0) \mathbb{1}(\nu_{-1}(\boldsymbol{\alpha}) > 0)\big] p_{\boldsymbol{\alpha},m}(t) \ , \qquad (3.26)
\end{aligned}$$

which, with recourse to Definition 10, reduces to $-J_-(t)$ when $j = s-1$, and is zero otherwise.

Case V: Attachment/detachment terms (right of step). Finally, we simplify attachment and detachment terms on the right of the step, all of which include the

prefactor ϕ_+ in (3.15). First, the attachment terms are

$$\begin{aligned}
&\sum_{\boldsymbol{\alpha},m} \nu_{j-s(\boldsymbol{\alpha},m)}(\boldsymbol{\alpha}) \mathbb{1}(\nu_{-1}(\boldsymbol{\alpha})=0) p_{\boldsymbol{\alpha}_+,m}(t) \\
&\quad = \sum_{\boldsymbol{\alpha},m} \left[\nu_{j-s(\boldsymbol{\alpha}_+,m)}(\boldsymbol{\alpha}_+) - \delta_{j,s(\boldsymbol{\alpha}_+,m)+1}\right] \mathbb{1}(\nu_1(\boldsymbol{\alpha}_+)=1) p_{\boldsymbol{\alpha}_+,m}(t) \\
&\quad = \sum_{\boldsymbol{\alpha},m} \nu_{j-s(\boldsymbol{\alpha},m)}(\boldsymbol{\alpha}) \mathbb{1}(\nu_1(\boldsymbol{\alpha})=1) p_{\boldsymbol{\alpha},m}(t) \\
&\qquad - \sum_{\boldsymbol{\alpha},m} \delta_{j,s(\boldsymbol{\alpha},m)+1} \mathbb{1}(\nu_1(\boldsymbol{\alpha})=1) p_{\boldsymbol{\alpha},m}(t) \ . \qquad (3.27)
\end{aligned}$$

Second, the detachment terms are

$$\begin{aligned}
&\sum_{\boldsymbol{\alpha},m} \nu_{j-s(\boldsymbol{\alpha},m)}(\boldsymbol{\alpha}) \mathbb{1}(\nu_1(\boldsymbol{\alpha})=1) p_{\boldsymbol{\alpha}^+,m}(t) \\
&\quad = \sum_{\boldsymbol{\alpha},m} \left[\nu_{j-s(\boldsymbol{\alpha}^+,m)}(\boldsymbol{\alpha}^+) + \delta_{j,s(\boldsymbol{\alpha}^+,m)+1}\right] \mathbb{1}(\nu_{-1}(\boldsymbol{\alpha}^+)=0) p_{\boldsymbol{\alpha}^+,m}(t) \\
&\quad = \sum_{\boldsymbol{\alpha},m} \nu_{j-s(\boldsymbol{\alpha},m)}(\boldsymbol{\alpha}) \mathbb{1}(\nu_{-1}(\boldsymbol{\alpha})=0) p_{\boldsymbol{\alpha},m}(t) \\
&\qquad + \sum_{\boldsymbol{\alpha},m} \delta_{j,s(\boldsymbol{\alpha},m)+1} \mathbb{1}(\nu_{-1}(\boldsymbol{\alpha})=0) p_{\boldsymbol{\alpha},m}(t) \ . \qquad (3.28)
\end{aligned}$$

Similar to the result in Case IV, equations (3.27) and (3.28), along with attachment and detachment terms in (3.15) on the right of the step only, give

$$\begin{aligned}
&\sum_{\boldsymbol{\alpha},m} \delta_{j,s(\boldsymbol{\alpha},m)+1} \big[Dk\phi_+ \mathbb{1}(\nu_{-1}(\boldsymbol{\alpha})=0) \\
&\qquad\qquad - D\phi_+ \mathbb{1}(\nu_1(\boldsymbol{\alpha})=1)\big] p_{\boldsymbol{\alpha},m}(t) \ . \qquad (3.29)
\end{aligned}$$

By Definition 10, equation (3.29) reduces to $J_+(t)$ when $j = s+1$, and is zero otherwise. This completes the proof of Proposition 3. □

The approach in Proposition 3 contrasts what was previously done in [71] in two essential ways: First, by focusing on the Eulerian density, we do not introduce

discrete advection terms that are always present away from the step in Lagrangian coordinates; such terms cannot be readily expressed in closed form, e.g. in terms of adatom densities, and therefore do not make the corresponding continuum terms apparent [71]. Second, the use of symbolic master equation (2.12) allows for the isolation of each atomistic process, and thus makes manifest non-trivial cancellations imparted by the microscale KRSOS model.

3.2.3.1 Discrete diffusion equation

One of the important consequences of Proposition 3 is that the adatom density, $\rho_j(t)$, evolves according to a discrete diffusion-type scheme when j is sufficiently far from the step. This discrete scheme is not exact, however; corrections resulting from multiply-occupied lattice sites are evident in (3.14).

When j is away from the step, equation (3.14) reduces to

$$\dot{\rho}_j(t) = D\Delta_j \varrho_j(t) + \frac{F}{(N-1)a} - \frac{1}{\tau}\varrho_j(t) \ , \tag{3.30}$$

where Δ_j is the second-order finite difference operator, i.e. $\Delta_j \varrho_j = \varrho_{j-1} - 2\varrho_j + \varrho_{j+1}$. The above equation involves the dilute density, $\varrho_j(t)$, on the right-hand side. On the other hand, in an exact discrete scheme, we would expect $\rho_j(t)$ to appear. In fact, it turns out that correction terms are differences in densities $\rho_j(t) - \varrho_j(t)$.

At this stage it is useful to point out that the form of these corrections should not depended on choice of the coordinate system. Indeed, the entire derivation of diffusion terms, i.e. those involving $\Delta_{\boldsymbol{\alpha}} p_{\boldsymbol{\alpha},m}(t)$, in the proof of Proposition 3 could be repeated for Lagrangian density, $c_j(t)$. The resulting discrete scheme involves

second-order differences $\Delta_j \mathfrak{c}_j(t)$. Accordingly, we define the"high-occupancy" corrections as

$$\hat{R}_{\hat{\jmath}}(t) = \sum_{\boldsymbol{\alpha}} \left[\nu_{\hat{\jmath}}(\boldsymbol{\alpha}) - \mathbb{1}(\nu_{\hat{\jmath}}(\boldsymbol{\alpha}) > 0)\right] p_{\boldsymbol{\alpha}}(t)/a \ . \tag{3.31}$$

The high-occupancy effect measured by (3.31) can be seen in the difference $\nu_{\hat{\jmath}}(\boldsymbol{\alpha}) - \mathbb{1}(\nu_{\hat{\jmath}}(\boldsymbol{\alpha}) > 0)$, which is nonzero only when two or more adatoms are at site $\hat{\jmath}$. In the following remark, we identify the feature of the KRSOS model that induces corrections of the form (3.31).

Remark 8. *The corrections (3.31) associated with discrete diffusion arise from the fact that the KRSOS model includes constant adatom hopping rates, regardless of the number of adatoms present at a given lattice site. In effect, atomistic configurations with multiple adatoms at the same lattice site introduce* kinetic interactions *between adatoms since only one adatom, e.g. the top adatom in a stack, is able to move [71].*

High-occupancy corrections (3.31) will be analyzed in Section 3.3.

3.2.3.2 Boundary conditions

In this section, we complement Proposition 2 with a mass-transport relation between discrete fluxes and densities near the step edge, which forms a discrete analog of Fick's law for diffusion. As the second main consequence of Proposition 3, high-occupancy corrections (3.31) play an important role. The effect of advection, which comes from step motion, is conspicuously absent from the discrete boundary conditions at the step edge; we attribute this absence to forbidden transitions in the

KRSOS model. It should be noted, however, that transitions at the step should not drastically alter the effect of advection away from the step; see Section 3.2.4.

To start, we note that the third and fourth lines of (3.14), multiplied by Kronecker delta $\delta_{j,s(\boldsymbol{\alpha},m)-1}$, correspond to

$$\begin{aligned} D\sum_{\boldsymbol{\alpha},m}\Big[&\mathbb{1}(\nu_{-2}(\boldsymbol{\alpha})>0)-\mathbb{1}(\nu_{-1}(\boldsymbol{\alpha})>0)\\ &+k\phi_{-}\mathbb{1}(\nu_{-1}(\boldsymbol{\alpha})=0)-\phi_{-}\mathbb{1}(\nu_{1}(\boldsymbol{\alpha})=0)\mathbb{1}(\nu_{-1}(\boldsymbol{\alpha})>0)\\ &=D\left[c_{-2}(t)-c_{-1}(t)\right]-a^{-1}J_{-}(t)+D\left[\hat{R}_{-2}(t)-\hat{R}_{-1}(t)\right]\ . \end{aligned} \tag{3.32a}$$

Here, J_{-} is defined by (3.10). The analogous result for terms associated with J_{+} can be reached for the last two lines of (3.14), which are multiplied by $\delta_{j,s(\boldsymbol{\alpha},m)+1}$. At the right of the step edge, we identify

$$\begin{aligned} D\sum_{\boldsymbol{\alpha},m}\Big[&\mathbb{1}(\nu_{2}(\boldsymbol{\alpha})>0)-\mathbb{1}(\nu_{1}(\boldsymbol{\alpha})>0)\\ &+k\phi_{+}\mathbb{1}(\nu_{-1}(\boldsymbol{\alpha})=0)-\phi_{+}\mathbb{1}(\nu_{1}(\boldsymbol{\alpha})=1)\\ &=D\left[c_{2}(t)-c_{1}(t)\right]+a^{-1}J_{+}(t)+D\left[\hat{R}_{2}(t)-\hat{R}_{1}(t)\right]\ . \end{aligned} \tag{3.32b}$$

It should be noted that the terms $\hat{R}_j(t)$ found in equations (3.32) are consistent with those present in the discrete analog of the diffusion equation.

In view of (3.32), we now extract appropriate discrete boundary conditions at the left ($j=s(\boldsymbol{\alpha},m)-1$) and right ($j=s(\boldsymbol{\alpha},m)+1$) of step edge from (3.14). We find

$$J_{\pm}(t)=\mp Da\left[c_{\pm2}(t)-c_{\pm1}(t)\right]\mp Da\left[\hat{R}_{\pm2}(t)-\hat{R}_{\pm1}(t)\right]\ . \tag{3.33}$$

Equations (3.33) are a discrete version of Fick's law including corrections to diffusive fluxes at each side of the step edge.

Remark 9. *In contrast to (3.3), the advection term at the step edge does not appear in* (3.33)*. We have not been able to derive this term from the atomistic model. We attribute this inability to the fact that certain atomistic configurations inhibit the motion of the step edge. Specifically, transitions where the step would advance by more than one lattice spacing or retreat when adatoms are present on top of the edge atom are forbidden, as seen in rates (2.3a) and (2.3b), respectively. In effect, these forbidden processes can cause adatoms to pile up in front of the step edge, thereby conserving mass at the atomistic scale. On the other hand, at the mesoscale, the step accumulates mass continuously as it moves past regions of nonzero adatom density. This mechanism is not captured in the KRSOS model.*

3.2.4 Advection away from the step

In this section, we develop a plausibility argument for the extraction of a discrete counterpart to the continuum-scale advection term, $v\frac{\partial \mathcal{C}}{\partial \hat{x}}$, which enters diffusion equation (3.2), from the atomistic model. This argument provides a heuristic reconciliation of continuum-scale advection with the atomistic and probabilistic perspectives of the master equation approach followed in in this thesis. We will invoke the notation $v = \dot{\varsigma}(t)$ for the average step velocity; $\varsigma(t)$ is the average step position introduced in Definition 7.

Consider the Eulerian adatom density of (3.7b), Definition 8. First, note that the corresponding sum can be conveniently rewritten as

$$\rho_j(t) = \sum_{n\in\mathbb{Z}} \sum_{(\boldsymbol{\alpha},m)\in\mathfrak{S}(n)} \nu_{j-s_0+n}(\boldsymbol{\alpha})\, p(\boldsymbol{\alpha}, m; t)/a \ , \tag{3.34}$$

where $|n|$ counts the total number of adatoms detached from ($n > 0$) or attached to ($n < 0$) the step edge and, thus, determines the microscopic position, $s_0 - n$, of the step on the lattice; $p(\boldsymbol{\alpha}, m; t) := p_{\boldsymbol{\alpha},m}(t)$ for notational convenience; and $\mathfrak{S}(n) := \{(\boldsymbol{\alpha}, m) \,\big|\, |\boldsymbol{\alpha}| = n + (m - m_0)\}$, the set of all allowed values of $(\boldsymbol{\alpha}, m)$ for fixed n.

In order to extract the advection term sufficiently away from the step edge, we take into account the decomposition of $p(\boldsymbol{\alpha}, m; t)$ into products of the form $p(\boldsymbol{\alpha}, m\big|n; t)\, \wp(n; t)$. In this product, $\wp(n; t)$ is the probability that the microscopic step lies at the lattice site $s_0 - n$ at time t, and $p(\boldsymbol{\alpha}, m\big|n; t)$ is the conditional probability for state $(\boldsymbol{\alpha}, m)$ to occur *given* that the step edge is at site $s_0 - n$. Hence, (3.34) is recast to the formula

$$\rho_j(t) = \sum_n \wp(n; t) \sum_{(\boldsymbol{\alpha},m)\in\mathfrak{S}(n)} \nu_{j-s_0+n}(\boldsymbol{\alpha})\, p(\boldsymbol{\alpha}, m\big|n; t)/a \ , \tag{3.35}$$

for fixed j. Clearly, the right-hand side of (3.35) becomes the discrete Lagrangian density $c_{\hat{\jmath}}(t)$ if $j - s_0 + n$ under the summation sign is replaced by the index $\hat{\jmath}$; cf. (3.7a) in Definition 8.

At this stage, by inspection of (3.35), we define

$$c(\hat{\jmath}\big|\mathfrak{N}; t) := \sum_{(\boldsymbol{\alpha},m)\in\mathfrak{S}(\mathfrak{N})} \nu_{j-s_0+\mathfrak{N}}(\boldsymbol{\alpha})\, p(\boldsymbol{\alpha}, m\big|\mathfrak{N}; t)/a \ . \tag{3.36}$$

This formula expresses the (conditional) Lagrangian adatom density at fixed site $\hat{\jmath}$ *given* that the step position is at site $s_0 - \mathfrak{N}$. Here, $\mathfrak{N}$ is the discrete random variable with values $n \in \mathbb{Z}$ that represents the number of adatoms detached from the step

edge. Accordingly, we compute

$$\dot{c}_{\hat{\jmath}}(t) = \sum_n \dot{\wp}(n;t) c(\hat{\jmath}\big|n;t) + \langle \dot{c}(\hat{\jmath}\big|\mathfrak{N};t)\rangle, \tag{3.37}$$

where $\langle f(\mathfrak{N};t)\rangle$ is the expectation of the random variable $f(\mathfrak{N};t)$ under the probability distribution $\wp(n;t)$, viz., $\langle f(\mathfrak{N};t)\rangle := \sum_n \wp(n;t) f(n;t)$, with $f(\ \cdot\ ;t) = \dot{c}(\hat{\jmath}\big|\ \cdot\ ;t)$.

Next, we show that (3.37) plausibly generates a discrete version of the anticipated advection term at long times. For this purpose, we hypothesize that $\wp(n;t)$ is well approximated by the Poisson distribution with parameter $\varsigma(t)/a$. This was demonstrated for case of conservative dynamics on large lattices ($N \gg 1$) in equilibrium; see (2.19). On the other hand, $\wp(n;t)$ should be approximately Poisson for sufficiently long times in the non-conservative case with $F > 0$ and $\tau^{-1} = 0$. To see this, consider (2.1) after marginalizing by $\boldsymbol{\alpha}$. The resulting equation,

$$\dot{p}_m(t) = \sum_m T_{m,m'} p_{m'}(t), \tag{3.38}$$

subject to $p_0(0) = 1$, is satisfied by the Poisson distribution $p_m(t) = \frac{(Ft)^m e^{-Ft}}{m!}$. Then, for $t \gg F^{-1}$, the Poisson hypothesis for $\wp(n;t)$ is expected to hold. At this stage, we do not have a quantitative argument supporting our hypothesis regarding $\wp(n;t)$ when $\tau^{-1} > 0$.

Assuming the Poisson hypothesis is true, we may write $\dot{\wp}(n;t) \approx [\dot{\varsigma}(t)/a]\{\wp(n-1;t) - \wp(n;t)\}$, bearing in mind that correction terms neglected in this formula should account for finite times and the effect of higher adatom numbers per site, controlled by k and F. By applying summation by parts in the screw-periodic setting of our

system we obtain

$$\sum_n \dot{\wp}(n;t)c(\hat{\jmath}\big|n;t) \approx [\dot{\varsigma}(t)/a] \sum_n \wp(n;t)\{c(\hat{\jmath}\big|n+1;t) - c(\hat{\jmath}\big|n;t)\}$$

$$= \dot{\varsigma}(t)a^{-1}\left\{\langle c(\hat{\jmath}\big|\mathfrak{N}+1;t)\rangle - \langle c(\hat{\jmath}\big|\mathfrak{N};t)\rangle\right\} \ . \tag{3.39}$$

Were it true that $\langle c(\hat{\jmath}\big|\mathfrak{N}+\ell;t)\rangle \approx \langle c(\hat{\jmath}-\ell\big|\mathfrak{N};t)\rangle$ for any integer ℓ, expressing the translation invariance of the adatom system relative to the step edge, (3.39) would imply

$$\sum_n \dot{\wp}(n;t)c(\hat{\jmath}\big|n;t) \approx -\dot{\varsigma}(t)a^{-1}\left\{\langle c(\hat{\jmath}\big|\mathfrak{N};t)\rangle - \langle c(\hat{\jmath}-1\big|\mathfrak{N};t)\rangle\right\} \ , \tag{3.40}$$

which is the discrete counterpart to $v\frac{\partial \mathcal{C}}{\partial \hat{x}}$ we seek. We leave it as an open question to what extent this approximation is true.

3.2.5 Step velocity law

In this section, we derive the anticipated mass conservation statement that involves the average step velocity, $\dot{\varsigma}(t)$; see Definition 7. This average is computed explicitly by differentiating (3.6) with respect to time, and formal application of master equations (2.1) and (2.12). The result is a step velocity law involving the difference of the fluxes $J_\pm$, which are defined in (3.10).

Proposition 4. (Discrete step velocity law) *The time evolution of the average step position, $\varsigma(t)$, defined in (3.6), is given by*

$$\dot{\varsigma}(t) = a\left[J_-(t) - J_+(t)\right] \ . \tag{3.41}$$

Hence, the BCF step velocity law (3.1) is a direct consequence of Definition 7 and the microscale dynamics of the KRSOS model.

Proof. We prove the proposition in two parts: (i) Using properties of the full master equation (2.1), we will show that deposition, desorption, and terrace hopping cannot contribute to step velocity; and (ii) we will calculate the contributions to $\dot{\varsigma}(t)$ from attachment and detachment using symbolic master equation (2.12).

First, by Definition 7 and master equation (2.1), the time evolution of $\varsigma(t)$ is described by

$$\begin{aligned}
\dot{\varsigma}(t) &= a \sum_{\boldsymbol{\alpha},m} s(\boldsymbol{\alpha},m)\dot{p}_{\boldsymbol{\alpha},m}(t) \\
&= a \sum_{\boldsymbol{\alpha},m} \sum_{\substack{(\boldsymbol{\alpha}',m') \\ \neq(\boldsymbol{\alpha},m)}} s(\boldsymbol{\alpha},m) \left[T_{(\boldsymbol{\alpha},m),(\boldsymbol{\alpha}',m')} p_{\boldsymbol{\alpha}',m'}(t) - T_{(\boldsymbol{\alpha}',m'),(\boldsymbol{\alpha},m)} p_{\boldsymbol{\alpha},m}(t) \right] \\
&= a \sum_{\boldsymbol{\alpha},m} \sum_{\boldsymbol{\alpha}',m'} \left[s(\boldsymbol{\alpha},m) - s(\boldsymbol{\alpha}',m') \right] T_{(\boldsymbol{\alpha},m),(\boldsymbol{\alpha}',m')} p_{\boldsymbol{\alpha}',m'}(t) \ . \qquad (3.42)
\end{aligned}$$

In (3.42) we invoke property (2.2f) of the transition rates to make the difference $s(\boldsymbol{\alpha},m) - s(\boldsymbol{\alpha}',m')$ appear. This formula makes it clear that any transition from state $(\boldsymbol{\alpha}',m')$ to $(\boldsymbol{\alpha},m)$ where the step position does not change *cannot contribute* to the step velocity. In the KRSOS model described in Section 2.1, the transitions that do not contribute to step velocity include deposition, desorption, and terrace diffusion.

Second, we isolate the attachment and detachment terms in (2.12) in the

following formula for $\dot{\varsigma}(t)$:

$$\begin{aligned}\dot{\varsigma}(t) = a\sum_{\boldsymbol{\alpha},m} s(\boldsymbol{\alpha},m)\Big\{ & D\phi_- \left[\mathbb{1}(\nu_{-1}(\boldsymbol{\alpha})=0)p_{\boldsymbol{\alpha}_-,m}(t) - \mathbb{1}(\nu_1(\boldsymbol{\alpha})=0)\mathbb{1}(\nu_{-1}(\boldsymbol{\alpha})>0)p_{\boldsymbol{\alpha},m}(t)\right] \\ & + Dk\phi_- \left[\mathbb{1}(\nu_1(\boldsymbol{\alpha})=0)\mathbb{1}(\nu_{-1}(\boldsymbol{\alpha})>0)p_{\boldsymbol{\alpha}^-,m}(t) - \mathbb{1}(\nu_{-1}(\boldsymbol{\alpha})=0)p_{\boldsymbol{\alpha},m}(t)\right] \\ & + D\phi_+ \left[\mathbb{1}(\nu_{-1}(\boldsymbol{\alpha})=0)p_{\boldsymbol{\alpha}_+,m}(t) - \mathbb{1}(\nu_1(\boldsymbol{\alpha})=1)p_{\boldsymbol{\alpha},m}(t)\right] \\ & + Dk\phi_+ \left[\mathbb{1}(\nu_1(\boldsymbol{\alpha})=1)p_{\boldsymbol{\alpha}^+,m}(t) - \mathbb{1}(\nu_{-1}(\boldsymbol{\alpha})=0)p_{\boldsymbol{\alpha},m}(t)\right]\Big\}. \end{aligned} \tag{3.43}$$

Equation (3.43) can be simplified using appropriate change-of-variable formulas and re-indexing the resulting sums. We perform each calculation separately in what follows:

$$\begin{aligned} & \sum_{\boldsymbol{\alpha},m} s(\boldsymbol{\alpha},m)\mathbb{1}(\nu_{-1}(\boldsymbol{\alpha})=0)p_{\boldsymbol{\alpha}_-,m}(t) \\ & \quad = \sum_{\boldsymbol{\alpha},m} \left[s(\boldsymbol{\alpha}_-,m)+1\right]\mathbb{1}(\nu_1(\boldsymbol{\alpha}_-)=0)\mathbb{1}(\nu_{-1}(\boldsymbol{\alpha}_-)>0)p_{\boldsymbol{\alpha}_-,m}(t) \\ & \quad = \sum_{\boldsymbol{\alpha}_-,m} \left[s(\boldsymbol{\alpha}_-,m)+1\right]\mathbb{1}(\nu_1(\boldsymbol{\alpha}_-)=0)\mathbb{1}(\nu_{-1}(\boldsymbol{\alpha}_-)>0)p_{\boldsymbol{\alpha}_-,m}(t) \\ & \quad = \sum_{\boldsymbol{\alpha},m} \left[s(\boldsymbol{\alpha},m)+1\right]\mathbb{1}(\nu_1(\boldsymbol{\alpha})=0)\mathbb{1}(\nu_{-1}(\boldsymbol{\alpha})>0)p_{\boldsymbol{\alpha},m}(t)\ , \end{aligned} \tag{3.44a}$$

where the change of variable occurs in the first equality, re-indexing in the second, and the final equality restates the result with more concise notation. The remaining

terms follow similarly. They are

$$\begin{aligned}
&\sum_{\boldsymbol{\alpha},m} s(\boldsymbol{\alpha},m)\mathbb{1}(\nu_1(\boldsymbol{\alpha})=0)\mathbb{1}(\nu_{-1}(\boldsymbol{\alpha})>0)p_{\boldsymbol{\alpha}^-,m}(t) \\
&\quad = \sum_{\boldsymbol{\alpha},m} \left[s(\boldsymbol{\alpha}^-,m)-1\right]\mathbb{1}(\nu_{-1}(\boldsymbol{\alpha}^-)=0)p_{\boldsymbol{\alpha}^-,m}(t) \\
&\quad = \sum_{\boldsymbol{\alpha}^-,m} \left[s(\boldsymbol{\alpha}^-,m)-1\right]\mathbb{1}(\nu_{-1}(\boldsymbol{\alpha}^-)=0)p_{\boldsymbol{\alpha}^-,m}(t) \\
&\quad = \sum_{\boldsymbol{\alpha},m} \left[s(\boldsymbol{\alpha},m)-1\right]\mathbb{1}(\nu_{-1}(\boldsymbol{\alpha})=0)p_{\boldsymbol{\alpha},m}(t)\ , \qquad (3.44b)
\end{aligned}$$

$$\begin{aligned}
&\sum_{\boldsymbol{\alpha},m} s(\boldsymbol{\alpha},m)\mathbb{1}(\nu_{-1}(\boldsymbol{\alpha})=0)p_{\boldsymbol{\alpha}_+,m}(t) \\
&\quad = \sum_{\boldsymbol{\alpha},m} \left[s(\boldsymbol{\alpha}_+,m)+1\right]\mathbb{1}(\nu_1(\boldsymbol{\alpha}_+)=0)\mathbb{1}(\nu_{-1}(\boldsymbol{\alpha}_+)>0)p_{\boldsymbol{\alpha}_+,m}(t) \\
&\quad = \sum_{\boldsymbol{\alpha}_+,m} \left[s(\boldsymbol{\alpha}_+,m)+1\right]\mathbb{1}(\nu_1(\boldsymbol{\alpha}_+)=0)\mathbb{1}(\nu_{-1}(\boldsymbol{\alpha}_+)>0)p_{\boldsymbol{\alpha}_+,m}(t) \\
&\quad = \sum_{\boldsymbol{\alpha},m} \left[s(\boldsymbol{\alpha},m)+1\right]\mathbb{1}(\nu_1(\boldsymbol{\alpha})=0)\mathbb{1}(\nu_{-1}(\boldsymbol{\alpha})>0)p_{\boldsymbol{\alpha},m}(t)\ , \qquad (3.44c)
\end{aligned}$$

and

$$\begin{aligned}
&\sum_{\boldsymbol{\alpha},m} s(\boldsymbol{\alpha},m)\mathbb{1}(\nu_1(\boldsymbol{\alpha})=1)p_{\boldsymbol{\alpha}^+,m}(t) \\
&\quad = \sum_{\boldsymbol{\alpha},m} \left[s(\boldsymbol{\alpha}^+,m)-1\right]\mathbb{1}(\nu_{-1}(\boldsymbol{\alpha}^+)=0)p_{\boldsymbol{\alpha}^+,m}(t) \\
&\quad = \sum_{\boldsymbol{\alpha}^+,m} \left[s(\boldsymbol{\alpha}^+,m)-1\right]\mathbb{1}(\nu_{-1}(\boldsymbol{\alpha}^+)=0)p_{\boldsymbol{\alpha}^+,m}(t) \\
&\quad = \sum_{\boldsymbol{\alpha},m} \left[s(\boldsymbol{\alpha},m)-1\right]\mathbb{1}(\nu_{-1}(\boldsymbol{\alpha})=0)p_{\boldsymbol{\alpha},m}(t)\ . \qquad (3.44d)
\end{aligned}$$

Finally, substitution of equations (3.44) into (3.43), with recourse to Definition 10,

yields

$$\dot{\varsigma}(t) = a \sum_{\boldsymbol{\alpha},m} \big[D\phi_- \mathbb{1}(\nu_1(\boldsymbol{\alpha}) = 0)\mathbb{1}(\nu_{-1}(\boldsymbol{\alpha}) > 0) - Dk\phi_- \mathbb{1}(\nu_{-1}(\boldsymbol{\alpha}) = 0) \\ + D\phi_+ \mathbb{1}(\nu_1(\boldsymbol{\alpha}) = 1) - Dk\phi_+ \mathbb{1}(\nu_{-1}(\boldsymbol{\alpha}) = 0) \big] p_{\boldsymbol{\alpha},m}(t)$$

$$= a \left[J_-(t) - J_+(t) \right] \ . \tag{3.45}$$

This completes the proof. □

3.3 Estimates for discrete corrections

In this section, we investigate the behavior of discrete corrections to the linear kinetic relation for flux at the step edge and adatom diffusion on the terrace; see Proposition 2 and equations (3.30)-(3.33). To do so, we invoke the "maximum principle", Proposition 1 (Chapter 2), to determine L^∞-bounds for two types of corrections: The corrective fluxes $f_\pm(t)$, found in (3.11), and the high-occupancy corrections to discrete density, $\hat{R}_j(t)$, in (3.31). The resulting estimates reveal the dependence of each type of correction on the parameters of the KRSOS model, particularly k and $\epsilon = F/D$.

Our approach can be outlined as follows: First, in view of Remark 2 (Chapter 2) for the initial data $p_{\boldsymbol{\alpha}}(0)$, we estimate $f_\pm(t)$ and $\hat{R}_j(t)$ in terms of the steady-state solution $p^{ss,\epsilon}_{\boldsymbol{\alpha}}$ of marginalized master equation (2.5). Second, by invoking the ϵ-series expansion of Section 2.3.1.3 for $p^{ss,\epsilon}_{\boldsymbol{\alpha}}$, we derive estimates for $f_\pm(t)$ and $\hat{R}_j(t)$; these signify corrections to the linear kinetic law for the adatom fluxes, $J_\pm$, and high-occupancy corrections to the discrete diffusion equation on the terrace, respectively.

This second stage of our derivation of bounds on discrete corrections makes use of the equilibrium distribution $p^{eq}_{\boldsymbol{\alpha}}$, equation (2.14), for ϵ^0-terms in our formal expansion, and the ϵ^1-terms found in (2.31). In principle, higher order terms can also be computed, but are neglected in our analysis.

Proposition 5. (Estimates for discrete correction terms) *If $F \geq \tau^{-1}$, the corrective fluxes (3.12) at the step edge satisfy the estimate*

$$f_{\pm}(t) = \mathcal{O}\left(\frac{k^2}{(1-k)a}\right) + \mathcal{O}\left(\frac{\epsilon N}{(1+\phi)a}\right) \ , \tag{3.46}$$

where $\phi = \phi_+$ or ϕ_-. Similarly, the high-occupancy corrections (3.31) to densities satisfy

$$\hat{R}_{\hat{\jmath}}(t) = \mathcal{O}\left(\frac{k^2}{(1-k)a}\right) + \mathcal{O}\left(\frac{\epsilon N}{a}\right) \ . \tag{3.47}$$

In (3.46) and (3.47), we write $f = \mathcal{O}(g)$ to indicate that as $a \to 0$, $|f/g|$ is bounded by a constant that is independent of time and the parameters of the KRSOS model.

Proof. We proceed to derive (3.46) and (3.47) through heuristics. Define

$$\begin{aligned}
\tilde{f}^{ss,\epsilon}_{+} &:= k\left[c^{eq} + \sum_{\boldsymbol{\alpha}} \mathbb{1}(\nu_{-1}(\boldsymbol{\alpha}) > 0) p^{ss,\epsilon}_{\boldsymbol{\alpha}}/a\right] \\
&\quad + \sum_{\boldsymbol{\alpha}} \mathbb{1}(\nu_1(\boldsymbol{\alpha}) > 1)\nu_1(\boldsymbol{\alpha}) p^{ss,\epsilon}_{\boldsymbol{\alpha}}/a \ , \qquad (3.48a) \\
\tilde{f}^{ss,\epsilon}_{-} &:= k\left[c^{eq} + \sum_{\boldsymbol{\alpha}} \mathbb{1}(\nu_{-1}(\boldsymbol{\alpha}) > 0) p^{ss,\epsilon}_{\boldsymbol{\alpha}}/a\right] \\
&\quad + \sum_{\boldsymbol{\alpha}} \mathbb{1}(\nu_1(\boldsymbol{\alpha}) > 0)\nu_{-1}(\boldsymbol{\alpha}) p^{ss,\epsilon}_{\boldsymbol{\alpha}}/a \\
&\quad + \sum_{\boldsymbol{\alpha}} \mathbb{1}(\nu_1(\boldsymbol{\alpha}) = 0)\mathbb{1}(\nu_{-1}(\boldsymbol{\alpha}) > 1)\left[\nu_{-1}(\boldsymbol{\alpha}) - 1\right] p^{ss,\epsilon}_{\boldsymbol{\alpha}}/a \ , \text{ and} \qquad (3.48b) \\
\hat{R}^{ss,\epsilon}_{\hat{\jmath}} &:= \sum_{\boldsymbol{\alpha}} \left[\nu_{\hat{\jmath}}(\boldsymbol{\alpha}) - \mathbb{1}(\nu_{\hat{\jmath}}(\boldsymbol{\alpha}) > 0)\right] p^{ss,\epsilon}_{\boldsymbol{\alpha}}/a \ . \qquad (3.48c)
\end{aligned}$$

By Remark 2 (Chapter 2) and exact formulas (3.12) and (3.31) for $f_{\pm}(t)$ and $\hat{R}_{\hat{\jmath}}(t)$, respectively, we have

$$|f_{\pm}(t)| \lesssim \tilde{f}_{\pm}^{ss,\epsilon} \text{ , and } |\hat{R}_{\hat{\jmath}}(t)| \lesssim \hat{R}_{\hat{\jmath}}^{ss,\epsilon} \text{ , } t > 0 \text{ .} \tag{3.49}$$

Inequalities (3.49) are not particularly useful since they do not explicitly manifest the dependence on the kinetic parameters of interest. We need to use some results from Chapter 2 in order to refine these estimates.

In correspondence to (2.31) for the truncated system, we write $p_{\boldsymbol{\alpha}}^{ss,\epsilon} = p_{\boldsymbol{\alpha}}^{ss,(0)} + \epsilon p_{\boldsymbol{\alpha}}^{ss,(1)} + \mathcal{O}(\epsilon^2)$, where $p_{\boldsymbol{\alpha}}^{ss,(l)}$ is the l-th order term of the underlying series expansion in $\epsilon = F/D$; in particular, $p_{\boldsymbol{\alpha}}^{ss,(0)} = p_{\boldsymbol{\alpha}}^{eq}$ is the zeroth-order contribution to the steady state. The constant entering the term $\mathcal{O}(\epsilon^2)$ may depend on parameters of the problem but is immaterial for our purposes. We will neglect terms with $l \geq 2$ in the ϵ-expansion for $p_{\boldsymbol{\alpha}}^{ss,\epsilon}$.

By inspection of (3.48), we define the following sums.

$$S_1^{(l)} := \sum_{\boldsymbol{\alpha}} \mathbb{1}(\nu_{-1}(\boldsymbol{\alpha}) > 0) p_{\boldsymbol{\alpha}}^{ss,(l)} \text{ ,} \tag{3.50a}$$

$$S_2^{(l)} := \sum_{\boldsymbol{\alpha}} \mathbb{1}(\nu_1(\boldsymbol{\alpha}) > 1) \nu_1(\boldsymbol{\alpha}) p_{\boldsymbol{\alpha}}^{ss,(l)} \text{ ,} \tag{3.50b}$$

$$S_3^{(l)} := \sum_{\boldsymbol{\alpha}} \mathbb{1}(\nu_1(\boldsymbol{\alpha}) > 0) \nu_{-1}(\boldsymbol{\alpha}) p_{\boldsymbol{\alpha}}^{ss,(l)} \text{ ,} \tag{3.50c}$$

$$S_4^{(l)} := \sum_{\boldsymbol{\alpha}} \mathbb{1}(\nu_1(\boldsymbol{\alpha}) = 0) \mathbb{1}(\nu_{-1}(\boldsymbol{\alpha}) > 1) \left[\nu_{-1}(\boldsymbol{\alpha}) - 1\right] p_{\boldsymbol{\alpha}}^{ss,(l)} \text{ ,} \tag{3.50d}$$

$$S_5^{(l)} := \sum_{\boldsymbol{\alpha}} \left[\nu_{\hat{\jmath}}(\boldsymbol{\alpha}) - \mathbb{1}(\nu_{\hat{\jmath}}(\boldsymbol{\alpha}) > 0)\right] p_{\boldsymbol{\alpha}}^{ss,(l)} \text{ .} \tag{3.50e}$$

Accordingly, formulas (3.48) are recast to the forms

$$\tilde{f}_{+}^{ss,\epsilon} = kc^{eq} + \frac{k}{a}\left[S_1^{(0)} + \epsilon S_1^{(1)}\right] + \frac{1}{a}\left[S_2^{(0)} + \epsilon S_2^{(1)}\right] + \mathcal{O}(\epsilon^2) \ , \tag{3.51a}$$

$$\begin{aligned}\tilde{f}_{-}^{ss,\epsilon} = kc^{eq} &+ \frac{k}{a}\left[S_1^{(0)} + \epsilon S_1^{(1)}\right] + \frac{1}{a}\left[S_3^{(0)} + \epsilon S_3^{(1)}\right] \\ &+ \frac{1}{a}\left[S_4^{(0)} + \epsilon S_4^{(1)}\right] + \mathcal{O}(\epsilon^2) \ .\end{aligned} \tag{3.51b}$$

First, we compute $S_i^{(0)}$ $(i = 1,\ 2,\ 3,\ 4,\ 5)$, which amount to contributions from the equilibrium solution of the master equation, for $F = 0$. By (2.14) and $0 < k < 1$, we write

$$\begin{aligned}S_1^{(0)} &= \frac{1}{Z}\sum_{\boldsymbol{\alpha}} \mathbb{1}(\nu_{-1}(\boldsymbol{\alpha}) > 0) k^{|\boldsymbol{\alpha}|} \\ &= \frac{1}{Z}\sum_{n=1}^{\infty} \begin{pmatrix} n+N-3 \\ \\ n-1 \end{pmatrix} k^n = k \ .\end{aligned} \tag{3.52}$$

The binomial coefficient in (3.52) is the number of n-particle configurations with at least one adatom in the site immediately to the left of the step. Similarly, we have

$$\begin{aligned}S_2^{(0)} &= \frac{1}{Z}\sum_{\boldsymbol{\alpha}} \mathbb{1}(\nu_1(\boldsymbol{\alpha}) > 1)\nu_1(\boldsymbol{\alpha}) k^{|\boldsymbol{\alpha}|} \\ &= \frac{1}{Z}\sum_{l=2}^{\infty} l k^l \sum_{n=l}^{\infty} \begin{pmatrix} n-l+N-3 \\ \\ n-l \end{pmatrix} k^{n-l} \\ &= (1-k)\sum_{l=2}^{\infty} l k^l = \frac{2k^2 - k^3}{1-k} \ ,\end{aligned} \tag{3.53}$$

$$
\begin{aligned}
S_3^{(0)} &= \frac{1}{Z}\sum_{\boldsymbol{\alpha}} \mathbb{1}(\nu_1(\boldsymbol{\alpha})>0)\nu_{-1}(\boldsymbol{\alpha})k^{|\boldsymbol{\alpha}|} \\
&= \frac{k}{Z}\sum_{l=1}^{\infty} lk^l \sum_{n=l+1}^{\infty} \left(\begin{array}{c} n-l-1+N-3 \\ \\ n-l-1 \end{array} \right) k^{n-l-1} \\
&= k(1-k)\sum_{l=1}^{\infty} lk^l = \frac{k^2}{1-k} \ , \qquad (3.54)
\end{aligned}
$$

$$
\begin{aligned}
S_4^{(0)} &= \frac{1}{Z}\sum_{\boldsymbol{\alpha}} \mathbb{1}(\nu_1(\boldsymbol{\alpha})=0)\mathbb{1}(\nu_{-1}(\boldsymbol{\alpha})>1)\left[\nu_{-1}(\boldsymbol{\alpha})-1\right]k^{|\boldsymbol{\alpha}|} \\
&= \frac{k}{Z}\sum_{l=2}^{\infty}(l-1)k^{l-1} \sum_{n=l}^{\infty} \left(\begin{array}{c} n-l+N-4 \\ \\ n-l \end{array} \right) k^{n-l} \\
&= k(1-k)^2\sum_{l=1}^{\infty} lk^l = k^2 \ , \qquad (3.55)
\end{aligned}
$$

and

$$
\begin{aligned}
S_5^{(0)} &= \frac{1}{Z}\sum_{\boldsymbol{\alpha}} \left[\nu_{\hat{\jmath}}(\boldsymbol{\alpha}) - \mathbb{1}(\nu_{\hat{\jmath}}(\boldsymbol{\alpha})>0)\right]k^{|\boldsymbol{\alpha}|} \\
&= \frac{1}{Z}\sum_{l=2}^{\infty}(l-1)k^l \sum_{n=l}^{\infty} \left(\begin{array}{c} n-l+N-3 \\ \\ n-l \end{array} \right) k^{n-l} \\
&= k(1-k)\sum_{l=1}^{\infty} lk^l = \frac{k^2}{1-k} \ . \qquad (3.56)
\end{aligned}
$$

We have followed the convention that the index l is used to account for restrictions on states coming from indicator functions and the index n replaces the number of adatoms, $|\boldsymbol{\alpha}|$.

All that remains is to compute terms proportional to ϵ. This task calls for estimating the sums $S_i^{(l)}$, defined in (3.50), for $l=1$. Hence, we would need to invoke the first-order steady-state solution, $p_{\boldsymbol{\alpha}}^{ss,(1)}$, of marginalized master equation (2.5).

As alluded to in Section 2.3.1.3, we do not have, strictly speaking, a simple closed-form solution. Instead, by restricting attention to a finite number of particle states ($|\boldsymbol{\alpha}| \leq M$), we provide approximations for the requisite (infinite) sums over $\boldsymbol{\alpha}$ in averages (3.50) by finite sums when $l = 1$. This approximation amounts to replacing the sums $S_i^{(1)}$ with quadratic forms of appropriately defined vectors, $\mathbf{y}_i \in \mathbb{R}^{\Omega(M)}$; thus, we write $S_i^{(1)} \approx \mathbf{y}_i^T \mathfrak{A}^\dagger \mathbf{z}$, where the vectors $\mathbf{y}_i$ have entries that correspond to the indicator functions and/or $\nu_{\pm 1}(\boldsymbol{\alpha})$ according to (3.50) and $\mathbf{z} = -\mathfrak{B}\mathbf{p}^0$.

Next, we obtain estimates for $S_i^{(1)}$ as follows:

$$\begin{aligned} |S_i^{(1)}| &\approx |\mathbf{y}_i^T \mathfrak{A}^\dagger \mathbf{z}| \\ &= \left| \left[\left(\frac{\mathbf{y}_i^T}{\mathbf{y}_i^T \mathbf{y}_i} \right)^T \right]^\dagger \mathfrak{A}^\dagger \left[\frac{\mathbf{z}^T}{\mathbf{z}^T \mathbf{z}} \right]^\dagger \right| \\ &= \left[\frac{\left| \mathbf{z}^T \mathfrak{A} \mathbf{y}_i \right|}{\mathbf{y}_i^T \mathbf{y}_i \, \mathbf{z}^T \mathbf{z}} \right]^\dagger = \frac{\mathbf{y}_i^T \mathbf{y}_i \, \mathbf{z}^T \mathbf{z}}{|\mathbf{z}^T \mathfrak{A} \mathbf{y}_i|} \\ &\lesssim \left| \mathbf{z}^T \mathfrak{A} \mathbf{y}_i \right|^{-1} , \end{aligned} \tag{3.57}$$

whenever $\mathbf{z}^T \mathfrak{A} \mathbf{y}_i \neq 0$. The above calculation uses several properties of the Moore-Penrose pseudoinverse, i.e. $\mathbf{y}^\dagger = \mathbf{y}^T / (\mathbf{y}^T \mathbf{y})$ provided $\mathbf{y} \neq \mathbf{0}$ (second line), $(\mathfrak{A}\mathfrak{B})^\dagger = \mathfrak{B}^\dagger \mathfrak{A}^\dagger$ (third line), and the pseudoinverse of a nonzero constant is its multiplicative inverse (fourth line). The last line of (3.57) results from observing that the numerator contributes a constant independent of model parameters for each i, provided $F \geq \tau^{-1}$. Since $\mathfrak{A}$, $\mathfrak{B}$, $\mathbf{p}^0$, and $\mathbf{y}_i$ are known, (3.57) is a computable estimate. Straightforward matrix-vector products yield

$$|S_i^{(1)}| \lesssim \begin{cases} \frac{N}{1+\phi} , & i = 1, 2, 3, 4, \\ N , & i = 5; \end{cases} \tag{3.58}$$

in the above, $\phi = \phi_+$ or ϕ_-. In our calculation of (3.58), we invoke the assumption that $F \geq \tau^{-1}$. Consequently, the desorption rate does not enter our estimates.

In summary, if the initial data of the atomistic system is near the steady state in the sense of (2.35), then "maximum principle" (2.32) implies (3.49). Inequalities (3.49) along with (3.50)–(3.58) yield estimates (3.46) and (3.47) for $0 < k < 1$, $F \geq \tau^{-1}$, and sufficiently small ϵ. This statement concludes our heuristic proof of Proposition 5. $\square$

A few comments on the above proposition are in order. First, it should be noted that estimates (3.46) and (3.47) can also be applied to the quasi-conservative parameter regime. To see this, recall that partition function (2.21) factorizes into $\boldsymbol{\alpha}$-dependent and m-dependent parts, and hence computation of sums (3.52)-(3.56) in that parameter regime is the same as the conservative case, i.e. $f_\pm(t)$ and $\hat{R}_j(t)$ are both $\mathcal{O}(\frac{k}{1-k}\,\frac{k}{a})$.

Second, we must emphasize that the estimates in Proposition 5 are based upon several assumptions and approximations, including: (i) application of the "maximum principle" (Proposition 1, Chapter 2); (ii) truncation of marginalized master equation for $\epsilon > 0$; (iii) asymptotics for the Laplace transform and formal power-series expansion for steady-steady distribution, $p^{ss}_{\boldsymbol{\alpha}}$; and (iv) L^∞-bounds for correction terms (3.12) and (3.31). Consequently, estimates (3.46) and (3.47) are not expected to be optimal. In particular, the bounds involving ϵ can likely be improved.

Finally, by Proposition 5, if we assume that $k/a = \mathcal{O}(1)$, $\phi \leq \mathcal{O}(1)$ [49, 71] and $\epsilon < \mathcal{O}(a^2)$, we can assert that $f_\pm(t)$ can be neglected when compared to the

linear-in-density part of the discrete flux $J_{\pm}(t)$. Furthermore, the corrections $\hat{R}_j(t)$ are small compared to density $c_j(t)$, and hence $\rho_j(t) - \varrho_j(t) \ll \rho_j(t)$ as well. These controlled approximations reveal a kinetic regime in which equations (3.11), (3.33), and the discrete diffusion equation in (3.14) reduce to discrete versions of linear kinetic relation (3.4), Fick's law (3.3) and the continuum diffusion equation for density. This observation motivates the next section.

3.4 Coarse graining

In this section, we derive the continuum step-flow equations of the discrete mesoscale model in the limit where the lateral lattice spacing, a, approaches zero, and the microscale kinetic parameters scale properly with a. Our formal argument forms an extension of the work in [71], which studied the case of conservative dynamics, to the non-conservative case. Accordingly, as $a \to 0$, we extract a set of BCF-type equations for adatom diffusion, boundary conditions at the step, and the step velocity law.

In view of Proposition 5, let us impose

$$k = \mathcal{O}(a) \ , \quad \epsilon = \mathcal{O}(a^3) \ , \text{ and } F \geq \tau^{-1} \ , \tag{3.59}$$

which ensure that high-occupancy corrections $\hat{R}_j(t)$ and $\rho_j(t) - \varrho_j(t)$ are small compared to the corresponding densities. On the other hand, we assume $\rho_j(t) \to \rho(x,t)$ and $c_j(t) \to \mathcal{C}(\hat{x},t)$ as the lattice parameter approaches zero, $a \to 0$. The Taylor expansion of $\rho(x,t)$ about $x = ja$ yields

$$\frac{\rho_{j-1}(t) - 2\rho_j(t) + \rho_{j+1}(t)}{a^2} = \frac{\partial^2 \rho}{\partial x^2}(ja,t) + \mathcal{O}(a^2) \ .$$

By the usual notion of macroscopic diffusion, it is natural to set $\mathcal{D} := Da^2 = \mathcal{O}(1)$, the surface diffusivity; and $\mathcal{F} := \frac{F}{(N-1)a}$, the deposition flux per unit length [49, 71]. Thus, (3.30), with (3.59), imply

$$\frac{\partial \rho}{\partial t} = \mathcal{D}\frac{\partial^2 \rho}{\partial x^2} + \mathcal{F} - \frac{1}{\tau}\rho - \mathcal{D}\frac{\partial^2 \mathfrak{R}}{\partial x^2} + \frac{1}{\tau}\mathfrak{R} \ , \tag{3.60}$$

as $a \to 0$, where $\mathfrak{R}(x,t)$ is the continuum limit of the high-occupancy corrections in Eulerian coordinates. By (3.59), the terms $\mathcal{F}$, $\mathcal{D}\ \partial^2\mathfrak{R}/\partial x^2$, and $\tau^{-1}\mathfrak{R}$ are $\mathcal{O}(a)$, and hence are negligible to leading order. Excepting corrections $\mathcal{D}\ \partial^2\mathfrak{R}/\partial x^2$ and $\tau^{-1}\mathfrak{R}$, the resulting equation for $\rho(x,t)$ is the anticipated diffusion equation in Eulerian coordinates; cf. (3.2). By sharpening estimates for ϵ in Proposition 5, $\mathcal{F}$ may subsequently appear as a leading-order term.

Furthermore, the observation that $\hat{R}_{\hat{\jmath}}(t) = \mathcal{O}(a)$ enables us to obtain Fick's law of diffusion at the step edge, via (3.33). By Taylor expanding the Lagrangian adatom density, $\mathcal{C}$, about $\hat{x} = \hat{\jmath}a$ with $\hat{\jmath} = 0$ for the right $(+)$ side of the step and $\hat{\jmath} = N-1$ for the left $(-)$ side of the step as $a \to 0$, we obtain the formulas

$$J_+(t) = -\mathcal{D}\left.\frac{\partial \mathcal{C}}{\partial \hat{x}}\right|_{\hat{x}=0^+} + \mathcal{O}(a) \ , \tag{3.61a}$$

$$J_-(t) = -\mathcal{D}\left.\frac{\partial \mathcal{C}}{\partial \hat{x}}\right|_{\hat{x}=L^-} + \mathcal{O}(a) \ , \tag{3.61b}$$

where $\hat{x} = \hat{\jmath}a$ and $L = Na = \mathcal{O}(1)$ by virtue of the screw-periodic boundary conditions. In the above, we used the expansions $c_2(t) - c_1(t) = a[(\partial\mathcal{C}/\partial\hat{x})|_{x=0^+} + \mathcal{O}(a)]$ and $c_{-2}(t) - c_{-1}(t) = a[-(\partial\mathcal{C}/\partial\hat{x})|_{x=L^-} + \mathcal{O}(a)]$. Notice that the advection term appearing in (3.3) is absent from (3.61) due to discrete dynamics, as explained in Remark 9. Nevertheless, (3.61) agrees with (3.3) to leading order since $v\mathcal{C}_\pm = \mathcal{O}(a)$.

Equations (3.61) need to be complemented with kinetic boundary conditions at the step edge. Hence, we now apply (3.11) with (3.12) and (3.46). First, we set $\kappa_\pm := D\phi_\pm a = \mathcal{O}(1)$ [49, 71]. Second, by inspection of estimate (3.46), we assume $\phi_\pm \leq \mathcal{O}(1)$ along with (3.59). Consequently, we can assert that $|f_\pm(t)| = \mathcal{O}(a)$. Thus, by (3.11) we obtain

$$J_+(t) = -\kappa_+ \left[\mathcal{C}(0^+, t) - c^{eq}\right] + \mathcal{O}(a) \ , \tag{3.62a}$$

$$J_-(t) = \kappa_- \left[\mathcal{C}(L^-, t) - c^{eq}\right] + \mathcal{O}(a) \ , \tag{3.62b}$$

as $a \to 0$; recall that $c^{eq} = \frac{k/a}{1-k} \approx k/a$ if $k = \mathcal{O}(a)$ [71].

The last component of the BCF model that emerges from the discrete equations is the step velocity law. This law is provided by (3.41); in this equation, the factor multiplying the difference in the adatom flux across the step edge equals Ω/a'. Thus, (3.41) is precisely (3.1) pertaining to the BCF model.

3.5 Characterizing discrete corrections with KMC simulations

In this section, we carry out KMC simulations to illustrate the behavior of adatom fluxes at the step edge and adatom diffusion on the terrace when model parameters allow the discrete corrections (3.12) and (3.31) to be large. We demonstrate that in a regime of high detachment or deposition flux, the boundary condition for the adatom fluxes at the step edge can deviate significantly from linear kinetic relation (3.62); thus, in principle the corrective fluxes, $f_\pm(t)$, may *not* be negligible. Furthermore, high-occupancy corrections are also shown to be significant for extreme values of k and ϵ.

At this stage we attempt to outline plausible conditions by which the conventional BCF model, particularly the linear kinetic relation for the flux, becomes questionable. By estimates (3.46) and (3.47) of Proposition 5, the microscale system may no longer be modeled in accord with the BCF theory if, for example: $k = O(1)$; or, $k = \mathcal{O}(a)$ and $\epsilon = \mathcal{O}(a)$. These conditions indicate situations in which high adatom densities may occur, because of large enough detachment rate at the step edge or high enough deposition onto the surface from above. In the following numerical study, we investigate the consequences of these parameter regimes for both the linear kinetic relation and adatom diffusion.

3.5.1 Corrections to linear kinetic relation

Since we have been unable to express the corrective fluxes $f_{\pm}$, found in (3.11), in terms of mesoscale quantities such as the adatom density, KMC simulations are our primary tool for characterizing their magnitude when compared to the linear-in-density part of the flux at the step edge. What we find is that for moderate values of k and ϵ, the linear kinetic relation (3.62), with neglect of the corrective fluxes, $f_{\pm}$, is found to provide a reasonably accurate approximation for the adatom flux at the step edge. In contrast, for extreme parameter values such as $k > 0.01$ or $\epsilon > 0.01$, the flux at at the step edge deviates from the conventional linear behavior. These deviations, which indicate that adatom flux may be a *nonlinear* function of density, manifest themselves differently in parameter regimes with (a) large k but small ϵ, compared to (b) small k, but large ϵ cases.

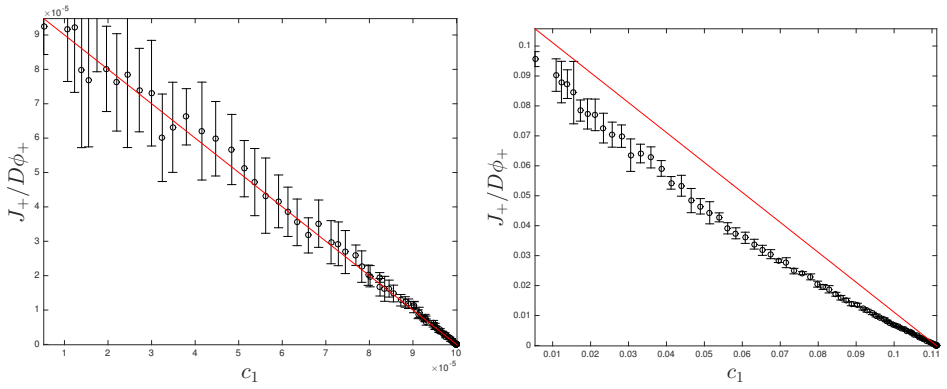

(a) (b)

Figure 3.2: Plots of KMC simulations (black circles) and linear kinetic relation (red line) for adatom flux versus density on the right of step edge for different values of detachment rate, with parameters $N = 50$, $D = 10^{10}$, $\phi_\pm = 1$, $\epsilon = 0$, $\tau^{-1} = 0$, and either (a) $k = 0.0001$ or (b) $k = 0.1$. In each plot, the solid line represents linear kinetic relation (3.62), by neglect of f_+. The error bars are determined by use of the standard deviation of flux in 10 ensembles of (a) 10^7 simulations and (b) 10^5 simulations.

First, let us consider the high-detachment rate case with zero deposition, as these are depicted in Figure 3.2. If the density is sufficiently close to its equilibrium value, c^{eq}, then the adatom flux at the step edge is approximately linear with density but with a slope that can be different from the value $D\phi_+ a$ predicted by kinetic law (3.62). For large enough k, the dependence of adatom flux on density evidently becomes nonlinear. This nonlinear behavior becomes more pronounced for larger k.

Next, consider a small detachment factor, k, but large ϵ; see Figure 3.3. We observe that for small ϵ, Figure 3.3(a), the flux computed via KMC simulations agrees reasonably well with linear kinetic law (3.62) for a wide range of values for the density to the right of the step, c_1. For a larger value of ϵ, Figure 3.3(b), the flux remains linear in the density with a slope equal to the predicted value, $D\phi_+ a$,

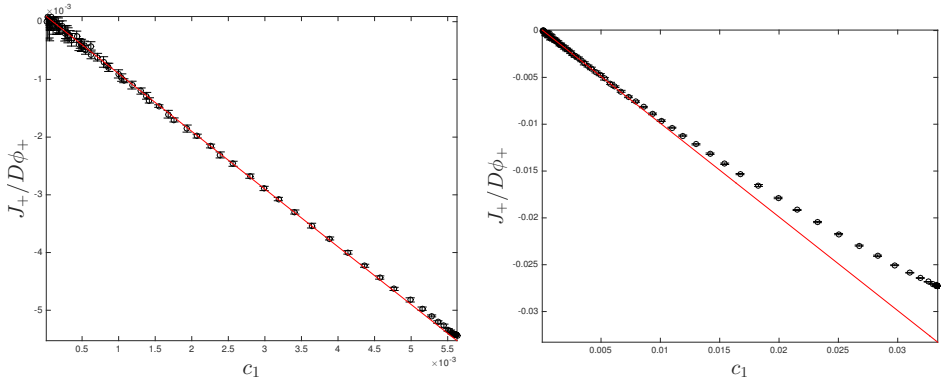

(**a**) (**b**)

Figure 3.3: Plots of KMC simulations (black circles) and linear kinetic relation (red line) for adatom flux versus density on the right of step edge for different values of detachment rate, with parameters $N = 50$, $D = 10^{10}$, $\phi_\pm = 1$, $k = 0.0001$, $\tau^{-1} = 0$, and either (a) $\epsilon = 0.01$ or (b) $\epsilon = 0.04$. In each plot, the solid line represents linear kinetic relation (3.62), by neglect of f_+. The error bars are determined by use of the standard deviation of flux in 10 ensembles of 10^5 simulations in each case.

as the density approaches its equilibrium value. However, as the adatom density increases, the nonlinear dependence of the flux is noticeable. The magnitude of this nonlinearity varies in direct correspondence with ϵ. It is worth noting that an increase in the deposition rate ϵ used in KMC simulations beyond the one used in Figure 3.3(b), even by a factor of two, drastically alters the long-time behavior of the system: Apparently, no steady state can be established for sufficiently large ϵ; see also Appendix B.

As described above, the high-k and high-ϵ cases, Figures 3.2(b) and 3.3(b), respectively, differ in the way that the corrective flux f_+ is manifested in the observed value of the flux. Let us make an effort to discuss the origin of this behavior in the context of the atomistic model by inspection of formula (3.12a). The first line in

these formulas contains the prefactor k along with a sum over states with one or more adatoms in the lattice site corresponding to the edge atom. This set of configurations does *not* allow for atom detachment; thus, according to this contribution to f_+, the change of the flux with density should be suppressed. This prediction should explain the behavior of the slope of the flux versus density as shown in Figure 3.2 as c_1 approaches c^{eq}. The remaining terms in (3.12a) come from two- or higher-particle states, which furnish significant contributions if k or ϵ is sufficiently large. These remaining corrections account for configurations in which attachment is inhibited, thus causing an overall increase of the flux out of the step. This prediction is consistent with Figure 3.3.

We have been unable to explicitly express the corrective fluxes, $f_\pm(t)$, as a function of adatom densities $c_{\pm 1}(t)$ on the basis of the analytical model. In order to quantify the nonlinear behavior of the flux near the step edge, we fit the fluxes computed by KMC simulations to polynomials of $c_1 - c^{eq}$. Figure 3.4 shows the fitted flux in two cases where deviations are significant: High k with small ϵ; and high ϵ with small k. In each case, a quadratic polynomial appears to adequately capture the behavior of the flux versus adatom density at the right of the step.

We conclude that a linear kinetic relation for the adatom flux at the step edge in principle does *not* suffice to capture the full range of phenomena displayed by the atomistic KRSOS model. Instead, it is more reasonable to propose a discrete expansion of the form

$$\mp J_\pm \approx \sum_{n=1}^{N_*} B_\pm^{(n)} \left[c_{\pm 1}(t) - c^{eq}\right]^n \ , \tag{3.63}$$

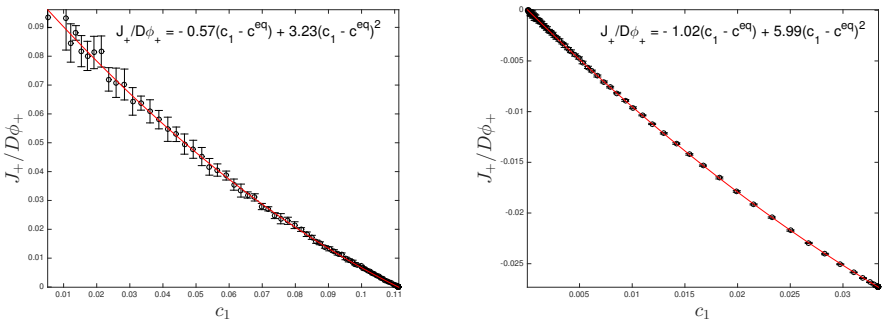

(**a**) (**b**)

Figure 3.4: Plots of KMC simulation data (black circles) and a quadratic fit (red curve) for adatom flux versus density on the right of step edge, for high detachment rate or high deposition rate. Model parameters include $N = 50$, $D = 10^{10}$, $\phi_{\pm} = 1$, and $\tau^{-1} = 0$, together with (a) $k = 0.1$ and $\epsilon = 0$; or (b) $k = 0.0001$ and $\epsilon = 0.04$. In each plot, the red curve is determined by fitting the data to the polynomial in (3.63) with $N_* = 2$. The error bars are determined by use of the standard deviation of flux in 10 ensembles of 10^5 simulations in each case.

where the number, N_*, would be speculated empirically. At the mesoscale, the corresponding constitutive relation for the flux at the step edge is a *nonlinear* kinetic relation. A systematic derivation of such a relation from the atomistic model is still elusive.

Remark 10. *Based on our KMC results, we expect the conventional linear kinetic relation (3.4) of the BCF model to be valid if*

$$\mathcal{A} := k + \frac{\epsilon}{\phi_+ + \phi_-} \ll 1 \ . \tag{3.64}$$

This empirical criterion appears less restrictive on ϵ than estimates (3.46) and (3.47), suggesting that the bounds in Proposition 5 may be improved. Accordingly, if $\mathcal{A}$ is large enough, then (nonlinear) terms with $n \geq 2$ should become significant.

In our KMC simulations, we observe that the linear kinetic relation for the adatom flux is reasonably accurate if the quantity $\mathcal{A}$ of (3.64) does not exceed 0.01.

3.5.2 Corrections to diffusion

Now we consider the effect of detachment rate and deposition rate on high-occupancy corrections (3.31), which influence the diffusion of adatoms on the terrace. In contrast to the corrective fluxes entering (3.11), the corrections to discrete diffusion can be expressed as differences in adatom density (3.7a) and dilute density (3.8a), which we measure in KMC simulations. Numerically, we find that the corrections, $\hat{R}_{\hat{\jmath}}$, vary in direct correspondence with detachment factor k and the deposition rate, measured by ϵ. In addition, our simulation results provide evidence that estimate (3.47) is conservative, at least in regard to dependence on ϵ.

First, we consider the behavior of $\hat{R}_{\hat{\jmath}}$ with detachment rate. Figure 3.5 shows snapshots of the density profile on the terrace at various times during KMC simulations, as well as the high-occupancy corrections measured in equilibrium. These plots indicate that the magnitude of corrections $\hat{R}_{\hat{\jmath}}$ are about a factor of k smaller than adatom densities, in agreement with the estimate in Proposition 5; see (3.56), which predicts the value of $\hat{R}_{\hat{\jmath}}$ in equilibrium ($\epsilon = 0$).

Next, let us discuss the ϵ-dependence of high-occupancy corrections $\hat{R}_{\hat{\jmath}}$. Figure 3.6 provides density plots in addition to the values of $\hat{R}_{\hat{\jmath}}$ measured in steady-state using KMC. For both plots in Figure 3.6, the magnitude of corrections are less than ϵ/a: For Figure 3.6(a), $\max_{\hat{\jmath}} \hat{R}_{\hat{\jmath}} < 0.01\epsilon/a$, whereas Figure 3.6(b) shows $\max_{\hat{\jmath}} \hat{R}_{\hat{\jmath}} \approx$

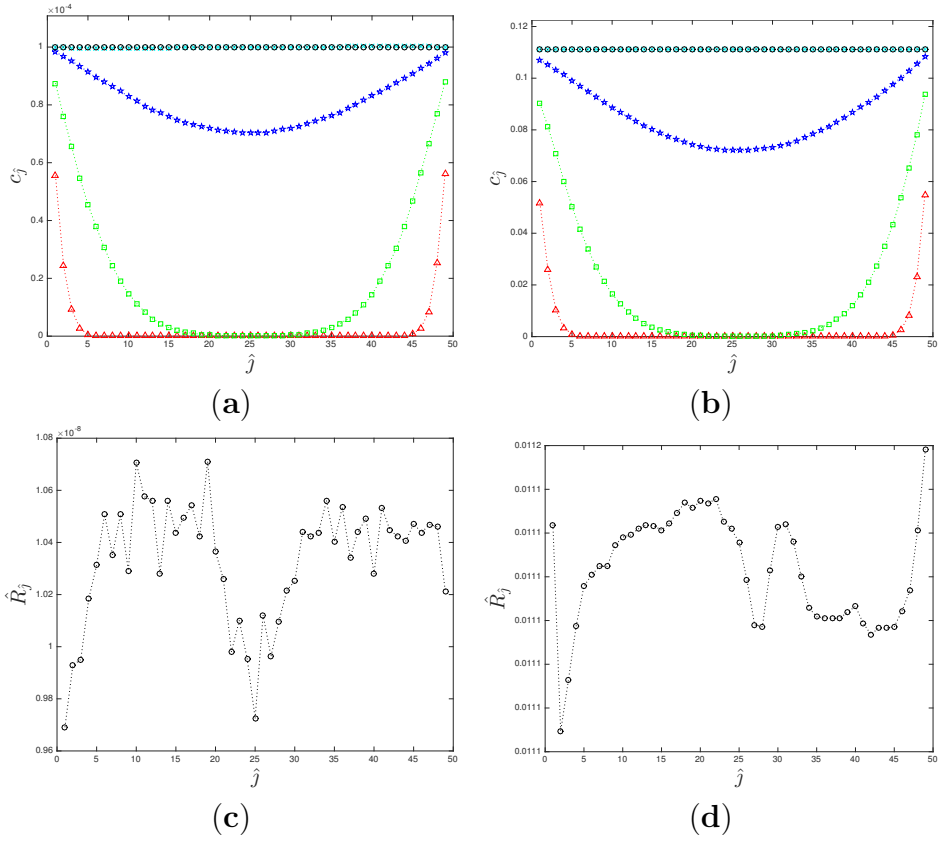

Figure 3.5: Snapshots of density and associated corrections when k is varied. Plots include: (a) and (b) adatom density, $c_{\hat{\jmath}}(t)$, computed from KMC simulations at times $t = 1.6 \times 10^{-10}$ (red triangles), 2.5×10^{-9} (green squares), 4.0×10^{-8} (blue stars), 6.3×10^{-7} (cyan x-marks), and 1×10^{-5} (black circles); (c) and (d) corrections, $\hat{R}_{\hat{\jmath}}$, defined in (3.31), computed from KMC simulations at time $t = 1.0 \times 10^{-5}$. Model parameters are chosen to be $N = 50$, $D = 10^{10}$, $\phi_{\pm} = 1$, $\epsilon = 0$, and $\tau^{-1} = 0$, together with (a) and (c) $k = 0.0001$; or (b) and (d) $k = 0.1$. Averages were obtained using (a) and (c) 10^8 simulations; or (b) and (d) 10^6 simulations. Notice that in (a) and (b) there is no apparent difference between density profiles at $t = 6.3 \times 10^{-7}$ (cyan x-marks) and $t = 1.0 \times 10^{-5}$ (black circles), indicating that the adatom density approaches equilibrium on the timescale of the simulations. Predicted value of equilibrium adatom density from (3.9) is (a) $c^{eq} = 0.0001$ or (b) $c^{eq} = 0.1111$. Predicted value of $\hat{R}_{\hat{\jmath}}$ in equilibrium is (c) $kc^{eq} = 10^{-8}$ or (d) $kc^{eq} = 0.01111$, in close agreement with the data.

ϵ/a. In comparison, Proposition 5 predicts that corrections are bounded by $N\epsilon/a$. Our KMC simulations indicate that sharper bounds for $\epsilon > 0$ contributions to discrete corrections, in (3.47), are plausible. For example, $\hat{R}_{\hat{\jmath}} = \mathcal{O}\left(\frac{k^2}{(1-k)a}\right) + \mathcal{O}\left(\frac{\epsilon}{a}\right)$ would not be unreasonable given our data.

In summary, the findings of our numerical study of high-occupancy corrections to adatom diffusion, $\hat{R}_{\hat{\jmath}}$, are consistent with estimate (3.47) of Proposition 5. Notably, for the case of conservative dynamics ($\epsilon = 0$), KMC simulations suggest that the estimate $\hat{R}_{\hat{\jmath}} = \mathcal{O}(k\, c^{eq})$ is optimal. Conversely, our numerics provide reasonably strong evidence that the ϵ-dependent estimates in Proposition 5 are not optimal. In principle, a better bound for these corrections could be determined empirically using KMC. However, we are unable to make such a prediction with our limited simulation data.

3.6 Summary and discussion

In this chapter, we derived discrete counterparts of various components of the BCF model, with corrections. First, the adatom fluxes $J_{\pm}(t)$, defined in terms of probability currents measuring the net detachment of atoms from the step, enabled us to derive the discrete analog of linear kinetic relation (3.4) in Proposition 2. Second, by applying a time derivative to adatom density $\rho_j(t)$ and invoking symbolic master equation (2.12), the discrete equation of motion found in Proposition 3 made manifest a discrete diffusion equation for adatom density, plus boundary conditions at the step edge. Third, Proposition 4 made further use of symbolic master

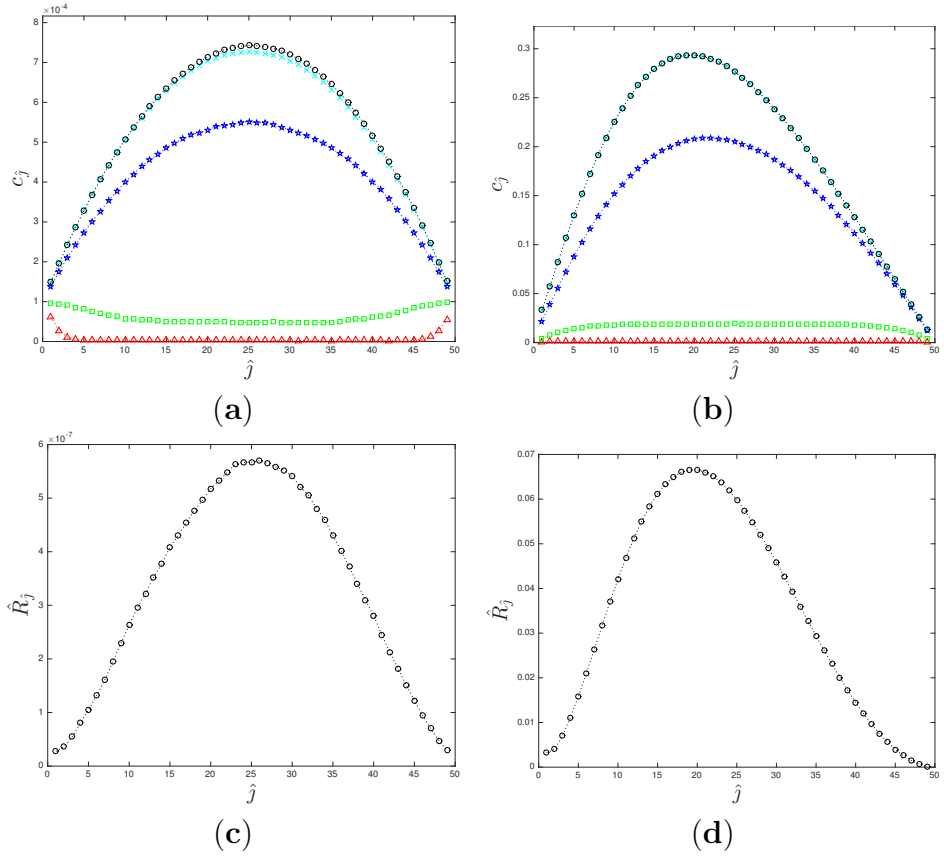

Figure 3.6: Snapshots of density and associated corrections when ϵ is varied. Plots include: (a) and (b) adatom density, $c_{\hat{\jmath}}(t)$, computed from KMC simulations at times $t = 1.6 \times 10^{-10}$ (red triangles), 2.5×10^{-9} (green squares), 4.0×10^{-8} (blue stars), 6.3×10^{-7} (cyan x-marks), and 1.0×10^{-5} (black circles); (c) and (d) corrections, $\hat{R}_{\hat{\jmath}}$, defined in (3.31), computed from KMC simulations at time $t = 1.0 \times 10^{-5}$. Model parameters are chosen to be $N = 50$, $D = 10^{10}$, $\phi_{\pm} = 1$, $k = 0.0001$, and $\tau^{-1} = 0$, together with (a) and (c) $\epsilon = 0.0001$; or (b) and (d) $\epsilon = 0.04$. Averages were obtained using (a) and (c) 10^7 simulations; or (b) and (d) 10^6 simulations. Notice that in (a) and (b) there is only a small change between density profiles at $t = 6.3 \times 10^{-7}$ (cyan x-marks) and $t = 1 \times 10^{-5}$ (black circles), indicating that the adatom density approaches steady state on the timescale of the simulations. Predicted bound for $\hat{R}_{\hat{\jmath}}$ in steady state is (c) $N\epsilon/a = 0.005$ or (d) $N\epsilon/a = 2$, which exceeds numerically obtained values considerably.

equation (2.12) to compute $\dot{\varsigma}(t)$, resulting in step velocity law (3.41).

We also pay special attention to the correction terms that emerge from our analysis, of which there are two types: Corrective fluxes $f_{\pm}(t)$ accompanying the discrete linear kinetic relation, and high-occupancy corrections $\hat{R}_{\hat{\jmath}}$ associated with discrete diffusion. Each of these arise from aspects of the underlying KRSOS model. As noted in Remark 7, the terms $f_{\pm}(t)$ are related to atomistic rules forbidding attachment and detachment in certain configurations. These rules are required in a 1D SOS-type model including steps. A useful discussion of this fact can be found in [71]. On the other hand, the high-occupancy corrections result from a modeling choice made in the formulation of the KRSOS model: Only a single adatom may hop away from multiply-occupied lattice sites. Compare this choice of discrete dynamics with Fick's law of diffusion, which postulates that flux (of adatoms in our case) is proportional to a gradient in density. If we interpret "gradient in density" for the atomistic system to be the difference of the number of adatoms at neighboring lattice sites, it would appear that the KRSOS model does not obey Fick's law of diffusion on account of the kinetic interaction of adatoms; see Remark 8. It is compelling to ask how a discrete model that *does obey* Fick's law of diffusion might differ from the KRSOS model introduced Chapter 2. This is addressed in the next chapter.

The final component of this chapter involves characterizing both types of corrections via analytical estimates, summarized in Proposition 5, and numerical computations, provided in Section 3.5. Our derivation of estimates in Section 3.3 relies on the "maximum principle", Proposition 1 (Chapter 2), as well as the formulas for equilibrium and steady-state distributions provided in Chapter 2. The main

application of our estimates is the coarse-graining of discrete BCF-like equations in Section 3.4, which requires that corrections are $\mathcal{O}(a)$ in the limit of small lattice spacing. One consequence of Proposition 5 in those formal calculations is that the mesoscale deposition flux, $\mathcal{F}$, should be $\mathcal{O}(a)$ in the continuum limit, and therefore negligible to leading order. In contrast, KMC simulations presented in Section 3.5 indicate that corrections may be small even if F, the microscale deposition rate, is larger that our analytical estimates require. As a result, we suspect that the bounds obtained in Section 3.3 are non-optimal for terms involving $\epsilon = F/D$; and therefore the mesoscale deposition flux entering (3.60) is actually a leading-order term in the continuum limit, as $a \to 0$, of the discrete diffusion equation induced by the atomistic dynamics of the KRSOS model.

Chapter 4: Alternate atomistic model

In this chapter, we introduce an *alternate* KRSOS model that results from the modification of a few transition rates of the KRSOS model defined in Chapter 2, and subsequently investigate the consequences of these modifications. Motivated by the conclusion in Chapter 3 concerning the apparent kinetic interaction between adatoms included in the original KRSOS model, the alternate KRSOS model allows adatoms to move in any configuration, *without* the restriction that only a single adatom may hop away from multiply-occupied lattice sites. This prescription is consistent with Fick's law of diffusion, and also forms a reasonable atomistic model of a single-step system in 1D.

Broadly speaking, the properties of the alternate KRSOS model are not different from the original KRSOS model. Nevertheless, it is interesting to ask how our simple modification of the original KRSOS model impacts the derivation of the BCF model. It is reasonable to expect, for example, that the alternate KRSOS model does not introduce the same high-occupancy corrections to discrete diffusion. Accordingly, the goal of this chapter is to explore the principal differences between our two atomistic models, and the consequences of using each model as a starting point for the derivation of a mesoscale model.

In this chapter, we provide the master equation for the alternate KRSOS model and derive the equilibrium distribution satisfying it for long enough times. It turns out that this equilibrium distribution differs considerably from the one obtained in Chapter 2 for the original KRSOS model. By recourse to the canonical ensemble of statistical mechanics, we attribute the difference in long-time behavior to the fact that adatoms in multiply-occupied lattice sites are *distinguishable* in the original KRSOS model, but *indistinguishable* in the alternate KRSOS model. This fundamental difference implies that the alternate KRSOS model is described by a different statistical distribution of particle states in equilibrium, which we also provide.

Following a similar approach as the one from Chapter 3, we use an "alternate master equation" in the derivation of a discrete, BCF-like description of evolution for averages such as adatom density and flux at the step edge. As anticipated, the discrete diffusion equation does not involve high-occupancy corrections, whereas the discrete analog of the linear kinetic relation does retain certain corrective fluxes, albeit in a much simplified form compared to (3.12) from the last chapter. In the last part of this chapter, we give a quantitative comparison of corrections that result from the original and alternate KRSOS models, computed via KMC simulations. *We find that corrections emerging from the alternate KRSOS model are universally smaller than the corresponding corrections in the original KRSOS model.*

4.1 Model definition

We now introduce an alternate KRSOS model that shares many attributes with the KRSOS model of [70, 71], which we used in Chapters 2 and 3. In fact, from a model definition standpoint, the two atomistic models are ostensibly the same. We will make use of the same notation to characterize the system, e.g., Definitions 1 and 2 (Chapter 2), as well as the PDF $p_{\boldsymbol{\alpha},m}(t)$ to express the time-dependent probability of finding the system in a given configuration. The evolution of this probability density is described by a master equation with rules for discrete transitions which differ from those in (2.2) in one essential way: In the alternate KRSOS model, adatoms move completely independently of one-another. While only three transition rates are affected, this philosophical change has widespread consequences.

In the remainder of this section, we define an alternate master equation that is devoid of adatom-adatom interactions, and explore the implications of this modification on the long-time behavior of the atomistic model. As was done for the original KRSOS model in Chapter 2, we find the equilibrium distribution describing the asymptotic behavior of the atomistic model when dynamics are conservative or quasi-conservative. At the end of the section, we comment on the steady-state solution for non-conservative dynamics.

4.1.1 Alternate master equation

Let us now make an attempt to outline, by way of example, the atomistic transitions that must be altered in the KRSOS model introduced in [71] in order to remove the kinetic interaction between adatoms. The simplest scenario illustrating the effect of kinetic interactions in the original model involves just two adatoms the same lattice site, e.g. $\boldsymbol{\alpha} = \{\hat{\imath}, \hat{\imath}\}$. If $\hat{\imath}$ is away from the step, the transition to $\{\hat{\imath}, \hat{\imath} \pm 1\}$ occurs with constant hopping rate D; only one adatom is allowed to hop away from site $\hat{\imath}$ even though two are present. Alternatively, if both adatoms are allowed to hop away, the transition from $\{\hat{\imath}, \hat{\imath}\}$ to $\{\hat{\imath}, \hat{\imath} \pm 1\}$ occurs with rate $2D$; see Figure 4.1. Accordingly, if $\boldsymbol{\alpha}$ describes a state where n adatoms are present at site $\hat{\imath}$, i.e. $\nu_{\hat{\imath}}(\boldsymbol{\alpha}) = n$, then the transition from $\boldsymbol{\alpha}$ to $\boldsymbol{\alpha}^{\hat{\imath}}_{\hat{\imath}\pm1}$ is assigned rate nD in the alternate KRSOS model. Hence, adatoms move completely independently on the terrace.

In addition to terrace hopping, there are two other types of transitions that we alter: (i) Attachment to the step edge from the left, and (ii) desorption. Again, we consider a scenario where $\nu_i(\boldsymbol{\alpha}) = n$. For (i), if $\hat{\imath} = -1$, so that there are n adatoms to the left of the step, then an adatom may attach to the step from the left with rate $nD\phi_-$. Note that the same kind of transition should not be possible from the right of the step when $n > 1$, which would result in the step advancing by more than one lattice site. Thus, attachment from the right is unchanged in the alternate KRSOS model. Finally, for (ii), since all adatoms are mobile, an adatom evaporates from site $\hat{\imath}$ with rate n/τ. Stated simply, adatoms leave multiply-occupied lattice

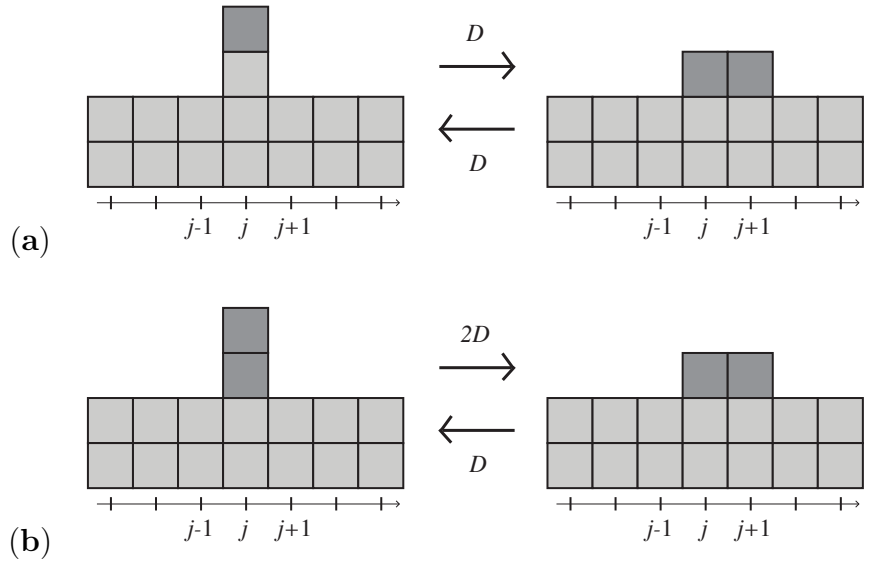

Figure 4.1: Example of adatom hopping transitions away from the step for (a) the original KRSOS model described in Chapter 2; and (b) the alternate KRSOS model described in Chapter 4. Mobile adatoms are shown in dark grey. In (a), only the top adatom in a stack may hop away from site j due to the kinetic interaction between adatoms. In (b), all adatoms are mobile, regardless of the presence of other adatoms.

sites with a rate proportional to the number of adatoms occupying that site.

With the above prototypical situations in mind, we now define the alternate master equation and accompanying rules for transitions between atomistic configurations. The probability of finding the system in state $(\boldsymbol{\alpha}, m)$ at time t evolves according to

$$\dot{p}_{\boldsymbol{\alpha},m}(t) = \sum_{\boldsymbol{\alpha}',m'} \mathcal{T}_{(\boldsymbol{\alpha},m),(\boldsymbol{\alpha}',m')} p_{\boldsymbol{\alpha}',m'}(t) \ , \tag{4.1}$$

with given initial data, $p_{\boldsymbol{\alpha},m}(0)$. As with previous master equations, $\mathcal{T}_{(\boldsymbol{\alpha},m),(\boldsymbol{\alpha}',m')}$ expresses the overall transition of the system from state $(\boldsymbol{\alpha}', m')$ to state $(\boldsymbol{\alpha}, m)$.

These transition rates are determined by the following rules:

$$\mathcal{T}_{(\boldsymbol{\alpha},m),(\boldsymbol{\alpha}',m')} = D\nu_{\hat{\imath}}(\boldsymbol{\alpha}'), \qquad \text{if } m = m' \text{ and } |\boldsymbol{\alpha}| = |\boldsymbol{\alpha}'| \text{ and } \boldsymbol{\alpha}' \setminus \boldsymbol{\alpha} = \{\hat{\imath}\} \text{ and } \Big|\,||\boldsymbol{\alpha} \setminus \boldsymbol{\alpha}'|| - ||\boldsymbol{\alpha}' \setminus \boldsymbol{\alpha}||\,\Big| = 1; \tag{4.2a}$$

$$\mathcal{T}_{(\boldsymbol{\alpha},m),(\boldsymbol{\alpha}',m')} = D\phi_{+}, \qquad \text{if } m = m' \text{ and } |\boldsymbol{\alpha}| = |\boldsymbol{\alpha}'| - 1 \text{ and } \boldsymbol{\alpha}' \setminus \tilde{\boldsymbol{\alpha}} = \{1\}; \tag{4.2b}$$

$$\mathcal{T}_{(\boldsymbol{\alpha},m),(\boldsymbol{\alpha}',m')} = D\phi_{-}\nu_{-1}(\boldsymbol{\alpha}'), \qquad \text{if } m = m' \text{ and } |\boldsymbol{\alpha}| = |\boldsymbol{\alpha}'| - 1 \text{ and } \boldsymbol{\alpha}' \setminus \tilde{\boldsymbol{\alpha}} = \{-1\}; \tag{4.2c}$$

$$\mathcal{T}_{(\boldsymbol{\alpha},m),(\boldsymbol{\alpha}',m')} = Dk\phi_{\pm}, \qquad \text{if } m = m' \text{ and } |\boldsymbol{\alpha}| = |\boldsymbol{\alpha}'| + 1 \text{ and } \boldsymbol{\alpha} \setminus \tilde{\boldsymbol{\alpha}}' = \{\pm 1\}; \tag{4.2d}$$

$$\mathcal{T}_{(\boldsymbol{\alpha},m),(\boldsymbol{\alpha}',m')} = \frac{\nu_{\hat{\imath}}(\boldsymbol{\alpha}')}{\tau}, \qquad \text{if } m = m' - 1 \text{ and } |\boldsymbol{\alpha}| = |\boldsymbol{\alpha}'| - 1 \text{ and } \boldsymbol{\alpha}' \setminus \boldsymbol{\alpha} = \{\hat{\imath}\}; \tag{4.2e}$$

$$\mathcal{T}_{(\boldsymbol{\alpha},m),(\boldsymbol{\alpha}',m')} = \frac{F}{N-1}, \qquad \text{if } m = m' + 1 \text{ and } |\boldsymbol{\alpha}| = |\boldsymbol{\alpha}'| + 1 \text{ and } |\boldsymbol{\alpha} \setminus \boldsymbol{\alpha}'| = 1; \tag{4.2f}$$

and, so that probability is conserved,

$$\mathcal{T}_{(\boldsymbol{\alpha}',m'),(\boldsymbol{\alpha}',m')} = \quad - \sum_{\substack{(\boldsymbol{\alpha},m) \\ (\boldsymbol{\alpha},m)\neq(\boldsymbol{\alpha}',m')}} \mathcal{T}_{(\boldsymbol{\alpha},m),(\boldsymbol{\alpha}',m')} \qquad \text{for all } (\boldsymbol{\alpha}', m'). \tag{4.2g}$$

All other transitions are assigned the rate zero; some notable examples include

$$\mathcal{T}_{(\boldsymbol{\alpha},m),(\boldsymbol{\alpha}',m')} = 0, \qquad \text{if } m = m' \text{ and } |\boldsymbol{\alpha}| < |\boldsymbol{\alpha}'| - 1 \text{ or } |\boldsymbol{\alpha}| > |\boldsymbol{\alpha}'| + 1; \tag{4.2h}$$

$$\mathcal{T}_{(\boldsymbol{\alpha},m),(\boldsymbol{\alpha}',m')} = 0, \qquad \text{if } m = m' \text{ and } |\boldsymbol{\alpha}| = |\boldsymbol{\alpha}'| + 1 \text{ and } -1 \in \boldsymbol{\alpha}'; \tag{4.2i}$$

$$\mathcal{T}_{(\boldsymbol{\alpha},m),(\boldsymbol{\alpha}',m')} = 0, \qquad \text{if } m = m' - 1 \text{ and } |\boldsymbol{\alpha}| \geq |\boldsymbol{\alpha}'|; \tag{4.2j}$$

$$\mathcal{T}_{(\boldsymbol{\alpha},m),(\boldsymbol{\alpha}',m')} = 0, \qquad \text{if } m = m' + 1 \text{ and } |\boldsymbol{\alpha}| \leq |\boldsymbol{\alpha}'|. \tag{4.2k}$$

In the above, the effect of allowing adatoms to move without kinetic interactions, indicated by factors $\nu_{\hat{\imath}}(\boldsymbol{\alpha}')$, is shown in rules (4.2a), (4.2c), and (4.2e), corresponding to terrace hopping, attachment from the left, and desorption, respectively; cf. (2.2). All other transition rates are identical to those introduced in Section 2.2.1.

4.1.2 Long-time behavior

In this section, we find the equilibrium distribution satisfying (4.1) and outline its important consequences. Particularly, we show that the number of adatoms on the terrace in equilibrium follow a Poisson distribution and subsequently find an expression for the equilibrium adatom density in the alternate KRSOS model. Throughout our exposition, we make an effort to point out differences with the original KRSOS model, many of which are negligible in certain asymptotic limits of N and k.

We begin by stating the main result of this section:

Proposition 6. (Equilibrium distribution of alternate KRSOS model) *The master equation for the alternate KRSOS model, (4.1), with transition rates (4.2), satisfies detailed balance conditions*

$$T_{(\boldsymbol{\alpha},m),(\boldsymbol{\alpha}',m')}\pi(\boldsymbol{\alpha}',m') = T_{(\boldsymbol{\alpha}',m'),(\boldsymbol{\alpha},m)}\pi(\boldsymbol{\alpha},m) \ , \tag{4.3}$$

where

$$\pi(\boldsymbol{\alpha},m) = \frac{k^{|\boldsymbol{\alpha}|}}{\prod_{\hat{\imath}}\nu_{\hat{\imath}}(\boldsymbol{\alpha})!}\left(\frac{F\tau}{(N-1)k}\right)^{m} \ . \tag{4.4}$$

Furthermore, if $\mathcal{R} = \frac{F\tau}{(N-1)k} < 1$ *and* m_0 *is a (finite) lower bound on mass, an equilibrium distribution exists since*

$$\mathfrak{Z} = \sum_{(\boldsymbol{\alpha},m)} \pi(\boldsymbol{\alpha},m) = e^{(N-1)k}\frac{\mathcal{R}^{m_0}}{1-\mathcal{R}} \tag{4.5}$$

is finite. Normalization of (4.4) by (4.5) yields the following equilibrium distribution

of alternate master equation (4.1):

$$p^{eq}_{\boldsymbol{\alpha},m} = \frac{e^{-(N-1)k} k^{|\boldsymbol{\alpha}|}}{\prod_{\hat{\imath}} \nu_{\hat{\imath}}(\boldsymbol{\alpha})!}(1-\mathcal{R})\mathcal{R}^{m-m_0} \ . \tag{4.6}$$

Proof. We prove the proposition in two parts: We (I) verify detailed balance conditions (4.3) for transition rates (4.2), and (II) compute normalization constant (4.5). By Theorem 2 in Appendix A, (I) and (II) imply the existence and uniqueness of equilibrium distribution (4.6).

Part I: Detailed balance. To show that transition rates (4.2) satisfy conditions (4.3), we must relate each transition to the corresponding reverse process. Accordingly, we consider three sets of transitions: terrace hopping, attachment/detachment, and deposition/desorption.

First, in the case of terrace hopping, we assume without loss of generality that the transition from $\boldsymbol{\alpha}'$ to $\boldsymbol{\alpha}$ involves an adatom hopping from site $\hat{\imath}^*$ to site $\hat{\imath}^* + 1$. Now, since $|\boldsymbol{\alpha}| = |\boldsymbol{\alpha}'|$ and $m = m'$, we have that

$$\begin{aligned}
T_{(\boldsymbol{\alpha},m),(\boldsymbol{\alpha}',m')}\pi(\boldsymbol{\alpha}',m') &= D\nu_{\hat{\imath}^*}(\boldsymbol{\alpha}')k^{|\boldsymbol{\alpha}'|}\left(\frac{F\tau}{(N-1)k}\right)^{m'}\prod_{\hat{\imath}}\frac{1}{\nu_{\hat{\imath}}(\boldsymbol{\alpha}')!} \\
&= Dk^{|\boldsymbol{\alpha}'|}\left(\frac{F\tau}{(N-1)k}\right)^{m'}\frac{1}{[\nu_{\hat{\imath}^*}(\boldsymbol{\alpha}')-1]!}\frac{1}{\nu_{\hat{\imath}^*+1}(\boldsymbol{\alpha}')!}\prod_{\hat{\imath}\neq\hat{\imath}^*,\hat{\imath}^*+1}\frac{1}{\nu_{\hat{\imath}}(\boldsymbol{\alpha}')!} \\
&= D\nu_{\hat{\imath}^*+1}(\boldsymbol{\alpha})k^{|\boldsymbol{\alpha}|}\left(\frac{F\tau}{(N-1)k}\right)^{m}\frac{1}{\nu_{\hat{\imath}^*}(\boldsymbol{\alpha})!}\frac{1}{\nu_{\hat{\imath}^*+1}(\boldsymbol{\alpha})!}\prod_{\hat{\imath}\neq\hat{\imath}^*,\hat{\imath}^*+1}\frac{1}{\nu_{\hat{\imath}}(\boldsymbol{\alpha})!} \\
&= T_{(\boldsymbol{\alpha}',m'),(\boldsymbol{\alpha},m)}\pi(\boldsymbol{\alpha},m) \ .
\end{aligned} \tag{4.7a}$$

Second, for attachment/detachment, consider the case where an atom detaches to the upper terrace in the transition from $\boldsymbol{\alpha}'$ to $\boldsymbol{\alpha}$. The corresponding transitions involving the lower terrace can be argued in the same way, but is simplified by the

fact that only states with one adatom immediately to the right of the step allow for attachment. For attachment/detachment on the left of the step, it is enough to show (4.3) when $\nu_{-1}(\boldsymbol{\alpha}) = n = |\boldsymbol{\alpha}| = |\boldsymbol{\alpha}'| + 1$ and $m = m'$. Then,

$$\begin{aligned} T_{(\boldsymbol{\alpha},m),(\boldsymbol{\alpha}',m')}\pi(\boldsymbol{\alpha}',m') &= Dk\phi_- k^{|\boldsymbol{\alpha}'|}\left(\frac{F\tau}{(N-1)k}\right)^{m'}\frac{1}{(n-1)!} \\ &= D\phi_- nk^{|\boldsymbol{\alpha}'|+1}\left(\frac{F\tau}{(N-1)k}\right)^{m'}\frac{1}{n!} \\ &= D\phi_- nk^{|\boldsymbol{\alpha}|}\left(\frac{F\tau}{(N-1)k}\right)^{m}\frac{1}{n!} \\ &= T_{(\boldsymbol{\alpha}',m'),(\boldsymbol{\alpha},m)}\pi(\boldsymbol{\alpha},m)\ . \end{aligned} \tag{4.7b}$$

Third, in the case of deposition/desorption, lets assume the transition $(\boldsymbol{\alpha}', m')$ to $(\boldsymbol{\alpha}, m)$ involves the deposition of a particle at site $\hat{\imath}^*$. Then it follows that, $|\boldsymbol{\alpha}| = |\boldsymbol{\alpha}'| + 1$, $m = m' + 1$, and $\nu_{\hat{\imath}^*}(\boldsymbol{\alpha}) = \nu_{\hat{\imath}^*}(\boldsymbol{\alpha}') + 1$, which imply

$$\begin{aligned} T_{(\boldsymbol{\alpha},m),(\boldsymbol{\alpha}',m')}\pi(\boldsymbol{\alpha}',m') &= \frac{F}{N-1}k^{|\boldsymbol{\alpha}'|}\left(\frac{F\tau}{(N-1)k}\right)^{m'}\prod_{\hat{\imath}}\frac{1}{\nu_{\hat{\imath}}(\boldsymbol{\alpha}')!} \\ &= \frac{[\nu_{\hat{\imath}^*}(\boldsymbol{\alpha}')+1]}{\tau}k^{|\boldsymbol{\alpha}'|+1}\left(\frac{F\tau}{(N-1)k}\right)^{m'+1}\frac{1}{[\nu_{\hat{\imath}^*}(\boldsymbol{\alpha}')+1]!}\prod_{\hat{\imath}\neq\hat{\imath}^*}\frac{1}{\nu_{\hat{\imath}}(\boldsymbol{\alpha}')!} \\ &= \frac{\nu_{\hat{\imath}^*}(\boldsymbol{\alpha})}{\tau}k^{|\boldsymbol{\alpha}|}\left(\frac{F\tau}{(N-1)k}\right)^{m}\frac{1}{\nu_{\hat{\imath}^*}(\boldsymbol{\alpha})!}\prod_{\hat{\imath}\neq\hat{\imath}^*}\frac{1}{\nu_{\hat{\imath}}(\boldsymbol{\alpha})!} \\ &= T_{(\boldsymbol{\alpha}',m'),(\boldsymbol{\alpha},m)}\pi(\boldsymbol{\alpha},m)\ . \end{aligned} \tag{4.7c}$$

Equations (4.7) prove the detailed balance conditions (4.3).

Part II: Normalization. All that remains is to compute the (finite) normaliza-

tion constant, $\mathfrak{Z}$, given by (4.5). Since $\sum_{\hat{\imath}} \nu_{\hat{\imath}}(\boldsymbol{\alpha}) = |\boldsymbol{\alpha}|$, we have that

$$\begin{aligned}
\mathfrak{Z} &= \sum_{\boldsymbol{\alpha},m} k^{|\boldsymbol{\alpha}|} \left(\frac{F\tau}{(N-1)k}\right)^m \prod_{\hat{\imath}} \frac{1}{\nu_{\hat{\imath}}(\boldsymbol{\alpha})!} \\
&= \sum_{\boldsymbol{\alpha}} \prod_{\hat{\imath}} \frac{k^{\nu_{\hat{\imath}}(\boldsymbol{\alpha})}}{\nu_{\hat{\imath}}(\boldsymbol{\alpha})!} \sum_{m=m_0}^{\infty} \left(\frac{F\tau}{(N-1)k}\right)^m \\
&= \sum_{n=0}^{\infty} \sum_{\substack{\boldsymbol{\alpha} \\ |\boldsymbol{\alpha}|=n}} \prod_{\hat{\imath}} \frac{k^{\nu_{\hat{\imath}}(\boldsymbol{\alpha})}}{\nu_{\hat{\imath}}(\boldsymbol{\alpha})!} \frac{\mathcal{R}^{m_0}}{1-\mathcal{R}} \\
&= \sum_{n=0}^{\infty} \frac{1}{n!} \sum_{\substack{\boldsymbol{\alpha} \\ |\boldsymbol{\alpha}|=n}} \frac{n!}{\prod_{\hat{\imath}} \nu_{\hat{\imath}}(\boldsymbol{\alpha})!} \prod_{\hat{\imath}} k^{\nu_{\hat{\imath}}(\boldsymbol{\alpha})} \frac{\mathcal{R}^{m_0}}{1-\mathcal{R}} \\
&= \sum_{n=0}^{\infty} \frac{1}{n!} \left[(N-1)k\right]^n \frac{\mathcal{R}^{m_0}}{1-\mathcal{R}} \\
&= e^{(N-1)k} \frac{\mathcal{R}^{m_0}}{1-\mathcal{R}} \, .
\end{aligned} \tag{4.8}$$

The penultimate line of (4.8) is found via the multinomial theorem. □

Equilibrium distribution (4.6) of the alternate KRSOS model corresponds to $p^{eq}_{\boldsymbol{\alpha},m}$ discussed in Chapter 2 for the quasi-conservative case; cf. (2.22) and (2.21). Interestingly, the mass-dependent components of each distribution, including the factor $\frac{\mathcal{R}^{m_0}}{1-\mathcal{R}}$ in their normalizing constants, are identical. The time-invariant distribution of the alternate KRSOS model for conservative dynamics, when mass is fixed, is highlighted in the following remark.

Remark 11. *When the dynamics of alternate KRSOS model are* conservative, *i.e.* $F = 0$ *and* $\tau^{-1} = 0$, *the equilibrium distribution satisfying master equation (4.1) with transition rates (4.2) follows directly from Proposition 6: If* $p_{\boldsymbol{\alpha},m}(0) = \delta_{m,m_0} p_{\boldsymbol{\alpha}}(0)$, *the (mass-independent) equilibrium is*

$$p^{eq}_{\boldsymbol{\alpha}} = \frac{e^{-(N-1)k} k^{|\boldsymbol{\alpha}|}}{\prod_{\hat{\imath}} \nu_{\hat{\imath}}(\boldsymbol{\alpha})!} \, . \tag{4.9}$$

Two important consequences of Proposition 6 and Remark 11 are the distribution of particle states and the calculation of the equilibrium adatom density, $\mathtt{c}^{\mathtt{eq}}$. First, let us determine the probability of n-particle configurations. By (4.9) and the multinomial theorem, we have that

$$\begin{aligned} \mathrm{P}\left(|\boldsymbol{\alpha}| = n\right) &= e^{-(N-1)k} \sum_{\substack{\boldsymbol{\alpha} \\ |\boldsymbol{\alpha}|=n}} k^{|\boldsymbol{\alpha}|} \prod_{\hat{\imath}} \frac{1}{\nu_i(\boldsymbol{\alpha})!} \\ &= \frac{e^{-(N-1)k}}{n!} \sum_{\substack{\boldsymbol{\alpha} \\ |\boldsymbol{\alpha}|=n}} \frac{n!}{\prod_{\hat{\imath}} \nu_i(\boldsymbol{\alpha})!} \prod_{\hat{\imath}} k^{\nu_i(\boldsymbol{\alpha})} \quad = \frac{[(N-1)k]^n \; e^{-(N-1)k}}{n!} \; . \end{aligned} \tag{4.10}$$

Evidently, the equilibrium distribution of particle states in the alternate KRSOS model is described by Poisson statistics. Recall that this is only true of the original KRSOS model in an asymptotic sense; see Section 2.3.1.1. We conclude that the mean and variance for the number of adatoms in equilibrium are

$$\langle n \rangle = (N-1)k \; , \tag{4.11}$$

and

$$\langle n^2 \rangle - \langle n \rangle^2 = (N-1)k \; . \tag{4.12}$$

Equation (4.11) shows excellent agreement with the results of KMC simulations in Figure 4.2.

Next, the equilibrium density is readily computed using (4.11), viz.,

$$\mathtt{c}^{\mathtt{eq}} = \frac{\langle n \rangle}{(N-1)a} = \frac{k}{a} \; . \tag{4.13}$$

In comparison to the equilibrium density of the original KRSOS model, (3.9), equation (4.13) differs by a factor of $(1-k)$. This difference is negligible in the dilute limit, i.e., $\mathtt{c}^{\mathtt{eq}} \sim c^{eq}$ as $k \to 0$.

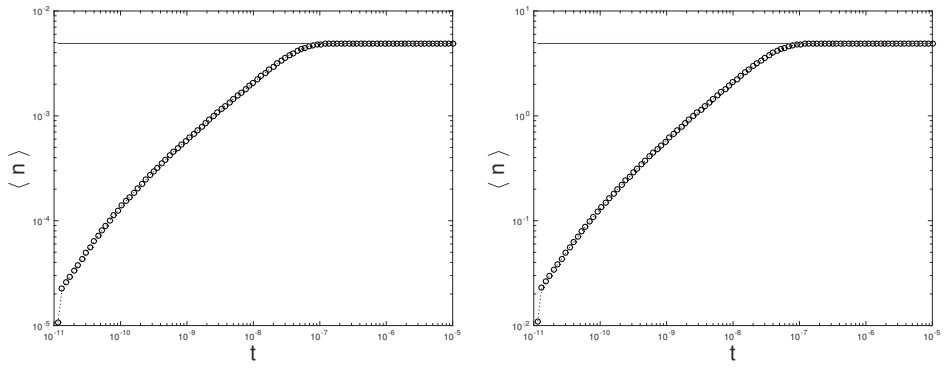

(**a**) (**b**)

Figure 4.2: The average particle number, $\langle n \rangle$, versus time t computed from KMC simulations of the alternate KRSOS model with conservative dynamics, where $F = 0$ and $\tau^{-1} = 0$. Simulation data (black circles) agrees with the predicted value (red line) found from equation (4.11) when (a) $k = 0.0001$ and (b) $k = 0.1$. The long-time value in the large-k case, plot (b), is markedly different than in the original KRSOS model; cf. Figure 2.3. In both (a) and (b) $N = 50$, $D = 10^{10}$ and $\phi_{\pm} = 1$. Averages were obtained using 10^8 and 10^6 simulations, respectively.

Before concluding this section, we are compelled to address two lingering questions: (i) What can be said about the long-time behavior of the alternate KRSOS model with non-conservative dynamics? And, (ii) Does the "maximum principle", Proposition 1, of Chapter 2 have any utility in the analysis of the alternate KRSOS model?

Question (i) is addressed in the next remark.

Remark 12. *When the dynamics of alternate KRSOS model are* non-conservative*,* $F > \frac{(N-1)k}{\tau}$*, an expression for the steady-state distribution of a truncated master equation may be obtained following the approach in Chapter 2. The important assumptions leading to equation (2.31) may be applied, without modification, to a marginalized version of alternate master equation (4.1), provided* $|\boldsymbol{\alpha}|$ *is bounded.*

In light of the observation in Remark 12, it would be easy to write down the formula corresponding to (2.31) for the alternate KRSOS model. However, since the goals of this chapter are slightly different from the previous two, such a formula is unnecessary. Instead of analytic estimates of discrete corrections, for which the analog of (2.31) would be useful, we address corrections numerically via KMC simulations in Section 4.3. Accordingly, with regard to question (ii), we do not utilize Proposition 1 in this chapter, even though it applies.

4.1.3 Canonical ensemble description of atomistic models

One peculiar feature of the alternate KRSOS model is the distinct form of equilibrium distribution (4.9) when compared to the corresponding equilibrium distribution for the original KRSOS model, i.e. $p_{\boldsymbol{\alpha}}^{eq} = (1-k)^{N-1}k^{|\boldsymbol{\alpha}|}$. Recall that we previously deduced the latter distribution by invoking the canonical ensemble of statistical mechanics. Taken at face value, the argument set forth in Section 2.3.1.1, which is based on the fact that the energy of configuration $\boldsymbol{\alpha}$ is $|\boldsymbol{\alpha}|E_N$, ostensibly applies to the alternate KRSOS model as well. It is compelling, therefore, to ask how the two results can be understood from the perspective of statistical mechanics. In the remainder of this section, we use the formalism of the canonical ensemble to show the essential difference between the two KRSOS models: In the original KRSOS model, adatoms located at a fixed lattice site are *distinguishable*, whereas in the alternate KRSOS model, they are *indistinguishable*.

It suffices to re-derive, on the basis of statistical mechanics arguments, the

partition functions (2.13) and (4.5) for the original and alternate KRSOS models, respectively. Let us now regard the one-step system as a collection of $N-1$ identical, non-interacting subsystems, distinguishable by the indices $\hat{\imath}$ labeling lattice sites. The energy associated with a site $\hat{\imath}$ occupied by $n_{\hat{\imath}}$ adatoms is $n_{\hat{\imath}}E_N$, hence the partition function for this subsystem is

$$\zeta_{\hat{\imath}} = \sum_{n_{\hat{\imath}}=0}^{\infty} g_{\hat{\imath}} \exp(-n_{\hat{\imath}}E_N/k_BT) = \sum_{n_{\hat{\imath}}=0}^{\infty} g_{\hat{\imath}} k^{n_{\hat{\imath}}} \ . \tag{4.14}$$

First, we assume that the $n_{\hat{\imath}}$ adatoms in site $\hat{\imath}$ are distinguishable. In that case, $g_{\hat{\imath}} = 1$ and (4.14) reduces to a geometric series whose sum is $\frac{1}{1-k}$. On the other hand, if the adatoms occupying $\hat{\imath}$ were indistinguishable, $g_{\hat{\imath}} = \frac{1}{n_{\hat{\imath}}!}$, implying $\zeta_{\hat{\imath}} = e^k$.

Now, since each lattice site, or subsystem, is identical, we conclude that the partition function for the $(N-1)$-site system is $\zeta_{\hat{\imath}}^{N-1}$. Therefore,

$$\zeta_{\hat{\imath}}^{N-1} = \begin{cases} \frac{1}{(1-k)^{N-1}} \ , & \text{distinguishable,} \\ e^{(N-1)k} \ , & \text{indistinguishable,} \end{cases} \tag{4.15}$$

which, upon inspection of (2.13) and (4.5), we conclude that the original KRSOS model assumes distinguishable adatoms while the alternate KRSOS model assumes they are indistinguishable.

A discrepancy between KRSOS models due to distinguishable versus indistinguishable adatoms is not altogether unsurprising in light of transition rates (2.2) and (4.2). The fact that the original KRSOS model allows only one adatom (i.e. the top adatom) to hop away from a stack of n adatoms suggests that the order in which adatoms reached that lattice site is important. On the contrary, in the alternate KRSOS model, since all n adatoms may hop away from a multiply-occupied

site, it is clear that the order in which adatoms reach that site, or are arranged in a stack, is inconsequential. We summarize the main observation of this section in the next remark.

Remark 13. *The discrepancy between equilibrium distribution (2.14) of the original KRSOS model and (4.9) of the alternate KRSOS model can be understood in terms of adatom distinguishability (or lack thereof). In the original KRSOS model, adatoms occupying a single site are distinguishable. In the alternate KRSOS model, adatoms occupying a single site are indistinguishable.*

4.2 Discrete BCF model revisited

In this section, we follow a similar program to the one presented in Chapter 3 in an attempt to derive discrete BCF-like equations of motion. The difference, of course, is that we use alternate master equation (4.1) with transition rates (4.2) in our calculations. The resulting equations of motion are quite similar to those derived in Section 3.2. A noteworthy difference between the two formulations is the *absence* of high-occupancy corrections to the discrete diffusion equation and discrete version of Fick's law when the underlying atomistic model is the alternate KRSOS model introduced in Section 4.1. On the other hand, corrections to the discrete linear kinetic relation are manifest in both formulations.

In what follows, we re-derive discrete versions of various aspects of the BCF model. First, in Section 4.2.1, we find formulas for discrete fluxes at the step edge by recourse to transition rates (4.2). Second, we determine a formula for $\dot{\rho}_j(t)$

using the alternate master equation, then extract a discrete diffusion equation and boundary conditions in Section 4.2.2. Finally, Section 4.2.3 establishes the discrete step velocity law resulting from the alternate KRSOS model. In each case, we focus on the aspects of derivations which differ from those in Chapter 3. Frequently, these aspects will somehow involve the atomistic processes of (i) terrace hopping, (ii) attachment from left, and (iii) desorption, all of which differ in the alternate KRSOS model from the original, as discussed in Section 4.1.1.

4.2.1 Flux at the step edge

Let us now establish formulas for the rightward adatom fluxes $\mathcal{J}_{\pm}(t)$ at the right $(+)$ and left $(-)$ of the step edge. These fluxes are given by formulas nearly identical to the ones in Definition 10 (Chapter 3), except we use transition rates $\mathcal{T}_{(\boldsymbol{\alpha},m),(\boldsymbol{\alpha}',m')}$ given by (4.2) instead of $T_{(\boldsymbol{\alpha},m),(\boldsymbol{\alpha}',m')}$, i.e.,

$$\mathcal{J}_{\pm}(t) = \pm \sum_{\boldsymbol{\alpha},m} \mathbb{1}(\nu_{-1}(\boldsymbol{\alpha}) = 0) \left[\mathcal{T}_{(\boldsymbol{\alpha}_{\pm},m),(\boldsymbol{\alpha},m)} p_{\boldsymbol{\alpha},m}(t) - \mathcal{T}_{(\boldsymbol{\alpha},m),(\boldsymbol{\alpha}_{\pm},m)} p_{\boldsymbol{\alpha}_{\pm},m}(t) \right] . \quad (4.16)$$

Proposition 7. (Discrete fluxes for alternate KRSOS model) *The discrete fluxes at the step edge in the alternate KRSOS model, $\mathcal{J}_{\pm}(t)$, defined in (4.16), can be written as*

$$\mathcal{J}_{\pm}(t) = \mp D\phi_{\pm} a \left[c_{\pm 1}(t) - \mathsf{c}^{\mathsf{eq}} \right] \mp D\phi_{\pm} a g_{\pm}(t) \ . \quad (4.17)$$

The terms $g_{\pm}(t)$ are

$$\begin{aligned} g_{+}(t) = k \sum_{\boldsymbol{\alpha}} & \mathbb{1}(\nu_{-1}(\boldsymbol{\alpha}) > 0) p_{\boldsymbol{\alpha}}(t)/a \\ & - \sum_{\boldsymbol{\alpha}} \mathbb{1}(\nu_{1}(\boldsymbol{\alpha}) > 1) \nu_{1}(\boldsymbol{\alpha}) p_{\boldsymbol{\alpha}}(t)/a \end{aligned} \quad (4.18a)$$

and

$$g_-(t) = k \sum_{\boldsymbol{\alpha}} \mathbb{1}(\nu_{-1}(\boldsymbol{\alpha}) > 0) p_{\boldsymbol{\alpha}}(t)/a$$
$$- \sum_{\boldsymbol{\alpha}} \mathbb{1}(\nu_1(\boldsymbol{\alpha}) > 0) \nu_{-1}(\boldsymbol{\alpha}) p_{\boldsymbol{\alpha}}(t)/a \ . \tag{4.18b}$$

Proof. The flux $\mathcal{J}_+(t)$, defined in (4.16), is identical to flux $J_+(t)$ from Chapter 3; see (3.13a) and Proposition 2. Still, the formula for $\mathcal{J}_+(t)$ in (4.17), which makes manifest the discrete linear kinetic law, *differs* from $J_+(t)$ in (3.11) on account of the discrepancy between the equilibrium adatom densities c^{eq} (alternate KRSOS model) and c^{eq} (original KRSOS model). Omitting redundant parts of the calculation, we may write (4.17) in the following way:

$$\begin{aligned}
\mathcal{J}_+(t) =& \sum_{\boldsymbol{\alpha},m} \mathbb{1}(\nu_{-1}(\boldsymbol{\alpha}) = 0) \left[T_{(\boldsymbol{\alpha}_+,m),(\boldsymbol{\alpha},m)} p_{\boldsymbol{\alpha},m}(t) - T_{(\boldsymbol{\alpha},m),(\boldsymbol{\alpha}_+,m)} p_{\boldsymbol{\alpha}_+,m}(t) \right] \\
=& Dk\phi_+ \left[1 - \sum_{\boldsymbol{\alpha}} \mathbb{1}(\nu_{-1}(\boldsymbol{\alpha}) > 0) p_{\boldsymbol{\alpha}}(t) \right] \\
& - D\phi_+ \sum_{\boldsymbol{\alpha}} \mathbb{1}(\nu_1(\boldsymbol{\alpha}) = 1) \nu_1(\boldsymbol{\alpha}) p_{\boldsymbol{\alpha}}(t) \\
=& D\phi_+ a \left[k/a - k \sum_{\boldsymbol{\alpha}} \mathbb{1}(\nu_{-1}(\boldsymbol{\alpha}) > 0) p_{\boldsymbol{\alpha}}(t)/a \right] \\
& - D\phi_+ a \left[c_1(t) - \sum_{\boldsymbol{\alpha}} \mathbb{1}(\nu_1(\boldsymbol{\alpha}) > 1) \nu_1(\boldsymbol{\alpha}) p_{\boldsymbol{\alpha}}(t)/a \right] \\
=& - D\phi_+ a \left[c_1(t) - \mathsf{c}^{\mathsf{eq}} \right] - D\phi_+ a g_+(t) \ ,
\end{aligned} \tag{4.19}$$

where $g_+(t)$ is given by (4.18a).

On the other hand, $\mathcal{J}_-(t)$ can be obtained by the following manipulations:

$$\begin{aligned}
\mathcal{J}_-(t) =& \sum_{\boldsymbol{\alpha},m} \mathbb{1}(\nu_{-1}(\boldsymbol{\alpha}) = 0) \left[T_{(\boldsymbol{\alpha},m),(\boldsymbol{\alpha}_-,m)} p_{\boldsymbol{\alpha}_-,m}(t) - T_{(\boldsymbol{\alpha}_-,m),(\boldsymbol{\alpha},m)} p_{\boldsymbol{\alpha},m}(t) \right] \\
=& D\phi_- \sum_{\boldsymbol{\alpha},m} \mathbb{1}(\nu_1(\boldsymbol{\alpha}) = 0) \nu_{-1}(\boldsymbol{\alpha}_-) p_{\boldsymbol{\alpha},m}(t) - Dk\phi_- \sum_{\boldsymbol{\alpha},m} \mathbb{1}(\nu_{-1}(\boldsymbol{\alpha}) = 0) p_{\boldsymbol{\alpha},m}(t) \\
=& D\phi_- \sum_{\boldsymbol{\alpha}} \mathbb{1}(\nu_1(\boldsymbol{\alpha}) = 0) \nu_{-1}(\boldsymbol{\alpha}_-) p_{\boldsymbol{\alpha}}(t) - Dk\phi_- \sum_{\boldsymbol{\alpha}} \mathbb{1}(\nu_{-1}(\boldsymbol{\alpha}) = 0) p_{\boldsymbol{\alpha}}(t) \\
=& D\phi_- a \left[c_{-1}(t) - \sum_{\boldsymbol{\alpha}} \mathbb{1}(\nu_1(\boldsymbol{\alpha}) > 0) \nu_{-1}(\boldsymbol{\alpha}) p_{\boldsymbol{\alpha}}(t)/a \right] \\
& - D\phi_- a \left[k/a - k \sum_{\boldsymbol{\alpha}} \mathbb{1}(\nu_{-1}(\boldsymbol{\alpha}) > 0) p_{\boldsymbol{\alpha}}(t)/a \right] \\
=& D\phi_- a \left[c_{-1}(t) - \mathsf{c}^{\mathsf{eq}} \right] + D\phi_- a \; g_-(t) \; . \qquad (4.20)
\end{aligned}$$

The correction $g_-(t)$ is defined in (4.18b). Notably, the second equality in (4.20) makes use of the transition rates for the alternate KRSOS model, (4.2), which meaningfully alter the formula for $\mathcal{J}_-(t)$, in contrast to the case of $\mathcal{J}_+(t)$. This calculation yields the stated result. □

The above proposition, in particular the appearance of corrective fluxes (4.18) in (4.17), indicates that discrete fluxes $\mathcal{J}_\pm(t)$ and $J_\pm(t)$, given in (3.11), are not *qualitatively* different from the viewpoint of a mesoscale BCF theory; there are discrete corrections to the linear kinetic law using either KRSOS model as a starting point. Be that as it may, the simplified form of correction terms (4.18) is more appealing than $f_\pm(t)$, equations (3.12), from Chapter 3. In addition to only consisting of two terms each, which imparts a computational advantage, $g_\pm(t)$ in (4.18) have symmetry with respect to the step edge: The second term in each describe the average over states that forbid attachment from the left ($-$) and right ($+$) due to the presence

of two or more particles. See also Remark 7.

4.2.2 Evolution equation for $\rho_j(t)$

In this section, we derive an evolution equation for adatom density $\rho_j(t)$ using master equation (4.1) with transition rates (4.2) corresponding to the alternate KRSOS model. From the resulting equation for $\dot{\rho}_j(t)$, we identify a difference scheme describing the diffusion of adatom density, as well as a discrete analog of Fick's law of diffusion near the step edge. Our main conclusion is that the dynamics of the alternate KRSOS model lead to an adatom diffusion equation which is *exact* in the limit of small lattice spacing. At the same time, Fick's law describing adatom flux toward the step is exact in the same scaling limit. In light of the results of Chapter 3, where high-occupancy corrections play an important role, the lack of discrete corrections suggests that the alternate KRSOS model is more proximate to the mesoscale BCF theory than the original KRSOS model. This statement is made more precise at the end of the section.

First, we state and prove how the (Eulerian) adatom density $\rho_j(t)$ changes in time. The main result of this section is given in the next proposition (cf. Proposition 3 in Chapter 3).

Proposition 8. (Evolution of discrete density for alternate KRSOS model) *When microscale evolution follows master equation (4.1) and rates (4.2), the time evolution*

of the discrete adatom density, $\rho_j(t)$, defined in (3.7b), is described by

$$\begin{aligned}\dot{\rho}_j(t) = D\left[\rho_{j-1}(t) - 2\rho_j(t) + \rho_{j+1}(t)\right] + \frac{F}{(N-1)a} - \frac{1}{\tau}\rho_j(t) \\ - \sum_{\boldsymbol{\alpha},m}\Bigg\{\delta_{j,s(\boldsymbol{\alpha},m)}\Big[D\nu_{-1}(\boldsymbol{\alpha}) + D\nu_1(\boldsymbol{\alpha}) + \frac{F}{N-1}\Big] \\ - \delta_{j,s(\boldsymbol{\alpha},m)-1}\Big[D\nu_{-1}(\boldsymbol{\alpha}) + Dk\phi_-\mathbb{1}(\nu_{-1}(\boldsymbol{\alpha}) = 0) \\ - D\phi_-\mathbb{1}(\nu_1(\boldsymbol{\alpha}) = 0)\nu_{-1}(\boldsymbol{\alpha})\Big] \\ - \delta_{j,s(\boldsymbol{\alpha},m)+1}\Big[D\nu_1(\boldsymbol{\alpha}) + Dk\phi_+\mathbb{1}(\nu_{-1}(\boldsymbol{\alpha}) = 0) \\ - D\phi_+\mathbb{1}(\nu_1(\boldsymbol{\alpha}) = 1)\Big]\Bigg\}p_{\boldsymbol{\alpha},m}(t)/a\ . \end{aligned} \tag{4.21}$$

Equation (4.21) is a direct consequence of Definition 8 (Chapter 3); see also (3.14).

Proof. We derive equation (4.21) directly via master equation (4.1) with transition rates (4.2). Most of the derivation is identical to the proof of Proposition 3. As such, we will omit redundant calculations and instead focus on the three types of transitions that differ in the alternate KRSOS model: (I) Diffusion, (II) desorption, and (III) attachment from the left. Each calculation makes use of (a) application of appropriate change-of-variable formulas to the functions $\nu_i(\boldsymbol{\alpha})$ and indicators thereof, and (b) re-indexing certain sums over states $(\boldsymbol{\alpha}, m)$.

Case I: Diffusion terms. When hopping events on the terrace occur with rates (4.2), the diffusion terms involved in $\dot{\rho}_j(t)$ are

$$\sum_{\boldsymbol{\alpha},m}\nu_{j-s(\boldsymbol{\alpha},m)}(\boldsymbol{\alpha})\Big\{\sum_{\substack{\hat{\imath}\\ \hat{\imath}\neq 0,\pm 1}}\mathbb{1}(\nu_{\hat{\imath}}(\boldsymbol{\alpha})>0)$$
$$\times\Big[\nu_{\hat{\imath}-1}(\boldsymbol{\alpha}^{\hat{\imath}}_{\hat{\imath}-1})p_{\boldsymbol{\alpha}^{\hat{\imath}}_{\hat{\imath}-1},m}(t)-2\nu_{\hat{\imath}}(\boldsymbol{\alpha})p_{\boldsymbol{\alpha},m}(t)+\nu_{\hat{\imath}+1}(\boldsymbol{\alpha}^{\hat{\imath}}_{\hat{\imath}+1})p_{\boldsymbol{\alpha}^{\hat{\imath}}_{\hat{\imath}+1},m}(t)\Big]\Big\}$$
$$+\mathbb{1}(\nu_1(\boldsymbol{\alpha})>0)\Big[\nu_2(\boldsymbol{\alpha}^1_2)p_{\boldsymbol{\alpha}^1_2,m}(t)-\nu_1(\boldsymbol{\alpha})p_{\boldsymbol{\alpha},m}(t)\Big]$$
$$+\mathbb{1}(\nu_{-1}(\boldsymbol{\alpha})>0)\Big[\nu_{-2}(\boldsymbol{\alpha}^{-1}_{-2})p_{\boldsymbol{\alpha}^{-1}_{-2},m}(t)-\nu_{-1}(\boldsymbol{\alpha})p_{\boldsymbol{\alpha},m}(t)\Big]\ . \tag{4.22}$$

When $\hat{\imath}\neq 0,\pm 1$, the averages involving $p_{\boldsymbol{\alpha}^{\hat{\imath}}_{\hat{\imath}\pm 1},m}(t)$ in (4.22) can be expressed as

$$\sum_{\boldsymbol{\alpha},m}\nu_{j-s}(\boldsymbol{\alpha})\mathbb{1}(\nu_{\hat{\imath}}(\boldsymbol{\alpha})>0)\nu_{\hat{\imath}\pm 1}(\boldsymbol{\alpha}^{\hat{\imath}}_{\hat{\imath}\pm 1})p_{\boldsymbol{\alpha}^{\hat{\imath}}_{\hat{\imath}\pm 1},m}(t)$$
$$=\sum_{\boldsymbol{\alpha},m}\left[\nu_{j-s}(\boldsymbol{\alpha}^{\hat{\imath}}_{\hat{\imath}\pm 1})+\delta_{\hat{\imath},j-s}-\delta_{\hat{\imath}\pm 1,j-s}\right]\mathbb{1}(\nu_{\hat{\imath}\pm 1}(\boldsymbol{\alpha}^{\hat{\imath}}_{\hat{\imath}\pm 1})>0)\nu_{\hat{\imath}\pm 1}(\boldsymbol{\alpha}^{\hat{\imath}}_{\hat{\imath}\pm 1})p_{\boldsymbol{\alpha}^{\hat{\imath}}_{\hat{\imath}\pm 1},m}(t)$$
$$=\sum_{\boldsymbol{\alpha},m}\nu_{j-s}(\boldsymbol{\alpha})\mathbb{1}(\nu_{\hat{\imath}\pm 1}(\boldsymbol{\alpha})>0)\nu_{\hat{\imath}\pm 1}(\boldsymbol{\alpha})p_{\boldsymbol{\alpha},m}(t)$$
$$+\sum_{\boldsymbol{\alpha},m}\left[\delta_{\hat{\imath},j-s}-\delta_{\hat{\imath}\pm 1,j-s}\right]\nu_{\hat{\imath}\pm 1}(\boldsymbol{\alpha})p_{\boldsymbol{\alpha},m}(t)\ , \tag{4.23}$$

where $s=s(\boldsymbol{\alpha},m)=s(\boldsymbol{\alpha}^{\hat{\imath}}_{\hat{\imath}\pm 1},m)$. Here we have used the familiar change-of-variable (first equality) and summation re-indexing (second equality) tricks. Note that the indicator, $\mathbb{1}(\nu_{\hat{\imath}\pm 1}(\boldsymbol{\alpha}^{\hat{\imath}}_{\hat{\imath}\pm 1})>0)$, appearing in the second equation is redundant, and therefore does not appear in the final expression.

Due to the alternate hopping scheme, equation (4.23) differs from (3.17) only by the inclusion of the additional factor of $\nu_{\hat{\imath}\pm 1}(\boldsymbol{\alpha})$, accounting for the fact that adatoms move independently in the alternate KRSOS model. This factor is the key to obtaining densities $\rho_j(t)$ in the difference scheme in the first line of (4.21) as opposed to dilute densities $\varrho_j(t)$ in (3.14).

Now we can re-write (4.22) using (4.23). Just as in the proof of Proposition 3, we complete the sum over $\hat{\imath} \neq 0, \pm 1$ by adding and subtracting the appropriate terms, the details for which we omit. The final result is

$$\sum_{\boldsymbol{\alpha},m} \Big\{ \nu_{j-s-1}(\boldsymbol{\alpha}) - 2\nu_{j-s}(\boldsymbol{\alpha}) + \nu_{j-s+1}(\boldsymbol{\alpha}) \\ + \left[\delta_{j,s-1} - \delta_{j,s}\right] \nu_{-1}(\boldsymbol{\alpha}) + \left[\delta_{j,s+1} - \delta_{j,s}\right] \nu_{1}(\boldsymbol{\alpha}) \Big\} p_{\boldsymbol{\alpha},m}(t) \ , \tag{4.24}$$

where again we simplify the notation by using $s = s(\boldsymbol{\alpha}, m)$. The final expression involves a discrete difference scheme for densities, $\rho_j(t)$, when j is sufficiently away from the step, plus terms which account for the presence of the step via Kronecker deltas.

Case II: Desorption terms. The derivation of terms pertaining to desorption follow the same pattern as the desorption terms in the proof of Proposition 3. Using the alternate transition rates (4.2), the desorption terms contributing to $\dot{\rho}_j(t)$ are

$$\sum_{\boldsymbol{\alpha},m} \nu_{j-s}(\boldsymbol{\alpha}) \sum_{\hat{\imath}>0} \left[\nu_{\hat{\imath}}(\boldsymbol{\alpha}_{\hat{\imath}}) p_{\boldsymbol{\alpha}_{\hat{\imath}},m+1}(t) - \nu_{\hat{\imath}}(\boldsymbol{\alpha}) p_{\boldsymbol{\alpha},m}(t)\right] \ . \tag{4.25}$$

We can re-write the first term as an average involving $p_{\boldsymbol{\alpha},m}(t)$, viz.,

$$\sum_{\boldsymbol{\alpha},m} \nu_{j-s}(\boldsymbol{\alpha}) \sum_{\hat{\imath}>0} \nu_{\hat{\imath}}(\boldsymbol{\alpha}_{\hat{\imath}}) p_{\boldsymbol{\alpha}_{\hat{\imath}},m+1}(t) \\ = \sum_{\hat{\imath}>0} \sum_{\boldsymbol{\alpha},m} \left[\nu_{j-s}(\boldsymbol{\alpha}_{\hat{\imath}}) - \delta_{\hat{\imath},j-s}\right] \nu_{\hat{\imath}}(\boldsymbol{\alpha}_{\hat{\imath}}) p_{\boldsymbol{\alpha}_{\hat{\imath}},m+1}(t) \\ = \sum_{\hat{\imath}>0} \sum_{\boldsymbol{\alpha},m} \left[\nu_{j-s}(\boldsymbol{\alpha}) - \delta_{\hat{\imath},j-s}\right] \nu_{\hat{\imath}}(\boldsymbol{\alpha}) p_{\boldsymbol{\alpha},m}(t) \ . \tag{4.26}$$

Since desorption events do not change the step position, $s = s(\boldsymbol{\alpha}, m+1) = s(\boldsymbol{\alpha}_{\hat{\imath}}, m)$ in the (4.26). Inserting the result of (4.26) into equation (4.25) gives the following

desorption term:

$$
\begin{aligned}
&-\sum_{\hat{\imath}>0}\sum_{\boldsymbol{\alpha},m}\delta_{\hat{\imath},j-s}\nu_{\hat{\imath}}(\boldsymbol{\alpha})p_{\boldsymbol{\alpha},m}(t) \\
&\qquad = -\sum_{\hat{\imath}}\sum_{\boldsymbol{\alpha},m}\delta_{\hat{\imath},j-s}\nu_{\hat{\imath}}(\boldsymbol{\alpha})p_{\boldsymbol{\alpha},m}(t) \\
&\qquad = -a\rho_j(t)\ . \qquad (4.27)
\end{aligned}
$$

Here we have used the fact that $\nu_0(\boldsymbol{\alpha}) = 0$. The final contribution of desorption, therefore, is $-\tau^{-1}\rho_j(t)$, as desired.

Case III: Attachment from the left. Finally, we derive the contribution to $\dot{\rho}_j(t)$ corresponding to attachment terms on the left of the step. Consider

$$
\begin{aligned}
&\sum_{\boldsymbol{\alpha},m}\nu_{j-s(\boldsymbol{\alpha},m)}(\boldsymbol{\alpha})\mathbb{1}(\nu_{-1}(\boldsymbol{\alpha})=0)\nu_{-1}(\boldsymbol{\alpha}_-)p_{\boldsymbol{\alpha}_-,m}(t) \\
&\quad = \sum_{\boldsymbol{\alpha},m}\left[\nu_{j-s(\boldsymbol{\alpha}^-,m)}(\boldsymbol{\alpha}^-)-\delta_{j,s(\boldsymbol{\alpha}^-,m)-1}\right]\mathbb{1}(\nu_1(\boldsymbol{\alpha}_-)=0)\nu_{-1}(\boldsymbol{\alpha}_-)p_{\boldsymbol{\alpha}^-,m}(t) \\
&\quad = \sum_{\boldsymbol{\alpha},m}\nu_{j-s(\boldsymbol{\alpha},m)}(\boldsymbol{\alpha})\mathbb{1}(\nu_1(\boldsymbol{\alpha})=0)\nu_{-1}(\boldsymbol{\alpha})p_{\boldsymbol{\alpha},m}(t) \\
&\qquad -\sum_{\boldsymbol{\alpha},m}\delta_{j,s(\boldsymbol{\alpha},m)-1}\mathbb{1}(\nu_1(\boldsymbol{\alpha})=0)\nu_{-1}(\boldsymbol{\alpha})p_{\boldsymbol{\alpha},m}(t)\ . \qquad (4.28)
\end{aligned}
$$

Thus, the attachment terms on the left of the step read

$$
\begin{aligned}
&\sum_{\boldsymbol{\alpha},m}\nu_{j-s(\boldsymbol{\alpha},m)}(\boldsymbol{\alpha})\Big[\mathbb{1}(\nu_{-1}(\boldsymbol{\alpha})=0)\nu_{-1}(\boldsymbol{\alpha}_-)p_{\boldsymbol{\alpha}_-,m}(t) \\
&\qquad -\mathbb{1}(\nu_1(\boldsymbol{\alpha})=0)\nu_{-1}(\boldsymbol{\alpha}_-)p_{\boldsymbol{\alpha},m}(t)\Big] \\
&\quad = \sum_{\boldsymbol{\alpha},m}\left[\nu_{j-s(\boldsymbol{\alpha}^-,m)}(\boldsymbol{\alpha}^-)-\delta_{j,s(\boldsymbol{\alpha}^-,m)-1}\right]\mathbb{1}(\nu_1(\boldsymbol{\alpha}_-)=0)\nu_{-1}(\boldsymbol{\alpha}_-)p_{\boldsymbol{\alpha}^-,m}(t) \\
&\quad = -\sum_{\boldsymbol{\alpha},m}\delta_{j,s(\boldsymbol{\alpha},m)-1}\mathbb{1}(\nu_1(\boldsymbol{\alpha})=0)\nu_{-1}(\boldsymbol{\alpha})p_{\boldsymbol{\alpha},m}(t)\ , \qquad (4.29)
\end{aligned}
$$

which, with recourse to (4.16), yields $-\mathcal{J}_-(t)$ when $j = s-1$, and is zero otherwise. This completes the proof of the proposition. $\square$

Utilizing Proposition 8, we readily deduce discrete equations describing adatom diffusion. When j is away from the step, equation (4.21) reduces to

$$\dot{\rho}_j(t) = D\Delta_j\rho_j(t) + \frac{F}{(N-1)a} - \frac{1}{\tau}\rho_j(t) \ . \tag{4.30}$$

In this equation, $\Delta_j\rho_j(t)$ is a second-order finite difference scheme for adatom density, $\frac{F}{(N-1)a}$ is the constant deposition rate per terrace length, and $\frac{1}{\tau}\rho_j(t)$ is the desorption rate of adatom density. Note that (4.30) is a discrete diffusion equation for the full density $\rho_j(t)$, cf. equation (3.30).

On the other hand, when $j = s(\boldsymbol{\alpha}, m) \pm 1$, lines 3-6 of equation (4.21) appear as the following boundary conditions:

$$\mathcal{J}_\pm(t) = \mp Da\left[c_{\pm 2}(t) - c_{\pm 1}(t)\right] \ , \tag{4.31}$$

where $\mathcal{J}_\pm(t)$ are given by (4.16). Equations (4.31) relate adatom fluxes on the left $(-)$ and right $(+)$ of the step with corresponding discrete gradients in density, i.e. Fick's law of diffusion for densities on the lattice. As we have seen previously, the effect of advection is conspicuously absent from (4.31) due to certain forbidden transitions in the atomistic model; see Remark 9 (Chapter 3).

We regard equations (4.30) and (4.31) as *exact* discrete analogs of the corresponding continuum BCF equations described in Section 3.1 in the sense that only mild scaling assumptions are required for coarse graining. In contrast, the discrete BCF equations found in Chapter 3 require elaborate estimates for discrete correction terms. Specifically, we make use of the estimates in Proposition 5 to determine

sufficient conditions for which corrections induced by the original KRSOS model are negligible. The scaling assumptions for coarse graining (4.30) and (4.31) are summarized next.

We assume $\rho_j(t) \to \rho(x,t)$ and $c_j(t) \to \mathcal{C}(\hat{x},t)$ as the lattice parameter approaches zero, $a \to 0$. Let us also assume $\mathcal{D} = Da^2 = \mathcal{O}(1)$ and $\mathcal{F} = \frac{F}{(N-1)a} = \mathcal{O}(1)$, then the limiting equation corresponding to (4.30) as $a \to 0$ is

$$\frac{\partial \rho}{\partial t} = \mathcal{D}\frac{\partial^2 \rho}{\partial x^2} + \mathcal{F} - \frac{1}{\tau}\rho \ . \tag{4.32}$$

Similarly, as $a \to 0$, (4.31) give

$$\mathcal{J}_{\pm}(t) = \mp \mathcal{D} \left.\frac{\partial \mathcal{C}}{\partial \hat{x}}\right|_{\pm} \ , \tag{4.33}$$

where the partial derivative is evaluated at $\hat{x} = 0^+$ and $\hat{x} = L^-$, respectively. Evidently, the limiting diffusion equation, (4.32), and Fick's law at the step, (4.33), do not depend on the scaling of the parameters (i) τ and (ii) k with lattice spacing. (i) is not surprising and is consistent with the results in Chapter 3. (ii) however, is strikingly different from previous results. Specifically, for the original KRSOS model, Proposition 5 asserts that k should be $\mathcal{O}(a)$ in order to neglect corrections to discrete diffusion equation and Fick's law, which is not the case for the alternate KRSOS model. The consequences of this last observation are outlined in the next remark.

Remark 14. *By Proposition 4.21, the evolution of $\rho_j(t)$, computed as an average over states whose evolution is governed by master equation (4.1) with rates (4.2), follow a discrete diffusion equation, (4.30),* without corrections. *Consequently, the*

coarse-grained mesoscale evolution equation (4.32) is exact *for all values of microscale parameters such that $D = \mathcal{O}(a^2)$ and $F = \mathcal{O}(1)$. In particular, this is true even for parameter regimes leading to high densities on the terrace.*

4.2.3 Step velocity law

Before concluding our derivation of discrete BCF-like equations associated with the alternate KRSOS model, for completeness, we must verify the relationship between step velocity and adatom flux at the step edge. It turns out, unsurprisingly, that the alternate KRSOS model upholds the familiar mass conservation statement of the BCF model. The final proposition of this chapter, and its painstakingly detailed proof, reveal the discrete underpinnings of step velocity law (3.1).

Proposition 9. (Discrete step velocity law for alternate KRSOS model) *When microscale evolution follows master equation (4.1) and rates (4.2), the time evolution of the average step velocity, $\varsigma(t)$, defined in (3.6), is given by*

$$\dot{\varsigma}(t) = a\left[\mathcal{J}_-(t) - \mathcal{J}_+(t)\right] \ . \tag{4.34}$$

Hence, the BCF step velocity law (3.1) is a direct consequence of Definition 7 (Chapter 3) and the microscale dynamics of the alternate KRSOS model.

Proof. The derivation of the step velocity law, when microscale dynamics are given by the alternate KRSOS model, follows the proof of Proposition 4 with one minor exception: The fluxes $\mathcal{J}_\pm(t)$ differ from $J_\pm(t)$; see Proposition 7. Note that the other modified processes, terrace diffusion and desorption, do not contribute to step motion; see (3.42) and subsequent discussion thereof.

Let us now isolate the attachment and detachment terms in $\dot{\varsigma}(t)$ for the alternate KRSOS model. They are

$$\begin{aligned}\dot{\varsigma}(t) = a\sum_{\boldsymbol{\alpha},m} s(\boldsymbol{\alpha},m)\Big\{ & D\phi_-\big[\mathbb{1}(\nu_{-1}(\boldsymbol{\alpha})=0)\nu_{-1}(\boldsymbol{\alpha}_-)p_{\boldsymbol{\alpha}_-,m}(t) \\ & - \mathbb{1}(\nu_1(\boldsymbol{\alpha})=0)\mathbb{1}(\nu_{-1}(\boldsymbol{\alpha})>0)p_{\boldsymbol{\alpha},m}(t)\big] \\ & + Dk\phi_-\left[\mathbb{1}(\nu_1(\boldsymbol{\alpha})=0)\mathbb{1}(\nu_{-1}(\boldsymbol{\alpha})>0)p_{\boldsymbol{\alpha}^-,m}(t) - \mathbb{1}(\nu_{-1}(\boldsymbol{\alpha})=0)p_{\boldsymbol{\alpha},m}(t)\right] \\ & + D\phi_+\left[\mathbb{1}(\nu_{-1}(\boldsymbol{\alpha})=0)p_{\boldsymbol{\alpha}_+,m}(t) - \mathbb{1}(\nu_1(\boldsymbol{\alpha})=1)p_{\boldsymbol{\alpha},m}(t)\right] \\ & + Dk\phi_+\left[\mathbb{1}(\nu_1(\boldsymbol{\alpha})=1)p_{\boldsymbol{\alpha}^+,m}(t) - \mathbb{1}(\nu_{-1}(\boldsymbol{\alpha})=0)p_{\boldsymbol{\alpha},m}(t)\right]\Big\}. \end{aligned} \tag{4.35}$$

Equation (4.35) can be simplified using appropriate change-of-variable formulas and re-indexing the resulting sums. Omitting redundant calculations, cf. Proposition 4 (Chapter 3), we compute the attachment term on the left of the step as

$$\begin{aligned} & \sum_{\boldsymbol{\alpha},m} s(\boldsymbol{\alpha},m)\mathbb{1}(\nu_{-1}(\boldsymbol{\alpha})=0)\nu_{-1}(\boldsymbol{\alpha}_-)p_{\boldsymbol{\alpha}_-,m}(t) \\ & \quad = \sum_{\boldsymbol{\alpha},m}\left[s(\boldsymbol{\alpha}_-,m)+1\right]\mathbb{1}(\nu_1(\boldsymbol{\alpha}_-)=0)\nu_{-1}(\boldsymbol{\alpha}_-)p_{\boldsymbol{\alpha}_-,m}(t) \\ & \quad = \sum_{\boldsymbol{\alpha},m}\left[s(\boldsymbol{\alpha},m)+1\right]\mathbb{1}(\nu_1(\boldsymbol{\alpha})=0)\nu_{-1}(\boldsymbol{\alpha})p_{\boldsymbol{\alpha},m}(t)\ , \end{aligned} \tag{4.36}$$

Thus, by substitution of equations (3.44b)-(3.44d) and (4.36) into (4.35), we find that

$$\begin{aligned}\dot{\varsigma}(t) &= a\sum_{\boldsymbol{\alpha},m}\big[D\phi_-\mathbb{1}(\nu_1(\boldsymbol{\alpha})=0)\mathbb{1}(\nu_{-1}(\boldsymbol{\alpha})>0) - Dk\phi_-\mathbb{1}(\nu_{-1}(\boldsymbol{\alpha})=0) \\ &\qquad + D\phi_+\mathbb{1}(\nu_1(\boldsymbol{\alpha})=1) - Dk\phi_+\mathbb{1}(\nu_{-1}(\boldsymbol{\alpha})=0)\big]p_{\boldsymbol{\alpha},m}(t) \\ &= a\left[\mathcal{J}_-(t)-\mathcal{J}_+(t)\right]\ , \end{aligned} \tag{4.37}$$

where $\mathcal{J}_\pm(t)$ are defined by (4.16). This completes the proof. □

It should be noted that Proposition 9 corresponds exactly to Proposition 4 from the Chapter 3, which corroborates step velocity law (3.1) using the original KRSOS model. Notably, this is the only point of intersection between the two discrete BCF-like models examined in this thesis, definitions of adatom fluxes in each case notwithstanding.

4.3 Discrete corrections: Numerical comparisons

As we have previously stated, our goal for this chapter is to complement the results of Chapters 2 and 3 by focusing on differences between the original and alternate KRSOS models, as well as the discrete BCF equations they respectively imply. Continuing in this approach, we now make an attempt to compare corrections to the discrete BCF equations from Chapter 3 to the ones obtained in Section 4.2. To do so, we simulate the original and alternate KRSOS models using KMC and compare: (i) a residual of the discrete diffusion equation, to be defined below, and (ii) the scaled adatom flux at the right of the step as a function of c_j. Generally speaking, we find that corrections to a discrete version of the BCF model are smaller for the alternate KRSOS model, especially for large detachment and deposition parameters, e.g. $k > 0.01$ and $F > 10^8$. In contrast, for dilute systems, when k and F are sufficiently small, the original and alternate KRSOS models produce nearly identical results.

In order to make meaningful comparisons between our two formulations, we must take into account that (i) the original KRSOS model induces corrections to

discrete diffusion, whereas the alternate model does not, and (ii) the equilibrium density appearing in the discrete linear kinetic relation is different in each case. To address issue (i), instead of plotting $\hat{R}_{\hat{\jmath}}$ as we did in Section 3.5.2, we compare the following residual:

$$\mathfrak{L}_{\hat{\jmath}} = \frac{c_{\hat{\jmath}}(t+\Delta t) - c_{\hat{\jmath}}(t)}{\Delta t} - D\Delta_{\hat{\jmath}} c_{\hat{\jmath}}(t) - v\partial_{\hat{\jmath}} c_{\hat{\jmath}}(t) + \frac{1}{\tau} c_{\hat{\jmath}}(t) - \frac{F}{(N-1)a} \,, \tag{4.38}$$

where Δt is a small time step between successive measurements of density in KMC simulations, v is the step velocity, $\partial_{\hat{\jmath}} c_{\hat{\jmath}} := c_{\hat{\jmath}} - c_{\hat{\jmath}-1}$ is the backward difference operator, and $1 < \hat{\jmath} < N-1$. Residual $\mathfrak{L}_{\hat{\jmath}}$ measures deviations of the discrete adatom density from the discrete diffusion equation. Next, to address (ii), we must scale adatom fluxes as well as $c_{\hat{\jmath}}$ by the appropriate equilibrium density. Specifically, in Figures 4.3 and 4.4, plots of the linear kinetic relation resulting from the original KRSOS model show $J_+ / [D\phi_+ c^{eq}]$ versus c_1/c^{eq}; and for the alternate KRSOS model, plots of the linear kinetic relation show $\mathcal{J}_+ / [D\phi_+ \mathtt{c}^{\mathtt{eq}}]$ versus $c_1/\mathtt{c}^{\mathtt{eq}}$.

Now that we have established measures of fidelity to a discrete BCF model, allowing the original and alternate KRSOS models to be compared on equal footing, we examine KMC simulation data for different values of k and F. First, consider the dependence of residual (4.38) and corrections to the discrete linear kinetic relation as a function of k. Figure 4.3 shows plots of (unscaled) density $c_{\hat{\jmath}}(t)$, residual $\mathfrak{L}_{\hat{\jmath}}$, and the scaled flux at the right of the step when (a) $k = 0.001$ and (b) $k = 0.1$, and $F = 0$. What we see are values of the residual which are at least three orders of magnitude smaller than the respective densities for both the original and alternate KRSOS models.Moreover, when k is small, the adatom flux at the step edge is

reasonably well approximated by the linear kinetic relation. Yet when k is large, the deviations from the predicted linear relation for adatom flux are noticeably greater for the original KRSOS model.

Next, we attempt to understand the effect of deposition flux on residual $\mathfrak{L}_j$ and the scaled flux at the right of the step. In Figure 4.4, which compares cases where (a) $F = 10^8$ and (b) $F = 4 \times 10^8$, we see a slightly different behavior in the residual plot than in the previous case: While values of the residual are consistently at least three orders of magnitude smaller than the respective densities, the residual for the alternate KRSOS model is considerably smaller in magnitude than the residual for the original KRSOS model. This effect is more pronounced for the larger value of F. Additionally, the discrete corrections to the linear relation for adatom flux are greater for the original KRSOS model than the alternate KRSOS model.

Using just a few cases for our numerical case study regarding corrections to discrete BCF-like equations, we draw two main conclusions about the original and alternate KRSOS models as starting points for the derivation of the BCF model. First, by inspecting the residual plots in Figures 4.3 and 4.4, we notice that the original KRSOS model induces larger corrections than the alternate KRSOS model when large gradients in adatom density are present. This is consistent with the existence of high-occupancy corrections resulting from kinetic adatom-adatom interactions in the original KRSOS model. Since these are not present in the alternate KRSOS model, residuals are small for all cases considered. Second, corrections to the linear kinetic relation exist for both KRSOS models, however, the corrections are smaller when formulating BCF-like equations using the alternate KRSOS model, at least in

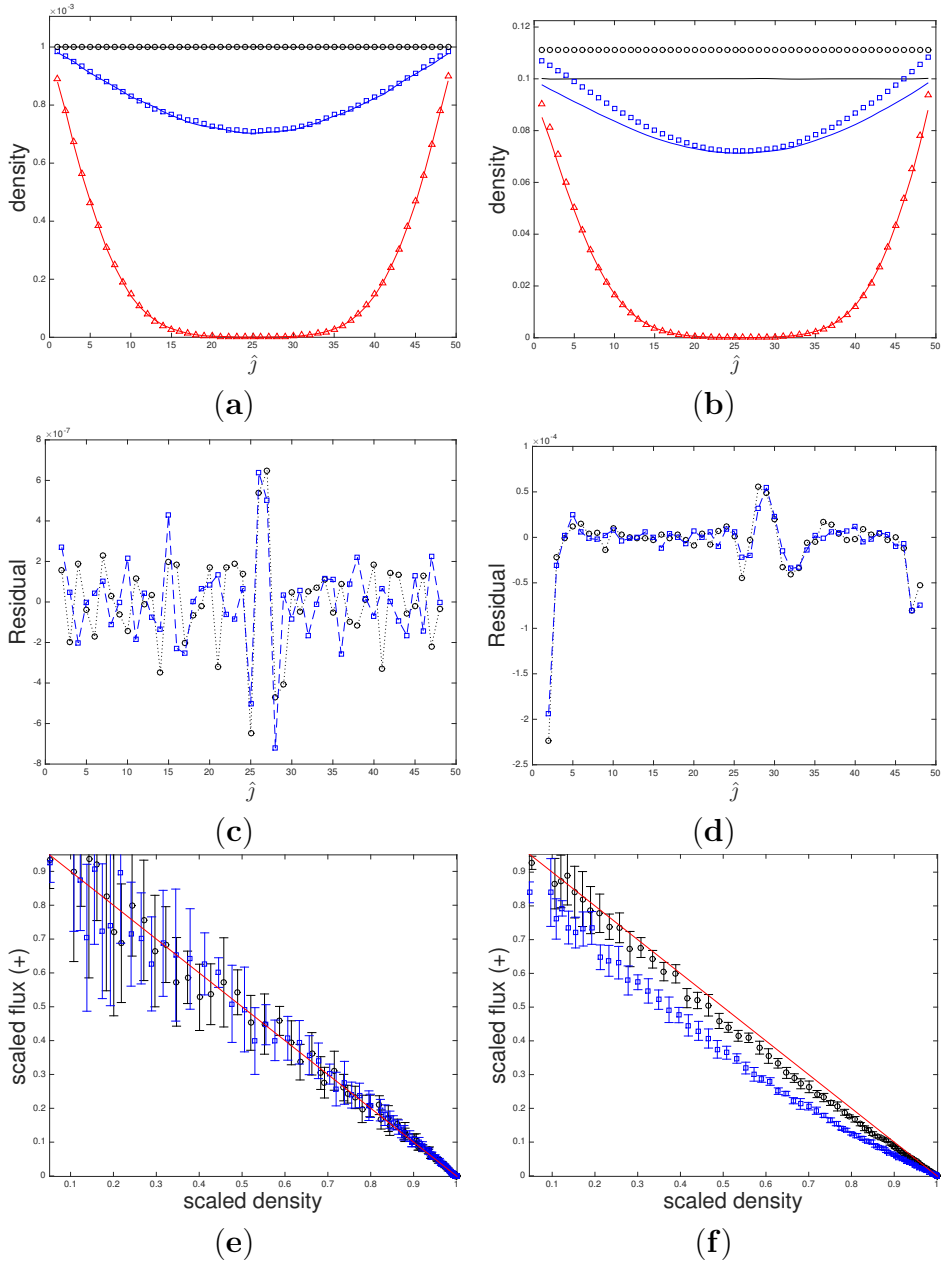

Figure 4.3: Comparison of KRSOS corrections when k is varied. Plots include: (a) and (b) adatom density, $c_{\hat{j}}(t)$, computed from KMC simulations of original KRSOS model (symbols) and alternate KRSOS model (solid lines) at times 2.5×10^{-9} (red), 4.0×10^{-8} (blue), and 1.0×10^{-5} (black); (c) and (d) residuals, $\mathfrak{L}_{\hat{j}}$, for original KRSOS model (blue squares) and alternate KRSOS model (black circles) at time $t = 10^{-5}$; and (e) and (f) adatom flux (prediction in red) at the right of the step for orginal KRSOS model (blue squares) and alternate KRSOS model (black circles), where, in each case, both coordinates are scaled by the appropriate equilibrium density. Model parameters are chosen to be $N = 50$, $D = 10^{10}$, $\phi_{\pm} = 1$, $F = 0$, and $\tau^{-1} = 0$, together with (a), (c) and (e) $k = 0.001$; or (b), (d) and (f) $k = 0.1$. Means and standard deviations were obtained using 10 ensembles of (a), (c) and (e) 10^6 simulations; or (b), (d) and (f) 10^5 simulations.

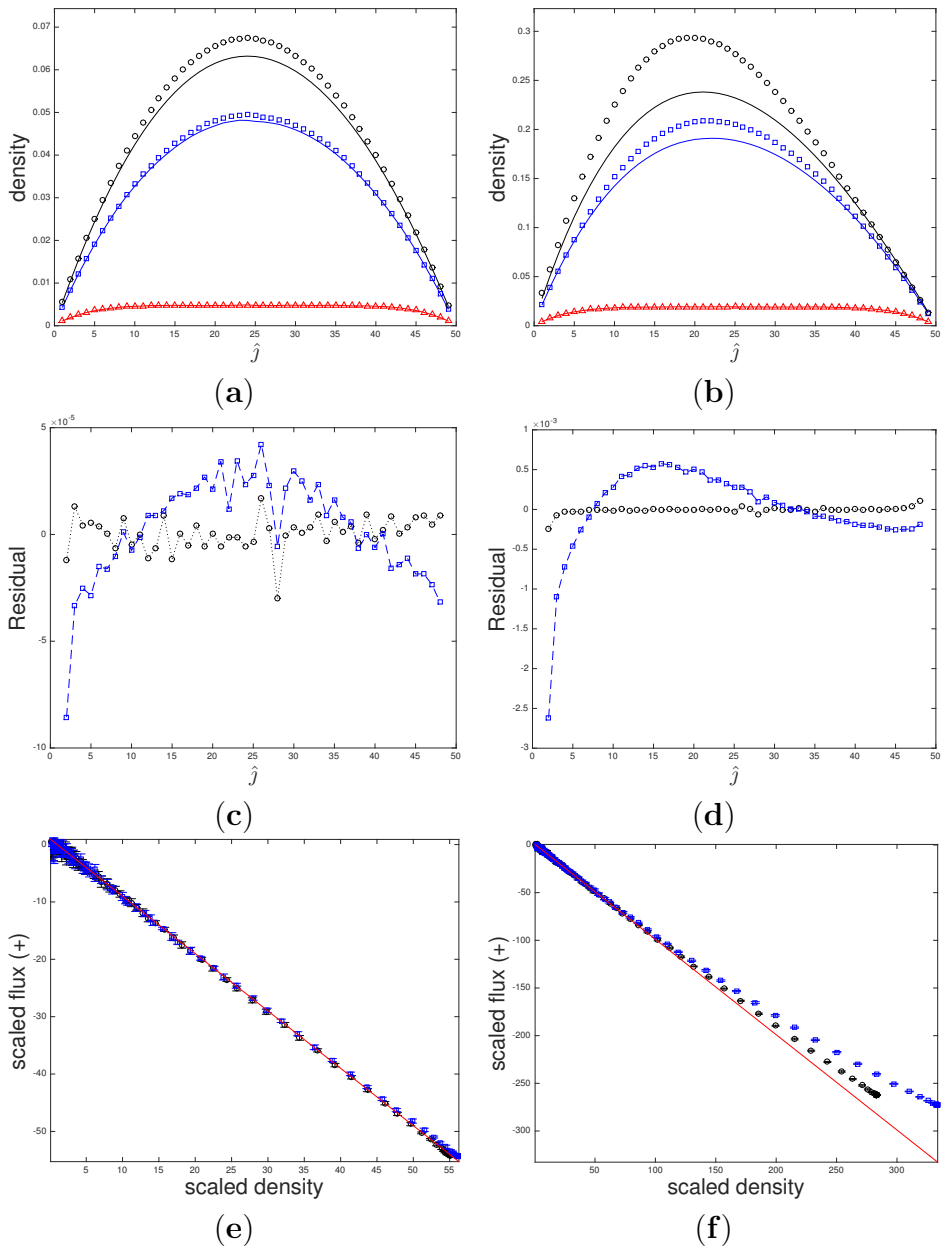

Figure 4.4: Comparison of KRSOS corrections when F is varied. Plots include: (a) and (b) adatom density, $c_{\hat{\jmath}}(t)$, computed from KMC simulations of original KRSOS model (symbols) and alternate KRSOS model (solid lines) at times 2.5×10^{-9} (red), 4.0×10^{-8} (blue), and 1.0×10^{-5} (black); (c) and (d) residuals, $\mathfrak{L}_{\hat{\jmath}}$, for original KRSOS model (blue squares) and alternate KRSOS model (black circles) at time $t = 10^{-5}$; and (e) and (f) adatom flux (prediction in red) at the right of the step for orginal KRSOS model (blue squares) and alternate KRSOS model (black circles) , where, in each case, both coordinates are scaled by the appropriate equilibrium density. Model parameters are chosen to be $N = 50$, $D = 10^{10}$, $\phi_{\pm} = 1$, $k = 0.0001$, and $\tau^{-1} = 0$, together with (a), (c) and (e) $F = 10^8$; or (b), (d) and (f) $F = 4\times10^8$. Means and standard deviations were obtained using 10 ensembles of 10^5 simulations in each case.

our limited data set. One plausible explanation of this conclusion is the fact that adatom densities are smaller in magnitude overall for the alternate KRSOS model, and therefore higher order terms in an expansion for flux such as (3.63) are less pronounced. This explanation is purely speculative at this point, however.

4.4 Summary and discussion

In this chapter, we investigated the consequences of altering one aspect of the KRSOS models introduced in Chapter 2, as well as the effect of that change on the discrete BCF-like equations emerging from this alternate KRSOS model. We found that the long-time behavior of the alternate KRSOS model differs appreciably from the original KRSOS model. In Section 4.1.3, we use an argument based on statistical mechanics to conclude that the discrepancy results from the indistinguishable nature of adatoms in the alternate KRSOS model. Another way in which the alternate KRSOS model diverges from the original is in the distribution of particle states in equilibrium: For the alternate KRSOS model, the number of adatoms on the terrace in equilibrium follow a Poisson distribution, whereas this was only true of the original KRSOS model in the limit of large N.

Equally interesting results were found concerning corrections to BCF-like equations satisfied by discrete averages over atomistic configurations of the alternate KRSOS model. In particular, the discrete diffusion equation for adatom density, (4.32), does not include correction terms, in contrast to the corresponding equation derived from the original KRSOS model. We conclude that the kinetic interaction between

adatoms is a crucial aspect of the original KRSOS model. At the same time, corrective fluxes appearing alongside discrete versions of the linear kinetic relation emerge from both the original and alternate KRSOS models. Intimately connected to the rules for attachment and detachment at the step edge [71], discrete corrections of this type appear to be unavoidable, though their effect may be more or less pronounced depending on other attributes of the underlying microscale model. For example, in Section 4.3, KMC simulations demonstrate that the corrections induced by the alternate KRSOS model are smaller than those resulting from the original KRSOS model.

In view of our conclusions regarding each KRSOS model studied in Part I of this thesis, it is compelling to ask which atomistic model is better suited to study the atomistic origins of the BCF model in $1+1$ dimensions. Unfortunately, there is no easy answer to a question as deep as this, but we attempt to outline some benefits of each. On one hand, the original KRSOS model is closer in spirit to traditional SOS models, where height columns typically only change by at most one atomic unit per hopping event with *constant* transition rate, making it an appealing starting model. On the other hand, the alternate KRSOS model includes adatom hopping that is consistent with Fick's law of diffusion, and consequently involves smaller corrections to discrete BCF-like equations. However, smaller corrections achieved by the alternate KRSOS model come at a cost: Kinetic interactions between adatoms are removed. In principle, there are always interactions between adatoms, so the inclusion of kinetic interactions, if not others, may be a desirable feature of an atomistic model. That said, neglecting kinetic interactions might make sense if we

wish to make comparisons between our 1D system and a similar, dilute 2D system, e.g. by projecting averages of the 2D system into 1D. We have not yet attempted to verify this conjecture. We summarize the key features of each KRSOS model in the table below.

Original KRSOS	Alternate KRSOS
Constant hopping rate D	$\boldsymbol{\alpha}$-dependent hopping rate $D\nu_j(\boldsymbol{\alpha})$
Non-Fickian hopping	Fickian hopping
Kinetic interactions	Non-interacting adatoms
Distinguishable adatoms	Indistinguishable adatoms
Corrections to diffusion equation	No corrections to diffusion equation
Corrections to LKR for adatom flux	(Smaller) corrections to LKR

PART II

Evolution of crystalline mounds: Atomistic scale, mesoscale, and macroscale

Chapter 5: Towards a mesoscale description of mound evolution

In this chapter, we investigate in $2+1$ dimensions the evolution of epitaxially grown mounds using atomistic and mesoscale models of crytal growth that include an Ehrlich-Schwoebel (ES) barrier [24, 88]. This potential energy barrier, experienced by atoms on stepped crystal surfaces, inhibits mass transport between atomic layers, leading to the formation of 3D structures on an otherwise vicinal surface in the presence of external material deposition. Our atomistic model, introduced in [94], is a solid-on-solid (SOS) model of a crystal surface that makes use of a deposition processes intended to mimic the effect of *transient mobility* (TM), i.e. a mechanism by which freshly deposited atoms have excess kinetic energy for a short time. At the mesoscale, we describe the surface using a BCF-like island dynamics model, presented in [68, 77], to which we add (i) the effect of TM in a manner consistent with microscale model, and (ii) a related mass transport process know as *downward funneling* (DF) [26].

In contrast to the ES barrier, DF and TM tend to *delay* the onset of mounding during growth. To capture the complex interplay between these mechanisms, we lean heavily on KMC simulations of the atomistic model. Simulations of the mesoscale island dynamics model are carried out using the level set method [65, 66, 90], which

is a promising computational framework that has successfully described epitaxial growth for at least fifteen years [13,19,68,69,73,77]. Employing the level set method for epitaxial growth, we demonstrate, in this chapter, how our incorporation of TM and DF into the island dynamics model results in a numerical description of mound evolution in *qualitative* agreement with KMC simulations.

5.0.1 Background

Before discussing specifics about our atomistic and mesoscale models or their numerical implementation, we provide a general review of mound growth. The basic processes involved in epitaxial growth include the deposition of atoms via molecular beam onto a substrate, the diffusion of adsorbed atoms (adatoms), the nucleation of adatoms resulting in the formation of small clusters or islands, the growth of islands, and finally the coalescence of islands until a full layer of material is formed and growth of subsequent layers continues following a simlar pattern. These processes have been described by a variety of models of crystal surfaces, including rate equations [3, 4, 79, 80], atomistic models [22], step-continuum models [36, 59], and by use of the level set method [68, 77]. In most of these cases, when external deposition is included and the interlayer transport of adatoms is inhibited by an ES barrier [24,88] at step edges (see Figure 5.1), islands may nucleate on top of islands, leading to the formation of 3D mounds and the overall roughening of the surface (for a general review of mound growth, see [28,57]). In many systems, "slope selection" is observed for long enough times, suggesting the existence of kinetic processes that

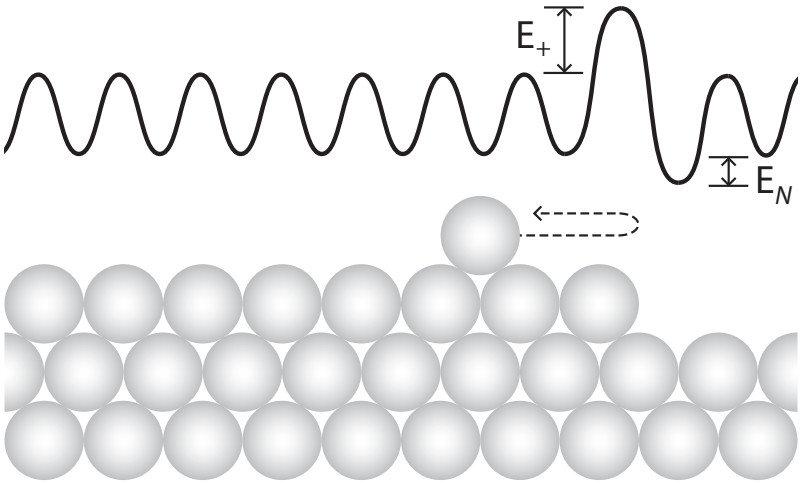

Figure 5.1: Side-view illustration of the effect of the Ehrlich-Schwoebel step edge barrier. An adatom diffusing toward a descending step edge must overcome an additional energy barrier E_+ in order to attach to the step. Larger barriers increase the probability that an adatom is reflected toward the center of the terrace.

favor downward transport of adatoms, in opposition to the effective uphill current induced by the ES barrier [26, 27, 94].

Two candidate processes that could explain the observed slope stabilization in experiments are DF [2, 16, 26, 27] and TM [21, 22, 27, 94, 95]. In both DF and TM, freshly deposited atoms quickly relax to energetically favorable positions near deposition sites, albeit in slightly different ways, overcoming possible ES barriers and contributing to a smoother growth front. So far, DF has received considerable attention in the epitaxial growth literature: It has been studied using molecular dynamics simulations of the deposition process [92, 112], incorporated into atomistic kinetic Monte Carlo (KMC) simulations [2, 16, 26, 27], and included in phenomenological step-continuum models [46, 47]. By comparison, relatively few studies focus on TM. There have been a few attempts to incorporate TM in atomistic models,

e.g. [21, 22, 94, 95], and only recently has TM been studied using a rate equation formalism [25, 60].

The goals of this chapter are twofold. First, we use it as an opportunity to extend the results in [94] by performing a systematic study of TM using KMC. Second, we translate simple models for DF and TM into a mesoscale island dynamics model of epitaxial growth. The prescriptions for DF and TM we employ are inspired by (i) the mesoscale description of DF used in the step-continuum models in [46, 47], and (ii) an atomistic description of TM that allows a deposited atom to relax to a nearby site with maximum coordination, i.e. where the atom will have the maximum number of nearest neighbors [94, 95]. The corresponding mesoscale, island dynamics description of these processes involves the modification of the deposition process at descending step edges and at both ascending and descending step edges, respectively, as well as step velocities. Starting from an island dynamics model that includes ES barriers at step edges [68], we incorporate DF and TM with the intention of making qualitative comparisons with the results of our KMC study. This is achieved, in part, using appropriately defined neighborhoods near steps for which DF and TM are active.

The remainder of this chapter is organized as follows. First, we review the SOS (atomistic) and island dynamics (mesoscale) models of $2+1$-dimensional crystal growth in Section 5.1. Next, Section 5.2 gives details for the modeling and numerical implementation of downward transport mechanisms in the level set method. Section 5.3 contains the results of both atomistic and mesoscale simulations. And finally, we provide some discussion of multiscale modeling of mound evolution in

Section 5.4.

5.1 Review of models

We begin by outlining the atomistic lattice-gas model and the island dynamics model we use to study mound evolution. A common feature of these models is the inclusion of an ES barrier at step edges, which, in the presence of a nonzero deposition rate leads to mound growth [105]. This is achieved by directly modifying the potential energy surface experienced by adatoms in the atomistic model, whereas, in the island dynamics model, step-edge barriers modify the boundary conditions of a PDE [68]. On the other hand, downward transport mechanisms leading to slope stabilization have been studied in several atomistic models, but are absent in the island dynamics model. We address this deficiency later in Section 5.2.

5.1.1 Atomistic models with downward transport

A well-known stochastic model for describing epitaxial growth is the SOS model [107]. In it, atoms may arrange themselves in a simple cubic (SC) crystal lattice, forming bonds with neighboring atoms. The solid-on-solid restriction forbids overhangs and bulk vacancies, and therefore the crystal surface may be represented by an array of height columns. During evolution, typically only one or two height columns change by a single atomic unit per transition. While the SOS model has several features in common with the KRSOS models introduced in Part I of this thesis, the SOS model does *not* include a kinetic restriction preventing terrace

atoms from becoming adatoms; atomic vacancies may form. Additionally, bonding between nearest-neighbor adatoms and the nucleation of small islands on terraces is an important feature of the SOS model in $2+1$ dimensions, in contrast to the $1+1$-dimensional KRSOS models, in which bonding between adatoms is forbidden.

In the KMC formulation of SOS, most transitions between nearby states in configuration space follow Arrhenius rates of the form $\nu \exp(-E/k_B T)$, where ν is an attempt frequency, E is the energy barrier separating two states, k_B is Boltzmann's constant and T is the substrate temperature. External material deposition from above occurs at a rate of F atoms per site per second. We neglect desorption for our current purpose, but it may also be included in KMC. A common choice for the energy barrier between states in SOS models is $E = E_S + nE_N$ where E_S is the barrier for surface diffusion, $n = 0, 1, \ldots, 4$ is the number of in-plane nearest neighbors prior to the transition, and E_N is a bonding energy. This energy barrier can be modified to account for changes in the potential energy surface an adatom experiences near step edges, i.e. the ES barrier, for which E_+ (we assume $E_- = 0$ in this section) is added to E. In our notation E_+ is the barrier at descending step edges, influencing interlayer transport between the step and the upper terrace and vice versa; see Figure 5.1.

In this chapter, we adopt the SOS model presented in [94], which is one of only a few KMC prescriptions for TM, although similar models of a TM-like deposition process were described earlier [21,22,111]. The deposition process in [94], pictured in Figure 5.3(b), has two stages: First, a lattice site is selected at random for deposition, then a local search within the square of side length $2R+1$ about the initially

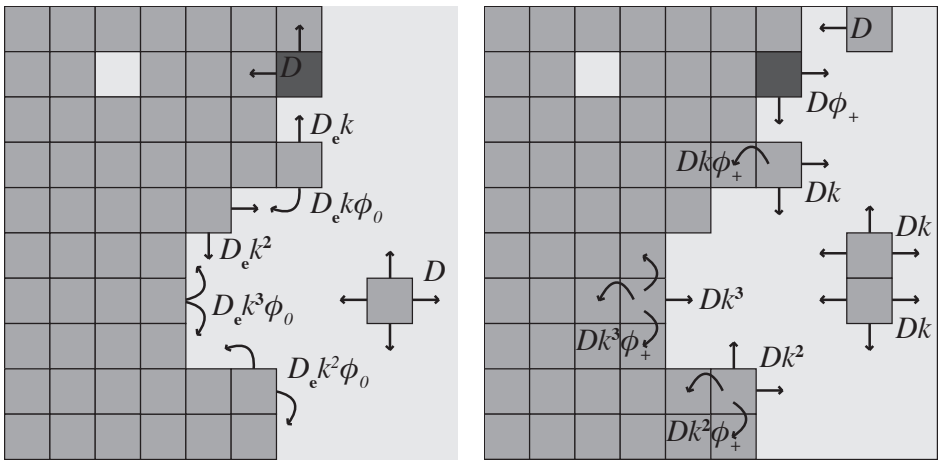

Figure 5.2: Top-view illustrations of the atomistic transitions allowed in our SOS model. Light grey squares represent lattice sites with height h_0 and dark grey squares represent lattice sites with height h_0+a. (a) Diffusive transitions include: Adatom hopping (rate D), edge diffusion to a vacant nearest-neighbor site (rate $D_\mathrm{e}k^n$ for n in-plane nearest neighbors), and edge diffusion to a vacant next-nearest-neighbor site (rate $D_\mathrm{e}k^n\phi_0$ for n in-plane nearest neighbors); (b) Attachment and detachment transitions include: Detachment to lower terrace (rate Dk^n for n in-plane nearest neighbors), attachment from lower terrace (rate D), detachment to upper terrace (rate $Dk^n\phi_+$ for n in-plane nearest neighbors), attachment from upper terrace (rate $D\phi_+$), and finally dimer dissociation (rate Dk) which is a special case of detachment to the lower terrace.

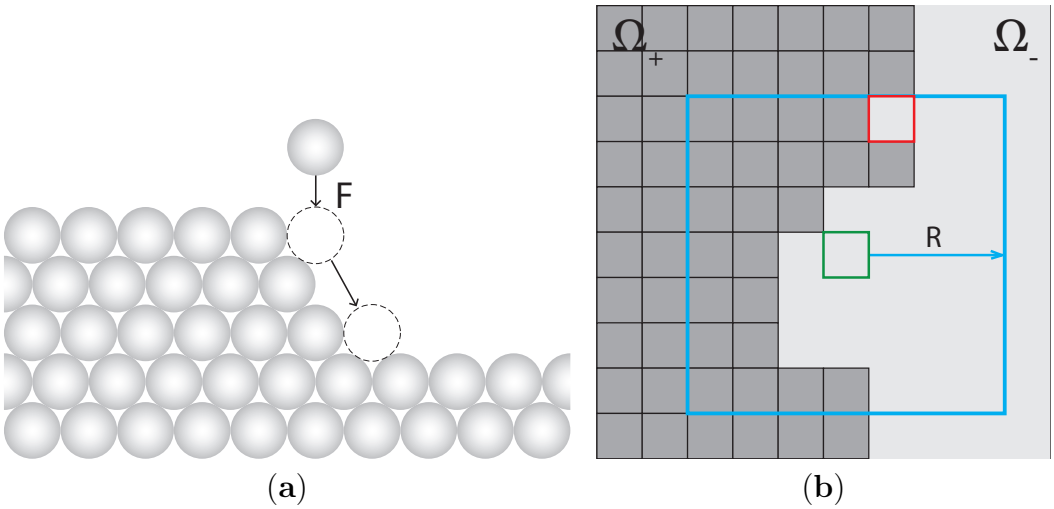

Figure 5.3: (a) Side-view illustration of the basic (geometric) downward funneling mechanism, where freshly deposited atoms (rate F) relax to an adsorption site with full support in a lower layer [26]. (b) Top-view illustration of the KMC prescription of transient mobility, where freshly deposited atoms relax to a nearby site with highest coordination. The site outlined in green is the lattice site initially chosen for deposition, the blue square indicates the sites explored during transient mobility, R is the search radius, and the site outlined in red is the final destination of the deposited atom after it has thermalized.

chosen site is performed for the site that would give the deposited atom highest coordination. If the search results in a unique maximum coordination number among the affected collection of sites, the deposited atom is placed in that site. In the event of a tie, the site closest to the initial site is selected. In this deposition process, R is a "search radius" that is supposed to reflect the transient kinetic energy imparted to the atom by deposition and adsorption.

In [94], using the search procedure described above, the authors show that TM can effectively oppose the ES barrier and lead to slope stabilization during growth. The extent of their simulation data, however, is quite limited: Only two parameter

sets were used. Later, in Section 5.3, we extend that study by methodically examining the effects of (i) the search radius R, (ii) ES barrier strength, measured by Arrhenius factor $\phi_+ = \exp(-E_+/k_BT)$, and (iii) nearest-neighbor bond strength, measured by the factor $k = \exp(-E_N/k_BT)$; see Figure 5.2 for examples of transitions allowed in our SOS model.

5.1.2 Island dynamics model of epitaxial growth

The island dynamics model we use in this chapter is a BCF-like mesoscale description of a vicinal crystal surface designed to be implemented using the level set method [66]. In it, monatomic layers are represented by the level sets of the function φ, i.e.

$$\Gamma_n(t) = \left\{\mathbf{x} \in \mathbb{R}^2 : \varphi(\mathbf{x}, t) = n\right\} \ , \tag{5.1}$$

where $\Gamma_n(t)$ is the set of islands in the nth layer at time t [13, 77].

Islands, in this formulation, grow in a direction normal to step edges with velocity $v = \mathbf{v} \cdot \mathbf{n}$, where $\mathbf{n}$ is the unit normal vector. The normal step velocity is given by [68, 77]

$$v = \left(\boldsymbol{\mathcal{D}}\nabla\rho^- - \boldsymbol{\mathcal{D}}\nabla\rho^+\right) \cdot \mathbf{n} + v_e \ . \tag{5.2}$$

The first term in the (5.2) expresses the net flux of adatoms to the step, and v_e is a contribution to normal velocity accounting for local changes via edge diffusion. In BCF treatments of step motion in 2D, one expects that $v_e \propto \partial_s[\mathcal{D}_e\partial_s(\tilde{\gamma}(s)\kappa(s))]$, where $\tilde{\gamma}(s)$ is step stiffness, $\mathcal{D}_e$ is the edge-adatom diffusivity and the partial derivative, ∂_s, is with respect to arc length [36, 59]. However, for technical reasons, imple-

mentations of the island dynamics model using level sets choose $v_e = \mathcal{D}_e\,[\kappa(s) - \kappa_{\text{ave}}]$ [13]. It is argued in [13] that this choice captures the essential physics of edge diffusion. While the nonphysical version of v_e leaves something to be desired from a modeling standpoint, we nevertheless use that formula in the island dynamics simulations presented in this chapter.

The adatom density $\rho = \rho(\mathbf{x}, t)$ evolves according to [68]

$$\frac{\partial \rho}{\partial t} = \nabla \cdot (\boldsymbol{\mathcal{D}} \nabla \rho) + F - 2\frac{d\mathcal{N}}{dt} \ . \tag{5.3}$$

In (5.3), $\boldsymbol{\mathcal{D}}$ is the (tensor) terrace diffusivity and $\frac{d\mathcal{N}}{dt}$ is the nucleation rate of islands. We will assume isotropic diffusivity, and hence model adatom density by [68, 73, 77]

$$\frac{\partial \rho}{\partial t} = \mathcal{D}\Delta\rho + F - 2\frac{d\mathcal{N}}{dt} \ , \tag{5.4}$$

where the loss term accounts for collisions between two adatoms that result in nucleation of small islands. It follows that [61, 62]

$$\frac{d\mathcal{N}}{dt} = \mathcal{D}\sigma_1 \int \rho^2(\mathbf{x}, t) d\mathbf{x} \ , \tag{5.5}$$

i.e. the change in island number density is proportional to the average value of adatom density squared. Here, σ_1 denotes the capture number of an adatom, frequently encountered in the rate equation descriptions of submonolayer growth (see e.g. [3, 4, 79, 80]). In the above description, a dimer nucleates when $\mathcal{N}(t)$ increases past an integer value [19], and may subsequently dissociate through the stochastic approach described in [73]. The location of nucleation is chosen randomly among available lattice sites with probability proportional to ρ^2. Justification for the deterministic choice for the *time* of nucleation, as well as the stochastic choice for the

location of nucleation is given in [78].

What remains to fully specify the island dynamics model are boundary conditions for adatom density at step edges. Complementing PDE (5.4) we have [68]

$$\rho^- = \rho^{eq} \ , \text{ and} \tag{5.6a}$$

$$\mathbf{n} \cdot \nabla \rho^+ + \frac{\mathcal{D}'}{\mathcal{D} - \mathcal{D}'}(\rho^+ - \rho^{\text{eq}}) = 0 \ . \tag{5.6b}$$

That is, on lower terraces $(-)$ or ascending step edges, the adatom density satisfies Dirichlet boundary condition (5.6a), where ρ^{eq} denotes the equilibrium density at the step edge. On the other hand, on upper terraces $(+)$ or descending step edges, we have a Robin boundary condition, where the normal flux, $\mathbf{n} \cdot \nabla \rho^+$, is proportional to the local deviation of adatom density from its equilibrium value. This is just the 2D version of the linear kinetic relation common to BCF models [36,59]. Note that since $\mathcal{D}$ is terrace diffusivity and $\mathcal{D}'$ is diffusivity across a step, the dimensionless factor $\frac{\mathcal{D}'}{\mathcal{D}-\mathcal{D}'}$ expresses the strength of the ES barrier [74]. For example, as $\mathcal{D}' \to \mathcal{D}$, the case of a small barrier, condition (5.6b) becomes a Dirichlet condition not unlike (5.6a). Also, it is the case that $\phi_+ = \frac{\mathcal{D}'}{\mathcal{D}}$, connecting the notation in (5.6) with that of Section 5.1.1.

In summary, PDE (5.4) supplemented by (5.5) and boundary conditions (5.6) determine the evolution of adatom density for fixed island boundary. Subsequently, the motion of island boundaries follow the local normal velocity (5.2), where choice of v_e is described above. For details on numerical implementation, see [19, 68, 73].

5.2 Mound evolution in a level set framework

DF and TM are atomistic processes whose inclusion in atomistic lattice-gas models is somewhat natural and well established in the literature on epitaxial growth [2,16,26–28,94]. In contrast, mesoscale and continuum models including DF or TM are less common. There is at least one case [46], however, where researchers include DF in a mesoscale step-dynamics model, and subsequently derive continuum equations for the evolution of mounds [47]. This inclusion of DF for step-dynamics relies on defining a narrow region within a fixed distance of a descending step edge for which all deposited material is incorporated into the step directly. Including DF in this way, slope stabilization can be studied via step-dynamics. We will take a similar approach to include both DF and TM in the level set-based island dynamics model. Specifically, we define a new parameter in the island dynamics model, d, as the distance over which either DF or TM affects deposition near step edges, and accordingly adjust the local step velocity field. The remainder of this section is devoted to describing the modeling and implementation considerations necessary to include DF and TM in the island dynamics model, to be simulated using the level set method.

5.2.1 Mesoscale modeling of downward transport mechanisms

In our mesoscale island dynamics model, both DF and TM have the same type of prescription: For all points in some neighborhood of a step, mass that would be deposited on the terrace is instead incorporated into the step directly. As a first

step to introducing these transport mechanisms into the island dynamics model, we must specify the neighborhood near steps impacted by DF and TM. Consider a monatomic island composed of points $\mathbf{x} \in \Omega_+$. We define the *signed distance function* of Ω_+ as

$$\psi(\mathbf{x};\Omega_+) = \begin{cases} \text{dist}(\mathbf{x},\partial\Omega_+) & \mathbf{x} \in \Omega_+ \ , \\ -\text{dist}(\mathbf{x},\partial\Omega_+) & \mathbf{x} \notin \Omega_+ \ , \end{cases} \tag{5.7}$$

where $\text{dist}(\mathbf{x},\partial\Omega_+) = \min_{\mathbf{y}\in\partial\Omega_+} |\mathbf{x}-\mathbf{y}|$. Now, let $\mathcal{S}_\pm(\Omega_+)$ denote the set of points within the distance d of $\partial\Omega_+$, *inside* the island $(+)$ and *outside* the island $(-)$, respectively. Hence, we write

$$\mathcal{S}_\pm(\Omega_+) = \{\mathbf{x} \mid 0 \le \pm\psi(\mathbf{x};\Omega_+) \le d\} \ . \tag{5.8}$$

Finally, (5.8) allows us to define the regions affected by DF and TM.

Definition 11. (Downward transport neighborhoods.) *In the island dynamics model, for each island Ω_+, the neighborhood where* downward funneling *is active is $\mathcal{S}_+(\Omega_+)$, and the neighborhood where* transient mobility *is active is $\mathcal{S}_+(\Omega_+)\cup\mathcal{S}_-(\Omega_+)$, where $\mathcal{S}_\pm(\Omega_+)$ are defined in (5.8). Restated in words, downward funneling impacts upper terraces only, within distance d, while transient mobility impacts both upper and lower terraces, within distance d on each side of the step; see Figure 5.4(a).*

Given Definition 11, all that remains is to specify how the normal velocity of the interface, v, should be modified to account for additional mass from DF or TM. A choice inspired by the atomistic mechanisms, i.e. DF as described in [2,16,26,27] and TM as described Section 5.1.1, involves *local* step geometry. Specifically, we calculate

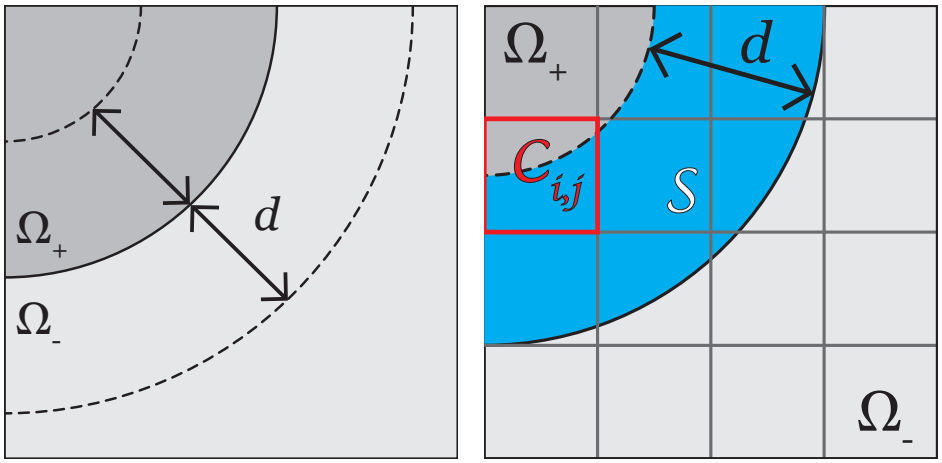

Figure 5.4: Top-view illustrations of regions affected by downward transport mechanisms in the level set framework. (a) An island, Ω_+ (dark grey), separated from the substrate, Ω_- (light grey), by the solid curve. Dashed curves are within distance d, representing the mesoscopic length scale of downward funneling or transient mobility, of the island boundary. (b) Anumerical grid superimposed over an island, Ω_+ (dark grey), separated from the substrate, Ω_- (light grey), by a solid curve, a set $\mathcal{S}$ (blue) indicating a region near an island boundary affceted by DF or TM, and a numerical cell $\mathcal{C}_{i,j}$ that intersects $\mathcal{S}$. Again, d is the length scale of downward funneling or transient mobility.

the additional normal velocity imparted to steps by each transport mechanism using the local curvature κ, and the constants d, F and a.

Next, insisting that mass is conserved, we compute: (i) The differential area, dA_v, swept out by a step with velocity v_{add}, (ii) the area dA_{df} added to the step via DF in time Δt, and (iii) the area dA_{tm} added to the step due to TM in time Δt. In doing so, we take the convention that a circular island has positive curvature. Furthermore, let us assume $v_{\text{add}}\Delta t < |\kappa|^{-1}$ and $d < |\kappa|^{-1}$. At the end of the section we will discuss remedies for geometries that violate this last assumption. When that assumption is satisfied, (i)-(iii) are calculated as the differential areas of sectors of circles, with angles $d\theta$, via formula $dA = d\theta/(2\kappa^2)$.

First, consider the additional terrace area added in time Δt to an island whose boundary advances with velocity v_{add}. In differential form, we have

$$\begin{aligned} dA_v &= |\kappa|^{-1}\left[v_{\text{add}}\Delta t + \frac{1}{2}\kappa(v_{\text{add}}\Delta t)^2\right] d\theta \\ &\approx \frac{v_{\text{add}}\Delta t}{|\kappa|} d\theta \ , \end{aligned} \tag{5.9}$$

where the approximation in (5.9) is made by neglect of the quadratic term in Δt. Second, the mass added to the growing front from DF or TM, instead of strips $\mathcal{S}_\pm$ near island boundaries, contributes differential terrace area $dA_\pm = \frac{a^2 F\Delta t}{|\kappa|}\left(d \mp \frac{1}{2}\kappa d^2\right) d\theta$. For DF, only dA_+ is considered, whereas TM uses the sum $dA_- + dA_+$.

The resulting contributions are

$$dA_{df} = \frac{a^2 F\Delta t}{|\kappa|}\left(d - \frac{1}{2}\kappa d^2\right) d\theta \ , \tag{5.10a}$$

and

$$dA_{tm} = 2d\frac{a^2F\Delta t}{|\kappa|}d\theta \ . \tag{5.10b}$$

The factor $a^2F\Delta t$ appearing in (5.10) converts deposited mass into terrace area.

Finally, by equating (5.9) with (5.10a) in the case of DF, and (5.9) with (5.10b) in the case of TM, the formula for the additional normal velocity, v_{add}, imparted to the step from each transport process is

$$v_{\text{add}} = \begin{cases} a^2F(d - \frac{1}{2}\kappa d^2) & \text{for DF,} \\ 2a^2Fd & \text{for TM.} \end{cases} \tag{5.11}$$

Notice that the above expression for DF, which involves asymmetry with respect to the step edge per Definition 11, involves the local step curvature, κ, but this term is eliminated in the expression for TM by symmetry. It is also worth noting that $v_{\text{add}} > 0$ whenever F and d are positive, and the local geometry is non-degenerate.

Before we conclude this section, it is important to mentioning how (5.11) should be modified when the assumptions $v_{\text{add}}\Delta t < |\kappa|^{-1}$ or $d < |\kappa|^{-1}$ are violated, examples of which include: Small islands, small holes or vacancies, and narrow terraces. In all of these potentially problematic cases, we forgo formulas (5.10) in favor of direct calculation of the areas $A_{df} = \int\limits_{\mathcal{S}_+} d\mathbf{x}$ and $A_{tm} = \int\limits_{\mathcal{S}_+\cup\mathcal{S}_-} d\mathbf{x}$. Accordingly, v_{add} is computed by distributing the requisite mass from DF or TM along appropriate step edges.

5.2.2 Implementation of downward transport mechanisms

We now outline the numerical methods used to simulate the island dynamics model within the level set framework, and modifications that allow for the inclusion

of DF and TM. For an overview of level set methods in a more general context, see [65,90]. The key idea of level set methods is the *implicit* representation of moving interfaces, which are typically the zero-level set of an auxiliary function φ. All physical information is encoded in an externally defined velocity field, $\mathbf{v}$. The level set function, φ, evolves according to a Hamilton-Jacobi equation: $\frac{\partial \varphi}{\partial t} + \mathbf{v} \cdot \nabla \varphi = 0$. Since the outward normal to the level set function is defined as $\mathbf{n} = \frac{\nabla \varphi}{|\nabla \varphi|}$, the level set equation may be written in terms of the normal velocity, $v_n = \mathbf{v} \cdot$, viz.,

$$\frac{\partial \varphi}{\partial t} + v_n \, |\nabla \varphi| = 0 \; . \tag{5.12}$$

In the case of the island dynamics model described in Section 5.1.2, without the mass transport mechanisms, v_n is the normal velocity in (5.2), which involves the difference in adatom fluxes at step edges, plus a curvature term intended to capture the effect of edge diffusion [77]. With inclusion of DF and TM, we take $v_n = v + v_{\text{add}}$, i.e. the original velocity (5.2) plus additional velocity (5.11).

At this stage, we should point out that curvature is calculated via $\kappa = \nabla \cdot \frac{\nabla \varphi}{|\nabla \varphi|}$, i.e. a second-order term, in the level set framework. As a result, (5.12) is no longer a Hamilton-Jacobi equation. However, for the purposes of numerical simulation, it should still be treated as a first-order hyperbolic PDE, as described in the seminal paper by Osher and Sethian [66]: Convective spatial derivatives are discretized using upwind methods, while second-order terms are discretized via centered differences. When including downward transport, we apply the same prescription to v_{add}. With or without this modification, the level set method employed for our island dynamics model solves (5.12) using a third-order essentially non-oscillatory (upwind) scheme

in space, whereas time integration is performed using a third-order total variation diminishing Runge-Kutta scheme [19]; see also [67, 93].

Next, let us discuss the numerical solution of the adatom concentration field. By Definition 11, the inclusion of DF or TM dictates that the deposition flux in certain neighborhoods of step edges may need to be adjusted. Suppose $\mathcal{S}$ is a region affected by DF or TM, to be defined in the level set framework later, and consider a uniform numerical grid with step-size h. For each cell, $\mathcal{C}_{i,j}$, that intersects $\mathcal{S}$, we compute

$$A_{i,j} = \int_{\mathcal{C}_{i,j} \cap \mathcal{S}} d\mathbf{x} \ , \tag{5.13}$$

i.e. the area of intersection, pictured in Figure 5.4(b). This can be done, for example, by the geometric integration method in [58]. Accordingly, the deposition flux $F_{i,j}$ is adjusted by the factor $1 - A_{i,j}/h^2$. After this adjustment is made for all numerical cells, we solve (5.4) subject to boundary conditions (5.6) using the finite-volume approach described in [68, 69].

It remains to specify $\mathcal{S}$ in the level set framework. To do so, we must find contours which are a distance d away from the level sets $\Gamma_n(t) = \{\mathbf{x} | \varphi(\mathbf{x}, t) = n\}$, $\Gamma_n(t) = \partial\Omega$ for some set Ω. This can be done using the "reinitialization" technique originally suggested by Sussman, Smereka, and Osher [100]. Employing the second order upwind scheme in [82], we calculate the signed distance function, $\psi(\mathbf{x}, \tau; \Omega)$, as the steady-state of the PDE

$$\begin{cases} \psi_\tau + \text{sign}(\psi^{(n)})(|\nabla\psi| - 1) = 0 \ , & (\mathbf{x}, \tau) \in \Omega \times [0, d] \ , \\ \psi(\mathbf{x}, 0) = \psi^{(n)} & \mathbf{x} \ , \in \Omega \ , \end{cases} \tag{5.14}$$

where $\psi^{(n)}(\mathbf{x}) = \varphi(\mathbf{x}, t) - n$, n is the level of interest, and τ is non-physical time. The result is a function ψ whose zero level set is $\Gamma_n(t)$ and is the signed distance function of Ω up to distance d. Note that $\psi = \pm d$ corresponds to an interface that lies in the region where $\psi^{(n)}$ is positive or negative, respectively. Consequently, strips of width d surrounding $\Gamma_n(t)$ in $\Omega_\pm$ are the sets $\mathcal{S}_\pm$ defined by (5.8). Recall that for the case of DF, only one of these sets is required, whereas for TM both are necessary.

For completeness, we outline the steps for the numerical simulation of the island dynamics model in the level set framework [19]:

1. Initialize adatom density, ρ, level set function, φ, and number of islands, $\mathcal{N}$.
2. Update $\mathcal{N}$ by (5.5) and seed an island if $\mathcal{N}$ is greater than the next integer value.
3. For each island, calculate the signed distance function ψ by solving (5.14); adjust deposition flux $F_{i,j}$ according to Definition 11.
4. Solve (5.4) subject to (5.6).
5. Compute $v_n = v + v_{\text{add}}$ using (5.2) and (5.11).
6. Update φ by solving (5.12).

5.3 Simulation results

We now describe our data collection methods as well as our numerical results for mound growth. First, we introduce statistical quantities that may be used to

capture important features of mound evolution; in particular, surface roughness, feature size, and mean surface slope. These quantities, measured in KMC and level set simulations of mound growth, allow us to capture the effects of adjusting important model parameters. Through our KMC simulations, we show that increasing the search radius R leads to a smoother surface with larger features and smaller slopes. Furthermore, increasing the strength of the ES barrier increases surface roughness and surface slopes, in addition to promoting smaller features. While level set data showing the response of the growing surface to changes in ES barrier are not available, we find the same qualitative behavior in our mesoscale description of mound growth by adjusting d as we do by adjusting R in KMC simulations.

5.3.1 Statistical characterization of surface morphology

Statistics for surface profiles obtained in KMC and level set simulations are most conveniently expressed using the height-height correlation function, $G(r, \theta)$. If $\mathbf{r}$ is the 2D position vector parallel to the high-symmetry plane of the crystal, and $h(\mathbf{r}, \theta)$ is the surface height as a function of position and coverage, then the height-height correlation function at coverage θ may be defined as

$$G(r, \theta) = \langle \tilde{h}(\mathbf{r}, \theta) \tilde{h}(\mathbf{0}, \theta) \rangle \ , \tag{5.15}$$

where $\tilde{h}(\mathbf{r}, \theta) = h(\mathbf{r}, \theta) - \langle h(\mathbf{r}, \theta) \rangle$ and the averages $\langle \cdot \rangle$ are computed over choice of origin $\mathbf{0}$, radius $r = |\mathbf{r}|$, and ensembles. In an effort to streamline the results of atomistic and mesoscale simulations, we measure the position $r = |\mathbf{r}|$ only at discrete points (integer multiples of lattice spacing, a) along the $x-$ and $y-$ axes, which run

parallel to the direction of nearest-neighbor bonding in SC geometry. This should minimize differences due to the crystalline anisotropy inherent in the SOS model, but neglected in our mesoscale treatment; see, for example, Figure 5.5.

When $G(r,\theta)$ is defined by (5.15), the surface roughness, $w(\theta)$, is computed via

$$w(\theta) = \sqrt{G(0,\theta)}\ . \tag{5.16}$$

In addition, the average feature size or "critical radius", $r_c(\theta)$, corresponds to the first zero of $G(\cdot,t)$. Accordingly, the average surface slope is the ratio w/r_c. Using $w(\theta)$, $r_c(\theta)$, and w/r_c, the respective scaling exponents for roughness, coarsening of features, and slope evolution can be computed for large enough values of θ. We will refer to β as the *roughening exponent* and γ as the *coarsening exponent*, i.e. $w \sim \theta^\beta$ and $r_c \sim \theta^\gamma$ for $\theta \gg 1$. Note that the exponent for slope evolution is just the difference $\beta - \gamma$.

In the remainder of this section, we summarize data obtained from KMC and level set simulations for the height-height correlation function (5.15), related statistics, and scaling exponents.

5.3.2 KMC simulations

We now provide the results of KMC simulations of the SOS model described in Section 5.1.1. Primary quantities of interest include mean surface roughness, $w(\theta)$, feature size $r_c(\theta)$, and slope $w(\theta)/r_c(\theta)$, which are obtained from the height-height correlation function (5.15) as described in Section 5.3.1. The values, and particularly

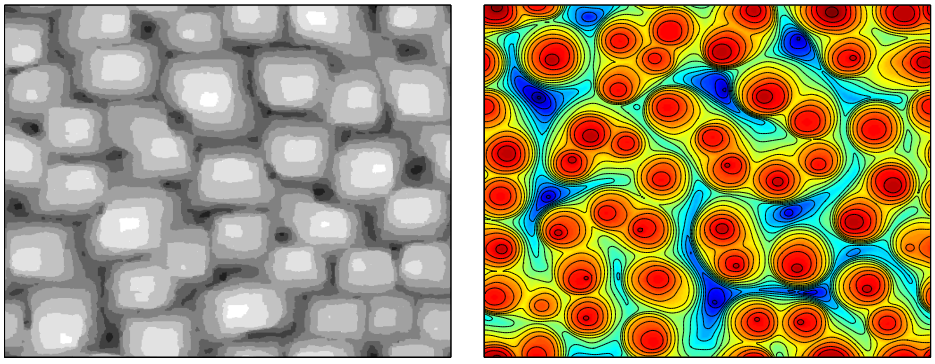

(**a**) (**b**)

Figure 5.5: Comparison of surface morphologies after 20 monolayers of deposition (a) on a 500×500 lattice in KMC with transient mobility. Parameters include $D/F = 10^6$, $k = 10^{-2}$, $\phi_+ = 10^{-2}$, and $R = 3$; (b) on a 181×181 lattice (256×256 numerical grind) in the level set-based island dynamics model including transient mobility. Parameters used are comparible to those in (a), except $d = 0.5$.

the scaling of these quantities, are expected to depend on model parameters, of which the search radius, R, associated with transient mobility and the ES barrier strength, measured by Arrhenius factor $\phi_+ = \exp(-E_+/k_BT)$, are central in our numerical study. What we find is that roughness (feature size) tends to decrease (increase) as R increases, for fixed θ, $\theta \gg 1$. Moreover, roughness (feature size) decreases (*increases*) as ϕ_+ decreases, for fixed θ, $\theta \gg 1$. A secondary observation is the apparent stabilization of surface slope for certain parameter values [94].

First, we summarize our numerical results for different values of the search radius, R. Figure 5.6 shows the dependence with R of the (a) height-height correlation function, (b) surface roughness, (c) feature size, and (d) surface slope. Although there are trends in each plot, Figures 5.6(b)-(d) express the effect of transient mobility most clearly: Increasing the search radius tends to produce a "smoother" surface

with larger features. Indeed, the exponents for roughening (β) and coarsening (γ) tell a similar story: As R increases from 1 to 5, β decreases from 0.22 to 0.16, and, at the same time, γ increases from about 0.08 to 0.20. The conclusion is that slope stabilization can be achieved for an appropriately chosen value of the search radius; see Figure 5.6(d).

Next, we describe the results of KMC simulations obtained as the factor ϕ_+ varies from 10^{-2} (weak ES barrier) to 10^{-5} (strong ES barrier). Figure 5.7 summarizes our results in two cases: (a) Small and (b) large detachment rate, measured by $k = \exp(-E_N/k_BT)$. In each case, after 100 monolayers of deposition, the largest value of ϕ_+ (smallest ES barrier) corresponds to the largest value of roughness. Upon examining the scaling exponent (Table 5.1), β, we see the largest values are obtained for $\phi_+ = 10^{-2}$, whereas smaller, approximately constant, exponents are found for $\phi_+ \leq 10^{-3}$. This behavior for roughness is somewhat unexpected.

		$\phi_+ = 10^{-2}$	$\phi_+ = 10^{-3}$	$\phi_+ = 10^{-4}$	$\phi_+ = 10^{-5}$
β	$k = 10^{-5}$	0.20	0.18	0.18	0.18
	$k = 10^{-2}$	0.31	0.26	0.25	0.25
γ	$k = 10^{-5}$	0.14	0.17	0.19	0.20
	$k = 10^{-2}$	0.15	0.18	0.18	0.19

Table 5.1: Scaling exponents β and γ obtained from the asymptotic slopes ($\theta \gg 1$) of the curves formed by log-log plots of $w(\theta)$ versus θ and $r_c(\theta)$ versus θ, respectively.

On the other hand, plots of feature size in Figure 5.7 seem to indicate that r_c increases with ϕ_+, i.e. smaller features result from larger ES barriers. Nevertheless, the measured values of the coarsening exponent, γ, shown in Table 5.1, demonstrate that r_c is growing *faster* for smaller ϕ_+ as θ approaches 100 monolayers. Evidently,

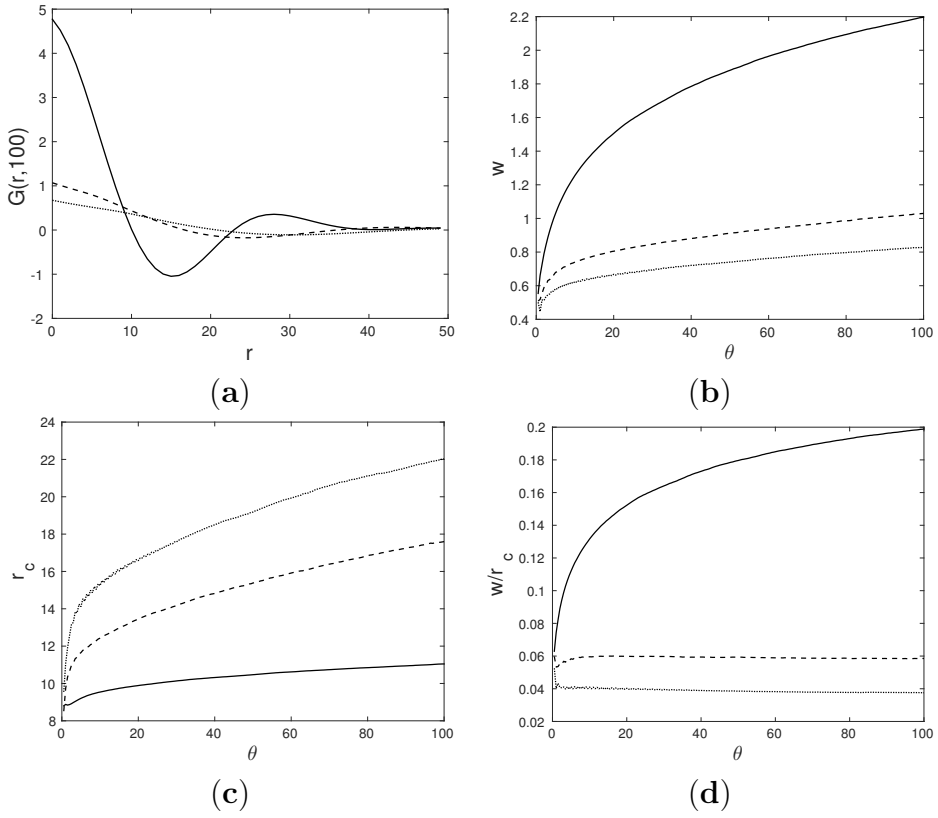

Figure 5.6: Height-height correlation, surface roughness, feature size, and slope in KMC simulations performed on a 500×500 lattice for three values of search parameter: $R = 1$ (solid line), $R = 3$ (dashed line), and $R = 5$ (dotted line). Plots include (a) height-height correlation versus radial distance r at $\theta = 100$; (b) surface roughness versus θ; (c) feature size versus θ; and (d) surface slope versus θ. The common set of parameters used are $F/D = 10^{-6}$, $k = 10^{-5}$, and $\phi_+ = 10^{-5}$. Curves represent the average of 10 independent simulations.

for smaller features, the effect of a fixed search radius R is more pronounced: For fixed $R > 0$, the amount of mass added to island boundaries by the search procedure is *greater* for small islands, relative to their size.

Before concluding our discussion of Figure 5.7, we should comment on the behavior of slope versus θ. For large detachment parameter, the slope is clearly still increasing after 100 monolayers of deposition, which is not the case when the detachment rate is small. Indeed, by inspection of Table 5.1, the difference $\beta - \gamma$ is positive in the former case, and close to zero in the later for all but one case. Hence, slope stabilization occurs in at least some of our simulated cases.

5.3.3 Level set simulations

We now summarize the results of level set simulations including DF and TM, as described in Sections 5.2.1 and 5.2.2. We should warn the reader that the results in this section are extremely limited due to the computational limitations of the legacy level set code[1] used to obtain them. In particular, only three simulations worth of data is available and only small coverages are reached ($\theta \leq 25$ monolayers) for each parameter set. Hence, reliable values of the scaling exponents β and γ have not yet been obtained. Nevertheless, we find it instructive to look at the effect of adjusting the parameter d, the mesoscale distance over which DF or TM is effective. Our data

[1] Christian Ratsch at UCLA provided us with a level set code that implements the island dynamics model described in this chapter. Its main components are outlined in [19], but improvements to the code have been made and additional physics has been added since that paper was published; see Section 5.1.2.

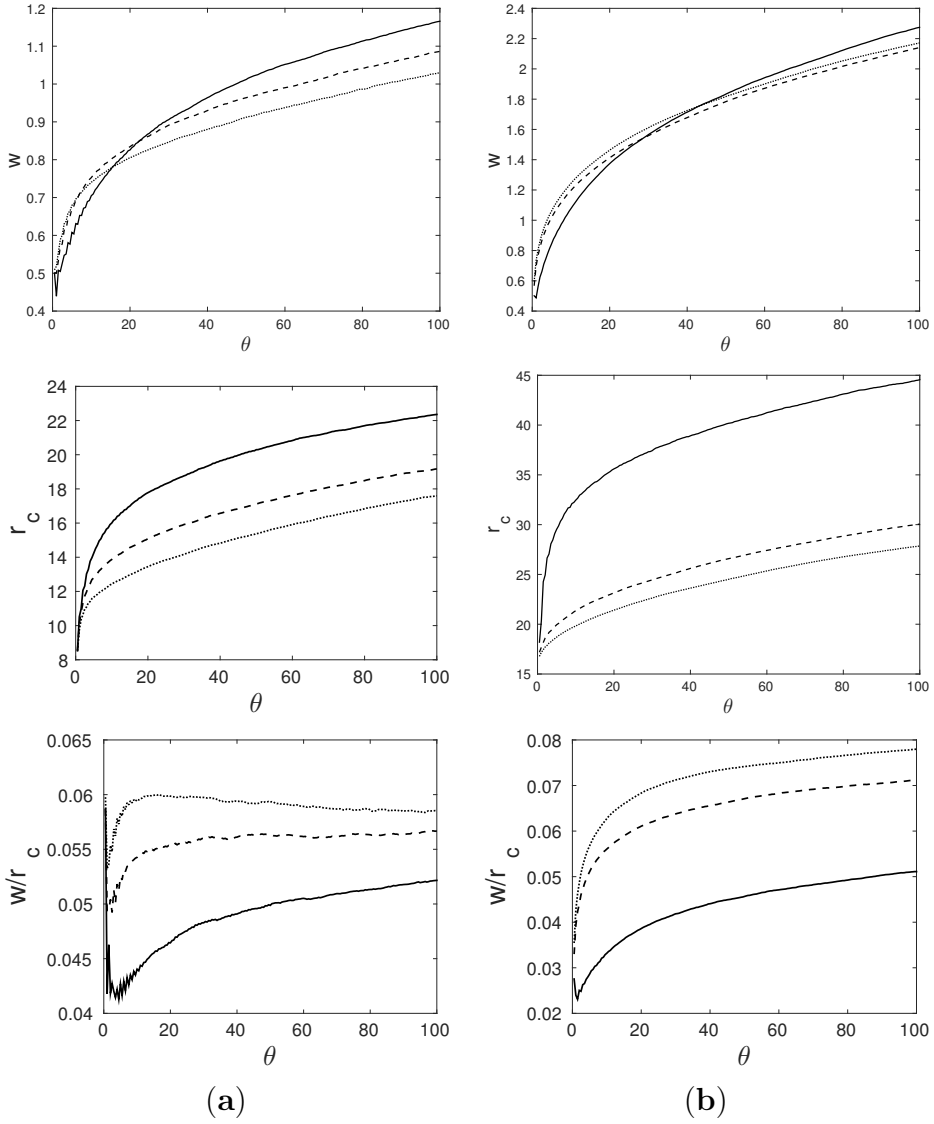

Figure 5.7: Surface roughness, feature size, and slope in KMC simulations performed on a 500×500 lattice for three values of step-edge barrier: $\phi_+ = 10^{-2}$ (solid line), $\phi_+ = 10^{-3}$ (dashed line), and $\phi_+ = 10^{-5}$ (dotted line). Top row: Surface roughness versus θ; Middle row: Feature size versus θ; and bottom row: Surface slope versus θ. The parameters used include $R = 3$, $F/D = 10^{-6}$, and (a) $k = 10^{-5}$ and (b) $k = 10^{-2}$. Curves represent the average of 10 independent simulations.

exhibit the same basic trends as those observed in the KMC simulations from the previous section. In some cases, there are even indications of slope stabilization.

Consider the response of surface evolution to changes in the parameter d. Figure 5.8 illustrates the effect of changing the distance over which DF and TM are active. When increasing d from $\frac{1}{2}a$ to a, the surface roughness decreases for both transport mechanisms. At the same time, increasing d leads to larger features. Thus, larger d yields smaller slopes. The dependence on d of roughness, feature size, and slope in our level set implementation of the island dynamics model is consistent with the R-dependence observed in KMC simulations including TM, shown in Figure 5.6. Additionally, the plots of slope in Figure 5.8 seem to indicate that slope has stabilized in a few cases. Overall, we conclude that there is qualitative agreement between the KMC and level set data when mound evolution is viewed as a function of the effective distance downward transport mechanisms are active.

Lastly, we also find it interesting to compare the two transport mechanisms: (a) DF, which affect deposition on upper terraces near steps, and (b) TM, which affects both upper and lower terraces. Generally speaking, surface roughness is smaller and feature sizes are larger for TM than DF for fixed d since more mass is transported to the step. In turn, surface slopes are smaller for TM, which is expected.

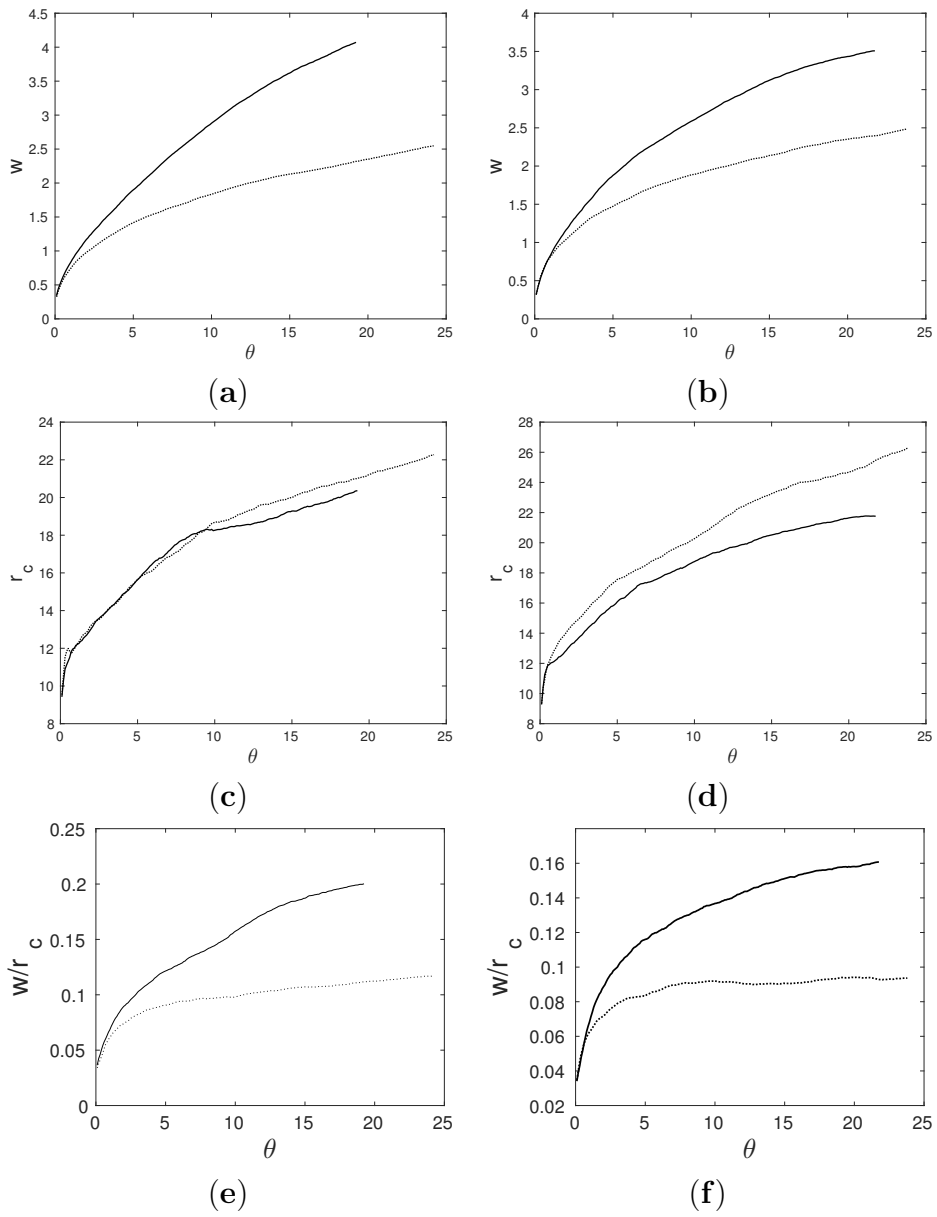

Figure 5.8: Surface roughness, feature size, and slope in LS simulations performed on a 181×181 lattice (256×256 numerical grid) for two values of d: $d = 0.5a$ (solid line), and $d = a$ (dotted line). Plots include (a) and (b) surface roughness versus θ; (c) and (d) feature size versus θ; and (e) and (f) surface slope versus θ. The parameters used include $F/\mathcal{D} = 10^{-6}$, $\mathcal{D}_{\rm det}/\mathcal{D} = 10^{-5}$, and $\mathcal{D}'/\mathcal{D} = \phi_+ = 10^{-2}$ in the case of (a), (c) and (e) downward funneling (upper terraces affected); or (b), (d) and (f) transient mobility (upper and lower terraces affected). Curves are computed from averages of three independent simulations.

5.4 Summary and discussion

In this chapter, we studied the effects of mass transport mechanisms DF and TM in two models that include the ES step-edge barrier. The extent to which these mechanisms alter the external deposition of atoms near step edges, measured by effective distances R (atomistic parameter) and d (mesoscale parameter), was shown to have an inverse relationship with surface roughness, w, and a direct relationship with feature size, r_c, in both atomistic and mesoscale simulations of mound growth. In several cases, the competition between downward transport mechanisms and the ES barrier lead to the stabilization of the average mound slope observed in KMC and level set simulations. This is consistent with previous results of atomistic [94] and mesoscale [46] studies of mound evolution that report "selected" slopes for high enough coverages. Additionally, we were able to describe the effect of increasing the ES barrier (decreasing ϕ_+) in atomistic simulations including TM with fixed R. At this stage, we are unaware of any comparable studies – theoretical, numerical or experimental – describing the change in surface features during mound growth as ϕ_+ varies. It will be interesting, then, if we are able to extend our numerical simulations of the island dynamics model to show similar trends.

Taking a different perspective than the approach of this chapter, which relies heavily on numerical experiments, it would be nice to place this work on firmer theoretical grounds. In particular, it is interesting that TM has not received more attention in the physics or applied mathematics literature. Our primary reference for its inclusion, [94], is one of very few atomistic models that attempt to capture,

even effectively, the initial transient behavior of atoms upon their adsorption to the surface. Moreover, there is quite a bit that can be done to develop SOS-type models of TM. The attractive feature of the model described in Section 5.1.1 is its simple incorporation into existing KMC codes. Still, the "search radius" prescription we have used leaves much to be desired as a model of the effect of TM.

One puzzling aspect is the geometry of the search neighborhood: For a simple cubic lattice, an adatom placed in the center of a square of side length $2R + 1$ as in Figure 5.3(b) can reach the boundary of the search region in R hopping events, yet requires a minimum of $2R$ hopping events to reach a corner of the square. It might be more realistic, for example, to define the search neighborhood based on the expected number of hopping events a freshly deposited atom undergoes prior to thermalization. This prescription is no more complex than the original. Going one step further, it is not at all unreasonable to track "hot" adatoms in a KMC simulation and assign them special hopping rates, which may even be time-dependent. Be that as it may, it is likely that other models or numerical methods, e.g. molecular dynamics (MD), would be better suited to describe TM. It is already common practice to study the deposition process via MD [112,113], so it is a good candidate for future investigations of TM.

Chapter 6: Decay of a faceted crystal structure

In this chapter, we propose a method of incorporating the motion of facets into a continuum thermodynamics framework that is consistent with a mesoscale BCF description of the surface. At the mesoscale, crystal surface evolution is driven by the motion of many atomically thick steps. At the macroscale, a PDE for the surface height outside the facet offers a plausible description, whereas physically relevant solutions to this PDE have singular behavior near the facet edge. We reconcile these two scales by imposing a step-driven discontinuity of the surface chemical potential across the facet edge, modifying the previously applied notion of a continuous chemical potential. We focus on an idealized model: a semi-infinite axisymmetric structure with a single facet in the absence of external material deposition or desorption. We study long-time surface relaxation, when the surface slope profile exhibits self-similarity.

At the macroscale, a PDE for the surface height profile the crystal structure we consider can be formulated using continuum thermodynamic principles away from the facet, which is a singularity of the surface free energy. To form a well-posed model, the facet may be treated as a free boundary [96]. "Natural" boundary conditions at the facet edge result from a variational interpretation of evolution;

the large-scale surface height, slope, step chemical potential and adatom flux are continuous across the facet edge [50, 64, 91, 96]. This view is not consistent with the motion of steps [51]. Inspired by work on an evaporation model [63], we consider a modified set of boundary conditions at the facet involving jump-discontinuities in the continuum-scale step chemical potential and the flux generating it [86]. In [63], the evolution PDE away from the facet is of second order; and the jump is introduced only for the generating flux of chemical potential. Here, the evolution PDE is of fourth order [50, 96, 110].

In this work, we empirically determine jump factors to be included in boundary conditions at the facet. These "jump" boundary conditions are shown to produce good agreement between the continuum PDE and results of many-step simulations when the factors are determined from the geometry of top steps of step simulations. Based on this observation, we develop a hybrid computational scheme that couples the continuous height profile to the motion of a few steps through our jump boundary conditions at the facet [86]. The coupled discrete-continuum computational scheme developed here offers an advantage over previous, related approaches, e.g. [34, 35, 50, 51, 96]. For example, in [50, 96] only natural boundary conditions are considered; and in [34, 35, 51] the entire many-step system is simulated. It is also worth noting that this approach bears resemblence with other multiscale methods, e.g. [10, 102, 108, 109], but is tailored to our specific problem and not expected to be widely applicable.

Our approach can be summarized as follows: (a) We empirically construct a global, macroscopic surface chemical potential, μ, that expresses (i) changes of the

continuum-scale free energy of many steps away from the facet and (ii) the annihilation of individual atomic steps on the facet. These distinct physical characterizations of μ must suitably be connected across the facet edge. To this end, we propose a jump condition that accounts for details inside a narrow region of a few steps, herein called the discrete boundary layer, near the facet. (b) We formulate a continuum theory outside the facet that implicitly accounts for the discrete boundary layer. The resulting free boundary problem for the facet consists of (i) a continuum equation for the self-similar surface slope away from the facet and (ii) boundary conditions by which the large-scale surface chemical potential and a flux generating it are forced to have jump discontinuities at the facet edge. For validation, we formulate and implement a computational scheme, henceforth referred to as the "hybrid scheme", to approximately solve our free boundary problem without resolving the full step system. As the time, t, advances, our scheme successively improves the slope profile through the solution of discrete equations for a few steps inside the boundary layer. We show by numerics that our scheme apparently converges to the surface slope profile computed via independent many-step simulations.

From a physical perspective, our approach exemplifies the key role of the surface chemical potential, μ, in reconciling two seemingly disparate notions: (i) the facet, a macroscopic object, and (ii) the (discrete) step. Our work indicates that the facet and the bulk of steps away from it can be treated as two distinct "phases" connected through an unusual jump condition for μ. The magnitude of this jump depends on the continuum surface profile and the curvatures of individual steps in the discrete boundary layer; this layer represents the microstructure of the interface

between the two phases.

6.1 Review of the BCF model for 2D steps

If we neglect step edge diffusion and evaporation, and assume that no material is deposited on the surface from above, the concentration $\mathcal{C}(\mathbf{r}, t)$ of adatoms on terraces obeys

$$\partial \mathcal{C}/\partial t = \nabla \cdot (D_{\rm s} \nabla \mathcal{C}) \ , \tag{6.1}$$

where $D_{\rm s}$ is the (constant for our purposes) terrace diffusivity. It is common in BCF formulations to assume adatom diffusion equilibrates quickly relative to step motion, so that $\partial \mathcal{C}/\partial t \approx 0$; in this case equation (6.1) is said to be *quasistatic*.

At the step, we impose the linear kinetic relations [36]

$$J_{\pm,\perp} = \kappa_{\pm}(\mathcal{C}_{\pm} - \mathcal{C}^{\rm eq}) \ . \tag{6.2}$$

Here, $J_{\pm,\perp}$ is the normal component of the adatom flux $\mathbf{J}_{\pm} = -D_{\rm s}\nabla\mathcal{C}$ on the upper $(+)$ or lower $(-)$ terrace, directed toward the step; $\kappa_{\pm}$ is the respective rate of attachment-detachment due to the Ehrlich-Schwoebel barrier [24,88]; $\mathcal{C}_{\pm}$ is the value of the adatom concentration at the step on the corresponding terrace; and $\mathcal{C}^{eq}$ is the equilibrium concentration at the step. For the diffusion-limited kinetics considered here, the diffusion length $D_{\rm s}/(\kappa_{\pm})$ should be small compared to a typical terrace width.

Equations (6.1) and (6.2) are linked to step energetics via the thermodynamics-

based formula [36]

$$\mathcal{C}^{\rm eq} = c_{\rm s}\,\exp\left(\frac{\mu_{\rm st}}{k_BT}\right) \approx c_s\left(1+\frac{\mu_{\rm st}}{k_BT}\right)\ , \tag{6.3}$$

where $\mu_{\rm st}$ is the step chemical potential, $c_{\rm s}$ is a constant concentration, and k_BT is the Boltzmann energy; $|\mu_{\rm st}| \ll k_BT$. If $U_{\rm st}$ is the step free energy per unit length, including step-step interactions, $\mu_{\rm st}$ is given by [52]

$$\mu_{\rm st} = \frac{\Omega}{a}\,\nabla\cdot(U_{\rm st}\,\mathbf{e}_\eta)\ , \qquad \eta = \eta_{\rm st}\ , \tag{6.4}$$

and thus may depend on the step configuration via $U_{\rm st}$. Here, Ω is atomic volume, a is step height, and step edge is described by $\eta = \eta_{\rm st}$ in a curvilinear coordinate system, say (η, ς), with unit normal vector $\mathbf{e}_\eta$; $U_{\rm st} = U(\eta, \varsigma)$. Note that if $U = \beta$, a constant step line tension, Eq. (6.4) yields $\mu_{\rm st} = (\Omega/a)\beta\,\kappa_{\rm st}$ where $\kappa_{\rm st}$ denotes the local step edge curvature [36, 74].

By mass conservation, the normal step velocity is [36]

$$v = \frac{\Omega}{a}(J_{+,\perp} + J_{-,\perp})\ . \tag{6.5}$$

Equations (6.1)–(6.5) describe the motion of step positions for prescribed initial data; the energy $U_{\rm st}$ is considered as known.

6.2 Continuum description of evolution

Next, for a monotone step train and diffusion-limited kinetics, we outline elements of the continuum theory away from the facet, in correspondence to the step flow description of Sec. 6.1. In the continuum limit, a/L approaches zero while the step density is kept fixed, where L is a typical macroscopic length.

First, the step velocity, v, approaches $|\nabla h|^{-1}\frac{\partial h}{\partial t}$ [52]. Accordingly, step motion law (6.5) becomes a mass conservation statement, viz.,

$$\frac{\partial h}{\partial t} + \Omega \nabla \cdot \mathbf{j} = 0 \ , \tag{6.6}$$

where $\mathbf{j}(\mathbf{r}, t)$ is the continuum-scale adatom mass flux.

Second, Eqs. (6.1)–(6.3) give rise to a constitutive relation between the flux, $\mathbf{j}(\mathbf{r}, t)$, and the macroscale step chemical potential, $\mu(\mathbf{r}, t)$ [52]:

$$\mathbf{j}(\mathbf{r}, t) = -\frac{c_s D_s}{k_B T}\mathbf{M} \cdot \nabla \mu \ , \tag{6.7}$$

where $\mathbf{M}$ is an orientation-dependent (dimensionless) tensor "mobility". For diffusion-limited kinetics, $\mathbf{M} = 1$, the unit tensor [45].

Third, by Eq. (6.4) the chemical potential μ is the variational derivative of the surface free energy, $E[h]$, the continuum limit of $aU_{\rm st}$ [52]:

$$\mu = \Omega \, \frac{\delta E}{\delta h} \ , \tag{6.8}$$

provided the variational derivative is well defined. Equation (6.8) expresses a thermodynamic principle. For entropic and force-dipole step-step interactions, the $E[h]$ of a vicinal surface reads [31, 52]

$$E[h] = \iint \left(g_0 + g_1 |\nabla h| + \frac{1}{3} g_3 |\nabla h|^3 \right) \, dS, \tag{6.9}$$

where g_0 is the energy per area of the (x, y)-reference plane, $g_1 a = \beta$, g_3 accounts for repulsive step-step interactions, $g_3 > 0$, and $dS = dx\, dy$. Note that, for this free energy, $\delta E[h]/\delta h$ is ill defined at surface regions where $\nabla h = 0$, which correspond to facets in this formulation (see Sec. 6.2.1). The variable μ is computed as

$$\mu = \Omega g_1 \nabla \cdot \boldsymbol{\xi} \ , \tag{6.10}$$

where

$$\boldsymbol{\xi} = -\left(1 + g|\nabla h|^2\right) \frac{\nabla h}{|\nabla h|} \ , \quad \mathbf{r}: \text{ outside the facet} \ , \tag{6.11}$$

and $g = g_3/g_1$ expresses the relative strength of step-step interactions and line tension; see also [63].

The combination of Eqs. (6.6), (6.7) and (6.10) with $\mathbf{M} = 1$, for diffusion-limited kinetics, yields a fourth-order PDE for the height profile, $h(\mathbf{r}, t)$, away from facets:

$$\frac{1}{B}\frac{\partial h}{\partial t} = -\nabla^2 \left(\nabla \cdot \boldsymbol{\xi}\right) \ . \tag{6.12}$$

Here, $\boldsymbol{\xi}$ is defined by Eq. (6.11) and $B = c_s D_s \Omega^2 g_1/(k_B T)$ is a material parameter [45].

6.2.1 Facet as a free boundary

We now discuss some aspects of the free-boundary point of view for a faceted structure. As is indicated in Sec. 6.3.3, the facet, where $\nabla h = 0$, is a singularity of PDE (6.12) with (6.11)). This difficulty can be systematically overcome using the subgradient formulation [30, 37, 42, 64], which is consistent with Spohn's approach [96] and the application of Fourier series expansions [91]. Accordingly, PDE (6.12) is extended *everywhere* to the whole domain; then, $\boldsymbol{\xi}$ must be appropriately defined on the facet. A mathematically plausible extension follows from the variational property that relaxation occurs as the steepest descent of the free energy, $E[h]$. This approach implies a prescription for a free boundary problem [96]: Apply PDE (6.12) away from the facet and ensuing, natural boundary conditions at the

facet edge that include: (i) continuity of surface height; (ii) continuity of positive slope, $|\nabla h|$; (iii) continuity of adatom flux; and (iv) continuity of step chemical potential. Consequently, the component of $\boldsymbol{\xi}$ normal to the facet edge is continuous. In addition, "far-field" conditions on a semi-infinite structure require that the height and positive slope approach their initial data far from the facet.

It has been demonstrated by simulations of a faceted axisymmetric crystal structure under diffusion-limited kinetics that the continuum solution determined through natural boundary conditions is not consistent with step motion [51]. For an analogous result in evaporation kinetics, see [63]. Therefore, the facet should be viewed as a special region where discrete effects, especially collapses of extremal steps, are significant, dramatically influencing the large-scale surface morphology [35].

To reconcile the discrepancy between predictions of the continuum model using natural boundary conditions and step simulations, in [51] the continuity of the continuum-scale step chemical potential, μ, is replaced by the step-drop condition, inspired by [35]. This latter condition requires that the facet height, $h_{\rm f}(t)$, decrease in increments of a single atomic height for each step collapse:

$$h_{\rm f}(t_{n+1}) - h_{\rm f}(t_n) = -a \ , \tag{6.13}$$

where t_n is the nth-step collapse time. Equation (6.13) can be viewed as a discrete derivative of $h_{\rm f}(t)$, $t \approx t_n$, and is approximately reduced to

$$\dot{h}_{\rm f} \approx -\frac{a}{\delta t(t)} \ , \quad \delta t(t) = t_{n+1} - t_n \ , \tag{6.14}$$

which imposes a vertical facet speed, given $\delta t(t)$ [51].

Condition (6.14) reveals a nonlocal coupling of facet motion with the surface profile through step flow; the value of $\delta t(t)$ in principle depends on the dynamics of the many-step system. This relation leads to predictions consistent with steps [51]; however, it is deemed as impractical for computation of large-scale surface morphologies. First, obtaining $\delta(t)$ requires simulations of a large number of steps. Second, Eq. (6.14) leads to a boundary condition sensitive to any errors in $\delta t(t)$.

An alternative to the step-drop condition was introduced in [63] for an evaporation model in a radial geometry. In that setting, crystal height evolves accord to second order PDE $\partial h/\partial t = -\nu\Omega g_1 \nabla \cdot \boldsymbol{\xi}$; ν is a material parameter. Then, the natural boundary conditions consist of continuity of height, slope, and flux variable $\boldsymbol{\xi}$ if $g_3 > 0$ [cf. Eqs. (6.10) and (6.11)]. The resulting free-boundary problem in principle yields predictions not consistent with step flow [63]. Instead of the use of the step-drop condition, the radial $\boldsymbol{\xi}$ in [63] is allowed to have a jump discontinuity at the facet edge [63]. The continuity of height and slope are left intact. Specifically, in axisymmetry, if $\xi_{\mathrm{f}}(r,t)$ is a quantity corresponding to the radial component of $\boldsymbol{\xi}$ on the facet and $r_{\mathrm{f}}(t)$ is the facet radius, the jump condition reads

$$\xi_{\mathrm{f}}(r,t)\big|_{r_{\mathrm{f}}^{-}(t)} = Q(t)\,\xi(r,t)\big|_{r_{\mathrm{f}}^{+}(t)}\,, \tag{6.15}$$

where $r_{\mathrm{f}}^{\pm}$ indicates a limit from outside $(+)$ or inside $(-)$ the facet, and $Q(t)$ represents a piecewise-constant multiplicative jump depending on the radii of two extremal steps at collapse times. If $r_i(t)$ is the ith step radius, $Q(t) = [r_{n+1}(t_{n-1}) + r_n(t_{n-1})]/[2r_{n+1}(t_{n-1})]$ for $t_{n-1} \le t < t_n$ is the geometric factor applied in boundary condition (6.15) that resulted in a continuum formulation consistent with step flow

simulations [63].

It may be argued that this formulation is not essentially different from applying the step-drop condition, since both approaches inject information about the nature of step collapses into the continuum setting. However, we believe that introducing jumps in thermodynamic quantities such as the step chemical potential offers at least two important advantages. First, from a physical viewpoint, this approach retains the thermodynamic structure of the boundary conditions at the facet edge. Second, the jump condition appears less sensitive to errors in the step collapse times; thus, it may be a viable candidate for a tractable computational scheme.

A common difficulty in the implementation of either Eq. (6.15) or the step drop condition (6.13) is the need for simulating a large number of particles via step flow. The hybrid discrete-continuum scheme presented in section 6.3 leverages the advantages of a thermodynamics-based formulation like the one in [63], while at the same time substantially reducing the number of steps which must be simulated.

6.3 Formulation

We now specialize our geometry to axisymmetric crystal shapes. Furthermore, we consider a regime where surface diffusion is the dominant mass transport mechanism, neglect any external flux of adatoms, and assume everywhere isotropic surface diffusivity. In this section, we first describe the geometry of the micro- and macroscale, provide respective equations of motion, and discuss potential boundary conditions for the continuum model in two cases: (i) a reference case employing

natural boundary conditions, and (ii) jump boundary conditions motivated by the use of (6.15) in [63]. Specifically, we give the empirically derived jump boundary conditions in both $xi(r,t)$ and $\mu(r,t)$ that are essential to the formulation of a hybrid scheme for computing the slope profile of the crystal. Finally, we outline the hybrid approach we employ in section 6.4.3.

6.3.1 Geometry

At the macroscale, the continuous crystal surface is represented by its height $h(r,t)$ as a function of radial position r and time. The facet, which has a fixed orientation of zero slope, is described by height $h_{\mathrm{f}}(t)$ and radius $r_{\mathrm{f}}(t)$, which tend to decrease and increase, respectively, in time.

At the mesoscale, the crystal consists of $N \gg 1$ layers of concentric circular steps of atomic height a and radii $\{r_i(t)\}_{i=1}^{N}$. We define the ith terrace as $r_i < r < r_{i+1}$. Through step flow, the top step of the structure, beginning with r_1, tends to decrease its radius monotonically to zero and collapse under the effects of line tension. We denote by t_n the nth collapse time: the smallest time t for which $r_1(t) = r_2(t) = \cdots = r_n(t) = 0$ and $r_{n+1}(t) > 0$. With steps acting as repulsive force-dipoles, preventing crossings, the discrete slope

$$m_i(t) = \frac{a}{r_{i+1}(t) - r_i(t)} \tag{6.16}$$

is positive for all $n \leq i \leq N-1$ and $t < t_n$.

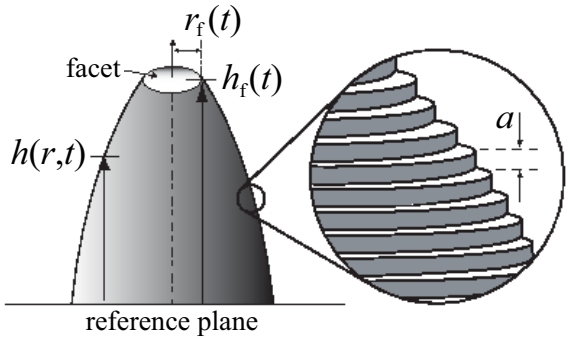

Figure 6.1: Geometry of axisymmetric crystal at macroscale (left) and mesoscale (right). The macroscale crystal height is $h(r,t)$ for polar coordinate r. The facet height and radius are $h_f(t)$ and $r_f(t)$, respectively. a is the mesoscale step height.

6.3.2 Mesoscale equations of motion

If the concentration of adatoms on the ith terrace is $C_i(r,t)$ then (6.1) can be written as

$$\frac{\partial C_i}{\partial t} = D_s \frac{1}{r}\frac{\partial}{\partial r}\left(r\frac{\partial C_i}{\partial r}\right), \quad r_i < r < r_{i+1}. \tag{6.17}$$

Using the quasistatic approximation, $C_i(r,t)$ satisfies the Laplace equation on the ith terrace, which in radial geometry has solution

$$C_i(r,t) = A_i(t)\ln(r) + B_i(t), \quad r_i < r < r_{i+1}. \tag{6.18}$$

If we denote J_i as the outward adatom flux on the ith terrace, using Fick's law $J_i = -D_s \left.\frac{\partial C_i}{\partial r}\right|_{r=r_i}$ the boundary conditions (6.2) are

$$D_s\frac{\partial C_i}{\partial r} = J_i = \kappa_+\left[C_i - C_i^{eq}\right], \quad r = r_i \tag{6.19a}$$

$$-D_s\frac{\partial C_i}{\partial r} = J_i = \kappa_-\left[C_i - C_{i+1}^{eq}\right], \quad r = r_{i+1}, \tag{6.19b}$$

where $\kappa_+(\kappa_-)$ is the kinetic rate of attachment-detachment at the up-step(down-step) edge and C_i^{eq} is the equilibrium concentration at the ith step, which is related to the step chemical potential through (6.3). Applying (6.19) to (6.18) and substituting (6.3), the resulting flux on the ith terrace is

$$J_i(r,t) = -\frac{D_s c_s}{k_B T}\frac{1}{r}\frac{\mu_{i+1}-\mu_i}{\ln\frac{r_{i+1}}{r_i}}, \tag{6.20}$$

assuming diffusion-limited kinetics, when $D_s/[\kappa_\pm(r_{i+1}-r_i)] \ll 1$.

The step chemical potential $\mu_i(r,t)$ is defined as the change in free energy associated with adding or removing an adatom to or from the ith step edge [36]. The total free energy is [50]

$$E_N = a\sum_i 2\pi r_i(t)\left[g_1 + g_3 V(r_i, r_{i+1})\right], \tag{6.21}$$

where $g_1 a$ is step line tension, $g_3 a$ is the strength of elastic dipole nearest-neighbor step interactions, and step-step interactions are determined by

$$V(r_i, r_{i+1}) = \frac{1}{3}\frac{2r_{i+1}}{r_{i+1}+r_i}\left(\frac{a}{r_{i+1}-r_i}\right)^2. \tag{6.22}$$

From (6.21) we calculate the step chemical potential by

$$\begin{aligned}\mu_i(r,t) &= \frac{\Omega}{a}\frac{1}{2\pi r_i}\frac{\partial E_N}{\partial r_i} \\ &= \frac{\Omega g_1}{r_i}\left\{1 + g\Phi_{i-1,i,i+1}\right\},\end{aligned} \tag{6.23}$$

where the (dimensionless) interaction term $\Phi_{i-1,i,i+1}$ is

$$\Phi_{i-1,i,i+1} = \frac{\partial\left[r_i V(r_i, r_{i+1}) + r_{i-1}V(r_{i-1}, r_i)\right]}{\partial r_i}. \tag{6.24}$$

Using (6.23) and (6.24), the discrete flux (6.20) can be expressed in terms of step radii $\{r_i(t)\}$.

It remains to express the ith step velocity, $v_i = \dot{r}_i = dr/dt$, in terms of step radii, $\{r_i(t)\}$, for $t_n \le t \le t_{n+1}$. Equation (6.5) and flux (6.20) result in a system of ODEs

$$\dot{r}_i = \frac{\Omega}{a}\left[J_{i-1}(r_i,t) - J_i(r_i,t)\right] \tag{6.25}$$

$$= \frac{c_s D_s \Omega}{k_B T}\frac{1}{a r_i}\left[\frac{\mu_{i+1}-\mu_i}{\ln\frac{r_{i+1}}{r_i}} - \frac{\mu_i - \mu_{i-1}}{\ln\frac{r_i}{r_{i-1}}}\right], \tag{6.26}$$

for $i \ge n+3$. The above equation must be modified when $i = n+1, n+2$ since these steps have fewer neighbors; in particular the second term in equation (6.25) is identically zero if $i = n+1$. In Section 6.4 we solve ODEs (6.25) subject to linear initial data $r_i(0) = i/N$, $1 \le i \le N$.

6.3.3 Macroscopic equations of motion

We now describe the macroscopic free boundary problem and natural boundary coditions. Later, in section 6.4.2, we numerically demonstrate that this formulation is not consistent with step flow [51]. In axisymmetric geometry, the PDE (6.12) becomes

$$\frac{1}{B}\frac{\partial h}{\partial t} = \frac{1}{r^3} + g\frac{1}{r}\frac{\partial}{\partial r} r \frac{\partial}{\partial r}\frac{1}{r}\frac{\partial}{\partial r}\left(r m^2\right), \quad r > r_{\mathrm{f}}(t), \tag{6.27}$$

where $m(r,t) = |\partial h(r,t)/\partial r|$ is positive surface slope. Differentiating both sides with respect to r, equation (6.27) may be expressed as a PDE for m:

$$\frac{1}{B}\frac{\partial m}{\partial t} = \frac{3}{r^4} - g\frac{\partial}{\partial r}\frac{1}{r}\frac{\partial}{\partial r} r \frac{\partial}{\partial r}\frac{1}{r}\frac{\partial}{\partial r}\left(r m^2\right), \tag{6.28}$$

which is valid away from the facet.

The boundary conditions for (6.28) include two conditions at infinity in addition to five conditions at the facet edge: continuity of (i) slope, (ii) height, (iii) flux, (iv) chemical potential, and (v) the variable

$$\boldsymbol{\xi} = \xi \mathbf{e}_r, \quad \xi = 1 + gm^2. \tag{6.29}$$

Note that (v) is needed to account for a time-dependent constant of integration, $b(t)$ which is ultimately eliminated in the final implementation. The seven boundary conditions are

$$m \to 1, \text{ and } \partial_r m \to 0 \text{ as } r \to \infty; \tag{6.30}$$

$$m(r_{\mathrm{f}}, t) = 0; \tag{6.31}$$

$$\frac{r_{\mathrm{f}}^3 \dot{h}_{\mathrm{f}}}{B} = 1 + g r_{\mathrm{f}} \left[-\partial_r m^2 + 2 r_{\mathrm{f}} \partial_r^2 m^2 + r_{\mathrm{f}}^2 \partial_r^3 m^2 \right] \big|_{r=r_{\mathrm{f}}}; \tag{6.32}$$

$$\frac{r_{\mathrm{f}}^3 \dot{h}_{\mathrm{f}}}{2B} = 1 + g r_{\mathrm{f}} \left[\partial_r m^2 + r_{\mathrm{f}} \partial_r^2 m^2 \right] \big|_{r=r_{\mathrm{f}}}; \tag{6.33}$$

$$\frac{1}{4B} \left(r_{\mathrm{f}}^3 \dot{h}_{\mathrm{f}} + r_{\mathrm{f}} b(t) \right) = 1 + g r_{\mathrm{f}} \, \partial_r m^2 \big|_{r=r_{\mathrm{f}}}; \tag{6.34}$$

$$\frac{1}{16B} \left(r_{\mathrm{f}}^3 \dot{h}_{\mathrm{f}} + 2 r_{\mathrm{f}} b(t) \right) = 1. \tag{6.35}$$

The details of the formulation of these conditions can be found in [50, 86]. In particular, (6.34) and (6.35) are found by extending μ and ξ *continuously* onto the facet by matching $\mu(r_{\mathrm{f}}^+, t)$ and $\xi(r_{\mathrm{f}}^+, t)$ (outside the facet) with

$$\mu_{\mathrm{f}} = \frac{\Omega g_1}{4B} \left(r^2 \dot{h}_{\mathrm{f}} + b(t) \right), \quad r < r_{\mathrm{f}}(t), \tag{6.36}$$

$$\xi_{\mathrm{f}} = \frac{1}{16B} \left(r^3 \dot{h}_{\mathrm{f}} + 2 r b(t) \right), \quad r < r_{\mathrm{f}}(t). \tag{6.37}$$

The PDE (6.28) along with boundary conditions (6.30)–(6.35) constitute our continuum model with *natural* boundary conditions.

6.3.3.1 Jump boundary conditions

Next, we relax the assumption of continuity in the chemical potential and the function ξ at the facet edge to accommodate a chemical potential on the facet which is distinct from the step chemical potential [86]. By introducing multiplicative jumps $Q_\mu(t)$ and $Q_\xi(t)$ into equations (6.34) and (6.35), respectively, we consider the more general boundary conditions

$$\frac{1}{4B}\left(r_{\mathrm{f}}^3\dot{h}_{\mathrm{f}} + r_{\mathrm{f}}b(t)\right) = Q_\mu(t)\left(1 + gr_{\mathrm{f}}\,\partial_r m^2\big|_{r=r_{\mathrm{f}}}\right), \tag{6.38}$$

$$\frac{1}{16B}\left(r_{\mathrm{f}}^3\dot{h}_{\mathrm{f}} + 2r_{\mathrm{f}}b(t)\right) = Q_\xi(t). \tag{6.39}$$

The jump factors included here allow for higher (lower) values of μ or ξ coming from outside the facet when $Q_\alpha > 1$ ($Q_\alpha < 1$), $\alpha = \mu, \xi$. Note that $Q_\mu = 1 = Q_\xi$ corresponds to continuity of μ and ξ. Our continuum model with *jump* boundary conditions consists of PDE (6.28) and conditions (6.30)–(6.33),(6.38),(6.39).

Later, in section 6.4, we compare the numerical solution of the continuum model with natural boundary conditions to the results of step simulations, which are known to disagree when the parameter g is small [51]. Using the modified boundary conditions (6.38) and (6.39), on the other hand, we show good agreement with step simulations when $Q_\mu(t)$ and $Q_\xi(t)$ are computed from a discrete factor involving the top steps in the discrete model. Consider the quantity

$$\mathcal{Q}_i(t; g) = \frac{1}{2}\left(\frac{r_{i+1} + r_i}{2r_{i+1}} + \frac{r_i + r_{i-1}}{2r_i}\right), \tag{6.40}$$

which depends on the geometry of the $(i-1)$th, ith, and $(i+1)$th steps. The values of jump $Q_\mu(t)$ and $Q_\xi(t)$ that result in agreement between macroscopic and

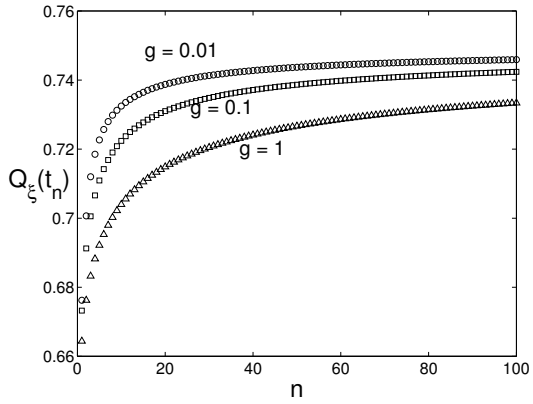

Figure 6.2: Step simulation data for values of piecewise constant jump factor $Q_\xi(t) = Q_\xi(t; g)$ in intervals $t_n \leq t \leq t_{n+1}$ as a function of collapse number, n. Circles represent data for weak step interaction, $g = 0.01$; squares represent $g = 0.1$; and triangles $g = 1$.

microscopic models are

$$Q_\mu := \mathcal{Q}_{n+1}^{-1}(t_n; g), \text{ and} \tag{6.41a}$$

$$Q_\xi := \mathcal{Q}_{n+1}(t_n; g), \tag{6.41b}$$

calculated at collapse times t_n, $n \gg 1$ [86]. Figure 6.2 shows the behavior of the jump factor corresponding to Q_ξ, from which we conclude that the jumps (6.41) approach constant values when $n \gg 1$.

It is important to note that the choice of jumps boundary conditions (6.38) and (6.39) as well as the jump factors in equations (6.40) and (6.41) are entirely *empirical*. While the jump described in the evaporation-condensation model of [63] could be attributed to a discrete factor appearing explicitly in the step ODEs in that case, there is no such discrete factor appearing in the step ODEs in the case of surface diffusion, i.e. (6.25). Therefore we insert an empirically chosen jump

factor in one boundary condition, and "compensate" with its reciprocal in another boundary condition, resulting in the jump formulation we describe above.

6.3.4 Hybrid two-scale approach

In principle, the application of jumps (6.41) in boundary conditions (6.38)-(6.39) requires the simulation of a large number of steps, which a good continuum theory hopes to avoid. To practically apply the jump formulation outlined in section 6.3.3.1, then, it would be convenient if we could estimate the g-dependent jumps without having to simulate a full system of steps. In this section we describe a hybrid discrete-continuum numerical scheme that allows us to estimate jumps from a reduced step system and solutions to the continuum model with natural boundary conditions.

Two important features of the jump boundary conditions described in the previous section are (i) that the jumps (6.41) seem to approach a g-dependent constant after many steps collapses (see Figure 6.2), and (ii) that they depend only on a small number of steps in the mesoscale model. These features are critical to our hybrid approach. In particular, if (ii) were not true and our jump factors had a global dependence on step positions, we would be forced to solve the full step system.

Another aspect of our continuum model that is key to formulating our hybrid scheme is the "far-field" boundary condition (6.30), i.e. conditions on the continuum slope profile at infinity. Far from the facet we expect the slope profile to resemble

initial data in both the mesoscale and macroscale settings. Leveraging this fact, we seek to simulate only a small number of steps near the facet, but utilize a continuum slope profile away from the facet. In this way, a hybrid discrete-continuum approach could enable us to estimate the jumps Q_μ and Q_ξ, by simulating $M \ll N$ steps. Later in section 6.4 we provide examples for various values of g using $M = 3$ steps in the reduced system and $N = 1000$ steps in the full step system.

Keeping the above elements in mind, an outline of our hybrid scheme is as follows: Starting from linear initial data, $r_i(0) = i/N$, $i = 1, ..., M$, we solve the step odes (6.25) for the first M steps only. In a full step flow simulation these steps are coupled to the motion of $r_i(t)$, $i \geq M + 1$, not captured by the hybrid scheme. Instead, we supply the positions of r_{M+1} and r_{M+2} through a relation based on the formula for discrete slope, equation (6.16):

$$r_{i+1}(t) \approx r_i(t) + \frac{a}{m\left(r_i(t), t\right)}. \tag{6.42}$$

In this relation, m is the continuum solution of the PDE (6.28) and t is the "continuous" time in the step solver.

By coupling the solution of (6.28) with the motion of a few "virtual" steps, iterations of our hybrid scheme can then be described by:

1. Compute $m(r, t)$ using the formulation outlined in section 6.3.3; using natural boundary conditions.

2. Simulate $M \ll N$ step ODEs (6.25) in the discrete boundary layer until one or more steps collapse; after each collapse, the first virtual step is added to step

simulations. The M step ODEs are always coupled to the continuum slope profile using virtual steps and equation (6.42).

3. Re-compute $m(r,t)$ using jump boundary conditions (6.38) and (6.39), where Q_μ and Q_ξ are estimated from the reduced step system.

4. Repeat steps 2 and 3 for several iterations.

Note that, in practice, we allow 4 steps to collapse in step 2 for the first iteration of this scheme before moving on to step 3, and each subsequent iteration only requires 1 step collapse.

So far, it has not been possible to predict *a priori* the number of iterations for our hybrid scheme to "converge". Issues of error estimation and convergence are known to be somewhat dubious in multiscale modeling and analysis (see, for example, [108, 109] for discussions of error estimation in multiscale schemes), and these issues are not pursued in this thesis. Later, in section 6.4.3, we show that the above outlined hybrid scheme produces a continuum solution in good agreement with simulations of the large step systems, and provide the *a posteriori* error found in a few cases.

6.4 Simulation results

In this section we give the details of our numerical simulations of the relaxation of an initial crystal cone at both the discrete and continuum scales. Specifically, we solve the step ODEs (6.25) and the PDE (6.28) subject to (i) natural

boundary conditions (6.30)–(6.35), and (ii) modified boundary conditions (6.30)–(6.33),(6.38),(6.39). After comparing the solutions of both continuum models to step simulations, we go on to present the results of our hybrid discrete-continuum approach.

6.4.1 Self-similarity

Starting from linear (conical) initial data $r_i(0) = i/N$, $i = 1, 2, \ldots, N$, integrate numerically the step ODEs (6.25). If $g > 0$, i.e. steps interact repulsively, and are not expected to cross. Therefore, step motion may be simulated for all time $t > 0$, and the discrete slopes $m_i = a/(r_{i+1} - r_i)$, $i = n + 1, \ldots N - 1$, calculated at collapse times $t = t_n$, remain bounded (that is, we do not observe finite time blow up). In Figure 6.3, we compare plots of discrete slopes versus r_i (inset) and $r_i/t^{1/4}$ at $t = t_n$, $1 \ll n \ll N$, for various n. This shows a collapse of data points onto a single curve in this scaling, indicating self-similarity. The same self-similar behavior is observed in step collapse times, which follow the scaling law $t_n \sim t^* n^4$ for $n \gg 1$ [35, 51]; see Figure 6.4.

Motivated by discrete self-similarity, we *assume* there exist self-similar solutions of the slope PDE (6.28). We are unaware, however, of any rigorous results concerning the existence of such continuum self-similar solutions. Following [51], we assume that $m(r, t) \approx \hat{m}(\eta)$ the variable $\eta = r/(Bt)^{1/4}$ and sufficiently large t; then PDE (6.28) is converted to a similarity ODE [51]. For ease of notation, we will remove the circumflex above the m in the above similarity slope variable and use

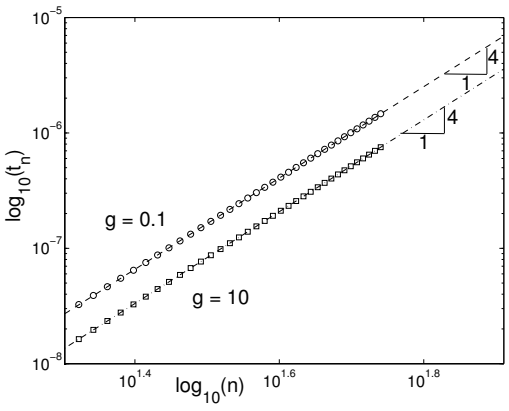

Figure 6.3: Log-log plot of collapse times t_n versus n, for step interaction parameters $g = 0.1$ and 10.

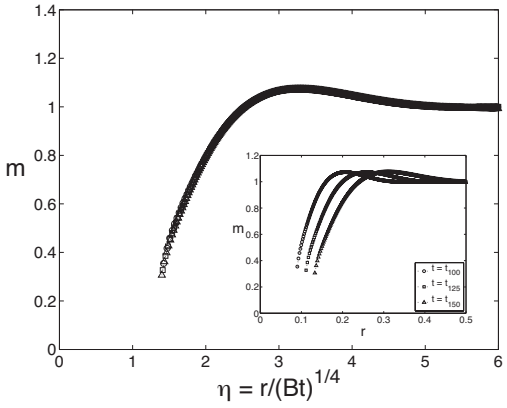

Figure 6.4: Discrete slope m_i versus radial coordinate r_i for different collapse times $t = t_n$ (inset) and scaled variable $r_i/(Bt_n)^{1/4}$ (main plot). The step interaction parameter is $g = 0.1$ and the number of collapsing steps is $n = 100$, 125 and 150.

prime to denote differentiation with respect to η. Thus, we may write

$$-\frac{\eta}{4}\frac{dm}{d\eta} = \frac{3}{\eta^4} - g\frac{d}{d\eta}\frac{1}{\eta}\frac{d}{d\eta}\eta\frac{d}{d\eta}\frac{1}{\eta}\frac{d}{d\eta}\left(\eta m^2\right), \tag{6.43}$$

for $\eta > \eta_{\rm f} = r_{\rm f}/(Bt)^{1/4}$, i.e. outside the facet.

The boundary conditions (6.30)–(6.33),(6.38),(6.39) are transformed similarly. They are

$$m \to 1, \text{ and } \frac{dm}{d\eta} \to 0 \text{ as } \eta \to \infty; \tag{6.44}$$

$$m(\eta_{\rm f}) = 0; \tag{6.45}$$

$$-\kappa\eta_{\rm f}^3 = 1 + g\eta_{\rm f}\left[-(m^2)' + 2\eta_{\rm f}(m^2)'' + \eta_{\rm f}^2(m^2)'''\right]\big|_{\eta=\eta_{\rm f}}; \tag{6.46}$$

$$\frac{1}{2}\kappa\eta_{\rm f}^3 = 1 - g\eta_{\rm f}\left[(m^2)' + \eta_{\rm f}(m^2)''\right]\big|_{\eta=\eta_{\rm f}}; \tag{6.47}$$

$$\frac{1}{8}\kappa\eta_{\rm f}^3 = 2Q_\xi - Q_\mu\left(1 + g\eta_{\rm f}\,(m^2)'\big|_{\eta=\eta_{\rm f}}\right), \tag{6.48}$$

where the values of Q_μ and Q_ξ are understood to be their respective asymptotic values after many step collapses, and $\kappa = -\dot{h}_{\rm f}(Bt)^{3/4}/B$. Equation (6.48) accounts for both conditions on μ and ξ, equations (6.38) and (6.39), after the constant of integration $b(t)$ is eliminated. If we take $Q_\mu = 1 = Q_\xi$ in the (6.48), removing the jump factors, we recover the natural boundary conditions; see also [51].

Self-similarity will play an important role in the results that follow. In particular, we use similarity solution $m(\eta)$ at all stages of our application of the hybrid scheme, even at small times t when slope profiles may not be self-similar. Therefore we expect significant error at early stages of simulation in the hybrid scheme. In practice, we observe that discrepancies between surface slopes computed using the hybrid scheme and those computed from many-step flow *decrease* significantly as

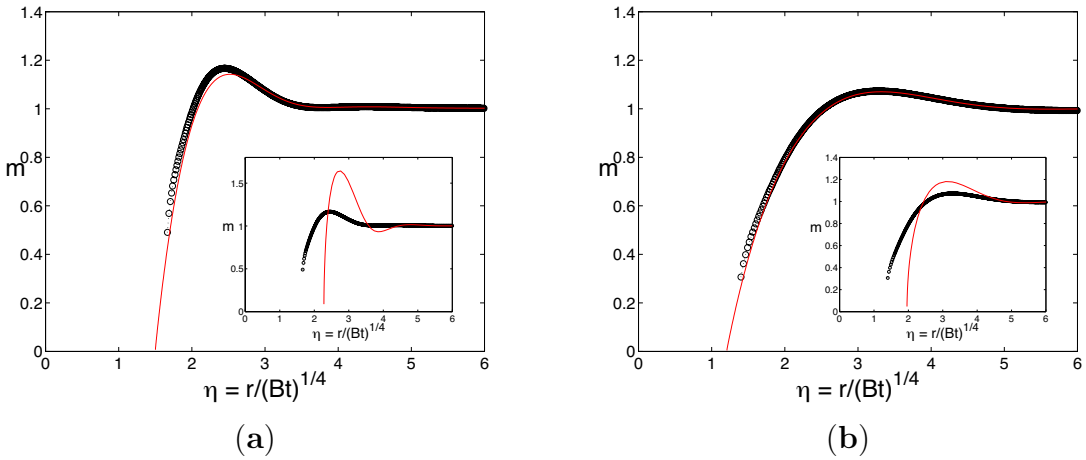

Figure 6.5: Comparison of discrete slope (circles) versus continuum slope (solid curve) using natural boundary conditions (inset) and continuum slope using jump boundary conditions (main plot) when (a) $g = 0.01$ and (b) $g = 0.1$.

the self-similarity assumption improves.

6.4.2 Comparing "natural" and jump boundary conditions

Applying the MATLAB boundary value problem solver bvp4c to the similarity ODE (6.43) and natural boundary conditions, (6.44)–(6.48) with $Q_\mu = 1 = Q_\xi$, we are able to calculate similarity solutions numerically for different values of step interaction parameter g. The inset plots in Figure 6.5 compares the solution of step ODEs with the solution of (6.43) subject to natural boundary conditions. For small values of the parameter g, the continuum model deviates significantly from step simulations. In contrast, the main plots of Figure 6.5, where we include jumps in μ and ξ computed from many-step flow using (6.40) and (6.41), the continuum solution is in good agreement with the solution of step ODEs (6.25).

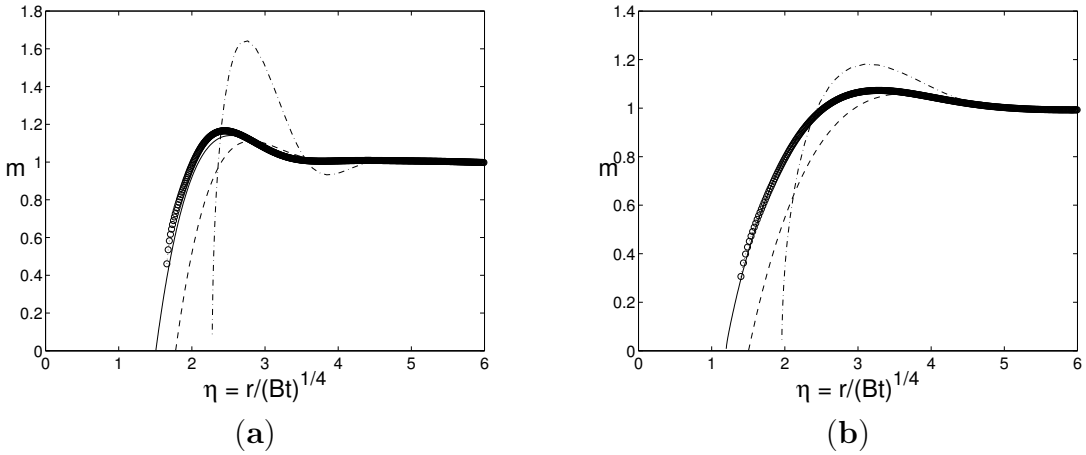

Figure 6.6: Comparison of discrete slope (circles) versus similarity solutions (curves) when (a) $g = 0.01$ and (b) $g = 0.1$. In (a), the dash-dot curve is the continuum slope computed using natural boundary conditions, the dashed curve results from 6 iterations of the hybrid scheme, and the solid curve results from 66 iterations of the hybrid scheme. In (b), the dash-dot curve is the continuum slope computed using natural boundary conditions, the dashed curve results from 1 iteration of the hybrid scheme, and the solid curve results from 16 iterations of the hybrid scheme.

6.4.3 Results of hybrid scheme

We now implement the hybrid scheme presented in section 6.3 for different values of step interaction parameter g. Note that the continuum solution used in applying the condition (6.42) is the *similarity* solution of (6.43) subject to boundary conditions (6.44)–(6.48). What we find is that the continuum similarity solution produced after several iterations of the hybrid scheme using only $M = 3$ virtual steps approaches the (self-similar) slope profile of computed from many-step simulations. This apparent "convergence" is illustrated in Figure 6.6 for $g = 0.01, 0.1$ and in Figure 6.7 for $g = 1$.

Evidently, the number of iterations of the hybrid scheme needed to produce

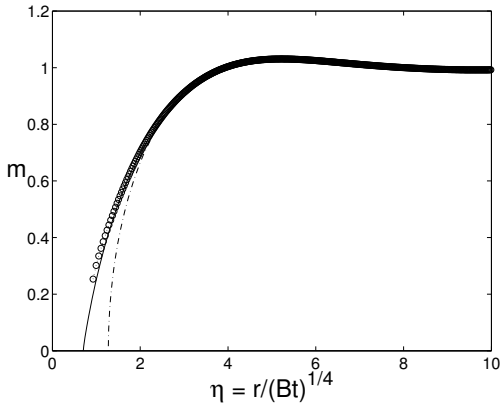

Figure 6.7: Comparison of discrete slope (circles) versus two similarity solutions when $g = 1$. The dash-dot curve is the continuum slope computed using natural boundary conditions and the solid curve results from 1 iteration of the hybrid scheme.

good agreement with the results of many-step simulations decreases with the step interaction parameter g in Figs. 6.6 and 6.7. This behavior is expected since larger step-step interactions tend to result in more uniformly spaced steps, leading to less variation in the slope profile near the facet. In some sense, large g regularizes the slope in a way that is more accurately described by a continuum theory using natural boundary conditions, allowing the hybrid scheme to converge quickly. For example, Figure 6.7 demonstrates that only a single iteration of the hybrid is necessary for the resulting continuum slope profile to give good agreement with many-step simulations. In contrast, for weak step interactions, steps tend to bunch near the facet, introducing a large variations in the slope profile. In that scenario, more iterations of the hybrid scheme are necessary to compensate for the fact that the initial profile (coming from a continuum theory with natural boundary conditions) is a worse approximation of step dynamics near the facet.

6.4.3.1 Error between discrete and continuum solutions

At this point it is necessary comment on our use of the term "convergence". Loosely speaking, we use this term to suggest qualitative agreement between certain discrete and continuum slope profiles. In a more rigorous context, convergence has a precise mathematical definition. Particularly, in numerical analysis, convergence is a property of iterative schemes whose numerical approximations approach the exact solution as a parameter, typically for a time step or mesh size, goes to zero. Our use of the term convergence is *not* intended to describe this property. Instead, we use this term to refer to the apparent tendency for continuum solutions computed using the hybrid scheme to approach slope profiles computed through many-step simulations. In fact, convergence in the sense that we use it here is certainly *not* equivalent to numerical convergence since we do not compare iterations to an exact solution, but rather to the discrete slope profile of an entirely separate model.

While visually appealing, Figure 6.6 need not be the only measure of convergence of the hybrid scheme, even when using our loose definition of the term. An additional measure or the discrepancy between a given continuum similarity solution and the slope profile resulting from step simulations could be invented using the Euclidean norm (ℓ^2-norm), for example.

If $m_i = a/(r_{i+1}(t_n) - r_i(t_n))$ is the discrete slope at the nth collapse time and $m(\eta)$ is a continuum similarity solution, we can compute a relative error between our continuum solution and the results of step simulations by

$$\epsilon(n;g) = \sqrt{\sum_{i \geq n+1} \left| \frac{m_i - m\left(\frac{r_i(t_n)}{t_n^{1/4}}\right)}{m_i} \right|^2} \tag{6.49}$$

Using this definition, we present the following table of relative errors between a reference discrete slope profile and the continuum similarity solution predicted by our hybrid scheme after several iterations. As previously noted, convergence is slowest for weak step interactions, therefore we only report such errors in the worst case we consider, $g = 0.01$.

Collapses	**Relative Error**			
n	$M = 3$	$M = 5$	$M = 7$	$M = 10$
0	4.2335	4.2335	4.2335	4.2335
10	0.1043	0.2417	0.2268	0.1531
20	0.0945	0.1065	0.0512	0.1340
30	0.0689	0.0811	0.0824	0.0874
40	0.0579	0.0617	0.0646	0.0660
50	0.0500	0.0524	0.0538	0.0536
60	0.0471	0.0281	0.0471	0.0282
70	0.0276	0.0276	0.0275	0.0274

In the above table, the value of error corresponding to 0 step collapses corresponds to the discrepancy between the discrete slope profile and the continuum slope resulting from the natural boundary conditions. The drop in error after just 10 step collapses is quite good. By 70 collapses the error for each value of M is less than 1% of the initial error, and the scheme has produced a continuum solution

that is in very good agreement with step simulations. Note that the relative errors are reported here in terms of step collapses; the corresponding number of iterations of the hybrid scheme are given by $n-4$, $n>0$, since we allow 4 steps to collapse in the first iteration of the hybrid scheme.

6.5 Discussion

In this section, we discuss plausible modifications of our formulation. In particular, we address a free boundary problem where a *single jump* is introduced. We also comment on the use of an alternate hybrid scheme in which the step ODEs are linked to the continuum theory via the step-drop condition [51]. Finally, we discuss open challenges in two spacial dimensions.

6.5.1 Boundary conditions with single jump

It is compelling to ask whether the jump factors of equations (6.40)-(6.41) can be chosen uniquely. We claim that, in the context of our empirical approach, the answer to this question is negative if the jump factors are evaluated at times different from the step collapse times, t_n. For example, let us consider the scenario where continuum equation (6.43) is solved numerically by imposition of only *one* jump condition. Specifically, suppose we choose to apply *either* the jump (Q_μ) in the chemical potential *or* the jump (Q_ξ) in the flux generating the chemical potential. Then, by our numerical computations the ensuing continuum theory predicts surface slopes *not* consistent with step motion if the jump is evaluated at

the step collapse times, t_n. This observation indicates that the sequence of times at which a single jump should be evaluated may not be *a priori* characterized; the sequence consists of adjustable parameters whose linkage to $r_i(t)$ appears as unknown and needs to be determined. This hypothetical formulation is deemed as impractical for viable computations of facet evolution. In contrast, the step collapse times tn are characterized by $r_n(t_n) = 0$, which can be incorporated into a hybrid scheme. Following this scenario of a single jump, our numerics also yield the sequence of times, $\hat{t}_n$, required to achieve agreement of continuum predictions with step simulations; $t_n < \hat{t}_n < t_{n+1}$. Each $\hat{t}_n$ is close to t_n for sufficiently large values of g.

6.5.2 Alternate hybrid scheme

It is of some interest to examine whether a viable hybrid scheme can be devised on the basis of step-drop condition (6.13) [51]. Although we have not yet reached a definitive conclusion in this direction, numerical results suggest that our "jump formulation" of boundary conditions (section 6.3.3.1), relying on discontinuities of two thermodynamic variables, forms a more viable approach.

First, we comment on a comparison of the two formulations. Evidently, the jump formulation maintains the thermodynamic structure of continuum theory, since it retains variables such as the chemical potential which is the variational derivative of the surface free energy outside the facet. On the other hand, the step-drop condition makes direct use of the vertical facet speed which is remotely connected

to the thermodynamic structure. In view of these features, we believe that the jump formulation bears certain advantages over the step-drop condition. For example, computations of the surface slope based on the former are more robust. We made an attempt to construct a hybrid scheme that iteratively utilizes the step-drop condition. Numerical results of this scheme indicate poor convergence after a large number of iterations, in contrast to the outcomes of the hybrid scheme in section 6.3.4. This behavior is possibly due to significant numerical error in the continuum solution because of error in the step collapse time differences, $t_{n+1} - t_n$, explicitly used in the step-drop condition.

6.5.3 Issues with facets in 2D

The extension of our formulation to full 2D, e.g., for periodic surface corrugations, calls for improvements of our approach. An emerging issue is to numerically solve the full PDE for the surface height, abandoning the assumption of self similarity for the positive surface slope. A plausible numerical treatment is offered by the finite element method, which has been a valuable tool in studies of surface morphological evolution, e.g., in [8]. However, commonly known versions of this method correspond to the reference case. The incorporation of jump conditions across the facet boundary into this method is an open problem. A related issue is the nature of the jumps at the edges of 2D, noncircular facets. In the radial setting, the jump factors, Q_μ and Q_ξ, depend on the radii of top steps. In a more general 2D setting, a plausible scenario is to use equation (6.40) by replacing r_i by the Lagrangian co-

ordinate of step motion invoked in [52]. In this context, it is of course necessary to formulate the respective equations of motion for steps by use of these Lagrangian coordinates.

Chapter 7: Conclusion and outlook

In this thesis, we have explored several multiscale aspects of crystal surface morphological evolution. A common theme among Chapters 2-6 is the BCF model of crystal growth, and derivatives thereof. Specifically, mesoscale steps are a critical component of our foray into the multiscale modeling, analysis, and simulation of epitaxial growth.

In Part I, we focused on simple, 1D descriptions of a single step with the goal of connecting atomistic KRSOS models to the mesoscale BCF model of step-flow. To that end, we made use of various modeling, analytical, and numerical tools. In particular, we (a) determined equilibrium and steady-state distributions for the KRSOS models we consider, (b) derived discrete counterparts of the BCF model from two atomistic models, and (c) characterized corrections appearing in our discete BCF equations analytically and numerically. The sources of the discrete corrections that emerged from our analysis are especially fascinating: On one hand, corrections to adatom diffusion result from a kinetic interaction between adatoms. On the other hand, the atomistic rules for attachment and detachment bring about corrections to the discrete version of the linear kinetic relation for adatom flux. Stated another way: The second type of correction results from the kinetic interaction *between adatoms*

and the step. Accordingly, we regard this type of interaction as a fundemental feature of 1D SOS-like models of vicinal crystals, as opposed to kinetic interactions among adatoms, which may or may not be present either due to a modeling choice, or by ensuring the system is sufficiently dilue [70, 71].

With the above observations in mind, let us now discuss consequences for the BCF model. First we note that the BCF model is a good approximation of the alternate KRSOS model over a wider range of atomistic parameters than the original KRSOS model because it avoids kinetic interactions between adatoms; for example, the diffusion equation is "exact" for all model parameters. Furthermore, the mesoscale boundary conditions at the step edge will include corrections whenever kinetic adatom-step interactions exist. If they could be removed, which is not possible in SOS models, the linear kinetic relation could also be made "exact". In this sense, the BCF model of a single step assumes that adatoms are completely non-interacting particles; they do not even interact with their environment. This idea extends to 2D models of crystal surfaces as well, where more general interactions between adatoms, and well as between adatoms and their environment, may be included. In this regard, we conjecture that a nonlinear kinetic relation for adatom flux at the step, like the one proposed in Chapter 3, could be derived in 2D. This will be interesting to pursue in future work.

In contrast to Part I, Part II of this thesis has a considerable focus on multiscale simulation. In it, we investigate features of 2D crystal growth and decay spanning three scales: Atomistic, mesoscale, and macroscale. Chapter 5 attempts to connect atomistic and mesoscale models of mound growth. These include the

Ehrlich-Schwoebel barrier at step edges, which induces an uphill mass current [105], and the effect of mass transport mechanisms that are known to lead to slope stabilization in unstable mound growth. Chapter 6 describes the decay of a faceted crystalline mound using a hybrid numerical scheme which couples the motion of a few mesoscale steps near the facet to the macroscale slope profile, governed by a fourth-order nonlinear PDE. Even though many of the results in these last two chapters are empirical, the numerical methods they influence can impart significant physical understanding. For example, the hybrid scheme we use in the facet problem highlights one of the pitfalls of deriving continuum models from discrete theories: Continuum models can overgeneralize aspects of the discrete theory, especially at singularities.

The work in this thesis points us toward many open questions. From Part I, there are at least three interesting issues regarding the KRSOS models that might be worth exploring: First, can we find a necessary condition guaranteeing the existence of a steady-state distribution satisfying the (non-truncated) marginalized master equation? For example, is there a deposition rate, F_{critical}, such that a steady-state exists provided $F \leq F_{\text{critical}}$? A promising direction for proving such a result is suggested by Foster's Theorem [23, 56], which generalizes the notion of Lyapunov stability in the theory of ordinary differential equations to Markov chains. Second, can the estimates involving $\epsilon = F/D$ in Proposition 5 be improved such that external deposition flux $\mathcal{F}$ becomes a leading order term in the continuum limit of our discrete BCF-like equations? While this would be nice to show without restricting the number of adatoms allowed on the terrace, there are advantages to truncation,

as demonstrated in Chapter 3. And third, going beyond the one-step setting, can we define a 1D KRSOS model of multiple steps that enables us to derive elastic or entropic step-step interactions? We leave this as a problem for near-future work.

In 2D, there are a myriad of open questions worth considering. One natural question to ask is if the approach carried out in Part I of this thesis can be applied in a 2D setting, even for a single step. In some respects, the answer is certainly yes. It is very reasonable, for example, to follow our approach in the derivation of a diffusion equation for adatoms, even with the nucleation of small islands. Along this line, there are already examples of this sort of derivation [61, 62]. However, a derivation for boundary conditions in 2D would be quite difficult due to complex step geometries. We speculate that the boundary conditions in 2D will also involve discrete corrections since adatoms still interact with steps. It would be a great achievement, for example, if our master equation approach could be used to derive the Gibbs-Thompson formula directly, and account for discrete corrections [43, 54, 55]. Another set of issues that might be worth exploring in 2D by our approach are predictions for step fluctuations [6, 89, 101], and the calculation of step free energy or stiffness in equilibrium [97, 98, 114].

The derivation of a complete mesoscale theory for small islands would be especially useful in the island dynamics model introduced in Chapter 5; it would be nice, for example, to include the effect of cluster diffusion [7, 40, 41, 48]. In this vein, we should recognize the island dynamics model and the level set framework as ripe with opportunities for modeling, analysis, and simulation. The level set method is a highly adaptable numerical method, capable of describing island dynamics which

include essentially any physics of steps we desire. Near future work, in this direction, should bring about the inclusion of elastic step-step interactions in the island dynamics model, as well as an improved incorporation of second-layer nucleation in the presence of Ehrlich-Schwoebel barriers [17, 44, 75, 76].

Appendix A: Selected results from theory of stochastic processes

In this appendix, we review some well known results from the theory of stochastic processes that are invoked in Chapters 2 and 4. The definitions and theorems in this section can be found in many texts on Markov processes, but the main results included here are borrowed from [39, 104].

We will focus on (continuous time) Markov processes which are *time-homogeneous*, *irreducible*, and have a discrete state space, $\mathcal{S}$, that is countably infinite. A stochastic process has the Markov property if, at any given time, the current state of the process contains all information to determine future behavior. Furthermore, it is time homogeneous if evolution is independent of time. The last assumption, irreducibility, implies that every state in $\mathfrak{S}$ can be reached from every other state [39].

Let $p_i(t)$ be the probability that a process is in state $i \in \mathfrak{S}$ at time t. For given initial data, the time evolution of $p_i(t)$ can be described by a *master equation*

$$\dot{p}_i(t) = \sum_{\substack{j\in\mathfrak{S}\\ j\neq i}} [T_{ij}p_j(t) - T_{ji}p_i(t)] \tag{A.1}$$

$$= \sum_{j\in\mathfrak{S}} T_{ij}p_j(t), \tag{A.2}$$

where T_{ij} is the transition rate from state j to state i[1]. Here, $T_{ii} = -\sum_{\substack{j\in\mathfrak{S}\\ j\neq i}} T_{ji}$. Strictly speaking, only one of (A.1) or (A.2) is necessary, but we find advantages

[1]Note that this notation, especially the order of the indices i and j, deviates from the convension

in both. In the former, we see a difference in *probability flux* into and out of state i, respectively. Equation (A.2), has the form of a matrix-vector product, which is used in Section 2.1.

Next, we turn our attention to the long time behavior of the distribution $p_i(t)$, which is governed by the stationary equations

$$\sum_{j\in\mathfrak{S}} T_{ij}p_j(t) = \sum_{j\in\mathfrak{S}} T_{ji}p_i(t). \tag{A.3}$$

This leads to our first definition:

Definition 12. (Steady-state distribution) *A steady-state or stationary distribution is a collection of positive numbers,* $\{\pi_i^{ss}\}_{i=1}^{\infty}$, $\sum_i \pi_i^{ss} = 1$, *that satisfy equation (A.3).*

Regarding the preceeding definition, we now characterize the existence of steady-state distributions in the following theorem [39].

Theorem 1. *If a steady-state distribution exists, it is unique, and is the limiting distribution of master equation (A.1). Furthermore, if we can find a collection of positive numbers that satisfy (A.3), but sum to infinity, no steady-state distribution exists.*

At this stage, two comments about Definition 12 are in order. First, in cases where the state space $\mathfrak{S}$ is actually finite, (unique) solutions to (A.3) always exist. This can shown in a variety of ways, including, e.g. (i) the construction of a suitable Lyapunov function, of which the statistical entropy is a notable example, (ii) Kirchhoff's network theory, or (iii) by the Perron-Frobenius theorem of linear

used in [39], but is more in line with [104].

algebra [39, 85, 104]. An example where no solution exists in the case of countably infinite $\mathfrak{S}$ is described in Section B.

Second, in regards to terminology, we use the term steady-state in the sense of statistical mechanics: it describes any stationary solution to the master equation (A.1), p_i^{ss}, in particular those for which the net probability fluxes $K_{ij} \equiv T_{ij}p_j^{ss} - T_{ji}p_i^{ss} \neq 0$. In some mathematical contexts not connected to statistical mechanics, a stationary solution with nonvanishing probability currents K_{ij} may be referred to as the "equilibrium distribution"; see [38, 85, 118, 119] for examples where equilibrium is viewed as a special stationary solution of master equations. The ensuing condition indicates a Markov process in equilibrium.

Definition 13. (Equilibrium distribution) *An equilibrium distribution is a steady-state distribution of (A.1) that also satisfies the detailed balance conditions*

$$T_{ij}p_j^{eq} = T_{ji}p_i^{eq}, \quad \text{for all } i, j. \tag{A.4}$$

The importance of detailed balance is paramount in equilibrium statistical mechanics, and extremely useful in determining the stationary solutions to the master equation (A.1). The next theorem illustrates this point.

Theorem 2. *If $\{\tilde{p}_i\}_{i=0}^{\infty}$ is a collection of positive numbers whose sum is finite, and $T_{ij}\tilde{p}_j = T_{ji}\tilde{p}_i$ for all i and j, then $\{\tilde{p}_i\}_{i=0}^{\infty}$ may be normalized to give the unique equilibrium distribution of master equation (A.1).*

Theorem 2 is invoked in Chapters 2 and 4 in order to obtain the equilibrium distributions of different versions of the KRSOS model.

The property of detailed balance ensures that the probability flux into and out of each state are balanced for equilibrium processes. In this regard, conditions (A.4) are intimately connected to the idea of *reversibility*. That is, a reversible Markov process has the property that, if time is reversed, the resulting process is indistinguishable from the original. For our purposes, we will regard the existance of $\{p_i^{eq}\}_{i=1}^{\infty}$ satisfying (A.4) as the defining feature of reversible processes. An equivalent characterization of reversibility is given by Kolmogorov's criteria on the transition rates of the master equation (A.1) [39]:

Theorem 3. (Kolmogorov's criteria) *A stationary Markov process is reversible if and only if its transition rates satisfy*

$$T_{i_0,i_1}T_{i_1,i_2}\cdots T_{i_{n-1},i_n}T_{i_n,i_0} = T_{i_0,i_n}T_{i_n,i_{n-1}}\cdots T_{i_2,i_1}T_{i_1,i_0} \tag{A.5}$$

for any finite sequence of states $i_1, i_2, \ldots, i_n \in \mathfrak{S}$.

The most appealing feature of Kolmogorov's criteria is that the existence of a unique equilibrium distribution satisfying the master equation (A.1) can be deduced from the *transition rates alone*, whereas Theorem 2 essentially requires us to guess the equilibrium distribution outright.

The class of reversible Markov processes are attractive from a modeling perspective since they describe a broad range of phenomena. Reversibility is also a desirable property analytically since it affords us a great deal of flexiblity in assigning (or perturbing) transition rates T_{ij}. The final theorem presented in this appendix illustrates one useful consequence of reversibility [39].

Theorem 4. (Truncation theorem) *If a reversible Markov process with state space* $\mathfrak{S}$ *and equilibrium distribution* p_i^{eq}, $i \in \mathfrak{S}$, *is truncated to the set* $\mathcal{A} \subset \mathfrak{S}$ *then the resulting Markov process is reversible and has equilibrium distribution*

$$\frac{p_i^{eq}}{\sum_j p_j^{eq}}, \quad i \in \mathcal{A}. \tag{A.6}$$

Theorem 4 justifies the truncation of the Markov process describing the KR-SOS models in certain parameter regimes.

Appendix B: On birth-death processes

In this appendix, we use a toy model for the birth-death Markov process (see, for example, [39]) to indicate that no steady state of the master equation (2.5) exists for large enough external deposition flux, F.

A birth-death process is a Markov process with infinitely many states, labeled by $n = 0, 1, \ldots$, for which transitions are only allowed between the n-th and $(n+1)$-th states. Our discrete KRSOS model has this structure if we classify configurations $\boldsymbol{\alpha}$ by the number of adatoms on the terrace, i.e., by the cardinality $|\boldsymbol{\alpha}| = n$ for $n = 0, 1, \ldots$. For our purposes, the detachment and deposition-from-above events correspond to births while attachment and desorption events correspond to deaths.

Let γ_n denote the rate for the transition from the n-particle state to the $(n+1)$-particle state (the process of "birth") and θ_n denote the rate for the transition from the n-particle state to the $(n-1)$-particle state ("death"); see Figure B.1. If p_n^{ss} is the steady-state probability of the n-particle configuration, we have the following balance equations.

$$\begin{aligned} \gamma_n p_n^{ss} &= \theta_{n+1} p_{n+1}^{ss} \ , \\ \gamma_0 p_0^{ss} &= \theta_1 p_1^{ss} \ . \end{aligned} \tag{B.1}$$

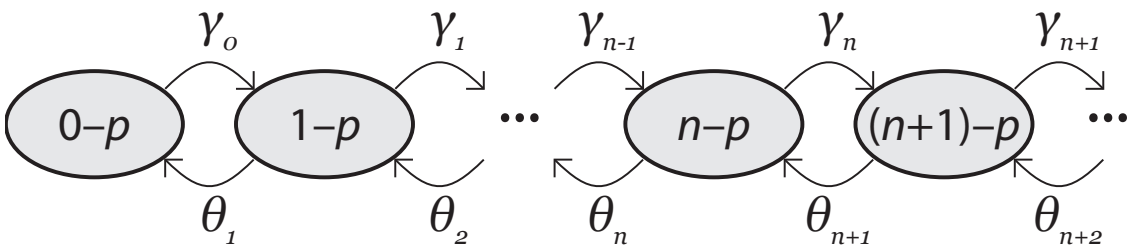

Figure B.1: Schematic of a birth-death Markov process showing the hierarchy of particle states and respective transitions. The arrows connecting successive states depict the underlying Markovian character of transitions. The symbol "n-p" stands for the n-particle state; γ_n denotes the transition from the n-particle to the $(n+1)$-particle state; and θ_n is the rate for the transition from the n-particle state to the $(n-1)$-particle state.

Solving (B.1) for p_n^{ss}, we find the formula

$$p_n^{ss} = \frac{\gamma_n \gamma_{n-1} \cdots \gamma_0}{\theta_{n+1}\theta_n \cdots \theta_1} p_0^{ss}, \tag{B.2}$$

which of course must satisfy the normalization constraint $\sum_{n=0}^{\infty} p_n^{ss} = 1$. This constraint can be written as

$$p_0^{ss} \sum_{n=0}^{\infty} \frac{\gamma_n \gamma_{n-1} \cdots \gamma_0}{\theta_{n+1}\theta_n \cdots \theta_1} < \infty \ . \tag{B.3}$$

In other words, if condition (B.3) does not hold, the probabilities in (B.2) are not normalizable and, thus, no steady state exists.

In our setting of epitaxial growth in 1D, the rates γ_n and θ_n are determined by the transition rates for attachment, detachment, deposition and desorption. These

rates satisfy the following equations.

$$\gamma_n = \frac{1}{p_n^{ss}} \sum_{\substack{\boldsymbol{\alpha} \\ |\boldsymbol{\alpha}|=n}} \Big\{ F + Dk(\phi_+ + \phi_-)\mathbb{1}(\nu_{-1}(\boldsymbol{\alpha}) = 0) \Big\} p_{\boldsymbol{\alpha}}^{ss}$$

$$= F + Dk(\phi_+ + \phi_-)a_n \ , \tag{B.4}$$

$$\theta_n = \frac{1}{p_n^{ss}} \sum_{\substack{\boldsymbol{\alpha} \\ |\boldsymbol{\alpha}|=n}} \Big\{ D\phi_+ \mathbb{1}\left(\nu_1(\boldsymbol{\alpha}) = 1\right) + D\phi_- \mathbb{1}\left(\nu_1(\boldsymbol{\alpha}) = 0\right)$$

$$\times \mathbb{1}\left(\nu_1(\boldsymbol{\alpha}) > 0\right) + \frac{1}{\tau} \sum_{i>0} \mathbb{1}\left(\nu_i(\boldsymbol{\alpha}) > 0\right) \Big\} p_{\boldsymbol{\alpha}}^{ss}$$

$$= D\phi_+ b_n + D\phi_- d_n + \frac{1}{\tau} e_n \ , \tag{B.5}$$

where a_n, b_n and d_n are the probabilities of n-particle configurations that forbid detachment, attachment from the right, and attachment from the left, respectively, and e_n is the average number of adatoms that may desorb from n-particle states. By (B.4) and (B.5), the ratio of birth and death rates is bounded below, i.e., we have the inequality

$$\frac{\gamma_n}{\theta_{n+1}} \geq \frac{F}{D(\phi_+ + \phi_-) + (N-1)/\tau} \quad (n = 0,\, 1,\, \ldots) \ . \tag{B.6}$$

We deduce that the condition $F > D(\phi_+ + \phi_-) + \frac{N-1}{\tau}$ implies that no steady state may exist because normalization condition (B.3) is violated. In the context of the 1D epitaxial system, having $F > D(\phi_+ + \phi_-) + \frac{N-1}{\tau}$ means that the rate particles are added to the system via deposition is faster than the rate particles leave by attachment and desorption. In this case, the number of particles on the terrace constantly grows with time and, hence, no steady state can be established.

Appendix C: Asymptotics of inverse Laplace transform

In this appendix, we derive formula (2.31) for the steady-state probability density. Our derivation relies on the following ideas. (i) We assume that $\epsilon = F/D$ is sufficiently small so that $[I - \epsilon V\mathfrak{D}(s)V^{-1}\mathfrak{B}]^{-1}$ exists and we can write this matrix as $\sum_{n=0}^{\infty}[\epsilon V\mathfrak{D}(s)V^{-1}\mathfrak{B}]^n$; and (ii) the quantity $\mathbf{p}^{ss}$, which is the limit of $\mathbf{p}(t)$ as $t \to \infty$, comes from contributions to the inverse Laplace transform of (2.30) corresponding to the pole at $s = \lambda_1 = 0$ in the Laplace complex (s-) domain. Recall that $\mathfrak{D}(s) := \text{diag}\{(s - D\lambda_j)^{-1}\}_{j=1}^{\Omega(M)}$, where λ_j are the eigenvalues of matrix $\mathfrak{A}$ of the deposition-free problem. For a review of basic techniques in computing inverse Laplace transforms, which we do not elaborate on here, see [84].

Let us now elaborate on these ideas. From (i) we may write $\mathbf{p}(t)$ as

$$\begin{aligned}\mathbf{p}(t) &= \frac{1}{2\pi i}\int_{\gamma-i\infty}^{\gamma+i\infty}\sum_{n=0}^{\infty}\left(\epsilon V\mathfrak{D}(s)V^{-1}\mathfrak{B}\right)^n V\mathfrak{D}(s)V^{-1}\mathbf{p}(0)e^{st}ds \\ &= \frac{1}{2\pi i}\sum_{n=0}^{\infty}\epsilon^n V\mathcal{I}_n(t)V^{-1}\mathbf{p}(0)\ , \end{aligned} \tag{C.1}$$

where γ is a positive constant and the integrals $\mathcal{I}_n(t)$ are defined by

$$\mathcal{I}_n(t) = \int_{\gamma-i\infty}^{\gamma+i\infty}\left(\mathfrak{D}(s)\tilde{\mathfrak{B}}\right)^n\mathfrak{D}(s)\,e^{st}ds\ ; \quad \tilde{\mathfrak{B}} := V^{-1}\mathfrak{B}V\ . \tag{C.2}$$

The integrand in (C.2) is a matrix resulting from the product $(\mathfrak{D}\tilde{\mathfrak{B}})^n\mathfrak{D}$, whose

entries have the form

$$\left[(\mathfrak{D}\tilde{\mathfrak{B}})^n\mathfrak{D}\right]_{ij} = \frac{\tilde{b}_{ik_1}\tilde{b}_{k_1k_2}\cdots\tilde{b}_{k_{n-2}k_{n-1}}\tilde{b}_{k_{n-1}j}}{(s-\lambda_i)(s-\lambda_{k_1})\cdots(s-\lambda_{k_{n-1}})(s-\lambda_j)}\ ; \tag{C.3}$$

$\tilde{b}_{kl}$ are appropriate coefficients independent of the Laplace variable, s.

By (ii) above, since we seek the steady-state solution $\mathbf{p}^{ss}$, the main contribution to the integral (C.2) comes from the pole at $s = \lambda_1 = 0$. The only terms which include $(s-\lambda_1)^{-1}$ are those with $j = 1$ in (C.3). This conclusion can be reached after simplification in the algebra, which can be described as follows. The rows of the matrix V^{-1} contain the left-eigenvectors of matrix $\mathfrak{A}$. Because of conservation of probability, by which the column sums of $\mathfrak{A}$ and $\mathfrak{B}$ are zero, we must have $(V^{-1})_{1i} = (V^{-1})_{1j}$ for all i, j. The matrix $V^{-1}\mathfrak{B}$, which forms the left matrix product in the $\tilde{\mathfrak{B}}$ defined in (C.2), must obey

$$\sum_i \left(V^{-1}\right)_{1i}(\mathfrak{B})_{ij} = 0 \quad \text{for all } j. \tag{C.4}$$

Hence, the right-hand side of (C.3) vanishes whenever any of the indices $i, k_1, k_2, \ldots k_{n-1}$ is equal to unity. Consequently, the steady-state contributions to integral (C.2) come only from simple poles at $s = \lambda_1$, specifically the terms in (C.3) for which $j = 1$.

If $n = 0$, integral (C.2) equals $e^{Dt\Lambda}$, the inverse transform of $\mathfrak{D}(s)$. If $n > 0$ an asymptotic expansion for $\mathcal{I}_n(t)$ as $t \to \infty$ may be computed using the residue

theorem, viz.,

$$
\begin{aligned}
[\mathcal{I}_n(t)]_{ij} &= \int_{\gamma-i\infty}^{\gamma+i\infty} \left[(\mathfrak{D}\tilde{\mathfrak{B}})^n \mathfrak{D}\right]_{ij} e^{st} ds \\
&= \int_{\gamma-i\infty}^{\gamma+i\infty} \frac{\tilde{b}_{ik_1}\tilde{b}_{k_1k_2}\cdots\tilde{b}_{k_{n-2}k_{n-1}}\tilde{b}_{k_{n-1}j}}{(s-\lambda_i)(s-\lambda_{k_1})\cdots(s-\lambda_{k_{n-1}})(s-\lambda_j)} e^{st} ds \\
&\sim 2\pi i \sum_{i,\, k_1,\, k_2,\, \ldots,\, k_{n-1}\neq 1} \frac{\tilde{b}_{ik_1}\tilde{b}_{k_1k_2}\cdots\tilde{b}_{k_{n-2}k_{n-1}}\tilde{b}_{k_{n-1}1}}{(-\lambda_i)(-\lambda_{k_1})\cdots(-\lambda_{k_{n-1}})} \\
&= \begin{cases} 2\pi i \left[\left(-\Lambda^\dagger \tilde{\mathfrak{B}}\right)^n\right]_{i1} , & j = 1 , \\ 0 , & j > 1 , \end{cases}
\end{aligned}
\tag{C.5}
$$

as $t \to \infty$. In the above calculation, the symbol $\sim$ implies that the respective result of contour integration leaves out contributions from poles other than $s = \lambda_1$ in the limit $t \to \infty$. For the same reason, all entries in the matrix $\mathcal{I}_n(t)$ other than the first column are asymptotically small and are neglected.

Finally, by substitution of asymptotic formula (C.5) into (C.1), we compute the steady-state probability distribution as

$$
\begin{aligned}
\mathbf{p}^{ss,\epsilon} &= \sum_{n=0}^{\infty} \epsilon^n V \left(-\Lambda^\dagger \tilde{\mathfrak{B}}\right)^n [\mathbf{e}_1, \mathbf{0}, \mathbf{0}, \ldots, \mathbf{0}] V^{-1} \mathbf{p}(0) \\
&= \sum_{n=0}^{\infty} \left(-\epsilon \mathfrak{A}^\dagger \mathfrak{B}\right)^n \mathbf{p}^0 ,
\end{aligned}
\tag{C.6}
$$

which leads to (2.31). In the above, we used the definition $\tilde{\mathfrak{B}} = V^{-1}\mathfrak{B}V$ along with $\mathfrak{A}^\dagger = V\Lambda^\dagger V^{-1}$. Equation (C.6) is written in terms of the equilibrium distribution, $\mathbf{p}^0$, which satisfies (2.9) when $\epsilon = 0$. This distribution can be derived in the same way as (2.14), or computed as $\mathbf{p}^0 = \lim_{t\to\infty} \exp(D\mathfrak{A}t)\mathbf{p}(0) = V[\mathbf{e}_1, \mathbf{0}, \mathbf{0}, \ldots, \mathbf{0}]V^{-1}\mathbf{p}(0)$, where $\mathbf{e}_1$ is the $\Omega(M)$-dimensional vector $\mathbf{e}_1 = (1, 0, 0, \ldots, 0)^T$.

Bibliography

[1] David M Ackerman and JW Evans. Boundary conditions for Burton-Cabrera-Frank type step-flow models: Coarse-graining of discrete 2d deposition-diffusion equations. *Multiscale Modeling & Simulation*, 9(1):59–88, 2011.

[2] Jacques G Amar. Effects of crystalline microstructure on epitaxial growth. *Physical Review B*, 54(20):14742, 1996.

[3] Jacques G Amar and Fereydoon Family. Critical cluster size: Island morphology and size distribution in submonolayer epitaxial growth. *Physical Review Letters*, 74(11):2066, 1995.

[4] GS Bales and DC Chrzan. Dynamics of irreversible island growth during submonolayer epitaxy. *Physical Review B*, 50(9):6057, 1994.

[5] Lev Balykov and Axel Voigt. A 2+ 1-dimensional terrace-step-kink model for epitaxial growth far from equilibrium. *Multiscale Modeling & Simulation*, 5(1):45–61, 2006.

[6] NC Bartelt, TL Einstein, and Ellen D Williams. Measuring surface mass diffusion coefficients by observing step fluctuations. *Surface Science*, 312(3):411–421, 1994.

[7] Alexander Bogicevic, Shudun Liu, Joachim Jacobsen, Bengt Lundqvist, and Horia Metiu. Island migration caused by the motion of the atoms at the border: Size and temperature dependence of the diffusion coefficient. *Physical Review B*, 57(16):R9459, 1998.

[8] Andrea Bonito, Ricardo H Nochetto, John Quah, and Dionisios Margetis. Self-organization of decaying surface corrugations: A numerical study. *Physical Review E*, 79(5):050601, 2009.

[9] Alfred B Bortz, Malvin H Kalos, and Joel L Lebowitz. A new algorithm for Monte Carlo simulation of Ising spin systems. *Journal of Computational Physics*, 17(1):10–18, 1975.

[10] Achi Brandt. Multiscale scientific computation: Review 2001. In *Multiscale and multiresolution methods*, pages 3–95. Springer, 2002.

[11] P. Bremaud. *Markov Chains: Gibbs Fields, Monte Carlo Simulation, and Queues*. Texts in Applied Mathematics. Springer New York, 2001.

[12] W-K_ Burton, N Cabrera, and FC Frank. The growth of crystals and the equilibrium structure of their surfaces. *Philosophical Transactions of the Royal Society of London A: Mathematical, Physical and Engineering Sciences*, 243(866):299–358, 1951.

[13] Russel E Caflisch, MF Gyure, Barry Merriman, SJ Osher, Christian Ratsch, DD Vvedensky, and JJ Zinck. Island dynamics and the level set method for epitaxial growth. *Applied Mathematics Letters*, 12(4):13–22, 1999.

[14] Russel E Caflisch, E Weinan, Mark F Gyure, Barry Merriman, and Christian Ratsch. Kinetic model for a step edge in epitaxial growth. *Physical Review E*, 59(6):6879, 1999.

[15] Stephen L Campbell and Carl D Meyer. *Generalized inverses of linear transformations*, volume 56. SIAM, 2009.

[16] KJ Caspersen and JW Evans. Metal homoepitaxial growth at very low temperatures: Lattice-gas models with restricted downward funneling. *Physical Review B*, 64(7):075401, 2001.

[17] Claudio Castellano and Paolo Politi. Spatiotemporal distribution of nucleation events during crystal growth. *Physical Review Letters*, 87(5):056102, 2001.

[18] Paolo Cermelli and Michel Jabbour. Multispecies epitaxial growth on vicinal surfaces with chemical reactions and diffusion. In *Proceedings of the Royal Society of London A: Mathematical, Physical and Engineering Sciences*, volume 461, pages 3483–3504. The Royal Society, 2005.

[19] Susan Chen, Barry Merriman, Myungjoo Kang, Russel E Caflisch, Christian Ratsch, Li-Tien Cheng, Mark Gyure, Ronald P Fedkiw, Christopher Anderson, and Stanley Osher. A level set method for thin film epitaxial growth. *Journal of Computational Physics*, 167(2):475–500, 2001.

[20] AA Chernov. The spiral growth of crystals. *Physics-Uspekhi*, 4(1):116–148, 1961.

[21] Shaun Clarke and Dimitri D Vvedensky. Growth kinetics and step density in reflection high-energy electron diffraction during molecular-beam epitaxy. *Journal of Applied Physics*, 63(7):2272–2283, 1988.

[22] Shaun Clarke and Dimitri D Vvedensky. Growth mechanism for molecular-beam epitaxy of group-iv semiconductors. *Physical Review B*, 37(11):6559, 1988.

[23] OLV Costa and François Dufour. A sufficient condition for the existence of an invariant probability measure for Markov processes. *Journal of Applied Probability*, pages 873–878, 2005.

[24] Gert Ehrlich and FG Hudda. Atomic view of surface self-diffusion: Tungsten on tungsten. *The Journal of Chemical Physics*, 44(3):1039–1049, 1966.

[25] Theodore L Einstein, Alberto Pimpinelli, Diego Luis González, and Josue R Morales-Cifuentes. Progress in characterizing submonolayer island growth: Capture-zone distributions, growth exponents, & hot precursors. In *Journal of Physics: Conference Series*, volume 640, page 012024. IOP Publishing, 2015.

[26] James W Evans, DE Sanders, Patricia A Thiel, and Andrew E DePristo. Low-temperature epitaxial growth of thin metal films. *Physical Review B*, 41(8):5410, 1990.

[27] JW Evans. Factors mediating smoothness in epitaxial thin-film growth. *Physical Review B*, 43(5):3897, 1991.

[28] JW Evans, PA Thiel, and Maria C Bartelt. Morphological evolution during epitaxial thin film growth: Formation of 2d islands and 3d mounds. *Surface Science Reports*, 61(1):1–128, 2006.

[29] Lawrence C Evans. Partial differential equations. *Graduate Studies in Mathematics*, 19, 1998.

[30] Mi-Ho Giga and Yoshikazu Giga. Very singular diffusion equations: second and fourth order problems. *Japan Journal of Industrial and Applied Mathematics*, 27(3):323–345, 2010.

[31] EE Gruber and WW Mullins. On the theory of anisotropy of crystalline surface tension. *Journal of Physics and Chemistry of Solids*, 28(5):875–887, 1967.

[32] J Harris and B Kasemo. On precursor mechanisms for surface reactions. *Surface Science*, 105(2):L281–L287, 1981.

[33] Kerson Huang. Statistical mechanics. 1987.

[34] Navot Israeli and Daniel Kandel. Profile scaling in decay of nanostructures. *Physical Review Letters*, 80(15):3300, 1998.

[35] Navot Israeli and Daniel Kandel. Profile of a decaying crystalline cone. *Physical Review B*, 60(8):5946, 1999.

[36] Hyeong-Chai Jeong and Ellen D Williams. Steps on surfaces: experiment and theory. *Surface Science Reports*, 34(6):171–294, 1999.

[37] Yohei Kashima. A subdifferential formulation of fourth order singular diffusion equations. *Advances in Mathematical Sciences and Applications*, 14:49–74, 2004.

[38] Sheldon Katz, Joel L Lebowitz, and Herbert Spohn. Nonequilibrium steady states of stochastic lattice gas models of fast ionic conductors. *Journal of Statistical Physics*, 34(3-4):497–537, 1984.

[39] Frank P Kelly. *Reversibility and stochastic networks*. Cambridge University Press, 2011.

[40] SV Khare, NC Bartelt, and TL Einstein. Diffusion of monolayer adatom and vacancy clusters: Langevin analysis and Monte Carlo simulations of their Brownian motion. *Physical Review Letters*, 75(11):2148, 1995.

[41] SV Khare and TL Einstein. Brownian motion and shape fluctuations of single-layer adatom and vacancy clusters on surfaces: Theory and simulations. *Physical Review B*, 54(16):11752, 1996.

[42] R Kobayashi and Yt Giga. Equations with singular diffusivity. *Journal of Statistical Physics*, 95(5-6):1187–1220, 1999.

[43] Badrinarayan Krishnamachari, James McLean, Barbara Cooper, and James Sethna. Gibbs-Thomson formula for small island sizes: Corrections for high vapor densities. *Physical Review B*, 54(12):8899, 1996.

[44] Joachim Krug, Paolo Politi, and Thomas Michely. Island nucleation in the presence of step-edge barriers: Theory and applications. *Physical Review B*, 61(20):14037, 2000.

[45] F Lançon and J Villain. Kinetics of ordering and growth at surfaces. 1990.

[46] Maozhi Li and JW Evans. Mound slope and shape selection during unstable multilayer growth: Analysis of step-dynamics models including downward funneling. *Physical Review B*, 73(12):125434, 2006.

[47] Maozhi Li, Yong Han, PA Thiel, and JW Evans. Formation of complex wedding-cake morphologies during homoepitaxial film growth of Ag on Ag(111): atomistic, step-dynamics, and continuum modeling. *Journal of Physics: Condensed Matter*, 21(8):084216, 2009.

[48] Alan Lo and Rex T Skodje. Diffusion and evaporation kinetics of large islands and vacancies on surfaces. *The Journal of Chemical Physics*, 111(6):2726–2734, 1999.

[49] Jianfeng Lu, Jian-Guo Liu, and Dionisios Margetis. Emergence of step flow from an atomistic scheme of epitaxial growth in 1+ 1 dimensions. *Physical Review E*, 91(3):032403, 2015.

[50] Dionisios Margetis, Michael J Aziz, and Howard A Stone. Continuum approach to self-similarity and scaling in morphological relaxation of a crystal with a facet. *Physical Review B*, 71(16):165432, 2005.

[51] Dionisios Margetis, Pak-Wing Fok, Michael J Aziz, and Howard A Stone. Continuum theory of nanostructure decay via a microscale condition. *Physical Review Letters*, 97(9):096102, 2006.

[52] Dionisios Margetis and Robert V Kohn. Continuum relaxation of interacting steps on crystal surfaces in 2+1 dimensions. *Multiscale Modeling & Simulation*, 5(3):729–758, 2006.

[53] Jeremy L Marzuola and Jonathan Weare. Relaxation of a family of broken-bond crystal-surface models. *Physical Review E*, 88(3):032403, 2013.

[54] James G McLean, B Krishnamachari, DR Peale, E Chason, James P Sethna, and BH Cooper. Decay of isolated surface features driven by the Gibbs-Thomson effect in an analytic model and a simulation. *Physical Review B*, 55(3):1811, 1997.

[55] Horia Metiu and George Rosenfeld. The evaporation rate of a one-atom-high island on a solid surface: a thermodynamic theory of the size dependence. *Surface Science*, 373(1):L357–L362, 1997.

[56] Sean P Meyn and Richard L Tweedie. Stability of Markovian processes III: Foster-Lyapunov criteria for continuous-time processes. *Advances in Applied Probability*, pages 518–548, 1993.

[57] Thomas Michely and Joachim Krug. *Islands, mounds and atoms*, volume 42. Springer Science & Business Media, 2012.

[58] Chohong Min and Frédéric Gibou. Geometric integration over irregular domains with application to level-set methods. *Journal of Computational Physics*, 226(2):1432–1443, 2007.

[59] Chaouqi Misbah, Olivier Pierre-Louis, and Yukio Saito. Crystal surfaces in and out of equilibrium: A modern view. *Reviews of Modern Physics*, 82(1):981, 2010.

[60] Josue R Morales-Cifuentes, TL Einstein, and Alberto Pimpinelli. How "hot precursors" modify island nucleation: A rate-equation model. *Physical Review Letters*, 113(24):246101, 2014.

[61] Andrea K Myers-Beaghton and Dimitri D Vvedensky. Nonlinear equation for diffusion and adatom interactions during epitaxial growth on vicinal surfaces. *Physical Review B*, 42(9):5544, 1990.

[62] Andrea K Myers-Beaghton and Dimitri D Vvedensky. Generalized Burton-Cabrera-Frank theory for growth and equilibration on stepped surfaces. *Physical Review A*, 44(4):2457, 1991.

[63] Kanna Nakamura and Dionisios Margetis. Discrete and continuum relaxation dynamics of faceted crystal surface in evaporation models. *Multiscale Modeling & Simulation*, 11(1):244–281, 2013.

[64] Irakli Vakhtangi Odisharia. *Simulation and analysis of the relaxation of a crystalline surface*. PhD thesis, New York University, 2006.

[65] Stanley Osher and Ronald Fedkiw. *Level set methods and dynamic implicit surfaces*, volume 153. Springer Science & Business Media, 2006.

[66] Stanley Osher and James A Sethian. Fronts propagating with curvature-dependent speed: algorithms based on hamilton-jacobi formulations. *Journal of Computational Physics*, 79(1):12–49, 1988.

[67] Stanley Osher and Chi-Wang Shu. High-order essentially nonoscillatory schemes for Hamilton-Jacobi equations. *SIAM Journal on Numerical Analysis*, 28(4):907–922, 1991.

[68] Joe Papac, Dionisios Margetis, Frederic Gibou, and Christian Ratsch. Island-dynamics model for mound formation: Effect of a step-edge barrier. *Physical Review E*, 90(2):022404, 2014.

[69] Joseph Papac, Frédéric Gibou, and Christian Ratsch. Efficient symmetric discretization for the Poisson, heat and Stefan-type problems with Robin boundary conditions. *Journal of Computational Physics*, 229(3):875–889, 2010.

[70] Paul N Patrone, TL Einstein, and Dionisios Margetis. From atoms to steps: The microscopic origins of crystal evolution. *Surface Science*, 625:37–43, 2014.

[71] Paul N Patrone and Dionisios Margetis. Connection of kinetic Monte Carlo model for surfaces to one-step flow theory in 1+ 1 dimensions. *Multiscale Modeling & Simulation*, 12(1):364–395, 2014.

[72] PN Patrone, RE Caflisch, and D Margetis. Characterizing equilibrium in epitaxial growth. *EPL (Europhysics Letters)*, 97(4):48012, 2012.

[73] M Petersen, C Ratsch, RE Caflisch, and A Zangwill. Level set approach to reversible epitaxial growth. *Physical Review E*, 64(6):061602, 2001.

[74] Alberto Pimpinelli and Jacques Villain. *Physics of crystal growth*, volume 53. Cambridge University Press, 1998.

[75] Paolo Politi and Claudio Castellano. Process of irreversible nucleation in multilayer growth. I. failure of the mean-field approach. *Physical Review E*, 66(3):031605, 2002.

[76] Paolo Politi and Claudio Castellano. Process of irreversible nucleation in multilayer growth. II. exact results in one and two dimensions. *Physical Review E*, 66(3):031606, 2002.

[77] C Ratsch, MF Gyure, RE Caflisch, F Gibou, M Petersen, M Kang, J Garcia, and DD Vvedensky. Level-set method for island dynamics in epitaxial growth. *Physical Review B*, 65(19):195403, 2002.

[78] C Ratsch, MF Gyure, S Chen, M Kang, and DD Vvedensky. Fluctuations and scaling in aggregation phenomena. *Physical Review B*, 61(16):R10598, 2000.

[79] C Ratsch and JA Venables. Nucleation theory and the early stages of thin film growth. *Journal of Vacuum Science & Technology A*, 21(5):S96–S109, 2003.

[80] C Ratsch, A Zangwill, P Šmilauer, and DD Vvedensky. Saturation and scaling of epitaxial island densities. *Physical Review Letters*, 72(20):3194, 1994.

[81] LI Rubinshteĭn. *The Stefan problem*, volume 27. American Mathematical Soc., 1971.

[82] Giovanni Russo and Peter Smereka. A remark on computing distance functions. *Journal of Computational Physics*, 163(1):51–67, 2000.

[83] M Saum and Tim P Schulze. The role of processing speed in determining step patterns during directional epitaxy. *Discrete and Continuous Dynamical Systems B*, 11:443–457, 2009.

[84] Joel L Schiff. *The Laplace transform: theory and applications*. Springer Science & Business Media, 2013.

[85] J Schnakenberg. Network theory of microscopic and macroscopic behavior of master equation systems. *Reviews of Modern Physics*, 48(4):571, 1976.

[86] Joshua P Schneider, Kanna Nakamura, and Dionisios Margetis. Role of chemical potential in relaxation of faceted crystal structure. *Physical Review E*, 89(6):062408, 2014.

[87] Tim P Schulze. Efficient kinetic monte carlo simulation. *Journal of Computational Physics*, 227(4):2455–2462, 2008.

[88] Richard L Schwoebel and Edward J Shipsey. Step motion on crystal surfaces. *Journal of Applied Physics*, 37(10):3682–3686, 1966.

[89] Walter Selke. Fluctuations of isolated and confined surface steps of monatomic height. *Physical Review E*, 90(1):012123, 2014.

[90] James Albert Sethian. *Level set methods and fast marching methods: evolving interfaces in computational geometry, fluid mechanics, computer vision, and materials science*, volume 3. Cambridge University Press, 1999.

[91] VB Shenoy and LB Freund. A continuum description of the energetics and evolution of stepped surfaces in strained nanostructures. *Journal of the Mechanics and Physics of Solids*, 50(9):1817–1841, 2002.

[92] Yunsic Shim and Jacques G Amar. Complex behavior in a simple system: Low-temperature Ag/Ag(100) growth revisited. *Physical Review B*, 81(4):045416, 2010.

[93] Chi-Wang Shu and Stanley Osher. Efficient implementation of essentially non-oscillatory shock-capturing schemes. *Journal of Computational Physics*, 77(2):439–471, 1988.

[94] Pavel Šmilauer and Dimitri D Vvedensky. Coarsening and slope evolution during unstable spitaxial growth. *Physical Review B*, 52(19):14263, 1995.

[95] Pavel Šmilauer, Mark R Wilby, and Dimitri D Vvedensky. Reentrant layer-by-layer growth: A numerical study. *Physical Review B*, 47(7):4119, 1993.

[96] Herbert Spohn. Surface dynamics below the roughening transition. *Journal de Physique I*, 3(1):69–81, 1993.

[97] TJ Stasevich and TL Einstein. Analytic formulas for the orientation dependence of step stiffness and line tension: Key ingredients for numerical modeling. *Multiscale Modeling & Simulation*, 6(1):90–104, 2007.

[98] TJ Stasevich, TL Einstein, RKP Zia, M Giesen, H Ibach, and F Szalma. Effects of next-nearest-neighbor interactions on the orientation dependence of step stiffness: Reconciling theory with experiment for Cu(001). *Physical Review B*, 70(24):245404, 2004.

[99] Josef Stoer and Roland Bulirsch. *Introduction to numerical analysis*, volume 12. Springer Science & Business Media, 2013.

[100] Mark Sussman, Peter Smereka, and Stanley Osher. A level set approach for computing solutions to incompressible two-phase flow. *Journal of Computational Physics*, 114(1):146–159, 1994.

[101] F Szalma, W Selke, and S Fischer. Dynamics of surface steps. *Physica A: Statistical Mechanics and its Applications*, 294(3):313–322, 2001.

[102] Ellad B Tadmor, Michael Ortiz, and Rob Phillips. Quasicontinuum analysis of defects in solids. *Philosophical Magazine A*, 73(6):1529–1563, 1996.

[103] FG Tricomi. *Integral Equations*. Dover, New York, 1985.

[104] NG Van Kampen. *Stochastic Processes in Physics and Chemistry*. Elsevier, 2011.

[105] J Villain. Continuum models of crystal growth from atomic beams with and without desorption. *Journal de Physique I*, 1(1):19–42, 1991.

[106] Arthur F Voter. Introduction to the kinetic Monte Carlo method. In *Radiation Effects in Solids*, pages 1–23. Springer, 2007.

[107] John D Weeks and George H Gilmer. Dynamics of crystal growth. *Adv. Chem. Phys*, 40(489):157–227, 1979.

[108] E Weinan, Bjorn Engquist, and Zhongyi Huang. Heterogeneous multiscale method: a general methodology for multiscale modeling. *Physical Review B*, 67(9):092101, 2003.

[109] E Weinan, Bjorn Engquist, Xiantao Li, Weiqing Ren, and Eric Vanden-Eijnden. Heterogeneous multiscale methods: a review. *Commun. Comput. Phys*, 2(3):367–450, 2007.

[110] E Weinan and Nung Kwan Yip. Continuum theory of epitaxial crystal growth. I. *Journal of Statistical Physics*, 104(1-2):221–253, 2001.

[111] DE Wolf and J Villain. Growth with surface diffusion. *EPL (Europhysics Letters)*, 13(5):389, 1990.

[112] Jianguo Yu and Jacques G Amar. Effects of short-range attraction in metal epitaxial growth. *Physical Review Letters*, 89(28):286103, 2002.

[113] Jianguo Yu and Jacques G Amar. Effects of short-range attraction in unstable metal(110) epitaxial growth: Molecular dynamics simulations for cu, ag, and al. *Physical Review B*, 74(15):155403, 2006.

[114] Harold JW Zandvliet. Step free energy of an arbitrarily oriented step on a rectangular lattice with nearest-neighbor interactions. *Surface Science*, 639:L1–L4, 2015.

[115] A Zangwill, CN Luse, DD Vvedensky, and MR Wilby. Equations of motion for epitaxial growth. *Surface Science*, 274(2):L529–L534, 1992.

[116] Renjie Zhao, David M Ackerman, and James W Evans. Refined BCF-type boundary conditions for mesoscale surface step dynamics. *Physical Review B*, 91(23):235441, 2015.

[117] Tong Zhao, John D Weeks, and Daniel Kandel. From discrete hopping to continuum modeling on vicinal surfaces with applications to Si(001) electromigration. *Physical Review B*, 71(15):155326, 2005.

[118] RKP Zia and B Schmittmann. Probability currents as principal characteristics in the statistical mechanics of non-equilibrium steady states. *Journal of Statistical Mechanics: Theory and Experiment*, 2007(07):P07012, 2007.

[119] Royce KP Zia and Beate Schmittmann. A possible classification of nonequilibrium steady states. *Journal of Physics A: Mathematical and General*, 39(24):L407, 2006.